

A Thesis Submitted for the Degree of PhD at the University of Warwick

Permanent WRAP URL:

<http://wrap.warwick.ac.uk/147681>

Copyright and reuse:

This thesis is made available online and is protected by original copyright.

Please scroll down to view the document itself.

Please refer to the repository record for this item for information to help you to cite it.

Our policy information is available from the repository home page.

For more information, please contact the WRAP Team at: wrap@warwick.ac.uk

Photoactive Diazido Platinum(IV) Anticancer Complexes

A thesis submitted in partial fulfilment of the
requirements for the degree of Doctor of Philosophy

By

Huayun Shi, *B. Sc.*

University of Warwick, Department of Chemistry
September 2019

Contents

Acknowledgements	i
Declaration	iii
Conferences	iv
Publications	iv
Abstract	vi
Abbreviations	ix
Chapter 1: Introduction	1
1.1. Cancer and cancer treatment	2
1.1.1. Cancer.....	2
1.1.2. Cancer treatment.....	3
1.2. Phototherapy	4
1.2.1. Photodynamic therapy (PDT)	6
1.2.2. Photoactivated chemotherapy (PACT).....	8
1.3. Platinum-based anticancer complexes	10
1.3.1. Platinum.....	10
1.3.2. Cisplatin and its analogues and derivatives	11
1.3.3. Pt(II) complexes with new mechanism of action	13
1.3.4. Photoactive platinum complexes	15
1.3.4.1. Photoactive Pt(II) complexes	15
1.3.4.2. Photoactive Pt(IV) complexes.....	18
1.4. Derivatisation of photoactive diazido Pt(IV) complexes.....	26
1.4.1. Dual action diazido Pt(IV) complexes.....	27
1.4.2. Targeted delivery of diazido Pt(IV) complexes	30
1.5. Research aims	35
1.6. References.....	36
Chapter 2: Experimental Methods	51
2.1. Materials	52
2.2. Instruments.....	54

2.2.1.	Nuclear magnetic resonance spectroscopy (NMR)	54
2.2.2.	Mass spectrometry (MS)	54
2.2.2.1.	Electrospray ionisation-mass spectrometry (ESI-MS).....	54
2.2.2.2.	HPLC coupled mass spectrometry (LC-MS)	55
2.2.3.	High performance liquid chromatography (HPLC).....	55
2.2.4.	UV-vis absorption spectroscopy.....	56
2.2.5.	Fluorescence spectroscopy	56
2.2.6.	X-ray crystallography	56
2.2.7.	Irradiation devices	57
2.2.8.	Electron paramagnetic resonance (EPR) spectroscopy	58
2.2.9.	Inductively coupled plasma optical emission spectroscopy/mass spectrometry (ICP-OES/MS)	59
2.2.9.1.	ICP-OES.....	59
2.2.9.2.	ICP-MS.....	60
2.2.10.	Confocal fluorescent microscopy	60
2.3.	Methods.....	60
2.3.1.	Dark stability and photodecomposition.....	60
2.3.2.	Nucleobase binding	61
2.3.3.	Cancer cell studies	61
2.3.3.1.	Cell maintainance.....	61
2.3.3.2.	Photo-dark cytotoxicity testing	62
2.3.3.3.	Metal accumulation in cancer cells	63
2.4.	References.....	64

Chapter 3: Photoactive Pt(IV) Complexes with Amino Acid Methyl Esters and Peptides

3.1.	Introduction.....	66
3.2.	Experimental.....	71
3.2.1.	Materials	71
3.2.2.	Synthesis and characterisation.....	72
3.2.2.1.	<i>Trans,trans,trans</i> -[Pt(py) ₂ (N ₃) ₂ (OH)(succ-NHS)] (3)	72
3.2.2.2.	General synthetic route for <i>trans,trans,trans</i> -[Pt(py) ₂ (N ₃) ₂ (OH)(succ-amino acid methyl ester)]	72

3.2.2.3.	<i>Trans,trans,trans</i> -[Pt(py) ₂ (N ₃) ₂ (OH)(succ-cp)] (8).....	74
3.2.3.	Methods and instrumentation	76
3.2.3.1.	HPLC purity test.....	76
3.2.3.2.	Extinction coefficient determination	76
3.2.3.3.	Electron paramagnetic resonance	77
3.2.3.4.	DNA melting temperature	77
3.2.3.5.	Photo-dark cytotoxicity testing	78
3.2.3.6.	Cellular accumulation of platinum.....	78
3.3.	Results.....	78
3.3.1.	Synthesis and characterisation.....	78
3.3.2.	Extinction coefficient studies	80
3.3.3.	Dark stability	81
3.3.4.	Photodecomposition followed by UV-vis and EPR	83
3.3.5.	Photoreactions with 5'-GMP	85
3.3.6.	DNA melting temperature	87
3.3.7.	Photocytotoxicity.....	88
3.3.8.	Cellular accumulation.....	89
3.4.	Discussion.....	90
3.4.1.	Synthesis and characterisation.....	90
3.4.2.	Dark stability and photodecomposition.....	91
3.4.3.	Photoreactions with 5'-GMP and DNA.....	92
3.4.4.	Photocytotoxicity and cellular accumulation	93
3.5.	Conclusion	93
3.6.	References.....	94
 Chapter 4: Mono- and Di-substituted Photoactive Pt(IV) Complexes		98
4.1.	Introduction.....	99
4.2.	Experimental.....	101
4.2.1.	Materials	101
4.2.2.	Synthesis and characterisation.....	102
4.2.3.	Methods and instrumentation	106
4.2.3.1.	HPLC purity test.....	106

4.2.3.2.	X-ray crystallography.....	107
4.2.3.4.	Interaction with avidin	107
4.2.3.5.	Photo-dark cytotoxicity testing	108
4.2.3.6.	Cellular accumulation of platinum.....	108
4.2.3.7.	Cellular morphological change	108
4.3.	Results.....	109
4.3.1.	Synthesis and characterisation.....	109
4.3.2.	X-ray crystallography	110
4.3.3.	Dark stability	115
4.3.4.	Extinction coefficient studies	117
4.3.5.	Cyclic voltammetry	117
4.3.6.	Photodecomposition	117
4.3.7.	Photoreactions with 5'-GMP followed by LC-MS.....	123
4.3.8.	Interaction with avidin.....	124
4.3.9.	Photocytotoxicity.....	125
4.3.10.	Cellular accumulation.....	127
4.3.11.	Cellular morphological change.....	129
4.4.	Discussion.....	130
4.4.1.	Synthesis and characterisation.....	130
4.4.2.	Dark stability, photodecomposition and photoproducts	131
4.4.3.	Photocytotoxicity, cellular accumulation and morphological change.....	132
4.5.	Conclusion	134
4.6.	References.....	135

Chapter 5: Photoactive Pt(IV) Complexes with Fluorescent and Photo-switchable Tags

	138
5.1.	Introduction.....	139
5.2.	Experimental.....	142
5.2.1.	Materials	142
5.2.2.	Synthesis and characterisation.....	142
5.2.3.	Methods and instrumentation	148
5.2.3.1.	HPLC purity test.....	148

5.2.3.2.	Extinction coefficient determination	148
5.2.3.3.	Interaction with HSA	148
5.2.3.5.	Cellular accumulation of platinum	149
5.3.	Results.....	149
5.3.2.	X-ray crystallography	151
5.3.6.	Photodecomposition	160
5.3.8.	Photoreactions with NADH.....	169
5.3.9.	Interaction between Pt(IV) complexes and HSA	170
5.3.10.	Photocytotoxicity.....	171
5.3.11.	Cellular accumulation.....	172
5.4.	Discussion	173
5.4.1.	Synthesis and characterisation.....	173
5.4.2.	Dark stability and photodecomposition	173
5.4.3.	Photoreactions with 5'-GMP and NADH.....	174
5.4.4.	Photocytotoxicity and cellular accumulation	174
5.6.	References.....	176
 Chapter 6: Heteronuclear Photoactive Complexes.....		180
6.1.	Introduction.....	181
6.2.	Experimental.....	182
6.2.1.	Materials	182
6.2.2.	Synthesis and characterisation.....	183
6.2.3.	Methods and instrumentation	184
6.2.3.1.	Purity test.....	184
6.2.3.2.	X-ray crystallography.....	185
6.2.3.3.	Radical trapping	185
6.2.3.4.	Photo-dark cytotoxicity testing	185
6.2.3.5.	Cellular accumulation of platinum.....	185
6.2.3.6.	Singlet oxygen (¹ O ₂) detection.....	186
6.2.3.7.	Detection of H ₂ O ₂	186
6.2.3.8.	ROS production in cell.....	186
6.2.3.9.	Confocal fluorescence microscopy	187

6.3.	Results.....	188
6.3.1.	Synthesis and characterisation.....	188
6.3.2.	X-ray crystallography.....	189
6.3.3.	Dark stability.....	193
6.3.4.	Extinction coefficient studies.....	193
6.3.5.	Cyclic voltammetry.....	194
6.3.6.	Photodecomposition.....	194
6.3.7.	Photoreactions with 5'-GMP.....	201
6.3.8.	Photoreactions with NADH.....	202
6.3.9.	Photocytotoxicity.....	203
6.3.10.	Cellular accumulation.....	205
6.3.11.	Singlet oxygen ($^1\text{O}_2$), hydrogen peroxide and radical generation.....	207
6.3.12.	ROS production in cells.....	209
6.3.13.	Cellular localisation and morphology.....	211
6.4.	Discussion.....	212
6.4.1.	Dark stability and photodecomposition.....	212
6.4.2.	Photoreactions with 5'-GMP and NADH.....	213
6.1.1.	Photocytotoxicity and cellular accumulation.....	214
6.1.2.	Singlet oxygen ($^1\text{O}_2$) detection and ROS production in cell.....	214
6.1.3.	Cellular localisation and morphology.....	215
6.2.	Conclusions.....	215
6.3.	References.....	216
Chapter 7: Conclusions.....		219
7.1.	Conclusions.....	220
7.2.	Future work.....	223
7.3.	References.....	225
Appendix.....		I

Acknowledgements

I appreciate sincerely all of people who have helped me during my PhD studies.

First of all, I would like to thank my supervisor Professor Peter J. Sadler for this great opportunity to work in one of the most prestigious groups in the field, for all of his invaluable guidance, support and patience. It is a great honour to work with such an excellent scientist.

Also, I would like to thank my financial support, a Chancellor's Scholarship from the University of Warwick.

A very big thanks goes to Dr. Abraha Habtemariam for teaching me so many things, for all of the discussion and encouragement, for always being patient to me, for helping me to adapt life in a foreign country as a PhD student.

Another big thanks goes to Dr. V. Venkatesh who guided me to start my research in the dark and always allowed me to use his fumehood.

I would like to thank Dr. Huaiyi Huang who taught me so many experiments both in chemistry and biology. There is no way for me to obtain so much nice data without his help.

I would like to thank Dr. Cinzia Imberti for revising all of my papers, chapters and applications tirelessly, and for her patience in the tedious cell-counting work.

Thank Dr. Isolda Romero-Canelón and Mrs. Ji-inn Song for their enlightenment in cell culture and SRB experiments.

I thank Dr. Jonathan chew for all of his encouragement when we were in C409 office.

I would like to thank all of the technical support from outside my group. Dr. Guy Clarkson for so many crystal structures, Dr. Lijiang Song, Mr. Phil Aston and Mr. James Morrey for training and assistance in MS and ICP, Dr. Ivan Prokes for NMR training. Dr. Ben Breeze and Dr.

Claudio Vallott for setting up the EPR instrument every time for me and the assistance in EPR spectra simulation. Mr. Ian Hands-Portman for confocal experiments. Dr. Nikola Chmel for fluorescence and CD spectroscopy training. Dr. Staniforth, Michael for setting up Infrared Fluorescence spectroscopy. A special thanks to Mr. Jason Noone for all of the IT support and saving my important data from the broken U dish.

I would also like to say thank you to other PJS member who have helped me, Dr. Samya Banerjee, Dr. Feng Chen, Dr. James Coverdale, Dr. Russell Needham, Dr. Jitka Pracharova, Wenying Zhang, and Hannah Bridgewater.

Finally, I would like to thank my parents for their unrequited love and support, and the tireless video chat when I encountered difficult times. They are the best parents in the world. To all of my friends in UK and China, thanks for all of their encouragement and help. I cannot survive without their help.

Declaration

I hereby declare that except where specific reference is made to other sources, the work contained in the Thesis is the original work of the author. It has been composed by myself and has not been submitted, in whole or in part, for any other degree, diploma, or other qualification.

Huayun Shi

September 2019

Conferences

- The 23rd International Symposium on the Photochemistry and Photophysics of Coordination Compounds (ISPPCC 2019), Hong Kong, China, 14th – 19th July, 2019.
- The 14th European Biological Inorganic Chemistry Conference (EuroBIC-14), Birmingham, UK, 26th – 30th August, 2018
- Dalton 2018, Warwick, UK, 3rd – 5th April, 2018
- The 12th International Symposium on Platinum Coordination Compounds in Cancer Chemotherapy (ISPCC 2017), Sydney, Australia, 10th – 14th December, 2017
- The RSC Photochemistry Group Meeting, Birmingham, UK, 14th – 15th September, 2017 (Poster prize)

Publications

- **H. Shi**, Q. Wang, V. Venkatesh, G. Feng, L. S. Young, I. Romero-Canelón, M. Zeng, P. J. Sadler, Photoactive platinum(IV) complex conjugated to a cancer-cell-targeting cyclic peptide, *Dalton. Trans.*, 2019, **48**, 8560–8564.
- **H. Shi**, C. Imberti, P. J. Sadler, Diazido platinum(IV) complexes for photoactivated anticancer chemotherapy, *Inorg. Chem. Front.*, 2019, **6**, 1623–1638.
- **H. Shi**, G. J. Clarkson, P. J. Sadler, Dual action photosensitive platinum(II) anticancer prodrugs with photoreleasable azide ligands, *Inorg. Chim. Acta*, 2019, **489**, 230–235.

- C. Vallotto, E. Shaili, **H. Shi**, J. S. Butler, C. J. Wedge, M. E. Newton, P. J. Sadler, Photoactivatable platinum anticancer complex can generate tryptophan radicals, *Chem. Commun.*, 2018, **54**, 13845–13848.
- **H. Shi**, I. Romero-Canelón, M. Hreusova, O. Novakova, V. Venkatesh, A. Habtemariam, G. J. Clarkson, J. Song, V. Brabec, P. J. Sadler, Photoactivatable cell-selective dinuclear trans diazido platinum(IV) anticancer prodrugs, *Inorg. Chem.*, 2018, **57**, 14409–14420.
- V. Venkatesh, N. Kumar Mishra, I. Romero-Canelón, R. R. Vernooij, **H. Shi**, J. P. C. Coverdale, A. Habtemariam, S. Verma, and P. J. Sadler. Supramolecular photoactivatable anticancer hydrogels, *J. Am. Chem. Soc.*, **2017**, 139, 5656–5659.

Abstract

This thesis is concerned with the design and mechanism of action of photoactive anticancer drugs. In particular, it focuses on the functionalisation of *trans*-diazido Pt(IV) complexes by conjugation of the axial ligands to other biologically-active molecules, to vectors and probes, and aims to red-shift the activation wavelength to allow activation deeper in tissues and enhance their cellular accumulation and photocytotoxicity.

In this thesis, photoactive *trans*-diazido Pt(IV) complexes with a general formula $[\text{Pt}(\text{N}_3)_2(\text{py})_2(\text{OR}_1)(\text{OR}_2)]$ have been synthesised and characterised by NMR, HPLC, ESI-MS, UV-vis and fluorescence spectroscopy, cyclic voltammetry, and X-ray crystallography.

Amino acids are alternative fuels for cancer cells, other than glucose, and thus can be used as targeting vectors in cancer therapy. Complexes **4–7** labeled with amino acid methyl esters and **8** functionalised with a cyclic peptide, exhibited dark stability and photodecomposition upon irradiation with visible light. Pt-GMP adducts, azidyl and hydroxyl radicals were detected from **4–6** upon irradiation, while the formation of these photoproducts was quenched by Trp in **7**. Significant photocytotoxicity and photoactivated Pt accumulation in A2780 ovarian cancer cells were observed for **4–8**.

Mono-substituted diazido Pt(IV) complexes **9–12** were compared with their di-substituted analogues **13–16**. As expected, di-substituted complexes displayed longer HPLC retention times and less negative reduction potentials, therefore lower dark stability in aqueous media than the mono-substituted complexes. However, more potent photocytotoxicity and higher cellular accumulation were detected for di-substituted complexes. Dramatic morphological changes in A2780 cells were observed after irradiation with **11**. Biotinylated **11** also formed a non-covalent adduct with avidin, which resulted in enhanced photocytotoxicity and cellular accumulation compared with **11** alone.

Fluorescence imaging can be used to monitor the pathway of drug within cells and tissues. Diazido Pt(IV) complexes conjugated to coumarin **19**, dansyl **20**, 1,8-naphthalimide **21–23**, and *trans* N=N bond containing azo ligand **24–26** were prepared. The photodecomposition of **19–23** with indigo (420 nm) – green (517 nm) light was monitored by the change of UV-vis absorption, LC-MS, EPR and increased fluorescence. *Trans*-azo ligands in these Pt(IV) complexes can undergo photo-switching to form the *cis*-azo complexes. Photoreactions with 5'-GMP and photo-oxidation of NADH were observed for these complexes. Complexes **19**, **23** and **24–26** displayed significant photocytotoxicity in cancer cells (465 nm), and **23** is also photocytotoxic with green light (520 nm).

Heteronuclear complexes **27** labelled with ferrocene and **28** with [Ir(ppy)₂(bpy-CH₂NH₂)]Cl have red-shifted absorption bands. Satisfactory dark stability for both complexes, and photodecomposition with long wavelength light (420–593 nm) for **27** and a fast rate (decomposition within 5 min) for **28** were observed. Azidyl and hydroxyl radicals, singlet oxygen and other ROS in aqueous solution and in cells were detected for both complexes. Low dark cytotoxicity and significantly enhanced photocytotoxicity were observed with longer excitation wavelength and shorter irradiation time. The higher lipophilicity of **27** and positive charge of **28** are regarded as the main reason for their high cellular accumulation. Ruptured nuclear membranes and released chromosomes were observed in A549 cells exposed to **28** and light, indicating its promising photocytotoxicity with the synergetic effect of the two different metal centres.

Overall, this work significantly advances the functionalisation of *trans*-diazido Pt(IV) complexes in axial positions. Cancer-targeting vectors, active anticancer drugs, fluorescent tags, photo-switchable dyes, and metal complexes have been conjugated to *trans*-diazido Pt(IV) complexes, resulting in photoactivation with long wavelength light, shorter

photodecomposition times, enhanced cellular accumulation and photocytotoxicity, and improved photo-induced cellular ROS levels.

Abbreviations

BCP	Block Copolymer
BODIPY	Boron-dipyrrromethene
CCD	Charge-coupled device
CDDP	Cisplatin
CT	Computer Tomography
CV	Cyclic Voltammetry
CYPMPO	5-(2,2-Dimethyl-1,3-propoxy cyclophosphoryl)-5-methyl-1-pyrroline <i>N</i> -oxide
DCA	Dichloroacetate
DCFH-DA	2',7'-Dichlorodihydrofluorescein diacetate
DEVD	–Asp–Glu–Val–Asp–
DIPEA	<i>N, N</i> -Diisopropylethylamine
DNA	Deoxyribonucleic Acid
DMAP	2-(Dimethylamino)pyridine
DMPO	5, 5-Dimethyl-pyrroline- <i>N</i> -oxide
DMS	dimethyl sulfide
ECACC	European Collection of Cell Cultures
EDC	1-Ethyl-3-(3-dimethylaminopropyl)carbodiimide
EDTA	Ethylenediaminetetraacetic Acid
EPR	Electron Paramagnetic Resonance
EPR (effect)	Enhanced Permeation and Retention
ER	Endoplasmic Reticulum
FA	Formic Acid

FDA	US Food and Drug Administration
FR	Folate Receptor
FRET	Fluorescence Resonance Energy Transfer
5'-GMP	Guanosine Monophosphate
GSH	Glutathione
HABA	2-(4-hydroxyphenylazo)benzoic acid
HBSS	Hank's Balanced Salt Solution
HNPAC	2-Hydroxy-2-(2-nitrophenyl)acetic acid
HDAC	Histone Deacetylase
HPLC	High Performance Liquid Chromatography
HSA	Human Serum Albumin
IC ₅₀	50% growth Inhibitory Concentration
LC-MS	Liquid Chromatography-Mass Spectrometry
ICP-OES	Inductively Coupled Plasma-Optical Emission Spectroscopy
ICP-MS	Inductively Coupled Plasma-Mass Spectrometry
IDO	Indoleamine-2,3-dioxygenase
LED	Light-Emitting Diode
LMCT	Ligand-to Metal Charge Transfer
MLT	Melatonin
MNP	2-Methyl-2-nitrosopropane
MOPEP	4-[2-(4-Methoxyphenyl)ethynyl]pyridine
MR	Magnetic Resonance
NAD	Nicotinamide Adenine Dinucleotide
NHS	<i>N</i> -Hydroxysuccinimide

NCI-60	60 human cancer cell lines used by National Cancer Institute
NIR	Near-infrared (780–2500 nm)
NMR	Nuclear Magnetic Resonance
PACT	Photoactivated Chemotherapy
PBS	Phosphate-Buffered Saline
PDK	Pyruvate Dehydrogenase Kinase
PDT	Photodynamic Therapy
PEG	Polyethylene Glycol
PhB	Phenylbutyrate
PI	Photocytotoxicity Index
RGD	–Arg–Gly–Asp–
RNA	Ribonucleic acid
ROS	Reactive Oxygen Species
RPMI-1640	Roswell Park Memorial Institute-1640
SAHA	Vorinostat (Suberanolohydroxamic acid)
SAR	Structure-Activity Relationship
SMVT	Sodium-dependent Multivitamin Transporter
SOSG	Singlet Oxygen Sensor Green
SubH	Suberoyl-bis-hydroxamic acid
TBTU	<i>O</i> -(Benzotriazol-1-yl)- <i>N,N,N',N'</i> -tetramethyluronium tetrafluoroborate
TEMPO	(2,2,6,6-Tetramethylpiperidin-1-yl)oxyl
TFA	Trifluoroacetic Acid
Trx	Thioredoxin

TPS	Tetraphenylsilole
UCL	Upconversion Luminescence
UCNP	Upconverting Nanoparticles
UVA	Ultraviolet A (315–400 nm)

Chapter 1

Introduction

This thesis is concerned with photoactive anticancer diazido Pt(IV) complexes. This Chapter gives an introduction to cancer and cancer treatment, phototherapy, platinum-based anticancer complexes and the derivatisation of photoactive diazido Pt(IV) complexes.

1.1. Cancer and cancer treatment

1.1.1. Cancer

Cancer is a group of genetic diseases involving uncontrolled growth and spread of cells. The earliest cancer record dates to 1600 BC in Egypt,¹ but cancer remains a great challenge and leading cause of death. An estimated 9.6 million deaths in 2018 were resulted from cancer globally and *ca.* 70% of them occur in countries with middle and low income.² The most common cancer in 2018 was lung cancer (2.09 million cases and 1.76 million deaths), followed by breast, colorectal, prostate, skin (non-melanoma) and stomach cancer.² Leukemia, brain tumours, lymphomas and solid tumours, such as neuroblastoma and Wilms tumour, are most common cancers in children.³ One in five men and one in six women will have cancer at some point in their lifetime under current estimates.⁴ Genetic mutations from environmental factors lead to 90–95% of cancer cases, and tobacco use is responsible for *ca.* 22% cancer death.^{5,6}

Cancerogenesis is a process consisting of initiation of a premalignant cell line and promotion of malignant growth according to the somatic mutation theory,⁷ while the tissue organisation field theory believes that cancerogenesis is defects of tissue architecture.⁸ The hallmarks of cancer were proposed by Hanahan and Weinberg,⁹ including self-sufficiency in growth signals, insensitivity to antigrowth signals, evasion of apoptosis, limitless replicative potential, sustained angiogenesis and tissue invasion and metastasis. Deregulated metabolism and evading the immune system were added to the list of hallmarks later.¹⁰ The six hallmarks dictate malignant growth collectively. Underlying these hallmarks are genome instability and

inflammation, which expedites their acquisition and fosters multiple hallmark functions, respectively.⁹ However, Lazebnik¹¹ pointed out that five hallmarks (except self-sufficiency in growth signals) are also characteristic of benign tumours, and Sonnenschein¹² argued that cancer is a tissue-based disease and these cell-based hallmarks are misleading.

1.1.2. Cancer treatment

Cancer treatment has undergone evolutionary changes, including surgery, radiation therapy, chemotherapy, targeted therapy (including immunotherapy such as monoclonal antibody therapy), hormonal therapy and synthetic lethality.

Surgery is efficient in bulk tumour removal, but it cannot guarantee the eradication of every cancer cell. Thus, surgery is normally accompanied by other forms of treatment. Radiation therapy kills cancer cells by high powered ionising radiations that damage DNA directly or by charged particles and free radicals. However, ionising radiations destroy both cancer and normal cells and results in side effects, such as vomiting, swelling, irreversible local damage to biological macromolecules.

Chemotherapy uses anticancer drugs to remit tumours, which can help other therapies, delay/prevent recurrence, slow down cancer progression, and relieve symptoms (palliative care).¹³ Since chemotherapeutic agents can potentially reach every cell in the body, it is an important cancer treatment modality, especially for advanced cancers. Modern chemotherapy started in the mid-1900s when nitrogen mustard was used to eradicate bone marrow and lymphoid tissues in patients with advanced lymphomas.¹⁴ From 1949 to 2014, sixty-one cytotoxicity-based anticancer drugs were approved by US Food and Drug Administration (FDA), including alkylating agents, antimicrotubule agents, and topoisomerase inhibitors.¹⁵ The major cellular targets of chemotherapeutic agents are DNA, proteins involved in

proliferation, and cellular redox systems.¹⁶ Unfortunately, chemotherapy suffers from a range of side-effects and long-term sequelae due to the poor selectivity of many anticancer drugs.

Targeted therapy is currently an active research area, since it is expected to be more efficient and selective than traditional treatments. Eighty-nine tumour-targeting drugs had been approved by the FDA by the end of 2014, and the majority of them were approved in the last two decades.¹⁵ Monoclonal antibodies and small-molecule drugs are two main types of targeted therapeutic agents. Enzymes and receptors are major drug targets. Significant challenges exist in targeted therapy since reliable predictive biomarkers are limited and genetic alterations have an impact on tumour behaviour which are not thoroughly understood.¹⁷

The location and grade of tumour, as well as the stage of cancer, need to be considered for the choice of treatment. Generally, small stage I tumours can be removed by surgery, while adjuvant therapy (e.g. chemotherapy, radiation therapy) is required to improve the effect of surgery in the treatment of advanced tumours.¹⁸

1.2. Phototherapy

The application of light in medicine dates back to ancient Egypt 4000 years ago, when sunlight was used for the treatment of vitiligo with plants.¹⁹ The father of modern phototherapy, Niels Finsen, was awarded the Nobel Prize in Physiology or Medicine in 1903, having used concentrated ultraviolet light to treat lupus vulgaris.²⁰ Phototherapy has attracted great attention in cancer treatment due to its high spatio-temporal controllability and minimal invasiveness. The choice of light wavelength in phototherapy is a compromise between light penetration and photon energy. According to the Planck–Einstein relation:

$$E = h\nu = hc / \lambda$$

where h is Planck's constant, λ is the wavelength of the radiation and c is the velocity of light, light with shorter wavelength possesses higher energy.²¹ However, the tissue penetration depth of light with short wavelength is smaller than that with long wavelength (Figure 1.1).^{22,23} The ideal wavelength range for phototherapy is between 600–800 nm, the so called “phototherapeutic window”, in which photons have enough energy (> 1.5 eV) and light penetration is sufficiently deep.²⁴

There are two main types of phototherapy, photodynamic therapy (PDT) and photoactivated chemotherapy (PACT).

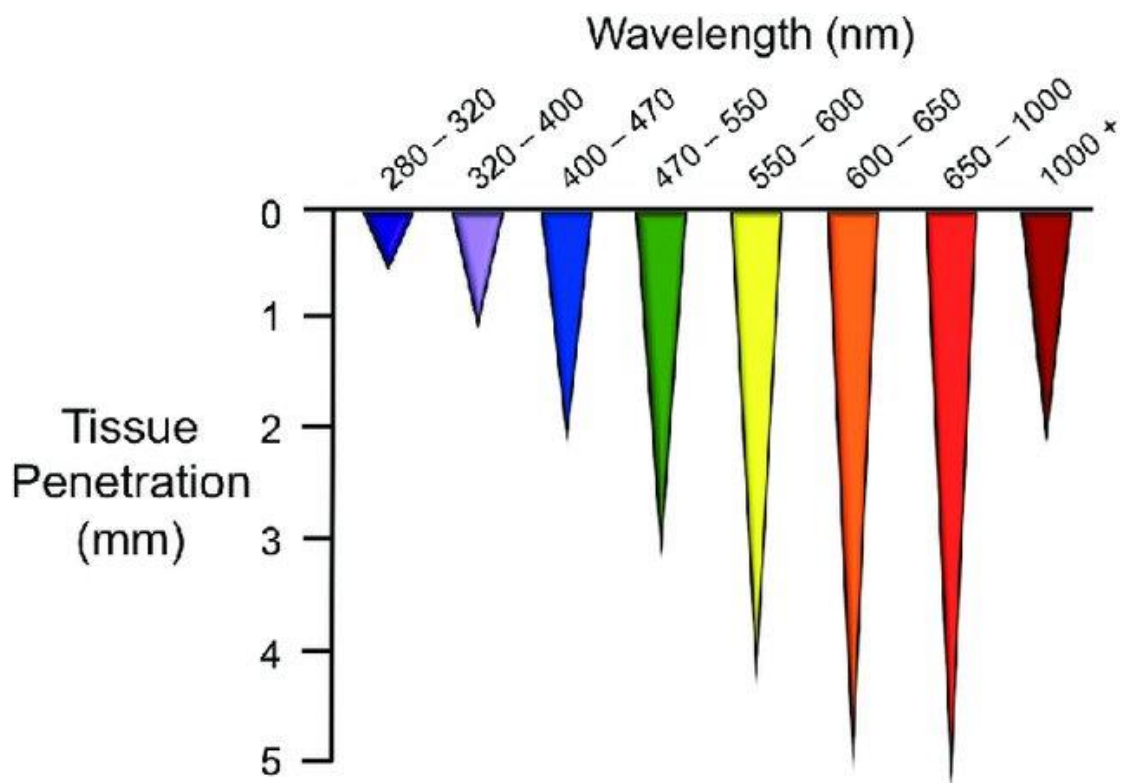


Figure 1.1. Penetration depth of light of different wavelengths in skin tissue. Adapted from *ref.*

23.

1.2.1. Photodynamic therapy (PDT)

PDT is a phototherapy used in the clinic to treat cancer, based on the combination of a photosensitiser, light and oxygen.²⁵ Upon irradiation with light at a specific wavelength, the photosensitiser can be excited and transfer its energy to the surrounding ground-state oxygen, forming radicals (Type I) or $^1\text{O}_2$ (Type II) that are cytotoxic to cancer cells and have short life time and diffusion distance, thus PDT causes only localised cellular damage (Figure 1.2).^{25,26} A major advantage of PDT is that repeated administration without cumulative long-term complications is possible since it is non-invasive.

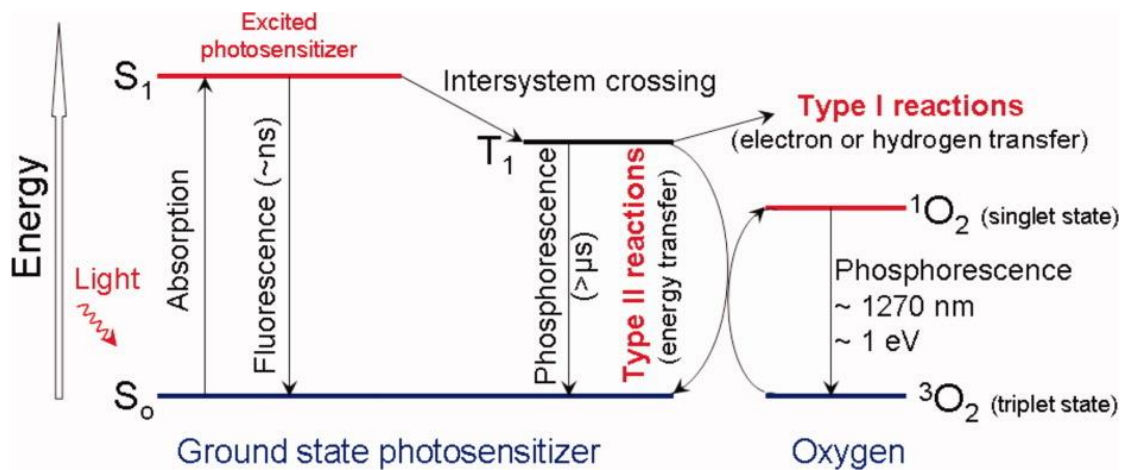


Figure 1.2. Photosensitisation processes illustrated by a modified Jablonski diagram. Light exposure takes a photosensitiser molecule from the ground singlet state (S_0) to an excited singlet state (S_1). The molecule in S_1 may undergo intersystem crossing to an excited triplet state (T_1) and then either form radicals via a Type I reaction or, more likely, transfer its energy to molecular oxygen ($^3\text{O}_2$) and form singlet oxygen ($^1\text{O}_2$), which is the major cytotoxic agent involved in photodynamic therapy. Adapted from *ref.* 26.

Porfimer sodium (Photofrin[®], Figure 1.3a) was the first photosensitiser clinically approved for cancer treatment. It can be activated by red light (630 nm) and remains the most widely

employed photosensitiser.^{26,27} 5-Aminolevulinic acid (Levulan[®], Figure 1.3b), a key biosynthesis precursor of protoporphyrin IX, can be applied topically or administered orally as a prodrug for PDT and is excreted rapidly from body with low side effects.²⁸ Its methyl ester derivative methyl aminolevulinate (Metvix[®], Figure 1.3c) has also been approved by FDA for its shorter incubation time.²⁹ Metal-based photosensitiser **WST-09** (Padoporfin, Figure 1.3d) and its soluble derivative **WST-11** were developed for the treatment of prostate cancer upon near infrared irradiation,³⁰ and **TLD-1433** (Figure 1.3e), a polypyridyl Ru(II) complex, has recently entered clinical trials for non-muscle-invasive bladder cancer.^{31,32}

However, the efficiency of PDT is highly dependent on oxygen, while the oxygen concentration in hypoxic tumour environments is low since tumours rapidly outgrow their blood supply. In addition, the skin photosensitivity caused by PDT, and appreciable dark toxicity of photosensitisers, limit the application of PDT.

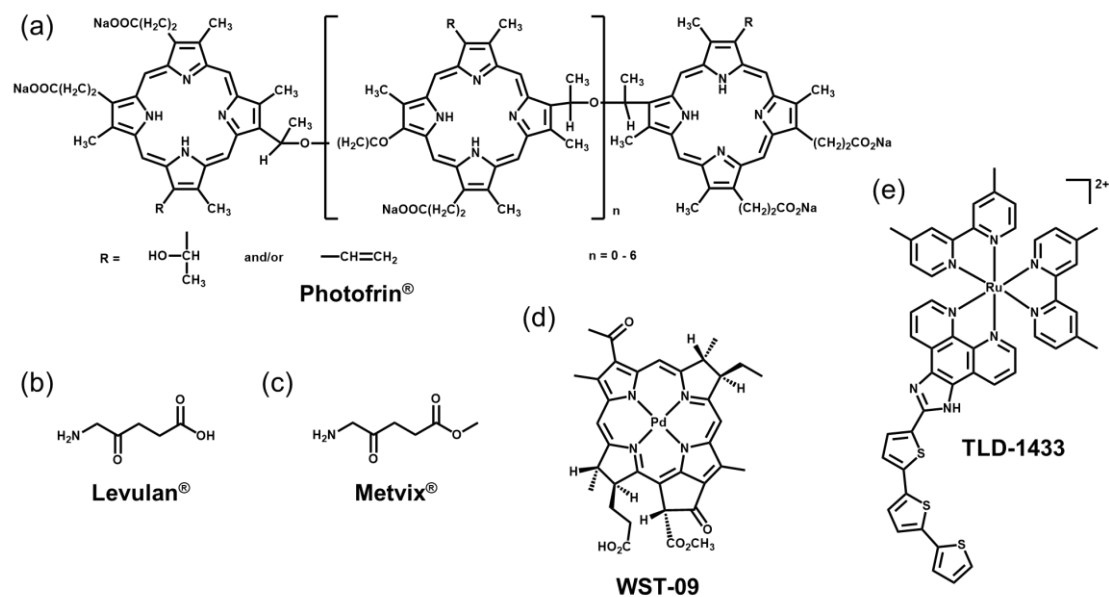


Figure 1.3. Selected PDT agents which have entered clinical trials or have been approved for clinical use.

1.2.2. Photoactivated chemotherapy (PACT)

PACT, in contrast to PDT, is an oxygen-independent phototherapy, which involves chemical changes of prodrugs upon irradiation (Figure 1.4).^{33,34} Activation of metal complex-based PACT can involve photoreduction, photosubstitution, photocleavage of ligand, or photoswitch, as illustrated below.

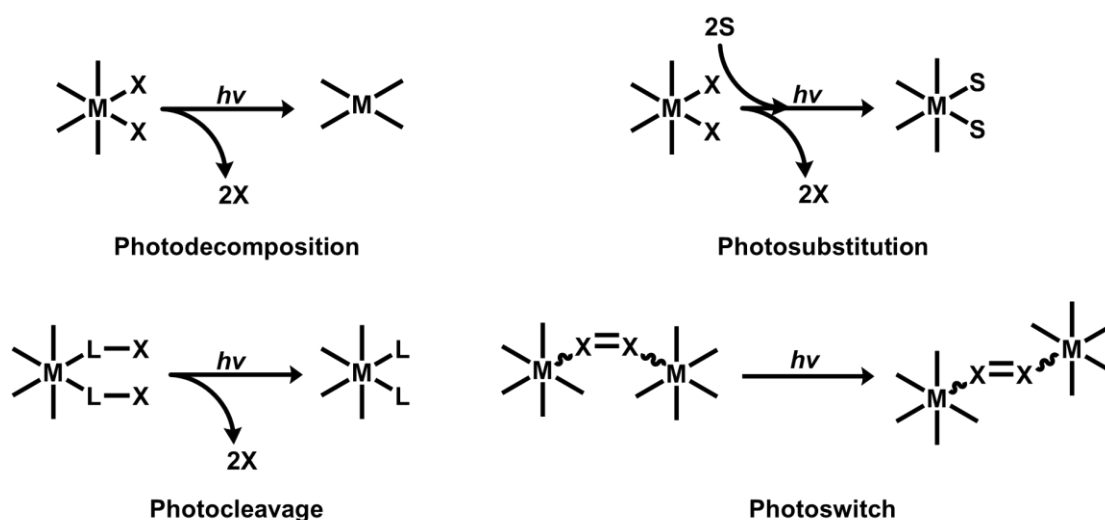


Figure 1.4. Some mechanisms of photoactivated chemotherapeutic agents. M represents a metal-based compound and X a photosensitive ligand/motif, S a solvent molecule, L a ligand.

- Pt(IV), Co(III) and Ti(IV) complexes can be photoreduced to release cytotoxic Pt(II), Co(II) and Ti(II) species and ligands.^{33,35-37}
- Upon irradiation, d^6 Ru(II), Rh(III), Ir(III), and Re(I) complexes generate triplet metal-to-ligand charge transfer ($^3\text{MLCT}$) excited states that interconvert into low-lying triplet metal-centered (^3MC) states. ^3MC undergoes fast ligand dissociation with substitution by solvent molecules.^{38,39}

- Bonds, such as C–C, C–O, C–N, N–O in the photosensitive ligand coordinated to metal can be cleaved *via* photon absorption by a nearby metal centre to regain the cytotoxicity of the “photocaged” complexes.⁴⁰
- Photoswitchable ligands alter the cytotoxic properties of complexes by adopting different forms upon irradiation with light.⁴¹

PACT is often compared with PDT since they both require light to activate the relatively non-toxic prodrugs.³⁴ Generally, PACT agents decompose upon irradiation, while PDT agents are photostable. The major advantage of PACT over PDT is its oxygen-independent mechanism of action, which improves the efficiency in hypoxic tumour. In addition, PACT coordination complexes often exhibit better aqueous solubility compared with lipophilic organic photosensitisers. Finally, PACT complexes can be activated by light over a wide range of energies, while the narrow absorption spectra of PDT dyes allows limited excitation wavelengths.

However, the development of PACT is still in its early days, and the performance of PACT complexes is not yet competitive with PDT photosensitisers. Some photosensitisers in the clinical trials exhibit extremely high photoindices (dark versus light, e.g. **TLD-1433**, up to 100,000),^{39,42} and some can be excited by near infrared (e.g. **WST-09**, 763 nm).³⁰ In contrast, the photoindices for PACT agents only reach 1880.⁴³ The longest excitation wavelengths reported for simple metal complex-based PACT agents are in the red region, which limits light penetration into tissue to a depth of *ca.* 5 mm.^{44,45} To enter clinical trials, more efforts are needed to investigate new PACT complexes.

1.3. Platinum-based anticancer complexes

1.3.1. Platinum^{46,47}

Platinum (Pt) is a rare element in Earth's crust with only 5 ppb abundance, and is one of the least reactive metals. The atomic number of platinum is 78 with an electron configuration of $[\text{Xe}] 4f^{14} 5d^9 6s^1$ and an atomic weight of 195.084 Da. Six isotopes of platinum, ^{190}Pt , ^{192}Pt , ^{194}Pt , ^{195}Pt , ^{196}Pt , and ^{198}Pt , are found in nature. Among them, ^{195}Pt is the most abundant isotope, comprising 33.83% of platinum, has a nuclear spin quantum number $I = 1/2$ and therefore is NMR active. The most common oxidation states of platinum are +2 and +4 with d^8 and d^6 electron configurations, respectively (Figure 1.5). Pt(II) is a soft Lewis acid that can form stable complexes with soft ligands, such as S or P donors. Pt(IV) is harder than Pt(II), and Pt(IV) complexes are more thermally stable and kinetically inert than Pt(II) complexes.⁴⁶

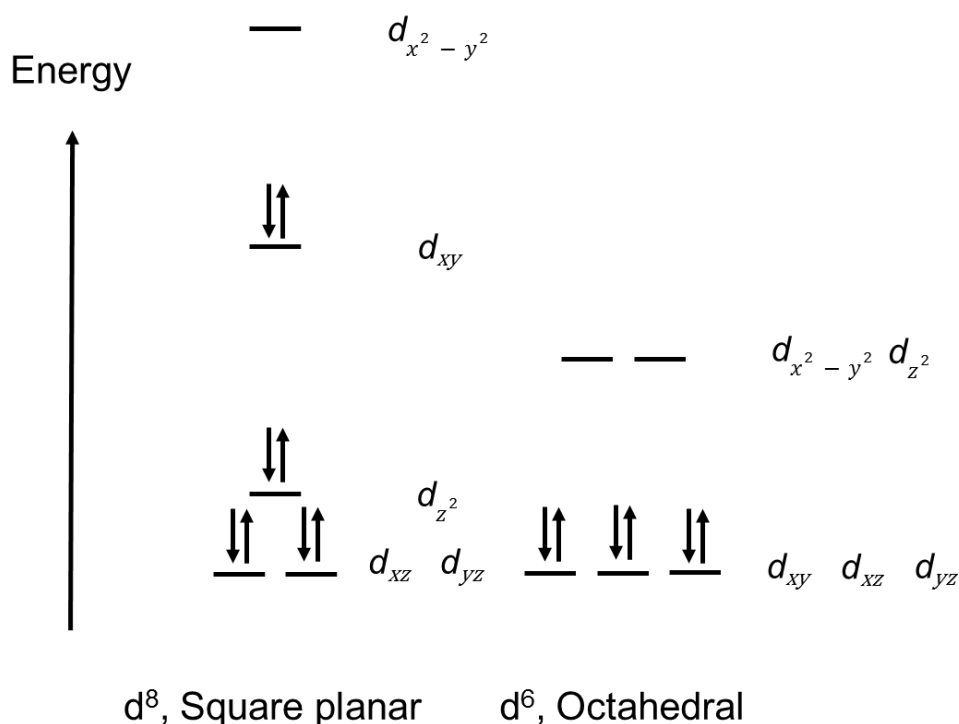


Figure 1.5. Splitting of the d-orbitals in crystal fields of square-planar (Pt(II), d^8) and octahedral (Pt(IV), d^6) symmetries. The electrons are configured in a strong ligand field.

1.3.2. Cisplatin and its analogues and derivatives

The serendipitous discovery of the antiproliferative properties of cisplatin in 1968 by B. Rosenberg provided a new avenue for design of anticancer drugs based on platinum complexes.^{48,49} Since cisplatin was approved by FDA in 1978 to treat testicular and ovarian cancers, platinum drugs are now used to treat over 40% of all cancer patients with chemotherapy.⁵⁰⁻⁵² Three analogues of cisplatin (carboplatin, oxaliplatin and nedaplatin, Figure 1.6a), have also been widely used in the clinic.⁵³⁻⁵⁵ Cisplatin reacts at the N7 position of guanine and adenine residues of DNA preferentially to form intrastrand or interstrand cross-links, which disrupts DNA structure in cell nuclei, ultimately leading to cell death (Figure 1.6b).⁵⁶⁻⁵⁸ Although DNA is regarded as the major target of cisplatin, only 1% of cisplatin reaches the nucleus.⁵⁹⁻⁶¹

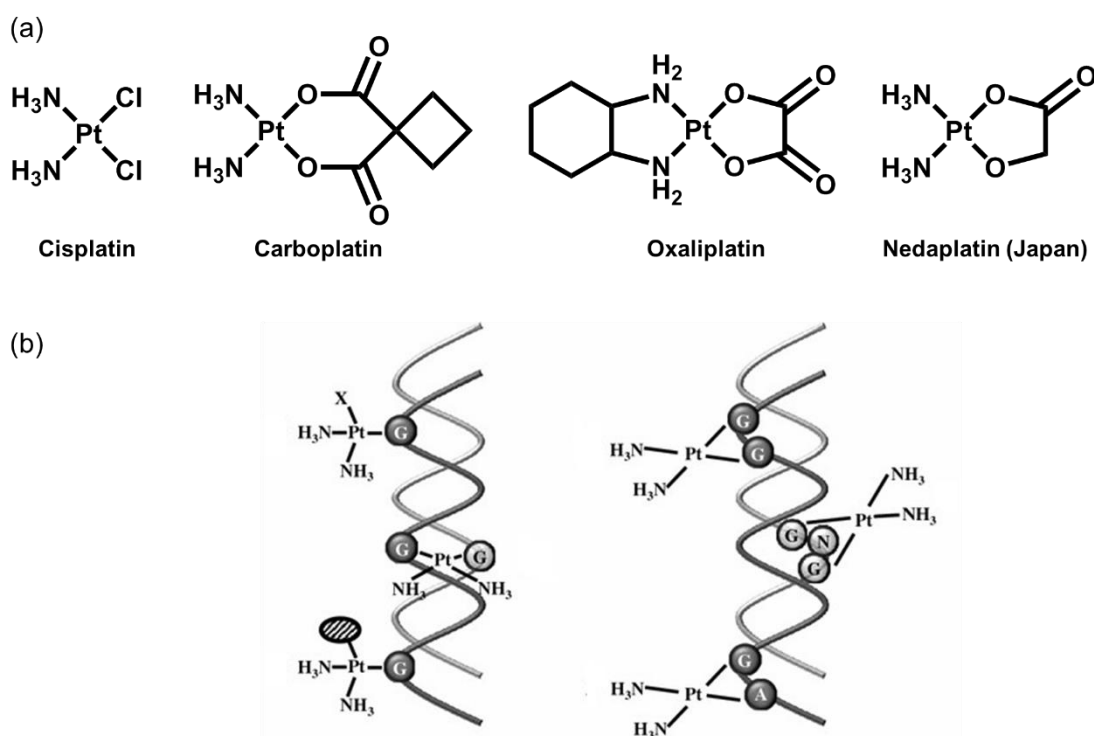


Figure 1.6. (a) Selected clinically approved Pt(II) anticancer drugs; (b) feasible cisplatin-DNA adducts. Adapted from *ref. 57*.

Cisplatin suffers from many disadvantages despite of its clinical success, including poor pharmacokinetics, dose-limiting side effects, restricted spectrum of anticancer activity, deficiency of discrimination between cancerous and healthy tissue, and high incidence of resistance in the clinic.^{62,63} Cisplatin resistance, both acquired and intrinsic, is a major complication in cancer chemotherapy, which may result from decreased intracellular accumulation of cisplatin, increased intracellular levels of certain sulphur-containing macromolecules, and increased DNA repair.^{50,64}

To minimise side effects and improve drug delivery and cancer selectivity, kinetically inert Pt(IV) complexes have been designed to keep the complex intact before reaching the cellular target.^{65,66} Pt(IV) complexes have to be reduced by bio-reductants (e.g. GSH, ascorbic acid, cysteine residues) to form active Pt(II) species to exert their anticancer activity.⁶⁷ Therefore, Pt(IV) complexes are regarded as prodrugs of the corresponding Pt(II) species.^{68,69}

Even though the anticancer activity of Pt(IV) complexes was recognised as early as that of cisplatin,⁴⁹ no Pt(IV) complex has been approved by the FDA yet (Figure 1.7).⁵² Iproplatin failed in clinical trials due to its lower activity than cisplatin,^{70,71} ormaplatin caused severe neurotoxicity in treated patients,⁷² and satraplatin was abandoned due to variability in drug uptake.⁷³ The orally active oxoplatin is a prodrug of cisplatin and is currently undergoing clinical trials.⁷⁴

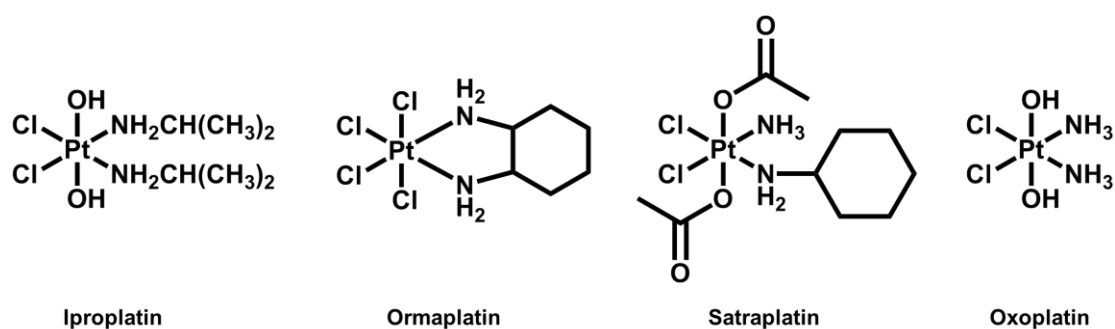


Figure 1.7. Selected Pt(IV) anticancer drugs investigated in clinical trials.

1.3.3. Pt(II) complexes with new mechanism of action

Early structure-activity relationship (SAR) studies stated that: (i) active platinum complexes must be *cis* geometry and uncharged; (ii) alkyl substituents in amine ligands reduce the anticancer activity; (iii) a pair of *cis*-leaving groups are necessary and should be adequately strongly bound.⁷⁵⁻⁷⁷ However, the development of Pt(II) complexes with new mechanisms of action has dispelled these notions.

Transplatin (Figure 1.8a), the *trans*-stereoisomer of cisplatin, exhibited no activity in cancer therapy. Two key factors are ascribed to the difference between *cis*- and *trans*-platinum complexes in cytotoxicity.^{78,79} Firstly, transplatin is kinetically more reactive than cisplatin, which makes the complex more susceptible to deactivation and leads to undesired side reactions. In addition, the lethal intrastrand GG cross-links formed by cisplatin are stereochemically inaccessible to the *trans* isomer. However, *trans*-Pt(II) complexes with heteroaromatic N-donors, iminoether ligands, and asymmetric aliphatic amine ligands were found to be anticancer active, with cytotoxicity comparable to cisplatin.^{65,78,79} More importantly, the different mechanisms of action of *trans*-Pt(II) complexes allow them to circumvent cisplatin resistance. *Trans*-[PtCl₂(NH₃)L] and *trans*-[PtCl₂L₂] (L = pyridine, quinoline, isoquinoline, thiazole, benzothiazole, iminoether or aliphatic amine) exhibited significant activities in cisplatin- and oxaliplatin-resistant cell lines.^{80,81} These complexes trigger DNA lesions of a different type and distribution from cisplatin.^{82,83} The bulky planar ligands increase the formation of monofunctional adducts and then interstrand cross-links.

Monofunctional Pt(II) complexes, with a general formulation *cis*-[PtCl(NH₃)₂(L)]⁺ (L = amine ligand), contain only one labile ligand and form at most one covalent bond to DNA.⁸⁴ *Cis*-[Pt(NH₃)₂(pyridine)Cl]⁺ (pyriplatin, Figure 1.8b) displays a preference to cells with high expression of organic cationic transporters 1 and 2.⁸⁵ Pyriplatin formed monofunctional lesions

on DNA, blocked cell cycle progression at the G2/M phase, and stalled RNA polymerase II. It therefore exerted a novel spectrum of activity compared with cisplatin in NCI-60 cytotoxicity screening studies.⁸⁶⁻⁸⁷ The subsequent development of phenanthriplatin with improved cytotoxicity was inspired by the success of pyriplatin.⁸⁸

Polynuclear Pt(II) complexes containing *trans*-{Pt(NH₃)₂Cl} motifs bridged by alkanediamine linkers of variable length are able to form unconventional 1,2-, 1,3-, and 1,4-interstand cross-links and overcome cisplatin resistance.^{89,90} The trinuclear Pt(II) complex bis[*trans*-diamminechloroPt(II)][μ -*trans*diamminebis(hexanediamine)Pt(II)]nitrate (**BBR3464**, Figure 1.8c) displays up to 1000-fold higher cytotoxicity than cisplatin in sensitive cell lines.^{52,91-93} However, severe systemic toxicity caused by BBR3464 was observed in clinical trials, so it did not enter Phase III trials.⁹⁴⁻⁹⁶ The replacement of labile chloride ligands on **BBR3464** with ammine groups or extended amine groups resulted in the generation of **TriplatinNC** (Figure 1.8d) and **TriplatinNC-A**, respectively.⁹⁷ They bind to DNA non-covalently through electrostatic and hydrogen-bonding interactions.

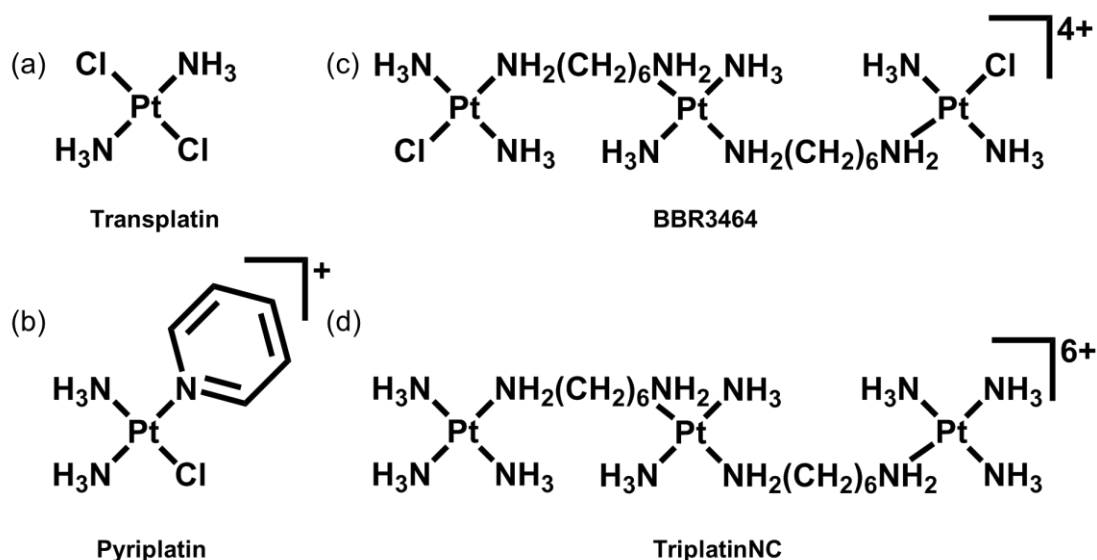


Figure 1.8. Selected Pt(II) anticancer drugs with new mechanisms of action.

In addition to **TriplatinNC** and **TriplatinNC-A**, some mononuclear Pt(II) complexes containing π -conjugated heterocyclic ligands can also bind to DNA non-covalently then unwind, bend, and distort DNA topology.⁹⁸⁻¹⁰⁰ Complexes $[\text{Pt}(\text{I}_L)(\text{A}_L)]^{2+}$ (I_L = phenanthroline-based ligands, A_L = diaminocycloalkane ligands) displayed high cytotoxicities and the chirality of the ancillary ligands determines the toxicity.¹⁰¹⁻¹⁰³

1.3.4. Photoactive platinum complexes

Both common oxidation states of platinum show a rich photochemistry; accordingly platinum complexes represent a major class of photoactive anticancer drugs.^{33,35,104} Some Pt(II) complexes have long-lived excited states and exhibit luminescence upon irradiation, therefore are frequently used in PDT. In contrast, photodissociation and photoreduction are the main photochemical processes of Pt(IV) complexes.

1.3.4.1. Photoactive Pt(II) complexes

Fluorescent Pt(II) complexes with high emission quantum yield, such as cyclometalated Pt(II) complexes, showed improved cytotoxicity upon irradiation and can be tracked within cells *via* fluorescence microscopy.¹⁰⁴⁻¹⁰⁶ The Pt(II) complex $[\text{Pt}(\text{thpy})(\text{bis-NHC})]^+$ (Hthpy = 2-(thiophen-2-yl)pyridine, Figure 1.9a) selectively localises in the endoplasmic reticulum (ER) domain and induces ER-stress and mitochondrial dysfunction, and exhibits a 28-fold improved photocytotoxicity towards HeLa cells.¹⁰⁵

Non-fluorescent Pt(II) complexes are often conjugated to highly fluorescent photosensitisers, such as porphyrins and BODIPY.¹⁰⁷⁻¹¹⁰ Tetraplatinated porphyrins (Figure 1.9b) displays IC_{50} values down to 19 nM with indigo light (420 nm) irradiation with phototoxic indices up to 5000

in a cisplatin-resistant cell line, showing a high synergism compared with the simple mixture of porphyrins and cisplatin.¹⁰⁷ Highly emissive Pt(II) supramolecular triangles (Figure 1.9c) bearing a pyridine-functionalised BODIPY ligand contain a combination of PDT and chemotherapeutic agents, and exhibit improved photocytotoxicity which overcomes cisplatin resistance in A2780cis ovarian cancer cells.¹⁰⁸

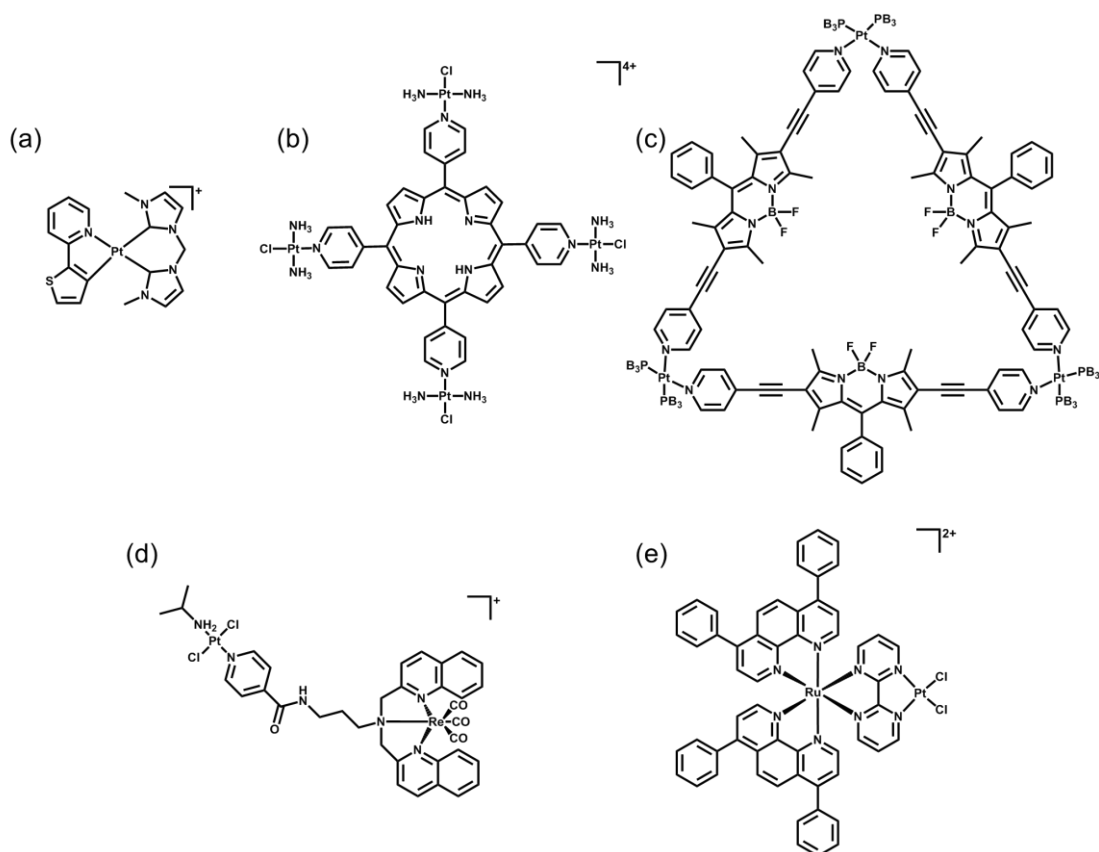


Figure 1.9. Selected Pt(II) complexes as PDT agents.

Pt(II) complexes can also be attached to other photoactive metal complexes that generate singlet oxygen upon irradiation. The heterobimetallic **Pt-LQ-Re** complex (Figure 1.9d) exhibits a broad emission band and a moderate singlet oxygen quantum yield, and is photocytotoxic in cancer cell lines.¹¹¹ Another heterobimetallic complex **RuPt** (Figure 1.9e)

can induce platination and damage to *mt*-DNA, cause mitochondrial dysfunction and apoptosis, and almost eliminate A549 solid tumours in nude mice.¹¹²

Most PACT Pt(II) agents belong to two main classes: photodissociation and photoswitch. Photodissociation consists of the photorelease of ligands from metal centres and the photocleavage of ligands, while photoswitch usually occurs in the coordinated ligands.

Transplatin (Figure 1.8a), despite being non-toxic in the dark, exhibits cytotoxicity comparable with cisplatin in the presence of UVA light.¹¹³ Increased interstrand cross-links in DNA formed by transplatin were detected upon irradiation since light can promote the loss of the second chloride of transplatin, which ultimately led to the enhanced cytotoxicity. Carboplatin (Figure 1.6a) also displayed increased DNA platination and cytotoxicity with UVA exposure.¹¹⁴

[Pt(curcumin)(NH₃)₂](NO₃) (Figure 1.10a) localises in the cytoplasm of HaCaT cells, where it releases curcumin and a cisplatin analogue upon irradiation with visible light, and forms platinum adducts with 5'-GMP and *ct*-DNA, thus causing cell death with IC₅₀ values of 12–18 μM, though it showed no cytotoxicity in the dark.¹¹⁵ The replacement of curcumin with a new acetylacetonone derivative IR797-acac resulted in a photolabile complexes (Figure 1.10b) that can release cytotoxic Pt(II) species and generate singlet oxygen upon irradiation.¹¹⁶ *Cis*-[PtCl₂(MOPEP)₂] (Figure 1.10c) undergoes two-photon-absorption decomposition when irradiated with a focused femto-second (fs) laser at the wavelength 600, 650 and 700 nm and releases the MOPEP ligands.¹¹⁷

Derivatives of *o*-nitrobenzyl alcohol are photosensitive and can be coordinated to platinum. The photo-induced internal redox process of [Pt(HNPAC)(NH₃)₂](NO₃) (HNPAC = 2-hydroxy-2-(2-nitrophenyl)acetic acid, Figure 1.10d) reduced its nitro group to nitroso group, while oxidising the hydroxyl group to a carbonyl group.¹¹⁸ The photo-induced backbone

breakage of the non-toxic [Pt(cage)] with *o*-nitrobenzyl alcohol ligand (Figure 1.10e) resulted in the release of active Pt(II) species and nitroso by-products.¹¹⁹

1,2-Dithienylethene derivatives are photoswitchable between open and closed forms. Pt(II) complexes with diarylethene ligands (Figure 1.10f) transformed to the closed form with UVA irradiation, while returned to open form with visible irradiation.^{41,120} The closed form was less voluminous and more planar with a greater π conjugation, thus exhibited better DNA binding ability and cytotoxicity, eventually.

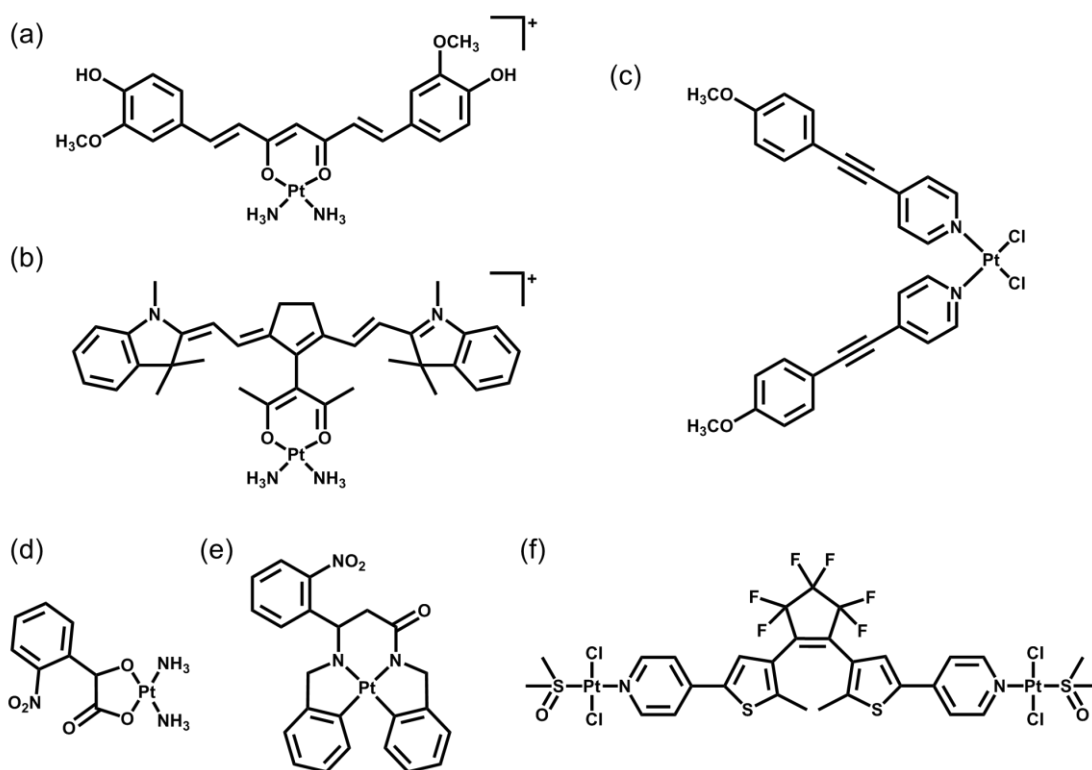


Figure 1.10. Selected Pt(II) complexes proposed as PACT agents.

1.3.4.2. Photoactive Pt(IV) complexes

Photodecomposition is an important chemical property of Pt(IV) complexes. The photolysis of $[\text{Pt}(\text{N}_3)_6]^{2-}$ leads to the formation of $[\text{Pt}(\text{N}_3)_4]^{2-}$ and even metallic Pt together with the release of nitrogen gas,^{121,122} and $[\text{Pt}(\text{Cl})_6]^{2-}$ can be converted into $[\text{Pt}(\text{Cl})_4]^{2-}$ or metallic Pt upon

irradiation with low-energy visible light.¹²³ Compared with their Pt(II) counterparts,¹²⁴ Pt(IV) complexes exhibit better dark stability owing to their kinetic inertness, therefore are potential photoactive prodrugs.^{125,126} Photoactive Pt(IV) complexes often contain leaving, axial and non-leaving equatorial ligands. Two main classes of photoactive Pt(IV) complexes based on different leaving ligands, namely diiodo- and diazido-Pt(IV) complexes, have been reported so far as anticancer prodrugs.

Diiodo-Pt(IV)-ethylenediamines bearing various axial ligands (Cl (a), OH (b), OCOCH₃ (c), OSO₂CH₃ (d), or OCOCF₃ (e), Figure 1.11) were reported as the first generation of photoactive Pt(IV) complexes with a general formula *trans,cis*-[Pt(X)₂I₂(en)].¹²⁷⁻¹³¹ Ethylenediamine was chosen as the non-leaving group since Pt(II)-ethylenediamine complexes are known antitumor agents. In addition, the chelating diamine could prevent photoisomerisation, thus simplifying the chemistry and avoiding the formation of a *trans*-Pt(II) photoproduct that cannot form the lethal intra-strand DNA cross-links. Iodide is a weak field ligand with a low optical electronegativity, thus the strong broad LMCT bands of these complexes were centred at around 400 nm with a tail extending out into the visible range. All of these complexes can be activated with light $\lambda_{\text{irr}} > 375$ nm, since iodide is also a good reducing ligand.

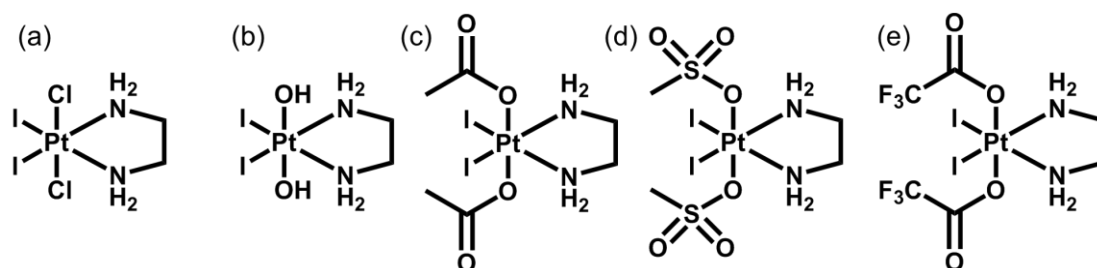


Figure 1.11. First generation of photoactive diiodo-Pt(IV) complexes.

Trans,cis-[Pt(Cl)₂I₂(en)] undergoes decomposition upon irradiation at $\lambda_{\text{irr}} = 410$ nm, accompanied by the covalent binding of Pt to DNA at a rate comparable to that of [PtCl₂(en)].¹²⁹

However, its application is limited due to the poor dark stability and short excitation wavelength. *Trans,cis*-[Pt(OH)₂I₂(en)], in contrast, was not remarkably affected by light, since photosubstitution of iodide ligands to water rather than photoreduction of Pt(IV) to Pt(II) occurred when it was exposed to light.¹³⁰ The most promising complex *trans,cis*-[Pt(OCOCH₃)₂I₂(en)] exhibited a 35% photo-induced enhancement in antiproliferative activity.¹²⁸

The main reason for the non-significant difference between the dark and light cytotoxicity of diiodo-Pt(IV) complexes might be ascribed to their facile reduction by cellular bioreductants (Figure 1.12).

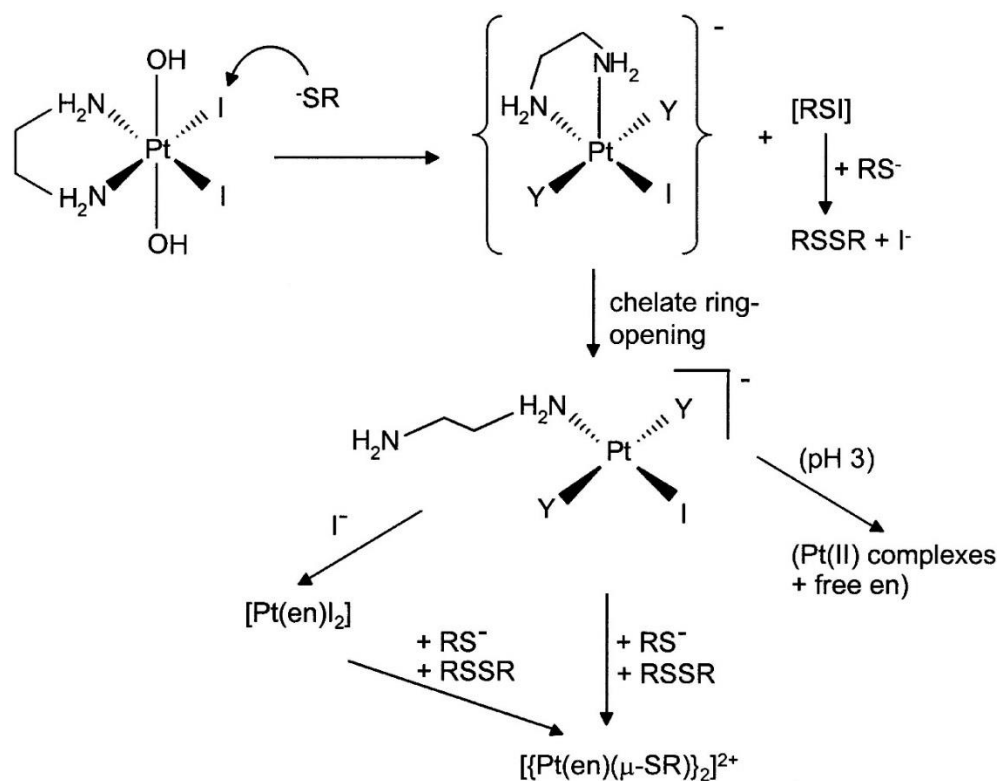


Figure 1.12. Proposed mechanism for the reduction of *trans,cis*-[Pt(OH)₂I₂(en)] by biologically important thiols. Adapted from *ref.* 130.

Transition metal azide complexes are often light sensitive.¹³² The first reported photoreduction of a Pt(IV) complex was *trans*-[Pt(N₃)₂(CN)₄]²⁻ by Vogler *et al.* in 1978.¹³³ Upon irradiation with UVA at 302 nm, the wavelength of its maximum electronic absorbance assigned to a ligand-to-metal (N₃→Pt) charge-transfer transition, *trans*-[Pt(N₃)₂(CN)₄]²⁻ was converted to [Pt(CN)₄]²⁻ *via* the formation of two azidyl radicals without a Pt(III) intermediate. The unstable azidyl radicals would react in water to release N₂, which prevents reoxidation of the platinum centre.¹³² Based on these results, the Sadler group has developed the second generation of photoactive Pt(IV) complexes, replacing iodides with azides.

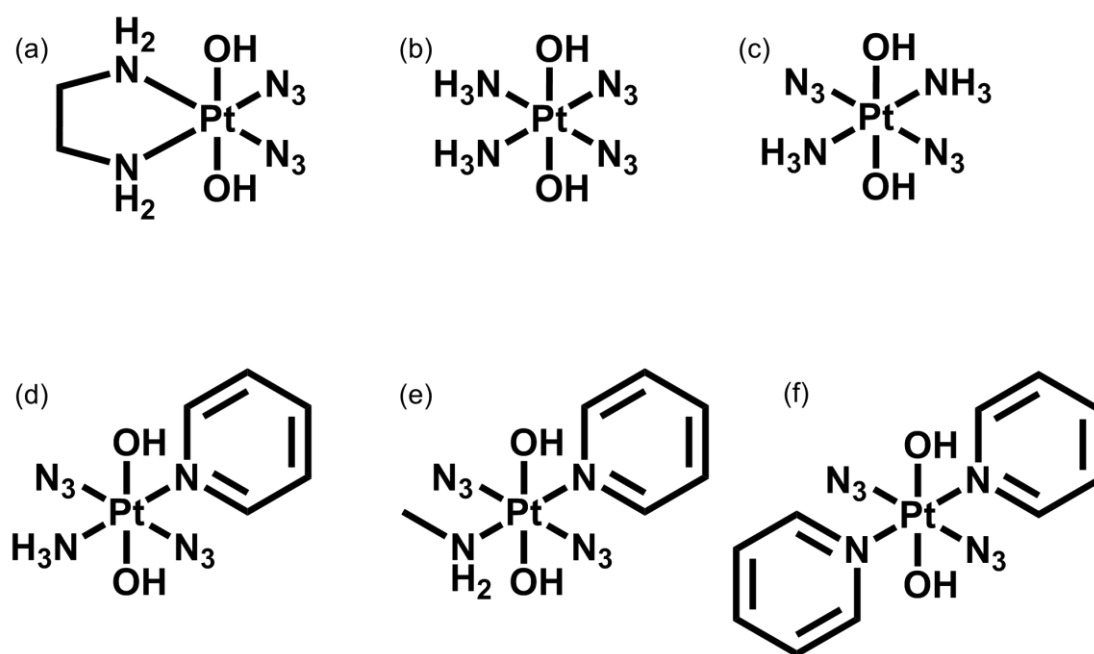


Figure 1.13. Second generation of photoactive diazido Pt(IV) complexes.

The first diazido Pt(IV) complexes, *cis,trans*-[Pt(en)(N₃)₂(OH)₂] (Figure 1.13a) and *cis,trans,cis*-[Pt(N₃)₂(OH)₂(NH₃)₂] (Figure 1.13b) were reported in 2003.¹³⁴ Both were quite stable under physiological conditions in the dark, while able to form Pt-GMP and Pt-GpG adducts upon visible light irradiation.¹³⁵ Cytotoxicity studies on these complexes exhibited very low inhibition in growth in the dark, but significantly enhanced cytotoxicity was observed upon

irradiation in both 5637 cells and cisplatin-resistant 5637 cells, even though to a less extent than cisplatin.¹³⁶ In addition, dramatic changes in the morphology of the cells were observed (Figure 1.14), including cellular shrinkage, loss of adhesion with neighbouring cells, a large amount of nuclear packing, and nuclei disintegration, when 5637 cells were treated with *cis,trans,cis*-[Pt(N₃)₂(OH)₂(NH₃)₂] only in the presence of light.¹³⁶

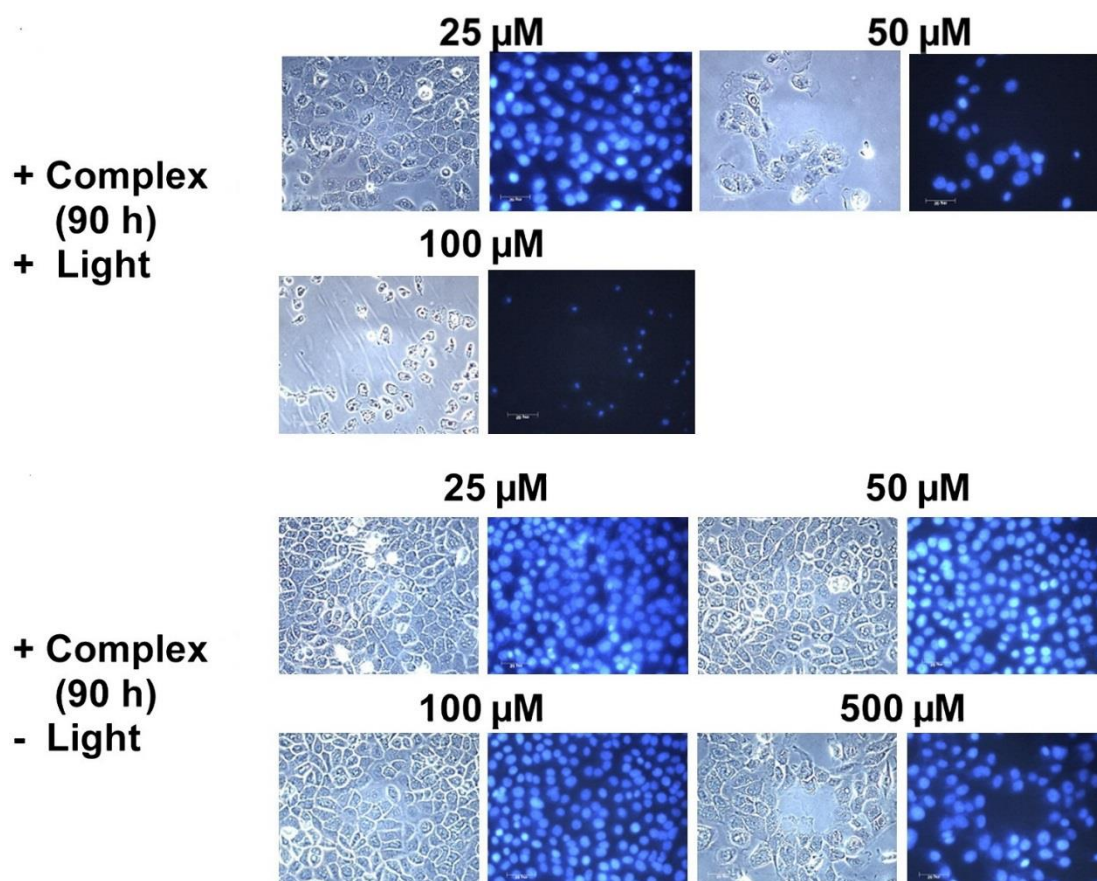


Figure 1.14. Fluorescence microscopy images of 5637 cells treated with *cis,trans,cis*-[Pt(N₃)₂(OH)₂(NH₃)₂] in the presence and absence of irradiation. Reproduced from *ref.* 136.

Photodecomposition of *cis,trans,cis*-[Pt(N₃)₂(OH)₂(NH₃)₂] in water resulted not only in the release of N₂, but also the generation of nitrene intermediates that can form dimethylsulfilimine adducts with dimethyl sulfide (DMS). The adduct can undergo a Stevens-like rearrangement in

which the Pt–N=SMe₂ group becomes Pt–N(H)–CH₂–SMe, giving a N-(methylthiomethylene)amido derivative. The derivative can release two hydroxyl radicals upon irradiation. (Figure 1.15).¹³⁷ Multinuclear NMR studies revealed the formation of *trans*-{Pt^{II}(NH₃)₂} fragment when *cis,trans,cis*-[Pt(N₃)₂(OH)₂(NH₃)₂] was irradiated, which suggested the involvement of photoisomerisation.¹³⁸ In addition, *cis,trans,cis*-[Pt(N₃)₂(OH)₂(NH₃)₂] produced 6 different Pt-coordinated 1-methylimidazole species in the presence of 1-methylimidazole upon irradiation, indicating its potential ability to bind to DNA and proteins.¹³⁸

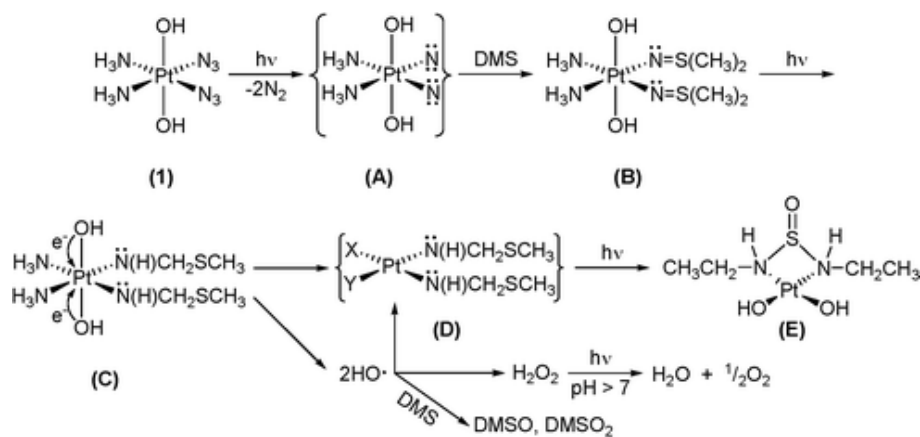


Figure 1.15. Possible mechanisms for nitrene-trapping and photoreduction (X, Y = NH₃ and/or OH). Adapted from *ref.* 137.

Intriguingly, the all-*trans* photoactive Pt(IV) prodrug, *trans,trans,trans*-[Pt(N₃)₂(OH)₂(NH₃)₂] (Figure 1.13c) exhibited higher aqueous solubility and a more intense and red-shifted LMCT band compared with its *cis* isomer.¹³⁹ Also, it was able to form a bis(5'-GMP) adduct rapidly under UVA and was more toxic toward cancer cells upon irradiation (as toxic as cisplatin).^{139,140} These results were opposite to the early structure-activity relationship that *cis* geometry was favourable for anticancer platinum complexes. More comparisons have been made by

incorporating a wide range of aliphatic and aromatic amines to diazido Pt(IV) complexes to confirm the superiority of *trans* configuration.^{140,141}

Replacement of an ammine ligand in *trans,trans,trans*-[Pt(N₃)₂(OH)₂(NH₃)₂] by a π -acceptor pyridine ligand resulted in the highly phototoxic complex *trans,trans,trans*-[Pt(N₃)₂(OH)₂(NH₃)(py)] (Figure 1.13d) that showed a 13–80× higher photocytotoxicity compared with cisplatin, and 15× that towards cisplatin-resistant ovarian cancer cells, A2780cis.¹⁴²⁻¹⁴⁴ This complex adopted a different mechanism of action from cisplatin, since p53 protein did not accumulate in cells when treated with it and irradiation. Also, an autophagic mechanism was envisaged for this complex.¹⁴⁴

Encouraged by the success of *trans,trans,trans*-[Pt(N₃)₂(OH)₂(NH₃)(py)], a series of ligands were introduced to replace one of the ammine ligands.^{145,146} Unfortunately, no significant influence was observed. However, the replacement of ammonia by methylamine (MA) results in the *trans,trans,trans*-[Pt(N₃)₂(OH)₂(MA)(Py)] (Figure 1.13e) that is distinguished from other diazido complexes by its ability to oxidise 5'-GMP *via* pathways involving singlet oxygen (¹O₂) and nitrene (Pt-N) intermediates.¹⁴⁷ Its thiazole (Tz)-containing analogue *trans,trans,trans*-[Pt(N₃)₂(OH)₂(MA)(Tz)] was more effective towards the resistant cell line, and the higher cytotoxicity of complexes with MA was due to the high stability of Pt-MA bonds.¹⁴⁸

Pyridine ligands appear to play an important role in the high phototoxicity and a mechanism of action different from cisplatin, and the complex with two pyridines, *trans,trans,trans*-[Pt(N₃)₂(OH)₂(py)₂] (Figure 1.13f), was found to be more stable in water and Eagle's balanced salt solution compared with its analogues.¹⁴⁹ Upon irradiation with UVA or visible blue light, *trans,trans,trans*-[Pt(N₃)₂(OH)₂(py)₂] exhibited significant toxicity toward a number of human cell lines with high phototoxic indices. No pyridine release was detected by ¹H NMR, which is in contrast to complexes with NH₃ and likely responsible for its higher efficacy. In the presence

of 5'-GMP, *trans*-[Pt(N₃)(py)₂(5'-GMP)]⁺ and *trans*-[Pt(py)₂(5'-GMP)₂]²⁺ were detected as photoproducts of *trans,trans,trans*-[Pt(N₃)₂(OH)₂(py)₂]. Comet assays showed that DNA-DNA or DNA-protein crosslinks could be induced by photoactivated *trans,trans,trans*-[Pt(N₃)₂(OH)₂(py)₂].¹⁵⁰ The nature of the DNA adducts are distinctly different from those induced by *cis*- or *trans*platin, and *trans,trans,trans*-[Pt(N₃)₂(OH)₂(py)₂] also exhibited a better ability to inhibit RNA synthesis. In addition to DNA, peptides and proteins can also be attacked by *trans,trans,trans*-[Pt(N₃)₂(OH)₂(py)₂] *via* sequence dependent platination and radical mechanisms upon irradiation.¹⁵¹ Platination of His, Glu, and Gln residues of Trx (an important enzyme in the redox signalling pathway) and oxidation of Met, Trp, and the Cys catalytic sites induced by *trans,trans,trans*-[Pt(N₃)₂(OH)₂(py)₂] upon irradiation can inhibit the activity of Trx enzyme and the Trx system, and increase the cellular ROS level.¹⁵² Azidyl radicals were also regarded as a key species for cell death. Furthermore, Trp can be oxidised by azidyl radicals to reduce the cytotoxicity of *trans,trans,trans*-[Pt(N₃)₂(OH)₂(py)₂], which made the photocytotoxicity of this complex switchable.¹⁵³ Trp radicals were also trapped, which might play an important role in the mechanism of action of the complex.¹⁵⁴

Diazido Pt(IV) complexes incorporating π -conjugated bidentate diimine ligands *trans,cis*-[Pt(bpy)(OAc)₂(N₃)₂] and *trans,cis*-[Pt(phen)(OAc)₂(N₃)₂] exhibited greater absorption at longer wavelengths compared with previously reported diazido Pt(IV) complexes.¹⁵⁵ Their photodecomposition can be observed upon irradiation with both UVA and visible green light.

Other than iodide and azide ligands, chloride is also a potential candidate as leaving ligand for photoactive Pt(IV) complexes. An early study revealed that the *cis*-dichloro analogues of the diiodo Pt(IV) complex *trans,cis*-[Pt(OH)₂Cl₂(en)] was stable in the presence of GSH in the dark and exhibited lower cytotoxicity.¹³¹ Both *trans*-[PtCl₂(2,2'-bpy)(MeNH₂)₂]Cl₂ (Figure 1.16a) and *mer*-[PtCl₃(2,2'-bpy)(MeNH₂)]Cl (Figure 1.16b) undergo photoreduction to Pt(II) species with the formation of HOCl.¹⁵⁶ Upon irradiation, complexes [PtCl₄(2,2'-bpy)] (Figure

1.16c) and *mer*-[PtCl₃(2,2'-bpy)(MeNH₂)]Cl were reduced to corresponding Pt(II) complexes and subsequently bind to N7 of G in oligonucleotide DNA models.¹⁵⁷ When the Pt(II) species had two chlorido ligands, bis-adducts at G(3) and G(6) of 5-CAGCTG were observed.

Some Pt(IV) complexes with chlorides, such as oxoplatin, even though are not photoactive on its own, exhibit photorelease of Pt(II) species when conjugated to specific nanoparticles.¹⁵⁸⁻¹⁶⁰

The Pt(IV) complex-based polyPPM nanogels generate ROS in an O₂-independent manner and release Pt(II) species upon irradiation (396 nm), therefore it is able to suppress the tumour growth of mice bearing both conventional A549 and drug resistant A549R lung cancer.¹⁵⁹

Folate-decorated and ICG-encapsulated nanoparticles (**Pt^{IV}-FINPs**) targeted to FR-overexpressing SKOV3 cells and showed enhanced anti-tumour efficacy upon NIR irradiation.¹⁶⁰

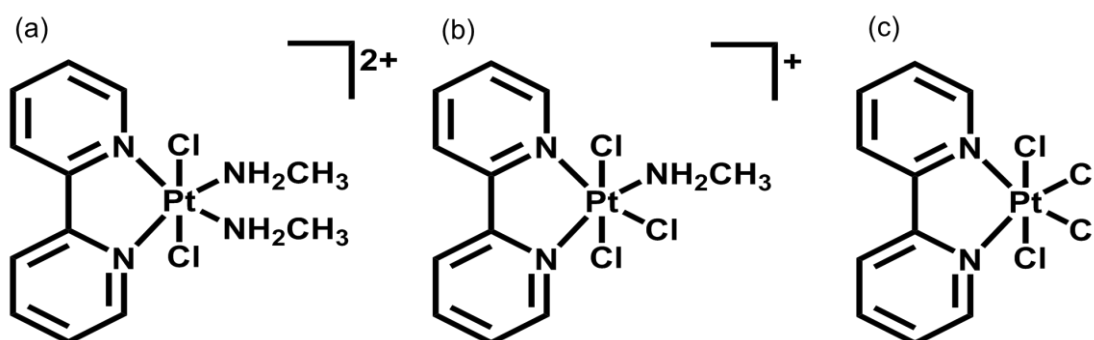


Figure 1.16. Photoactive Pt(IV) complexes with chlorides as leaving ligands.

1.4. Derivatisation of photoactive diazido Pt(IV) complexes

Axial ligands of photoactive Pt(IV) complexes affect the reduction potential of Pt(IV) greatly and might also be released from platinum centre upon photoreduction to Pt(II). Generally, Pt(IV) complexes with a lower reduction potential exhibit higher stability to reductants (depending on the axial ligand: $\Gamma > \text{Cl}^- > \text{OAc}^- > \text{OH}^-$).¹⁶¹ Thus, hydroxide ligands enhance aqueous solubility

and also stabilise the Pt(IV) oxidation state.⁶⁸ Derivatisation of the detachable axial ligand can be used to improve their pharmacological properties without interfering with the ultimate mode of action of the active Pt(II) species or the potential production of reactive species.

1.4.1. Dual action diazido Pt(IV) complexes

The combination of photoactive Pt(IV) complexes with other anticancer active agents, such as stable radicals, enzyme inhibitors, or photosensitisers, results in dual action prodrugs that release not only Pt(II) species and azidyl radicals, but also corresponding cytotoxic agents, and therefore improve the performance of the drug by synergy.

The TEMPO radical was conjugated to *trans,trans,trans*-[Pt(N₃)₂(OH)₂(py)₂] to increase its photocytotoxicity (Figure 1.17a).¹⁶² The presence of the TEMPO radical in the complex was confirmed by EPR spectroscopy. Upon irradiation with blue light (420 nm), azidyl and TEMPO radicals are released, accompanied with the formation of toxic Pt(II) species.

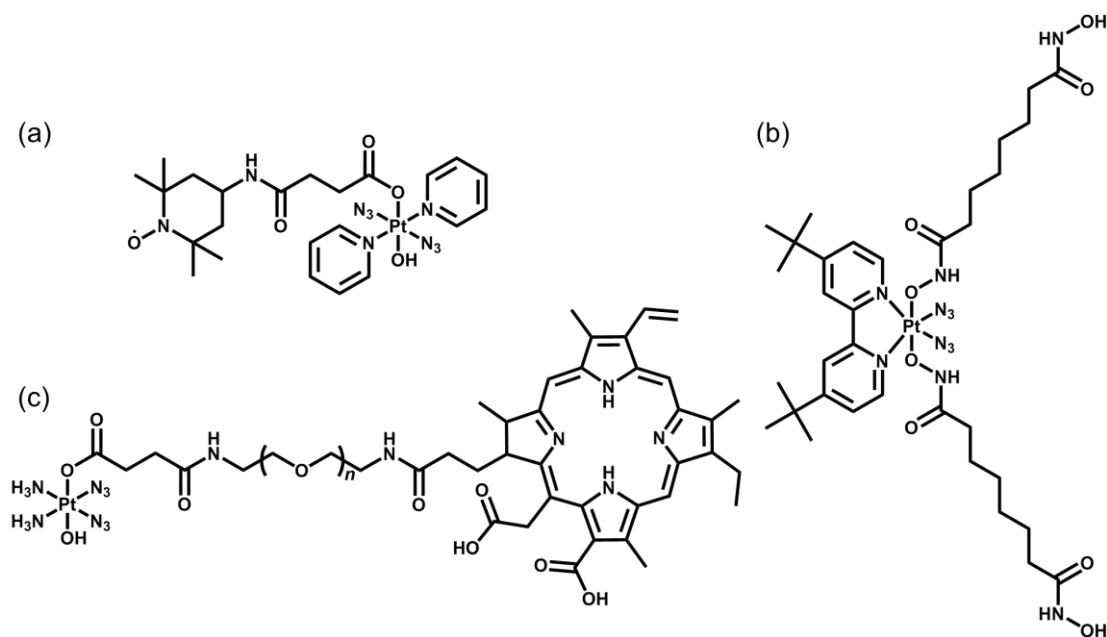


Figure 1.17. Dual action photoactive diazido Pt(IV) complexes.

Suberoyl-bis-hydroxamic acid (SubH) is a histone deacetylase (HDAC) inhibitor, which exhibits a profound dose-dependent inhibition in tumour cell proliferation and shows potent synergistic interaction with antitumor Pt(II) complexes.¹⁶³ Two SubH ligands have been attached to the axial position of *cis,trans*-[Pt(N₃)₂(OH)₂(*t*Bu₂bpy)] to generate diazido Pt(IV) complexes, *cis,trans*-[Pt(N₃)₂(Sub)₂(*t*Bu₂bpy)] (Figure 1.17b) that was stable in the dark.¹⁶⁴ *Cis,trans*-[Pt(N₃)₂(Sub)₂(*t*Bu₂bpy)] released SubH and cytotoxic Pt(II) species, which target similar DNA regions as cisplatin, efficiently upon UVA irradiation. Photoactivated *cis,trans*-[Pt(N₃)₂(Sub)₂(*t*Bu₂bpy)] exhibited significant cytotoxicity in cancer cells with a low resistance factor compared with cisplatin and its Pt(IV) derivatives containing inactive axial ligands. This suggested a different mechanism of action involving inhibition of HDAC that allowed platinum species to access chromatin DNA, introduced effective steric blockage of RNA polymerase II and formed DNA adducts (e.g. interstrand cross-links).

Chlorin e6 is a photosensitizer that produces ROS from ³O₂ with light.¹⁶⁵ However, the oxygen-dependent mechanism is limited in hypoxic tumour environments. *Cis,trans,cis*-[Pt(N₃)₂(OH)₂(NH₃)₂] was selected as a O₂-self generating prodrug to be conjugated to chlorin e6 to alleviate the hypoxia and generate oxygen for PDT.¹⁶⁶ The dual action amphiphilic oligomer Ce6-PEG-Pt(IV) (CPP, Figure 1.17c) can self-assemble into micelles, and upconversion nanoparticles NaYbF₄: Tm@CaF₂ were co-assembled to convert NIR irradiation into shorter wavelength that can decompose diazido Pt(IV) complex. Dramatically enhanced photocytotoxicity was observed for this PACT-PDT system in hypoxic tumour models.

Curcumin is a well-known traditional medicine and a photosensitizer with anticancer activity.¹⁶⁷ Curcumin-loaded Dex-Pt(N₃) nanoparticles generate instant ROS by curcumin and Pt(II) species from Pt(N₃), and thus exhibit enhanced photocytotoxicity and *in vivo* antitumor efficacy with low systemic toxicity to KM mice bearing subcutaneous H22 murine hepatocarcinoma model (Figure 1.18).¹⁶⁸

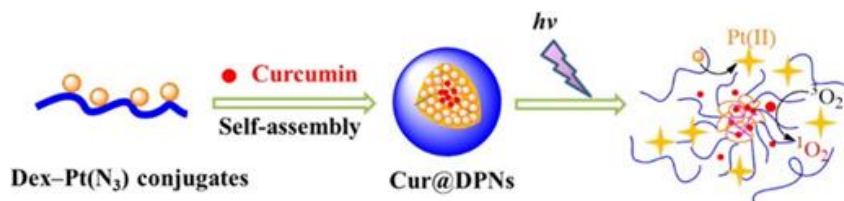


Figure 1.18. Preparation and photodecomposition of curcumin-loaded Dex-Pt(N₃) nanoparticles. Adapted from *ref.* 166.

A peptide probe with a fluorescence resonance energy transfer (FRET) pair consisting of a far-red fluorescence donor Cy5 and a NIR quencher Qsy21 that can be activated by caspase-3, a key enzyme in apoptosis, was loaded onto silica coated upconversion-luminescent nanoparticles (UCNP) together with *trans,trans,trans*-[Pt(N₃)₂(OH)₂(py)₂] (Figure 1.19).¹⁶⁹ UCNP allow photodecomposition of platinum complexes upon irradiation with NIR, which triggered apoptosis owing to the cytotoxicity to ovarian cancer cells. Caspase-3 activated in apoptosis cleaved the probe peptide and released Cy5 from the quencher Qsy21, thus turning on the emission of the fluorescent dye and enabling imaging of apoptosis in living cells. Also, when both of the peptide probe and Pt(IV) complex were conjugated to HSA nanocarriers instead of UCNP, improved photocytotoxicity and real-time imaging was achieved upon UVA irradiation.¹⁷⁰

The conjugate of Yb/Tm-codoped UCNP and *trans,trans,trans*-[Pt(N₃)₂(OH)₂(NH₃)(py)] is reported to exhibit better tumour inhibition under NIR irradiation than that under direct UV irradiation.¹⁷¹ Notably, this nanosystem functioned as a theranostic agent, whose therapeutic action can be informed and guided by different imaging modalities, such as upconversion luminescence (UCL), magnetic resonance (MR) and computer tomography (CT).

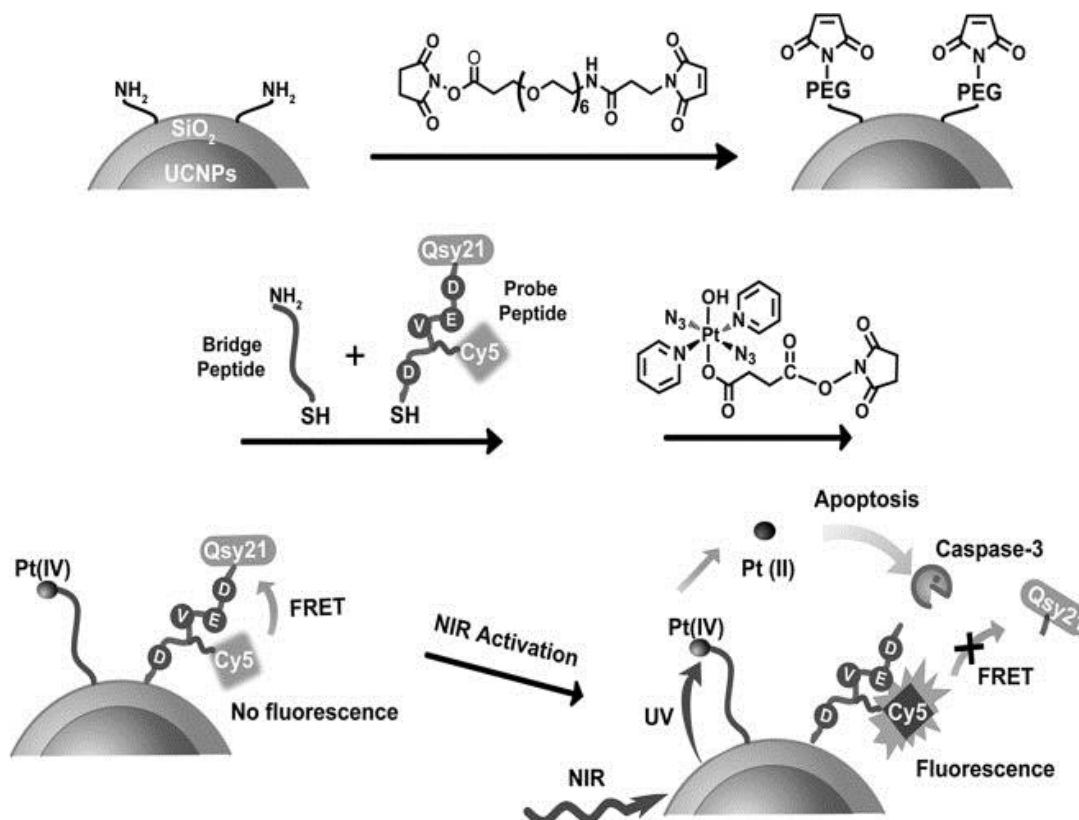


Figure 1.19. Schematic illustration of NIR light activation of Pt(IV) prodrug and intracellular apoptosis imaging through upconversion-luminescent nanoparticles. Adapted from *ref.* 169.

1.4.2. Targeted delivery of diazido Pt(IV) complexes

One of the major advantages of phototherapy over chemotherapy is the spatio-temporal selectivity. However, photoactive prodrugs without preference to cancer cells cannot accumulate in tumours efficiently, which results in the need for higher concentrations to achieve therapeutic efficacy, increasing the risk of side effects. The conjugation with cancer targeting vectors can improve the selectivity of Pt(IV) agents, increasing their accumulation in cancer cells, and enabling the prodrugs to be activated specifically within cancer cells.

Overexpression of particular receptors in cancer cells provides ideal targeting sites for drug delivery. The RGD sequence (–Arg–Gly–Asp–) can be recognised selectively by $\alpha_v\beta_3$ and $\alpha_v\beta_5$

integrins, which are overexpressed on the surface of several tumour cells and are related to tumour angiogenesis.^{172,173} A conjugate of photoactive Pt(IV) prodrug *trans,trans,trans*-[Pt(N₃)₂(OH)₂(py)₂] and a cyclic RGD-containing peptide c(RGDfK) was designed for cancer targeting with dual control over selectivity (Figure 1.20a).¹⁷⁴ Even though the IC₅₀ values for cells treated with the irradiated Pt–c(RGDfK) conjugate were higher than its parent succinylated complex, the selectivity was remarkably enhanced based on the levels of expression of α_vβ₃ and α_vβ₅ integrins. In addition, the cellular uptake of Pt(IV) prodrug increased when attached to c(RGDfK), especially for cells overexpressing α_vβ₃ and α_vβ₅ integrins. Another example of drug targeting for *trans,trans,trans*-[Pt(N₃)₂(OH)₂(py)₂] is its conjugate with guanidinoneomycin, which is a RNA-binding ligand and allows the complex to be taken up by cancer cells in a selective proteoglycan-dependent manner (Figure 1.20b).¹⁷⁵ The photoproducts with 5'-GMP or 5'-dCATGGCT for the Pt–guanidinoneomycin conjugate were similar to those of the parent complexes in the same conditions. Similar to Pt–c(RGDfK) conjugate, the Pt–guanidinoneomycin conjugate exhibited an enhanced cellular uptake with a preference to the malignant melanoma cell line.

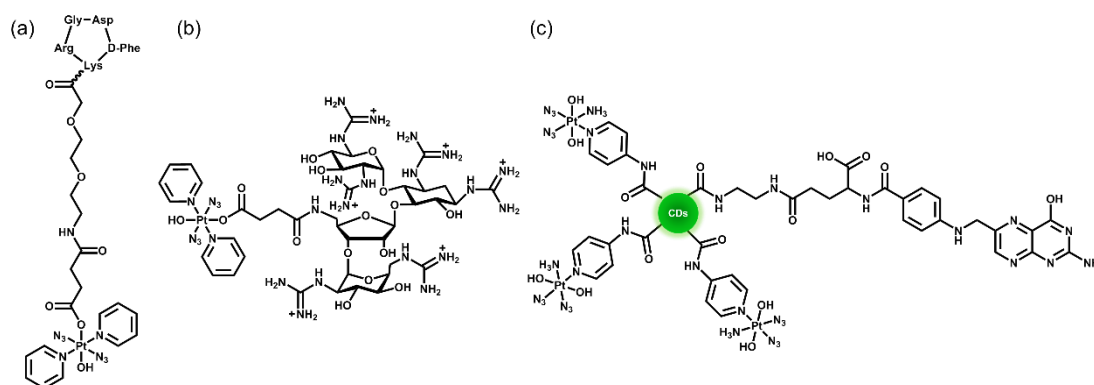


Figure 1.20. Photoactive diazido Pt(IV) complexes functionalised with cancer cell targeting axial ligands.

The Pt^{IV}-N₃-FA@CDs nanoplatfrom (Figure 1.20c) with a photoactive Pt(IV) azide prodrug and folic acid (FA) molecules covalently loaded on carbon dots exhibited a preference to folate receptor FR-positive [FR(+)] human cervical HeLa cells over FR-negative [FR(-)] human breast MCF-7 tumour cells.¹⁷⁶

Nanoparticle-based drug delivery systems have attracted particular attention due to their enhanced accumulation in tumour tissue through the enhanced permeation and retention (EPR) effect, which is caused by the leaky nature of angiogenic blood vessels of solid tumours.^{158,177-179} Photo-responsive block copolymer (BCP) micelles have been widely investigated for their drug delivery application in cancer therapy.¹⁸⁰

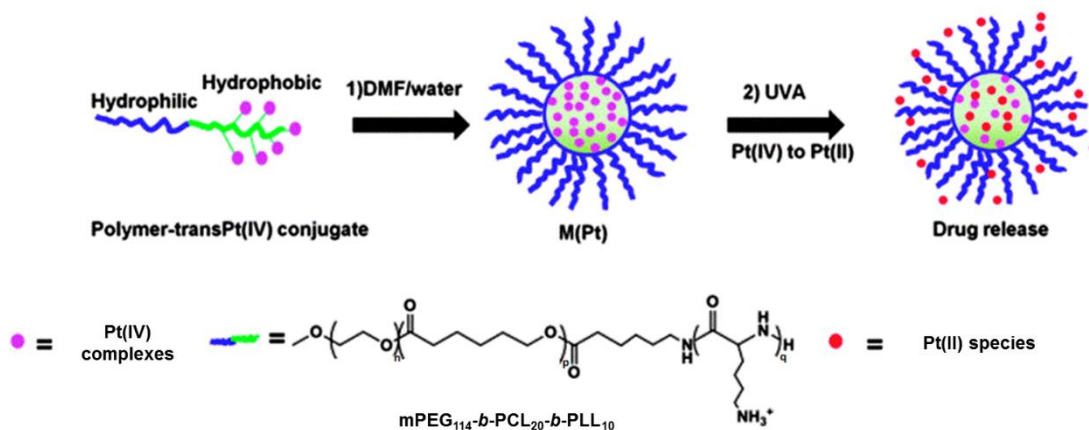


Figure 1.21. Preparation and photodecomposition of micelles assembled by mPEG₁₁₄-b-PCL₂₀-PLL₁₀ polymer with diazido Pt(IV) complexes. Adapted from *ref.* 182.

A triblock copolymer methoxy-poly(ethylene glycol)-*block*-poly(ϵ -caprolactone)-*block*-poly-L-lysine, mPEG₁₁₄-b-PCL₂₀-PLL₁₀ that comprises of mPEG ($n = 114$), polycaprolactone ($p = 20$) and poly-L-lysine ($q = 10$) self-assembles in aqueous solution, with polycaprolactone forming the core and Pt(IV) complex *cis,trans*-[Pt(1R, 2R-DACH)(N₃)₂(OH)₂] covalently encapsulated inside the hydrophobic core via an amide linkage (Figure 1.21).¹⁸¹ The micelles

exhibited greatly enhanced cellular accumulation and photocytotoxicity to ovarian cancer SKOV-3 cells compared with polymer free prodrug analogues. Importantly, *in vivo* studies revealed that conjugation to micelles enhanced the blood circulation half-life of the Pt(IV) complex by 10-fold. Improved inhibition efficacy against H22 murine hepatocarcinoma and decreased systemic toxicity were also demonstrated for the micelles. *Trans,trans,trans*-[Pt(N₃)₂(OH)₂(NH₃)₂] was also attached to biodegradable polymer mPEG₁₁₄-*b*-PCL₂₀-PLL₁₀ that can self-assemble into micelles with the hydrophobic chain and Pt species as the core to protect Pt(IV) prodrugs from deactivation in blood circulation.¹⁸² The micelles displayed comparable IC₅₀ values to cisplatin upon irradiation and a resistant factor (A2780CDDP/A2780) 5× lower than cisplatin. The same micelles loaded with more sterically hindered *trans,trans,trans*-[Pt(N₃)₂(OH)₂(NH₃)(py)] was > 100× more effective than cisplatin upon UVA irradiation (Figure 1.22).¹⁸³

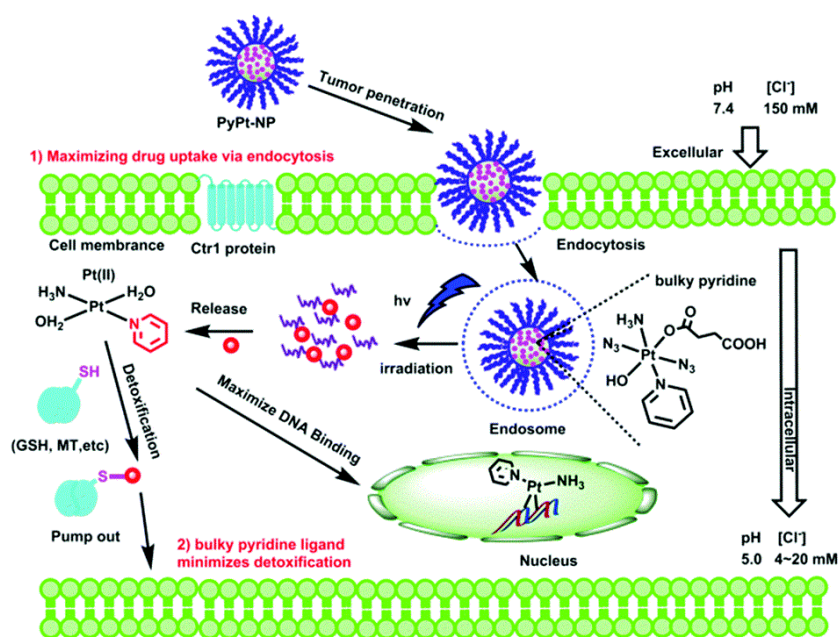


Figure 1.22. Delivery of sterically hindered Pt drugs attached to micelles. Adapted from *ref.*

183.

Trans,trans,trans-[Pt(N₃)₂(OH)₂(py)₂] has been conjugated to a tri-block copolymer as a stimuli-responsive co-monomer to form a photosensitive micelle.¹⁸⁴ The *in vivo* experiments revealed that the light irradiated micelle was 3–4× effective to BALB/c nude mice bearing A549 xenografts than the prodrug and cisplatin with lowest body weight loss, which provides an alternative to cisplatin to avoid neurotoxicity and nephrotoxicity. *Cis,trans,cis*-[Pt(N₃)₂(OH)₂(NH₃)₂] loaded amphiphiles with one lactose molecule self-assemble into micelles, while amphiphiles with two lactose molecules form vesicles instead. These nanoparticles displayed photocytotoxicity with liver cancer targeting ability. In addition, the platinum distribution in mice can be determined by fluorescence signals, CT values and ICP-MS.¹⁸⁵

For surface tumours, such as non-melanoma skin cancer, topical medication is an ideal way for precise localisation. G₄K⁺ hydrogels are biocompatible polymers with flexibility and high water content that allow them to mimic natural tissues.¹⁸⁶⁻¹⁸⁹ Pt(IV) based **Pt-G₄K⁺B** hydrogels (Figure 1.23) exhibit potent photocytotoxicity towards A2780cis cisplatin-resistant ovarian cancer cells, while displaying negligible cytotoxicity to MRC-5 normal fibroblast cells.¹⁸⁹

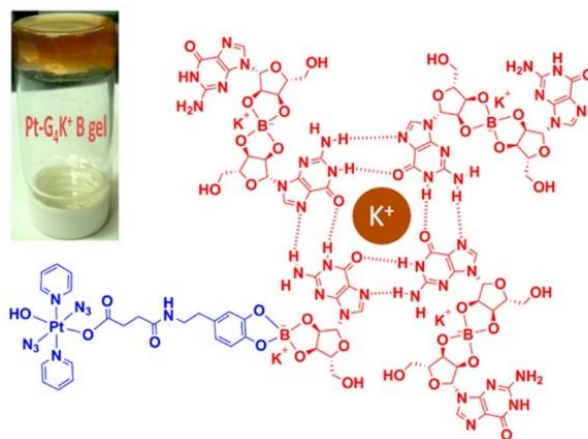


Figure 1.23. Schematic illustration of self-assembled **Pt-G₄K⁺B** hydrogel. Adapted from *ref.*

189.

1.5. Research aims

Trans,trans,trans-[Pt(N₃)₂(OH)₂(py)₂] is the most promising photoactive Pt(IV) complex in our group to date, which exhibits low dark cytotoxicity and significant photocytotoxicity upon irradiation with blue light. However, this complex suffers from a lack of targeting to cancer cells, and lack of activation by longer wavelength light. The general aim of this work is to synthesise and characterise novel photoactive diazido Pt(IV) complexes based on *trans,trans,trans*-[Pt(N₃)₂(OH)₂(py)₂] with one or more improvements as listed below, investigate their photophysical and photochemical properties, determine their anticancer activities, and further understand their mechanisms of action.

- To improve the selectivity and accumulation in cancer cells of diazido Pt(IV) complexes by introducing cancer cell-targeting amino acids, peptides and vitamins.
- To enhance the photocytotoxicity of diazido Pt(IV) complexes by conjugating them to small molecule anticancer agents, enzyme inhibitors, and mitochondria-targeting molecules.
- To generate photodecomposition of diazido Pt(IV) complexes with longer wavelength irradiation by incorporating dyes or complexes which absorb at longer excitation wavelengths.
- To investigate mechanisms of action by attaching fluorescent molecules or complexes to diazido Pt(IV) complexes and studying their behaviours within cells.
- To identify the photoproducts of diazido Pt(IV) complexes, including Pt(II) species, radicals and other cytotoxic species, and investigate their interactions with biomolecules.

1.6. References

1. S. I. Hajdu, *Cancer*, 2011, **117**, 1097–102.
2. WHO, <https://www.who.int/en/news-room/fact-sheets/detail/cancer>.
3. P. Kaatsch, *Cancer Treat. Rev.*, 2010, **36**, 277–285.
4. R. L. Siegel, K. D. Miller, A. Jemal, *CA Cancer J. Clin.*, 2019, **69**, 7–34.
5. P. Anand, A. B. Kunnumakara, C. Sundaram, K. B. Harikumar, S. T. Tharakan, O. S. Lai, B. Sung, B. B. Aggarwal, *Pharm. Res.*, 2008, **25**, 2097–2116.
6. GBD 2015 Risk Factors Collaborators, *Lancet*, 2016, **388**, 1659–1724.
7. M. Sorsa, *J. Toxicol. Environ. Health*, 1980, **6**, 977–982.
8. C. Sonnenschein, A. M. Soto, *Mol. Carcinog.*, 2000, **29**, 205–211.
9. D. Hanahan, R. A. Weinberg, *Cell*, 2000, **100**, 57–70.
10. D. Hanahan, R. A. Weinberg, *Cell*, 2011, **144**, 646–674.
11. Y. Lazebnik, *Nat. Rev. Cancer.*, 2010, **10**, 232–233.
12. C. Sonnenschein, A. M. Soto, *J. Biosci.*, 2013, **38**, 651–663.
13. P. Kumawat, H. Kumar, *Eur. J. Biomed. Pharm. Sci.*, 2018, **5**, 203–219.
14. L. S. Goodman, M. M. Wintrobe, W. Dameshek, M. J. Goodman, A. Gilman, M. T. McLennan, *J. Am. Med. Assoc.*, 1946, **132**, 126–132.
15. J. Sun, Q. Wei, Y. Zhou, J. Wang, Q. Liu, H. Xu, *BMC Syst. Biol.*, 2017, **11**, 87–102.
16. T. Bagnyukova, I. G. Serebriiskii, Y. Zhou, E. A. Hopper-Borge, E. A. Golemis, I. Astsaturov, *Cancer Biol. Ther.*, 2010, **10**, 839–853.

17. Y. K. Chae, A. P. Pan, A. A. Davis, S. P. Patel, B. A. Carneiro, R. Kurzrock, F. J. Giles, *Mol. Cancer Ther.*, 2017, **16**, 2645–2655.
18. https://en.wikipedia.org/wiki/Cancer_staging.
19. J. D. Spikes, *Primary Photoprocesses in Biology and Medicine*, Plenum Press, New York, 1985, 209–227.
20. N. R. Finsen, *Phototherapy*, Edward Arnold, London, 1901.
21. G. Stochel, M. Brindell, W. Macyk, Z. Stasicka, K. Szacilowski, *Bioinorganic Photochemistry*, John Wiley & Sons, Ltd., Chichester, 2009.
22. K. Szaciłowski, W. Macyk, A. Drzewiecka-Matuszek, M. Brindell, G. Stochel, *Chem. Rev.*, 2005, **105**, 2647–2694.
23. D. Barolet, *Semin. Cutaneous Med. Surg.*, 2008, **27**, 227–238.
24. B. C. Wilson, M. S. Patterson, *Photodynamic Therapy of Neoplastic Disease*, CRC Press, Boca Raton, 1990, 129–144.
25. D. E. J. G. J. Dolmans, D. Fukumura, R. K. Jain, *Nat. Rev. Cancer*, 2003, **3**, 380–387.
26. P. Agostinis, K. Berg, K. A. Cengel, T. H. Foster, A. W. Girotti, S. O. Gollnick, S. M. Hahn, M. R. Hamblin, A. Juzeniene, D. Kessel, M. Korbelik, J. Moan, P. Mroz, D. Nowis, J. Piette, B. C. Wilson, J. Golab, *CA: Cancer J. Clin.*, 2011, **61**, 250–281.
27. V. H. Fingar, T. J. Wieman, P. S. Haydon, *Photochem. Photobiol.*, 1997, **66**, 513–517.
28. Y. W. Yew, Y. C. Lai, Y. L. Lim, W. S. Chong, C. Theng, *J. Drugs Dermatol.*, 2016, **15**, 727–732.
29. M. H. Gold, *J. Clin. Aesthet. Dermatol.*, 2009, **2**, 44–47.

30. Q. Chen, Z. Huang, D. Luck, J. Beckers, P. Brun, B. C. Wilson, A. Scherz, Y. Salomon, F. W. Hetzel, *Photochem. Photobiol.*, 2002, **76**, 438–445.
31. P. Kaspler, S. Lazic, S. Forward, Y. Arenas, A. Mandela, L. Lilge, *Photochem. Photobiol. Sci.*, 2016, **15**, 481–495.
32. J. Fong, K. Kasimova, Y. Arenas, P. Kaspler, S. Lazic, A. Mandela, L. Lilge, *Photochem. Photobiol. Sci.*, 2015, **14**, 2014–2023.
33. N. J. Farrer, L. Salassa, P. J. Sadler, *Dalton Trans.*, 2009, **48**, 10690–10701.
34. S. Bonnet, *Dalton Trans.*, 2018, **47**, 10330–10343.
35. P. J. Bednarski, F. S. Mackay, P. J. Sadler, *AntiCancer Agents Med. Chem.*, 2007, **7**, 75–93.
36. A. K. Renfrew, N. S. Bryce, T. Hambley, *Chem. Eur. J.*, 2015, **21**, 15224–15234.
37. J. Paradies, J. Crudass, F. MacKay, L. J. Yellowlees, J. Montgomery, S. Parsons, L. Oswald, N. Robertson, P. J. Sadler, *J. Inorg. Biochem.*, 2006, **100**, 1260–1264.
38. A. Juris, V. Balzani, F. Barigelletti, S. Campagna, P. Belser, A. Von Zelewsky, *Coord. Chem. Rev.*, 1988, **84**, 85–277.
39. S. Monro, K. L. Colón, H. Yin, J. Roque, P. Konda, S. Gujar, R. P. Thummel, L. Lilge, C. G. Cameron, S. A. McFarland, *Chem. Rev.*, 2019, **119**, 2, 797–828.
40. T. Joshi, V. Pierroz, C. Mari, L. Gemperle, S. Ferrari, G. Gasser, *Angew. Chem., Int. Ed.*, 2014, **53**, 2960–2963.
41. A. Presa, G. Vázquez, L. A. Barrios, O. Roubeau, L. Korrodi-Gregório, R. Pérez-Tomás, P. Gamez, *Inorg. Chem.*, 2018, **57**, 4009–4022.

42. G. Shi, S. Monro, R. Hennigar, J. Colpitts, J. Fong, K. Kasimova, H. Yin, R. DeCoste, C. Spencer, L. Chamberlain, A. Mandel, L. Lilge, S. A. McFarland, *Coord. Chem. Rev.*, 2015, **282–283**, 127–138.
43. A. N. Hidayatullah, E. Wachter, D. K. Heidary, S. Parkin, E. C. Glazer, *Inorg. Chem.*, 2014, **53**, 10030–10032.
44. L. N. Lameijer, D. Ernst, S. L. Hopkins, M. S. Meijer, S. H. C. Askes, S. E. Le Dévédec, S. Bonnet, *Angew. Chem., Int. Ed.*, 2017, **56**, 11549–11553.
45. M. H. Al-Afyouni, T. N. Rohrabough, J. K. F. Al-Afyouni, C. Turro, *Chem. Sci.*, 2018, **9**, 6711–6720.
46. F. R. Hartley, *The chemistry of platinum and palladium: with particular reference to complexes of the elements*, Wiley, Weinheim, 1973.
47. N. N. Greenwood, A. Earnshaw, *Chemistry of the Elements*, Elsevier, Oxford, 1997.
48. B. Rosenberg, L. Van Camp, T. Krigas, *Nature*, 1965, **205**, 698–699.
49. B. Rosenberg, L. Van Camp, J. E. Trosko, V. H. Mansour, *Nature*, 1969, **222**, 385–386.
50. L. Kelland, *Nat. Rev. Cancer*, 2007, **7**, 573–584.
51. S. C. Sweetman, *Martindale: The complete drug reference*, Pharmaceutical Press, London, 2007.
52. N. J. Wheate, S. Walker, G. E. Craig, R. Oun, *Dalton Trans.*, 2010, **39**, 8113–8127.
53. T. Boulikas, A. Pantos, E. Bellis, P. Christofis, *Cancer Ther.*, 2007, **5**, 537–583.
54. A.S. Abu-Surrah, M. Kettunen, *Curr. Med. Chem.*, 2006, **13**, 1337–1357.
55. T. Boulikas, M. Vougiouka, *Oncol. Rep.*, 2003, **10**, 1663–1682.

56. A. Eastman, *Pharmacol. Ther.*, 1987, **34**, 155–166.
57. M. Crul, R. C. van Waardenburg, J. H. Beijnen, J. H. Schellens, *Cancer Treat. Rev.*, 2002, **28**, 291–303.
58. L. Nejd, J. Kudr, I. Blazkova, D. Chudobova, S. Skalickova, B. Ruttkay-Nedecky, V. Adam, R. Kizek, *Platinum Metals in the Environment*, Springer-Verlag, Heidelberg, 2015, 401–415.
59. B. Benedetti, E. Peterson, P. Kabolizadeh, A. Martinez, R. Kipping, N. P. Farrell, *Mol. Pharm.*, 2012, **8**, 940–948.
60. I. Khalaila, C. S. Allardyce, C. S. Verma, P. J. Dyson, *ChemBioChem*, 2005, **6**, 1788–1795.
61. J. Reedijk, *Chem. Rev.*, 1999, **99**, 2499–2510.
62. E. Wong, C. M. Giandomenico, *Chem. Rev.*, 1999, **99**, 2451–2466.
63. B. J. Pages, D. L. Ang, E. P. Wright, J. R. Aldrich-Wright, *Dalton Trans.*, 2015, **44**, 3505–3526.
64. J. Reedijk, *Eur. J. Inorg. Chem.*, 2009, **2009**, 1303–1312.
65. T. C. Johnstone, K. Suntharalingam, S. J. Lippard, *Chem. Rev.*, 2016, **116**, 3436–3486.
66. X. Han, J. Sun, Y. Wang, Z. He, *Med. Res. Rev.*, 2015, **35**, 1268–1299.
67. D. Gibson, *J. Inorg. Biochem.*, 2019, **191**, 77–84.
68. M. D. Hall, T. W. Hambley, *Coord. Chem. Rev.*, 2002, **232**, 49–67.
69. C. F. Chin, D. Y. Q. Wong, R. Jothibas, W. H. Ang, *Curr. Top. Med. Chem.*, 2011, **11**, 2602–2612.

70. V. H. C. Bramwell, D. Crowther, S. O'Malley, R. Swindell, R. Johnson, E. H. Cooper, N. Thatcher, A. Howell, *Cancer Treat. Rep.*, 1985, **69**, 409–416.
71. Q. Mi, S. S. Shu, C. X. Yang, C. Gao, X. Zhang, X. Luo, C. H. Bao, X. Zhang, J. Niu, *Clin. Eng. Radiat. Oncol.*, 2018, **7**, 231–247.
72. M. Gordon, S. Hollander, *J. Med.*, 1993, **24**, 209–265.
73. M. J. McKeage, F. Raynaud, J. Ward, C. Berry, D. O'Dell, L. R. Kelland, B. Murrer, P. Santabarbara, K. R. Harrap, I. R. Judson, *J. Clin. Oncol.*, 1997, **15**, 2691–2700.
74. U. Olszewski, F. Ach, E. Ulsperger, G. Baumgartner, R. Zeillinger, P. Bednarski, G. Hamilton, *Met. Based Drugs*, 2009, **2009**: 348916.
75. M. J. Cleare, J. D. Hoeschele, *Platinum Met. Rev.*, 1973, **17**, 2–13.
76. M. J. Cleare, J. D. Hoeschele, *Bioinorg. Chem.*, 1973, **2**, 187–210.
77. B. Rosenberg, L. Van Camp, E. B. Grimley, A. J. Thomson, *J. Biol. Chem.*, 1967, **242**, 1347–1352.
78. M. Coluccia, G. Natile, *Anti-Cancer Agents Med. Chem.*, 2007, **7**, 111–123.
79. G. Natile, M. Coluccia, *Coord. Chem. Rev.*, 2001, **216–217**, 383–410.
80. L. R. Kelland, C. F. J. Barnard, K. J. Mellish, M. Jones, P. M. Goddard, M. Valenti, A. Bryant, B. A. Murrer, K. R. Harrap, *Cancer Res.*, 1994, **54**, 5618–5622.
81. R. Prokop, J. Kasparkova, O. Novakova, V. Marini, A. M. Pizarro, C. Navarro-Ranninger, V. Brabec, *Biochem. Pharmacol.*, 2004, **67**, 1097–1109.
82. A. Žáková, O. Novaková, Z. Balcarova, U. Bierbach, N. Farrell, V. Brabec, *Eur. J. Biochem.*, 1998, **254**, 547–557.

83. V. Brabec, K. Nepelchova, J. Kasparikova, N. Farrell, *J. Biol. Inorg. Chem.*, 2000, **5**, 364–368.
84. W. I. Sundquist, D. P. Bancroft, S. J. Lippard, *J. Am. Chem. Soc.*, 1990, **112**, 1590–1596.
85. K. S. Lovejoy, R. C. Todd, S. Zhang, M. S. McCormick, J. A. D'Aquino, J. T. Reardon, A. Sancar, K. M. Giacomini, S. J. Lippard, *Proc. Natl. Acad. Sci. U.S.A.*, 2008, **105**, 8902–8907.
86. K. S. Lovejoy, M. Serova, I. Bieche, S. Emami, M. D'Incalci, M. Broggin, E. Erba, C. Gespach, E. Cvitkovic, S. Faivre, E. Raymond, S. J. Lippard, *Mol. Cancer Ther.*, 2011, **10**, 1709–1719.
87. D. Wang, G. Zhu, X. Huang, S. J. Lippard, *Proc. Natl. Acad. Sci. U.S.A.*, 2010, **107**, 9584–9589.
88. G. Y. Park, J. J. Wilson, Y. Song, S. J. Lippard, *Proc. Natl. Acad. Sci. U.S.A.*, 2012, **109**, 11987–11992.
89. Y. Zou, B. Van Houten, N. Farrell, *Biochemistry*, 1994, **33**, 5404–5410.
90. D. Yang, S. S. G. E. van Boom, J. Reedijk, J. H. van Boom, N. Farrell, A. H. J. Wang, *Nat. Struct. Biol.*, 1995, **2**, 577–578.
91. P. Perego, C. Caserini, L. Gatti, N. Carenini, S. Romanelli, R. Supino, D. Colangelo, I. Viano, R. Leone, S. Spinelli, G. Pezzoni, C. Manzotti, N. Farrell, F. Zunino, *Mol. Pharmacol.*, 1999, **55**, 528–534.
92. J. D. Roberts, J. Peroutka, G. Beggiolin, C. Manzotti, L. Piazzoni, N. Farrell, *J. Inorg. Biochem.*, 1999, **77**, 47–50.

93. C. Billecke, S. Finnis, L. Tahash, C. Miller, T. Mikkelsen, N. P. Farrell, O. Bogler, *Neuro-Oncol.*, 2006, **8**, 215–226.
94. G. Pratesi, P. Perego, D. Polizzi, S. C. Righetti, R. Supino, C. Caserini, C. Manzotti, F. C. Giuliani, G. Pezzoni, S. Tognella, S. Spinelli, N. Farrell, F. Zunino, *Br. J. Cancer*, 1999, **80**, 1912–1919.
95. C. Sessa, G. Capri, L. Gianni, F. Peccatori, G. Grasselli, J. Bauer, M. Zucchetti, L. Vigano, A. Gatti, C. Minoia, P. Liati, S. Van Den Bosch, A. Bernareggi, G. Camboni, S. Marsoni, *Ann. Oncol.*, 2000, **11**, 977–983.
96. P. Calvert, A. N. Hughes, A. Azzabi, M. Verill, G. Camboni, E. Verdi, A. Bernareggi, M. Zucchetti, C. Minoia, C. Sessa, J. Carmichael, A. Calvert, *Proc. Am. Soc. Clin. Oncol.*, 2000, **19**, abstr 921F.
97. Y. Qu, A. Harris, A. Hegmans, A. Petz, P. Kabolizadeh, H. Penazova, N. Farrell, *J. Inorg. Biochem.*, 2004, **98**, 1591–1598.
98. C. R. Brodie, J. G. Collins, J. R. Aldrich-Wright, *Dalton Trans.*, 2004, 1145–1152.
99. D. M. Fisher, P. J. Bednarski, R. Grünert, P. Turner, R. R. Fenton, J. R. Aldrich-Wright, *ChemMedChem*, 2007, **2**, 488–495.
100. D. M. Fisher, R. R. Fenton, J. R. Aldrich-Wright, *Chem. Commun.*, 2008, 5613–5615.
101. A. M. Krause-Heuer, R. Grünert, S. Kühne, M. Buczkowska, N. J. Wheate, D. D. Le Pevelen, L. R. Boag, D. M. Fisher, J. Kasparkova, J. Malina, P. J. Bednarski, V. Brabec, J. R. Aldrich-Wright, *J. Med. Chem.*, 2009, **52**, 5474–5484.
102. K. B. Garbutcheon-Singh, P. Leverett, S. Myers, J. R. Aldrich-Wright, *Dalton Trans.*, 2013, **42**, 918–926.

103. S. Kemp, N. J. Wheate, D. P. Buck, M. Nikac, J. G. Collins, J. R. Aldrich-Wright, *J. Inorg. Biochem.*, 2007, **101**, 1049–1058.
104. K. Mitra, *Dalton Trans.*, 2016, **45**, 19157–19171.
105. T. Zou, C. Lok, Y. M. E. Funga, C. M. Che, *Chem. Commun.*, 2013, **49**, 5423–5425.
106. S. W. Lai, Y. Liu, D. Zhang, B. Wang, C. N. Lok, C. M. Che, M. Selke, *Photochem Photobiol.*, 2010, **86**, 1414–1420.
107. A. Naik, R. Rubbiani, G. Gasser, B. Spingler, *Angew. Chem., Int. Ed.*, 2014, **53**, 6938–6941.
108. J. Zhou, Y. Zhang, G. Yu, M. R. Crawley, C. R. P. Fulong, A. E. Friedman, S. Sengupta, J. Sun, Q. Li, F. Huang, T. R. Cook, *J. Am. Chem. Soc.*, 2018, **140**, 7730–7736.
109. V. Ramu, S. Gautam, A. Garai, P. Kondaiah, A. R. Chakravarty, *Inorg. Chem.*, 2018, **57**, 1717–1726.
110. Y. Zhong, H. Zhang, W. Liu, X. Zheng, Y. Zhou, Q. Cao, Y. Shen, Y. Zhao, P. Z. Qin, L. Ji, Z. Mao, *Chem. Eur. J.*, 2017, **23**, 16442–16446.
111. L. Quental, P. Raposo, F. Mendes, I. Santos, C. Navarro-Ranninger, A. Alvarez-Valdes, H. Huang, H. Chao, R. Rubbiani, G. Gasser, A. G. Quiroga, A. Paulo, *Dalton Trans.*, 2017, **46**, 14523–14536.
112. Y. Zheng, D. Zhang, H. Zhang, J. Cao, C. Tan, L. Ji, Z. Mao, *Chem. Eur. J.*, 2018, **24**, 18971–18980.
113. P. Heringova, J. Woods, F. S. Mackay, J. Kasparkova, P. J. Sadler, V. Brabec, *J. Med. Chem.*, 2006, **49**, 7792–7798.
114. J. Mlcouskova, J. Stepankova, V. Brabec, *J. Biol. Inorg. Chem.*, 2012, **17**, 891–898.

115. K. Mitra, S. Gautam, P. Kondaiah, A. R. Chakravarty, *Angew. Chem., Int. Ed.*, 2015, **54**, 13989–13993.
116. K. Mitra, C. E. Lyons, M. C. T. Hartman, *Angew. Chem. Int. Ed.*, 2018, **57**, 10263–10267.
117. Y. Zhao, G. M. Roberts, S. E. Greenough, N. J. Farrer, M. J. Paterson, W. H. Powell, V. G. Stavros, P. J. Sadler, *Angew. Chem., Int. Ed.*, 2012, **51**, 11263–11266.
118. D. Liu, J. Ma, W. Zhou, W. He, Z. Guo, *Inorg. Chim. Acta*, 2012, **393**, 198–203.
119. K. L. Ciesienski, L. M. Hyman, D. T. Yang, K. L. Haas, M. G. Dickens, R. J. Holbrook, K. J. Franz, *Eur. J. Inorg. Chem.*, 2010, **15**, 2224–2228.
120. A. Presa, R. F. Brissos, A. B. Caballero, I. Borilovic, L. Korrodi-Gregório, R. Pérez-Tomás, O. Roubeau, P. Gamez, *Angew. Chem. Int. Ed.*, 2015, **54**, 4561–4565.
121. A. Vogler, J. Hlavatsch, *Angew. Chem. Int. Ed.*, 1983, **22**, 154–155.
122. A. Vogler, C. Quett, H. Kunkely, *Ber. Bunsen-Ges. Phys. Chem.*, 1988, **92**, 1486–1492.
123. R. E. Cameron, A. B. Bocarsly, *Inorg. Chem.*, 1986, **25**, 2910–2913.
124. J. P. Macquet, J. L. Butour, *J. Nat. Cancer Inst.*, 1983, **70**, 899–905.
125. J. L. Van der Veer, A. R. Peters, J. Reedijk, *J. Inorg. Biochem.*, 1986, **26**, 137–142.
126. R. M. Roat, J. Reedijk, *J. Inorg. Biochem.*, 1993, **52**, 263–274.
127. N. A. Kratochwil, P. J. Bednarski, H. Mrozek, A. Vogler, J. K. Nagle, *Anticancer Drug Des.*, 1996, **11**, 155–171.
128. N. A. Kratochwil, M. Zabel, K. J. Range, P. J. Bednarski, *J. Med. Chem.*, 1996, **39**, 2499–2507.

129. N. A. Kratochwil, J. A. Parkinson, P. J. Bednarski, P. J. Sadler, *Angew. Chem. Int. Ed.*, 1999, **38**, 1460–1463.
130. N. A. Kratochwil, Z. Guo, P. S. Murdoch, J. A. Parkinson, P. J. Bednarski, P. J. Sadler, *J. Am. Chem. Soc.*, 1998, **120**, 8253–8254.
131. N. A. Kratochwil, P. J. Bednarski, *Arch. Pharm. Pharm. Med. Chem.*, 1999, **332**, 279–285.
132. J. Šima, *Coord. Chem. Rev.*, 2006, **250**, 2325–2334.
133. A. Vogler, A. Kern, *Angew. Chem. Int. Ed.*, 1978, **17**, 524–525.
134. P. Müller, B. Schröder, J. A. Parkinson, N. A. Kratochwil, R. A. Coxall, A. Parkin, S. Parsons, P. J. Sadler, *Angew. Chem. Int. Ed.*, 2003, **42**, 335–339.
135. J. Kašpárková, F. S. Mackay, V. Brabec, P. J. Sadler, *J Biol. Inorg. Chem.*, 2003, **8**, 741–745.
136. P. J. Bednarski, R. Grünert, M. Zielzki, A. Wellner, F. S. Mackay, P. J. Sadler, *Chem. Biol.*, 2006, **13**, 61–67.
137. L. Ronconi, P. J. Sadler, *Chem. Commun.*, 2008, **2**, 235–237.
138. H. I. A. Phillips, L. Ronconi, P. J. Sadler, *Chem. Eur. J.*, 2009, **15**, 1588–1596.
139. F. S. Mackay, J. A. Woods, H. Moseley, J. Ferguson, A. Dawson, S. Parsons, P. J. Sadler, *Chem. Eur. J.*, 2006, **12**, 3155–3161.
140. N. J. Farrer, J. A. Woods, V. P. Munk, F. S. Mackay, P. J. Sadler, *Chem. Res. Toxicol.*, 2010, **23**, 413–421.
141. H. C. Tai, Y. Zhao, N. J. Farrer, A. E. Anastasi, G. Clarkson, P. J. Sadler, R. J. Deeth, *Chem. Eur. J.*, 2012, **18**, 10630–10642.

142. F. S. Mackay, J. A. Woods, P. Heringová, J. Kašpárková, A. M. Pizarro, S. A. Moggach, S. Parsons, V. Brabec, P. J. Sadler, *Proc. Natl. Acad. Sci. USA*, 2007, **104**, 20743–20748.
143. A. F. Westendorf, A. Bodtke, P. J. Bednarski, *Dalton Trans.*, 2011, **40**, 5342–5351.
144. A. F. Westendorf, J. A. Woods, K. Korpis, N. J. Farrer, L. Salassa, K. Robinson, V. Appleyard, K. Murray, R. Grünert, A. M. Thompson, P. J. Sadler, P. J. Bednarski, *Mol. Cancer Ther.*, 2012, **11**, 1894–1904.
145. A. F. Westendorf, L. Zerzankova, L. Salassa, P. J. Sadler, V. Brabec, P. J. Bednarski, *J. Inorg. Biochem.*, 2011, **105**, 652–662.
146. F. S. Mackay, S. A. Moggach, A. Collins, S. Parsons, P. J. Sadler, *Inorg. Chim. Acta*, 2009, **362**, 811–819.
147. Y. Zhao, N. J. Farrer, H. Li, J. S. Butler, R. J. McQuitty, A. Habtemariam, F. Wang, P. J. Sadler, *Angew. Chem. Int. Ed.*, 2013, **52**, 13633–13637.
148. Y. Zhao, J. A. Woods, N. J. Farrer, K. S. Robinson, J. Pracharova, J. Kasparkova, O. Novakova, Huilin Li, Luca Salassa, Ana M. Pizarro, Guy J. Clarkson, Lijiang Song, Viktor Brabec, P. J. Sadler, *Chem. Eur. J.*, 2013, **19**, 9578–9591.
149. N. J. Farrer, J. A. Woods, L. Salassa, Y. Zhao, K. S. Robinson, G. Clarkson, F. S. Mackay, P. J. Sadler, *Angew. Chem. Int. Ed.*, 2010, **49**, 8905–8908.
150. J. Pracharova, L. Zerzankova, J. Stepankova, O. Novakova, N. J. Farrer, P. J. Sadler, V. Brabec, J. Kasparkova, *Chem. Res. Toxicol.*, 2012, **25**, 1099–1111.
151. C. A. Wootton, C. Sanchez-Cano, A. F. Lopez-Clavijo, E. Shaili, M. P. Barrow, P. J. Sadler, P. B. O'Connor, *Chem. Sci.*, 2018, **9**, 2733–2739.

152. J. Du, Y. Wei, Y. Zhao, F. Xu, Y. Wang, W. Zheng, Q. Luo, M. Wang, F. Wang, *Inorg. Chem.*, 2018, **57**, 5575–5584.
153. J. S. Butler, J. A. Woods, N. J. Farrer, M. E. Newton, P. J. Sadler, *J. Am. Chem. Soc.*, 2012, **134**, 16508–16511.
154. C. Vallotto, E. Shaili, H. Shi, J. S. Butler, C. J. Wedge, M. E. Newton, P. J. Sadler, *Chem. Commun.*, 2018, **54**, 13845–13848.
155. F. S. Mackay, N. J. Farrer, L. Salassa, H. C. Tai, R. J. Deeth, S. A. Moggach, P. A. Wood, S. Parsons, P. J. Sadler, *Dalton Trans.*, 2009, 2315–2325.
156. Y. Nakabayashi, A. Erxleben, U. Létinois, G. Pratviel, B. Meunier, L. Holland, B. Lippert, *Chem. Eur. J.*, 2007, **13**, 3980–3988.
157. C. Loup, A. T. Vallina, Y. Coppel, U. Létinois, Y. Nakabayashi, B. Meunier, B. Lippert, G. Pratviel, *Chem. Eur. J.*, 2010, **16**, 11420–11431.
158. H. Xiao, L. Yan, E. M. Dempsey, W. Song, R. Qi, W. Li, Y. Huang, X. Jing, D. Zhou, J. Ding, X. Chen, *Prog. Polym. Sci.*, 2018, **87**, 70–106.
159. D. Guo, S. Xu, Y. Huang, H. Jiang, W. Yasen, N. Wang, Y. Su, J. Qian, J. Li, C. Zhang, X. Zhu, *Biomaterials*, 2018, **177**, 67–77.
160. Y. Sun, T. Shi, L. Zhou, Y. Zhou, B. Sun, X. Liu, *J. Microencapsul.*, 2017, **34**, 675–686.
161. L. T. Ellis, H. Meng Er, T. W. Hambley, *Aust. J. Chem.*, 1995, **48**, 793–806.
162. V. Venkatesh, C. J. Wedge, I. Romero-Canelón, A. Habtemariam, P. J. Sadler, *Dalton Trans.*, 2016, **45**, 13034–13037.
163. L. Ning, D. Y. Greenblatt, M. Kunnimalaiyaan, H. Chen, *Oncologist*, 2008, **13**, 98–104.

164. J. Kasparikova, H. Kostrhunova, O. Novakova, R. Křikavová, J. Vančo, Z. Trávníček, V. Brabec, *Angew. Chem. Int. Ed.*, 2015, **54**, 14478–14482.
165. A. Juzeniene, *Photodiagnosis Photodyn. Ther.*, 2009, **6**, 94–96.
166. S. Xu, X. Zhu, C. Zhang, W. Huang, Y. Zhou, D. Yan, *Nature Commun.*, 2018, **9**:2053.
167. S. Banerjee, A. R. Chakravarty, *Acc. Chem. Res.*, 2015, **48**, 7, 2075–2083.
168. S. He, Y. Qi, G. Kuang, D. Zhou, J. Li, Z. Xie, X. Chen, X. Jing, Y. Huang, *Biomacromolecules*, 2016, **17**, 2120–2127.
169. Y. Min, J. Li, F. Liu, E.K.L. Yeow, B. Xing, *Angew. Chem. Int. Ed.*, 2014, **53**, 1012–1016.
170. X. Li, J. Mu, F. Liu, E. W. P. Tan, B. Khezri, R. D. Webster, E. K. L. Yeow, B. Xing, *Bioconjugate Chem.*, 2015, **26**, 955–961.
171. Y. Dai, H. Xiao, J. Liu, Q. Yuan, P. Ma, D. Yang, C. Li, Z. Cheng, Z. Hou, P. Yang, J. Lin, *J. Am. Chem. Soc.*, 2013, **135**, 18920–18929.
172. M. Friedlander, P. C. Brooks, R. W. Shaffer, C. M. Kincaid, J. A. Varner, D. A. Cheresh, *Science*, 1995, **270**, 1500–1502.
173. J. S. Desgrosellier, D. A. Cheresh, *Nat. Rev. Cancer*, 2010, **10**, 9–22.
174. A. Gandioso, E. Shaili, A. Massaguer, G. Artigas, A. González-Cantó, J. A. Woods, P. J. Sadler, V. Marchán, *Chem. Commun.*, 2015, **51**, 9169–9172.
175. E. Shaili, M. Fernández-Giménez, S. Rodríguez-Astor, A. Gandioso, L. Sandín, C. García-Vélez, A. Massaguer, G. J. Clarkson, J. A. Woods, P. J. Sadler, V. Marchán, *Chem. Eur. J.*, 2015, **21**, 18474–18486.
176. X. Yang, H. Xiang, L. An, S. Yang, J. Liu, *New J. Chem.*, 2015, **39**, 800–804.
177. M. Imran, W. Ayub, I. S. Butler, Z. Rehman, *Coord. Chem. Rev.*, 2018, **376**, 405–429.

178. H. Maeda, *J. Control. Release*, 2012, **164**, 138–144.
179. H. Wei, R. Zhuo, X. Zhang, *Prog. Polym. Sci.*, 2013, **38**, 503–535.
180. Y. Zhao, *Macromolecules*, 2012, **45**, 3647–3657.
181. H. Xiao, G. T. Noble, J. F. Stefanick, R. Qi, T. Kiziltepe, X. Jing, B. Bilgicer, *J. Control. Release*, 2014, **173**, 11–17.
182. H. Song, W. Li, R. Qi, L. Yan, X. Jing, M. Zheng, H. Xiao, *Chem. Commun.*, 2015, **51**, 11493–11495.
183. H. Song, X. Kang, J. Sun, X. Jing, Z. Wang, L. Yan, R. Qi, M. Zheng, *Chem. Commun.*, 2016, **52**, 2281–2283.
184. D. Zhou, J. Guo, G. B. Kim, J. Li, X. Chen, J. Yang, Y. Huang, *Adv. Healthcare Mater.*, 2016, **5**, 2493–2499.
185. S. He, C. Li, Q. Zhang, J. Ding, X. Liang, X. Chen, H. Xiao, X. Chen, D. Zhou, Y. Huang, *ACS Nano.*, 2018, **12**, 7272–7281
186. G. M. Peters, L. P. Skala, T. N. Plank, B. J. Hyman, G. N. M. Reddy, A. Marsh, S. P. Brown, J. T. Davis, *J. Am. Chem. Soc.*, 2014, **136**, 12596–12599.
187. G. M. Peters, L. P. Skala, T. N. Plank, H. Oh, G. N. M. Reddy, A. Marsh, S. P. Brown, S. R. Raghavan, J. T. Davis, *J. Am. Chem. Soc.*, 2015, **137**, 5819–5827.
188. T. N. Plank, J. T. Davis, *Chem. Commun.*, 2016, **52**, 5037–5040.
189. V. Venkatesh, N. K. Mishra, I. Romero-Canelón, R. R. Vernooij, H. Shi, J. P. C. Coverdale, A. Habtemariam, S. Verma, P. J. Sadler, *J. Am. Chem. Soc.*, 2017, **139**, 5656–5659.

Chapter 2

Experimental Methods

This Chapter describes the general experimental techniques and instrumentation used in this thesis. Particular methods for individual experiments are described in the appropriate Chapters.

2.1. Materials

All materials were used as obtained from commercial sources unless otherwise stated. K_2PtCl_4 , NaN_3 , H_2O_2 (30%), 5'-guanosine monophosphate disodium salt (5'-GMP- Na_2), deoxyribonucleic acid from calf thymus (*ct*-DNA), 5, 5-dimethyl-pyrroline-*N*-oxide (DMPO), and formic acid (FA) were obtained from Sigma-Aldrich. Pyridine, trifluoroacetic acid (TFA) and all solvents for common use were analytical reagent grade from Fisher Scientific and used as supplied. Distilled water was purified using a Millipore water purification system. Water used in ICP-OES was purified using Purelab UHQ water purification system.

Parental Pt(IV) complexes *trans,trans,trans*-[Pt(py) $_2$ (N $_3$) $_2$ (OH) $_2$] (**1**, Figure 2.1) and *trans,trans,trans*-[Pt(py) $_2$ (N $_3$) $_2$ (OH)(succH)] (**2**, Figure 2.1) were prepared according to literature methods.^{1,2}

Trans,trans,trans-[Pt(py) $_2$ (N $_3$) $_2$ (OH) $_2$] (**1**). K_2PtCl_4 (200 mg, 481.9 μ mol) was dissolved in H_2O (1.4 mL) and pyridine (0.47 mL) was added. The solution was stirred at 363 K for 1 h and NaN_3 (628 mg, 10449.3 μ mol) in H_2O (4.0 mL) was added dropwise. The mixture was stirred at 363 K for 2 h after addition and allowed to cool down. The yellow precipitate was filtered and washed with water and ethanol. The solid was suspended in H_2O_2 (10 mL) and allowed to react at 318 K overnight, producing a yellow solution. The solution was filtered and the filtrate was lyophilised. The complex was purified by column chromatography on silica gel (5% methanol + 95% DCM). 1H NMR (D_2O , 400 MHz): 8.72 (d, $J = 6.2$ Hz, $J^{195}Pt-^1H = 26.6$ Hz,

4H, $H_{ortho\ py}$), 8.21 (t, $J = 7.7\text{ Hz}$, 2H, $H_{para\ py}$), 7.75 (t, $J = 6.9\text{ Hz}$, 4H, $H_{meta\ py}$). ESI-MS: $[M + Na]^+$ (m/z) Calc., 494.1; Found, 494.0.

***Trans,trans,trans*-[Pt(py)₂(N₃)₂(OH)(succH)] (2).** *Trans,trans,trans*-[Pt(py)₂(N₃)₂(OH)₂] (50 mg, 106.2 μmol) and succinic anhydride (15 mg, 149.9 μmol) were suspended in DMF and allowed to react at 348 K overnight. After evaporation to dryness, the oily residue was re-dissolved in acetone (2 mL). A yellow solid was obtained by excessive addition of diethyl ether then filtered and dried in air. ¹H NMR (DMSO-*d*₆, 400 MHz): 12.04 (s, H, COOH), 8.82 (d, $J = 5.7\text{ Hz}$, $J^{195\text{ Pt}-1\text{ H}} = 26.4\text{ Hz}$, 4H, $H_{ortho\ py}$), 8.28 (t, $J = 7.6\text{ Hz}$, 2H, $H_{para\ py}$), 7.83 (t, $J = 6.8\text{ Hz}$, 4H, $H_{meta\ py}$), 3.68 (s, H, OH), 2.45 (t, $J = 6.6\text{ Hz}$, 2H, CH₂), 2.36 (t, $J = 6.6\text{ Hz}$, 2H, CH₂). ESI-MS: $[M + Na]^+$ (m/z) Calc., 594.1; Found, 593.9.

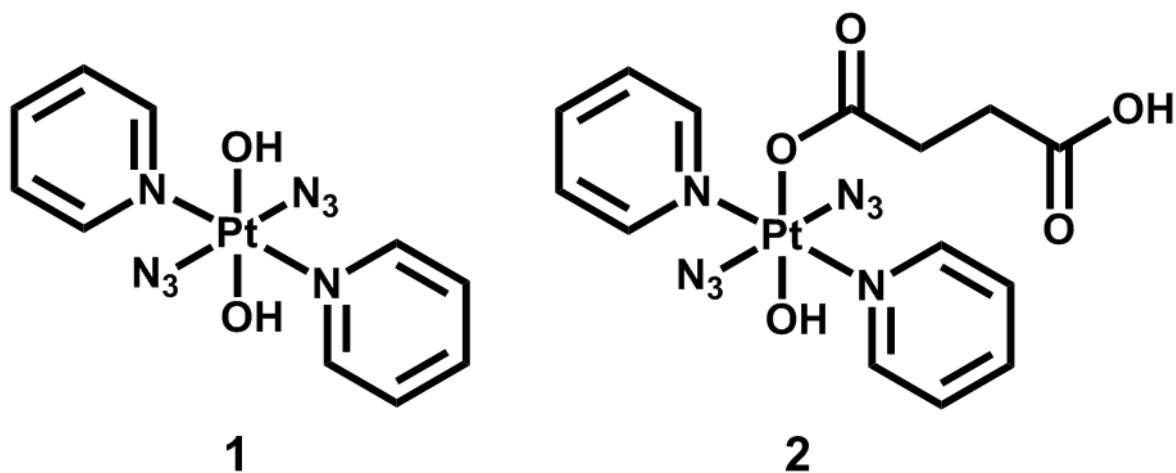


Figure 2.1. Parent Pt(IV) complexes *trans,trans,trans*-[Pt(py)₂(N₃)₂(OH)₂] (1) and *trans,trans,trans*-[Pt(py)₂(N₃)₂(OH)(succH)] (2)

2.2. Instruments

2.2.1. Nuclear magnetic resonance spectroscopy (NMR)³

Isotopes possessing a nuclear spin of $\frac{1}{2}$ (or $> \frac{1}{2}$) are detectable by NMR. In this thesis, ^1H and ^{13}C NMR spectra were acquired at 298 K on Bruker Avance III 400 MHz or Bruker Avance III HD 300 MHz, Bruker Avance III HD 400 MHz, Bruker Avance III HD 500 MHz spectrometers for characterisation. Samples were prepared in 5 mm NMR tubes with 0.5 mL appropriate solvent. ^1H NMR chemical shifts were internally calibrated with the residual peaks of solvent MeOD- d_4 (3.49 ppm), DMSO- d_6 (2.50 ppm) or CHCl_3 (7.26 ppm).⁴ In ^{13}C NMR, JMOD (J Modulation) pulse sequences produce spectra in which the positive signals are from CH_2 or quaternary carbons and the negative signals are from CH and CH_3 groups. The signals of quaternary carbons were generally of low intensity due to their longer spin-lattice relaxation time T_1 and smaller NOEs (Nuclear Overhauser Effect).⁵ Spectra were processed using Bruker Topspin 3.2 or MestReNova.

2.2.2. Mass spectrometry (MS)

2.2.2.1. Electrospray ionisation-mass spectrometry (ESI-MS)⁶

ESI-MS is a soft-ionisation mass spectrometric technique for the measurement of the mass-to-charge ratios of ions. ESI-MS spectra were recorded on an Agilent 6130B single quadrupole detector instrument at 298 K with a scan range of m/z 50–2000 for positive ions. Samples were prepared in methanol or aqueous solution. Data were analysed using Data Analysis (Bruker Daltonics). The distinctive isotopic distribution pattern of platinum can aid the detection of

platinum-containing species, including 6 stable isotopes, ^{190}Pt (0.0014 %), ^{192}Pt (0.782 %), ^{194}Pt (32.967 %), ^{195}Pt (33.832 %), ^{196}Pt (25.242 %), ^{198}Pt (7.163 %).

2.2.2.2. HPLC coupled mass spectrometry (LC-MS)

LC-MS is widely used in the analytical separations and quantification of compounds. LC-MS was carried out on a Bruker Amazon X mass spectrometer connected online with an Agilent 1260 HPLC system with an Agilent ZORBAX Eclipse XDB-C18 column (250 × 4.6 mm, 5 μm). Mobile phases consisted of 0.1% formic acid in HPLC grade H₂O (solvent A) and 0.1% formic acid in HPLC grade CH₃CN (solvent B). A linear gradient of 10% to 80% B in 30 min was employed with flow rate at 1 mL/min. UV detection was made at 254 nm and the mass spectrometer was operated in electrospray positive mode with a scan range 50–3000 m/z. 20 μL sample solution was upload by an automatic sample delivery system. Data were analysed using Data Analysis (Bruker Daltonics).

2.2.3. High performance liquid chromatography (HPLC)

HPLC is a technique in analytical chemistry used to separate, identify, and quantify each component in a mixture. In this work, HPLC was mainly used to assess the purity of new complexes, using an Agilent 1100 HPLC system with an Agilent ZORBAX Eclipse XDB-C18 column (250 × 4.6 mm, 5 μm). Mobile phases consisted of 0.1% trifluoroacetic acid in HPLC grade H₂O (solvent A) and 0.1% trifluoroacetic acid in HPLC grade CH₃CN (solvent B). A linear gradient of 10% B to 80% B in 30 min was employed with flow rate at 1 mL/min. Samples were detected by UV absorption at 254 nm using the signal at 360 nm as reference.

2.2.4. UV-vis absorption spectroscopy

UV-vis absorption spectroscopy is routinely used in the quantitative determination of solutions to study electronic excitations of molecules. UV-vis absorption spectra were recorded on a Varian Cary 300 UV-vis spectrophotometer in 1 cm path-length quartz cuvettes at 298 K unless otherwise stated. The spectral width was 200–800 nm and the bandwidth was 1.0 nm, the scan rate was set to 600 nm/min. Neat solvent was recorded for reference. Data were processed with OriginPro 2016. Pt concentrations were measured by ICP-OES for extinction coefficients determination.

2.2.5. Fluorescence spectroscopy

Fluorescence spectroscopy is a complementary technique of absorption spectroscopy that analyses fluorescence from a sample. Fluorescence spectra were recorded on a Jasco FP-6500 spectrofluorometer at 298 K. Excitation wavelength and slit width are mentioned in specific Chapters. Neat solvent was recorded for reference in the same condition. Data were processed with OriginPro 2016.

2.2.6. X-ray crystallography

The data collection, structure determination and refinement were carried out by Dr Guy Clarkson at the University of Warwick.

X-ray crystallography is a non-destructive technique used to determine the atomic and molecular structure of a crystal.⁷ A suitable crystal was selected and mounted on a Mitegen head with Fomblin oil and placed on an Xcalibur Gemini diffractometer with a Ruby CCD area

detector. The crystal was kept at 150(2) K during data collection. Using Olex2,⁸ the structure was solved with the ShelXT⁹ structure solution program using Direct Methods and refined with the ShelXL¹⁰ refinement package using Least Squares minimisation. The solved structures were analysed by Mercury 3.8.

2.2.7. Irradiation devices

Photoactivation of platinum complexes was carried out at 293 K. The light sources (Figure 2.2) include: (i) LZC-ICH2 photoreactor (Luzchem Research Inc.) equipped with a temperature controller and 8 Luzchem LZC-420 lamps without light filtration; (ii) LED465E (Thorlabs, Epoxy-Encased LED, 465 nm, 20 mW); (iii) LED light sources (BASETech model no. SP-GU10 230 V~50 Hz 1.3-2.1 W) with $\lambda_{\text{max}} = 463, 517$ or 593 nm; (iv) 96-array of LEDs constructed by Mr Rod Wesson, Electrical and Electronics Workshop, University of Warwick. The LEDs used for blue light were Multicomp OVL-5523 5 mm LEDs with a dominant wavelength of 465 nm and a power of 4.8 mW cm^{-2} per LED once constructed into the array. The LEDs used for green light were Multicomp OVL-5524 5 mm LEDs with a dominant wavelength of 520 nm and a power of 11.7 mW cm^{-2} per LED once constructed into the array.

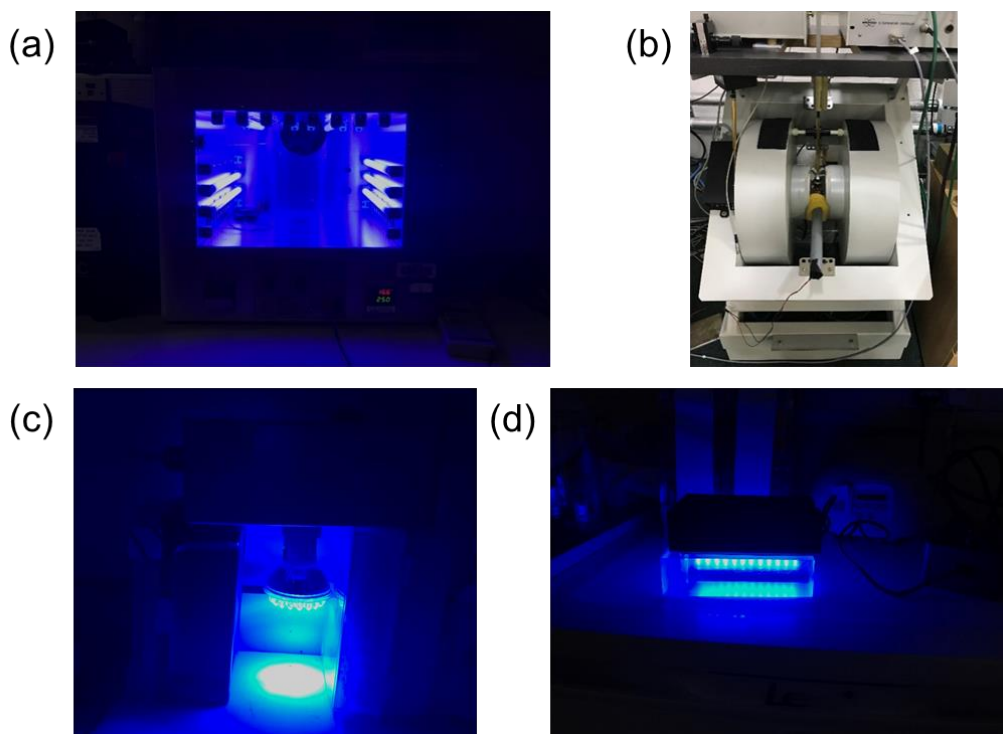


Figure 2.2. Light sources used in this thesis: (a) LXC-ICH2 photoreactor (Luzchem Research Inc.) equipped with a temperature controller and 8 Luzchem LXC-420 lamps without light filtration; (b) LED465E; (c) LED light sources with $\lambda_{\max} = 463$ nm; (d) 96-array of blue LEDs.

2.2.8. Electron paramagnetic resonance (EPR) spectroscopy¹¹

EPR is a method used for studying materials with unpaired electrons, which has analogous basic concepts to NMR and is particularly useful for investigating metal complexes or organic radicals. The EPR spectra were recorded on a Bruker EMX (X-band) spectrometer at 298 K. Samples (*ca.* 100 μL) in aqueous solution were prepared and transferred using a plastic syringe with metal needle to a standard quality quartz tube with inner diameter of 1.0 mm and outer diameter of 2.0 mm (Wilma LabGlass) and sealed with parafilm. Typical key EPR spectrometer settings were modulation amplitude 1.0 G, microwave power 6.32 mW, 1.0×10^5 receiver gain, conversion time 5.12 ms, time constant 5.12 ms, sweep width 200 G. The light

irradiation source was mounted between the EPR magnets, supported by a foam sponge, to maintain its position throughout the EPR sample measurements. The distance from the tip of the irradiation light bulb to the EPR cavity was *ca.* 3 cm. Data were processed by Matlab R2016b with easyspin 5.1.12.

2.2.9. Inductively coupled plasma optical emission spectroscopy/mass spectrometry (ICP-OES/MS)

An inductively coupled plasma (ICP) is a type of plasma source in which the energy is supplied by electric currents produced by electromagnetic induction. The platinum concentration in aqueous solutions was determined by ICP-OES or ICP-MS in this work.

2.2.9.1. ICP-OES

ICP-OES experiments were carried out on a PerkinElmer Optima 5300 DV optical emission spectrometer with an AS-93 plus autosampler. The emission wavelengths detected for Pt were 265.945, 214.423, 299.797, 204.937 and 193.700 nm. The intensities of the spectral lines are measured by CID semiconductor detectors. Samples were calibrated with 8 standards prepared from a stock of 1000 ppm Pt solutions obtained from Sigma Aldrich in 3.6% HNO₃ with miliQ water at the following concentrations: 700, 600, 500, 400, 300, 200, 100, 50 ppb. Data analysis was carried out on WinLab32 (version 3.4.1).

2.2.9.2. ICP-MS

ICP-MS was carried out on an Agilent 7500 Series ICP-MS spectrometer in no-gas mode. The concentration of an isotope (element) in the sample can be quantified by the intensity of the m/z peak in the mass spectrum. 12 standards prepared from a stock of 1000 ppm Pt solutions obtained from Sigma Aldrich in 3.6% HNO₃ with miliQ water at the following concentrations: 500, 250, 100, 50, 25, 10, 5, 2.5, 1, 0.5, 0.25, 0.1 ppb. Data acquisition was carried out using ICP-MS TOP with an internal standard of ¹⁶⁶Er (50 ppb), and processing was carried out using Offline Data Analysis (ChemStation version B.03.05, Agilent Technologies, Inc.).

2.2.10. Confocal fluorescent microscopy

The fluorescence images were recorded on a confocal microscope (LSM 880, AxioObserver) with corresponding λ_{ex} and λ_{em} . Samples were prepared in glass-bottom cell culture dishes (CELLview) as attached live cells and stained by specific membrane permeable dyes according to exact requirements. Data were processed in ZEN (blue edition) for Windows.

2.3. Methods

2.3.1. Dark stability and photodecomposition

Complexes were dissolved in 5% DMSO and 95% phenol red-free RPMI-1640 to test the dark stability. Typically, the absorption spectra of the complexes prepared immediately and after 2 h incubation were compared to confirm the dark stability. For complexes with low aqueous solubility, GSH was incubated with complexes for 2 h and LC-MS was used to determine the dark stability. The photodecomposition of complexes in aqueous solution was monitored by

UV-vis, fluorescence spectroscopy and LC-MS at different time intervals after irradiation at 298 K.

2.3.2. Nucleobase binding

The mixture of complexes (30 μM) and 2 equiv. of Guanosine 5'-monophosphate disodium salt (5'-GMP- Na_2) in aqueous solution was incubated in the dark, then the photoreaction was monitored by LC-MS at different time intervals after irradiation with blue light (420 nm).

2.3.3. Cancer cell studies

2.3.3.1. Cell maintainance¹²

A2780 human ovarian carcinoma, A549 human caucasian lung carcinoma, PC3 human prostate carcinoma, and MRC-5 human foetal lung fibroblasts were obtained from the European Collection of Cell Cultures (ECACC). All cells were grown in Roswell Park Memorial Institute medium (RPMI-1640) with phenol red. All media were supplemented with 10% of foetal calf serum and 1% penicillin/streptomycin.

Cells were stored in ampoule(s) in liquid nitrogen. Ampoules were defrosted in a water bath (310 K), then cells were transferred to falcon tubes, centrifuged to remove supernatant freezing medium, and re-suspended in media (5 mL) in T25 culture flasks. Cells were grown in T75 culture flasks as adherent monolayers at 310 K in a humidified atmosphere containing 5% CO_2 and passaged using regularly 0.25% trypsin/EDTA at approximately 80% confluence.

2.3.3.2. Photo-dark cytotoxicity testing

Approximately 15000 cells were seeded per well in 96-well plates. Independent duplicate plates were used, one for dark experiment while the other for irradiated. The cells were pre-incubated in drug-free media with phenol red containing medium at 310 K for 24 h before adding different concentrations of the compounds to be tested. Complexes were dissolved first in DMSO and then diluted in phenol red-free RPMI-1640 to make the stock solution of the drug. These stock solutions were further diluted using phenol-red free cell culture medium until working concentrations were achieved, in these solutions the maximum DMSO concentration was in all cases $< 0.5\%$ v/v. Cells were exposed to the drugs with different concentrations for 1 h. Then one plate was irradiated for 1h using 96-array of LEDs (4.8 mW cm^{-2} per LED at 465 nm, or 11.7 mW cm^{-2} per LED at 520 nm), while the dark plate was kept in the incubator. After irradiation, supernatants of both plates were removed by suction and cells were washed with phosphate-buffered saline (PBS). Photocytotoxicity are determined after another 24 h recovery at 310 K in drug-free phenol-containing medium by comparison to untreated controls which were only exposed to media. Untreated controls were also compared between the irradiated and the non-irradiated plates to ensure that the differences in cell survival were not statistically relevant, hence guaranteeing that the light source by itself cannot cause cell death. The sulforhodamine B (SRB) assay was used to determine cell viability (Figure 2.3).¹³ Absorbance measurements of the solubilised dye (on a Promega microplate reader using a 500 nm filter) allowed the determination of viable treated cells compared to untreated controls. IC_{50} values (concentrations which caused 50% of cell death), were determined as the average of triplicates and their standard deviations were calculated. Stock concentrations for all metal complexes used in these biological assays were adjusted/verified after ICP-OES metal quantification.

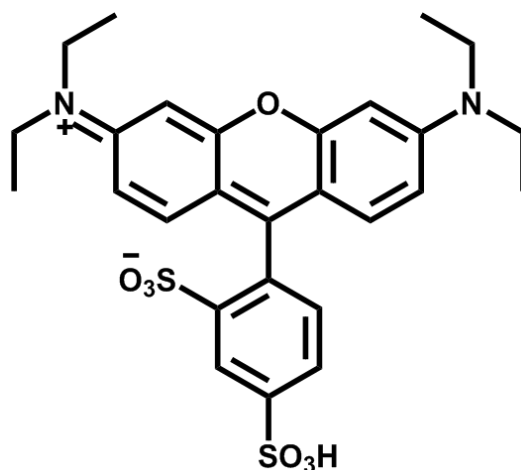


Figure 2.3. Chemical structure of sulforhodamine B.

2.3.3.3. Metal accumulation in cancer cells

For platinum cellular accumulation studies, approximately 4.5 million cells in 10 mL medium were plated in 100 mm Petri dishes and allowed to attach for 24 h. Then the plates were exposed to the solutions of complexes. Additional plates were incubated with medium alone as a negative control. After 1 h incubation in the dark at 310 K, the cells were rinsed three times with cold PBS and harvested by trypsinisation. The number of cells in each sample was counted manually using a haemocytometer. Then the cells were centrifuged to obtain the whole cell pellet for ICP-MS analysis. All experiments were conducted in triplicate. The whole cell pellets were dissolved in concentrated 72% nitric acid (200 μ L), and the samples were then transferred into Wheaton v-vials (Sigma-Aldrich) and heated in an oven at 343 K overnight. The vials were then allowed to cool and each cellular sample solution was transferred into a vial and diluted with Milli-Q water (3.8 mL), to obtain a final HNO₃ concentration of approximately 3.6%.

2.4. References

1. N. J. Farrer, J. A. Woods, L. Salassa, Y. Zhao, K. S. Robinson, G. Clarkson, F. S. Mackay, P. J. Sadler, *Angew. Chem. Int. Ed.*, 2010, **49**, 8905–8908.
2. V. Venkatesh, C. J. Wedge, I. Romero-Canelón, A. Habtemariam, P. J. Sadler, *Dalton Trans.*, 2016, **45**, 13034–13037.
3. T. Claridge, *High-resolution NMR techniques in organic chemistry series*, Elsevier, Pergamon, 1990.
4. H. E. Gottlieb, V. Kotlyar, A. Nudelman, *J. Org. Chem.*, 1997, **62**, 7512–7515.
5. P. Hore, *Nuclear magnetic resonance*, Oxford University Press, New York, 2001.
6. W. Henderson and J. McIndoe, *Mass spectrometry of inorganic, coordination, and organometallic compounds*, Wiley, Hoboken, NJ, 2005.
7. S. T. Misture, R. L. Snyder, *Encyclopedia of Materials: Science and Technology*, Elsevier, Pergamon, 2001.
8. O. V. Dolomanov, L. J. Bourhis, R. J. Gildea, J. A. K. Howard, H. Puschmann, *J. Appl. Cryst.*, 2009, **42**, 339–341.
9. G. M. Sheldrick, *Acta Cryst.*, 2015, **A71**, 3–8.
10. G. M. Sheldrick, *Acta Cryst.*, 2015, **C71**, 3–8.
11. M. Brustolon, *Electron paramagnetic Resonance: A Practitioner's Toolkit*, Wiley, Hoboken, NJ, 2009.
12. J. M. Davis, *Basic cell culture*, Oxford University Press, Oxford, 2002.
13. V. Vichai, K. Kirtikara, *Nat. Protoc.*, 2006, **1**, 1112–1116.

Chapter 3

**Photoactive Pt(IV)
Complexes with Amino Acid
Methyl Esters and Peptides**

3.1. Introduction

Amino acid, the basic unit of peptides and proteins, contains basic amine (-NH₂) and acidic carboxyl (-COOH) functional groups, and a unique side chain.¹ Twenty proteinogenic amino acids are known as standard amino acids. They are encoded by triplet codons directly, and nine of them are essential for humans since they cannot be synthesised *de novo* in the human body.² Cancer metabolism is distinct from normal cells to accommodate the continuous proliferation and expansion, resulting in higher nutrient demands.³ Similar to glucose, amino acids are also used by cancer cells as fuel, thus are employed in targeted cancer therapy.⁴ Dietary serine and glycine restriction can induce p53-dependent metabolic remodelling and reduce tumour growth in mouse model.^{5,6} In addition, serine deprivation significantly enhanced anticancer activity of biguanides.⁷ The absence of glutamine, asparagine and arginine supply can cause death of cancer cells, therefore amino acid-specific depleting enzymes have been employed to treat cancer by inducing amino acid deprivation.⁸

Platinum complexes with amino acids and their derivatives have been extensively explored as anticancer drugs, owing to their preferential accumulation in cancer cells.⁹⁻¹² Amino acids can be coordinated to platinum complexes through their principal amino (N), carboxylate (O), and chemical functionalities in side chains (S, N, O).¹³ Amino acids have been attached to Pt(II) complexes to deliver the active {Cl₂Pt}²⁺ moiety selectively, and reduce the side effects of cisplatin (Figure 3.1a).^{14,15} Less Pt(IV) complexes with amino acids have been reported due to the difficulty in synthesis and purification.¹³

Indoleamine-2,3-dioxygenase (IDO) is an immunosuppressive enzyme in human tumours that can catalyse the degradation of tryptophan.¹⁶ (D)-1-methyltryptophan serves as an inhibitor of IDO to stimulate antitumor immunity.¹⁷ Pt(IV) complexes bearing (D)-1-Methyltryptophan kill

cancer cells by a combined mechanism of immunomodulation and DNA cross-link-triggered apoptosis (Figures 3.1b and c).¹⁸

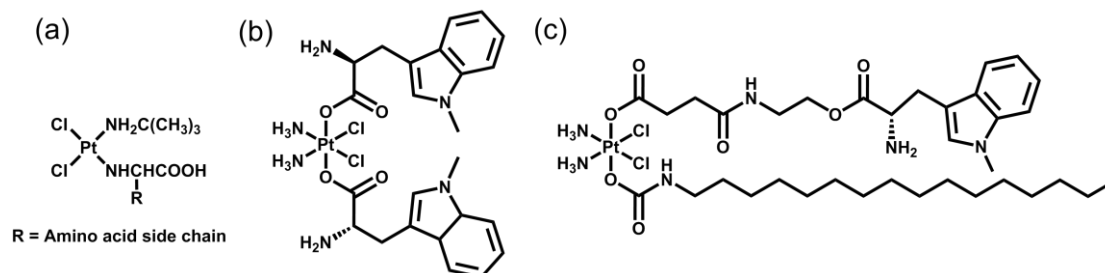


Figure 3.1. Platinum complexes with amino acids and their derivatives.

In addition to single amino acids, peptides with corresponding sequences can allow targeted drug delivery of conjugated drugs owing to the overexpression of specific receptors on the surface of cancer cells. The RGD (–Arg–Gly–Asp–)-containing cyclic peptide c(RGDfK) can be conjugated to Pt(IV) prodrugs for drug delivery in cancer cells with high $\alpha_v\beta_3$ and $\alpha_v\beta_5$ expression. Mono- and bi-conjugated platinum complexes with c(RGDfK) (Figure 3.2a) display greater cancer inhibition than the non-targeting analogues.¹⁹ These complexes are internalised by $\alpha_v\beta_3$ and $\alpha_v\beta_5$ integrins. One RGD ligand was sufficient for recognition since bi-conjugated complex did not exhibit superiority over its mono counterpart. The monomeric c(RGDfK) and tetrameric RAFT- $\{c(\text{RGDfK})\}_4$ were also conjugated to the Pt(IV) prodrug of picoplatin (Figures 3.2b and c);²⁰ 2.6× and 20× improvements, respectively, in antiproliferation effect were observed towards SK-MEL-28 melanoma cells with high expression of both integrins for the complexes with monomeric and tetrameric RGD peptide. Significant increases in cellular platinum accumulation were also detected in SK-MEL-28 treated with complexes containing RGD. In contrast, decreased cytotoxicity and negligible effect on accumulation in the negative CAPAN-1 pancreatic cells were caused by the conjugation of RGD to picoplatin. The Pt(IV) prodrug functionalised by cancer targeting c(RGDfK) and caspase-3 enzyme

specific DEVD (–Asp–Glu–Val–Asp–) with tetraphenylsilole (TPS) fluorophore that possessed aggregation-induced emission accumulated selectively in $\alpha_v\beta_3$ overexpressed cancer cells (Figure 3.2d).²¹ Reduction of the Pt(IV) prodrug released the cytotoxic Pt(II) species and induced apoptosis, and therefore switched on the fluorescence of TPS. This dual action conjugate allowed not only anticancer activity, but also real-time imaging of apoptosis induced by the drug. Notably, a conjugate of c(RGDfK) and photoactive diazido Pt(IV) complex was reported, which displayed a preference towards SK-MEL-28 melanoma cancer cells that overexpress the $\alpha_v\beta_3$ integrin (Figure 1.20a).²²

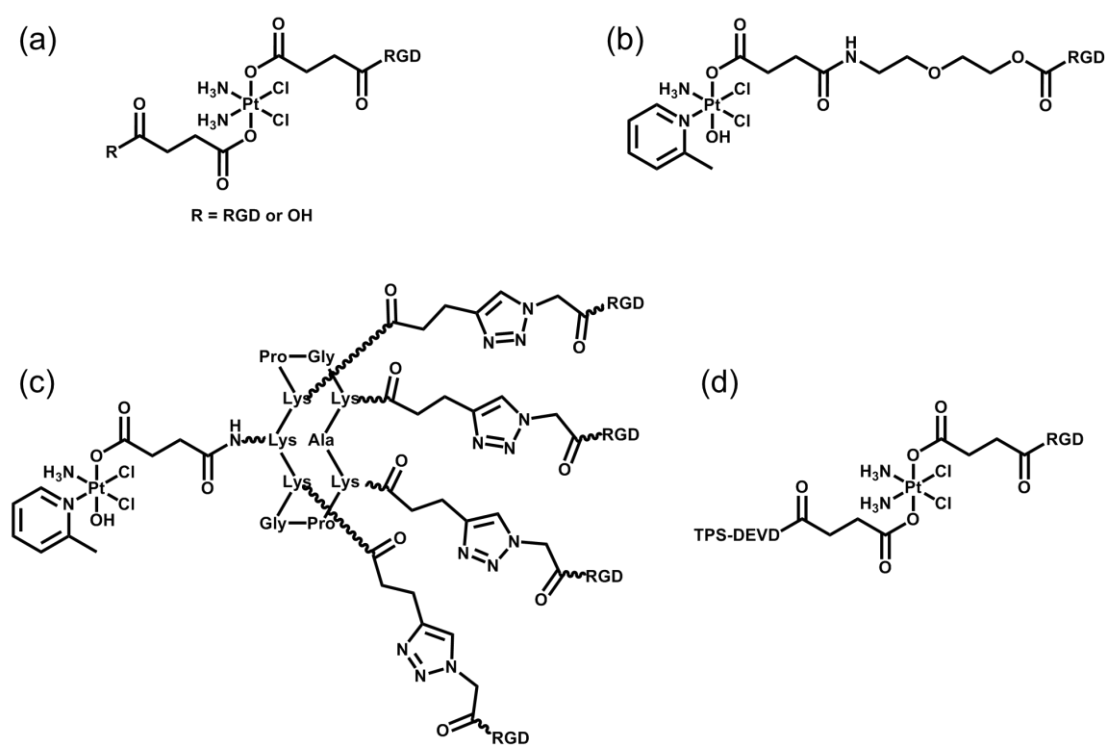


Figure 3.2. Pt(IV) complexes containing c(RGDfK). RGD = c(RGDfK).

Human serum albumin (HSA) can be used as a carrier to deliver Pt(IV) prodrugs efficiently *via* the EPR effect by which molecules of certain sizes trend to accumulate more in tumour than normal tissues, and stabilises Pt(IV) from reduction before reaching targeted sites. Maleimide-conjugated Pt(IV) complexes bind to the free thiol group (cysteine at position 34)

of albumin in the bloodstream (Figure 3.3a-c).^{23,24} Increased plasma half-life, tumour accumulation and higher activity were observed for Pt(IV) complexes with maleimide in CT-26-bearing mice. Pt(IV) prodrug with long hydrophobic C₁₆ chain displayed non-covalent albumin binding with a binding constant (K_a) of $1.04 \times 10^6 \text{ M}^{-1}$ (Figure 3.3d).²⁵ Although the complexation with HSA did not enhance the cytotoxicity of Pt(IV) prodrugs *in vitro*, its rate of reduction by ascorbate was decreased by HSA, which resulted in a higher stability in blood. When the photoactive Pt(IV) complex *trans,trans,trans*-[Pt(py)₂(N₃)₂(OH)₂] (1) was attached to HSA with an apoptotic sensitive fluorescent probe, improved photocytotoxicity and real-time imaging was achieved upon UVA irradiation.²⁶

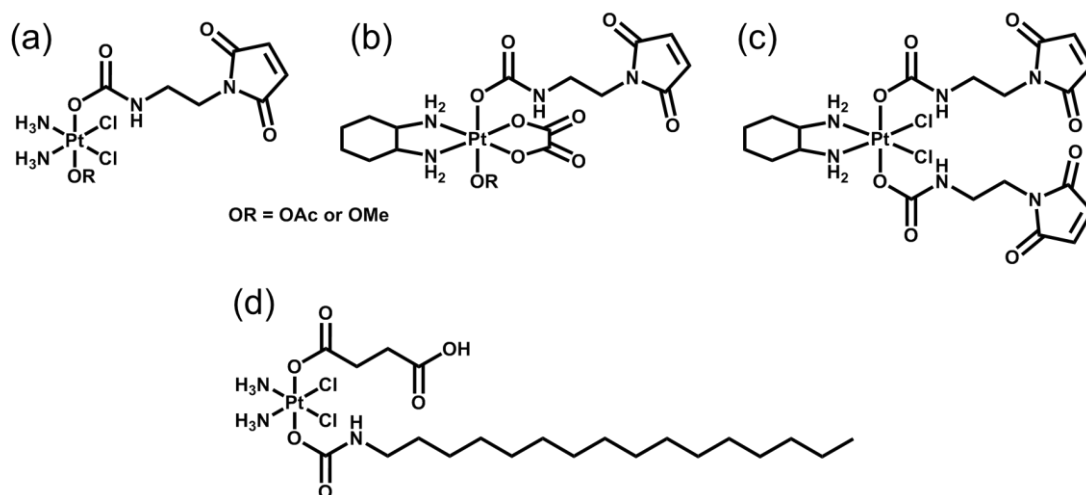


Figure 3.3. Pt(IV) complexes bind to HSA.

DNA is traditionally regarded as the main target of anticancer platinum complexes.²⁷ However, recent studies revealed that amino acids, peptides and proteins are also important targets for cytotoxicity.²⁸ As a “soft” metal ion, Pt(II) tends to bind strongly to “soft” atoms (e.g. sulfur donors). Therefore, cisplatin is able to form adducts with sulfur-containing biomolecules, such as Met, Cys, glutathione, albumin and transferrin.²⁸ Pt(II) species are released from diazido Pt(IV) prodrugs upon irradiation, which allows the binding to peptides and proteins with

specific amino acids. Photoactivated **1** induced only mono-platinated adducts with different amino acids in the peptide SubP, while both mono- and di-platinated adducts with a preference for His in the peptide K³-Bom were observed.²⁹ Platination of His, Glu, and Gln residues in Trx occurred when treated with complex **1** and blue light.³⁰ Intriguingly, diazido Pt(IV) prodrugs possess not only photoplatination, but also photooxidation ability that can oxidise nucleotides and amino acids. Photooxidation in SubP induced by **1** occurred only at Met, whereas photooxidation of both Met and Trp were observed for K³-Bom.²⁹ Photooxidation of Met, Trp, and the Cys catalytic sites inhibited the activity of Trx enzyme and increased the cellular ROS levels.³⁰

Notably, the azidyl radicals generated by **1** upon irradiation were quenched in the presence of Trp, which reduced the photocytotoxicity.³¹ The Trp analogue melatonin (MLT) and peptide pentagastrin containing Trp could also quench azidyl radicals in a similar way as Trp.³² The resulting Trp and MLT radicals were trapped by 2-methyl-2-nitrosopropane (MNP).³²

In this Chapter, four diazido Pt(IV) complexes containing amino acid methyl esters and a Pt(IV) conjugate with a cyclic peptide c(CRWYDENAC) were synthesised (Scheme 3.1). Amino acid methyl esters rather than amino acids with free carboxylic acid were introduced in this work to facilitate the purification of the complexes and improve their lipophilicity. In addition, to investigate the difference in the side chains is the major purpose of this work. The methyl esters of leucine (**4**), glycine (**5**), tyrosine (**6**) and tryptophan (**7**) were conjugated to **1** in this Chapter owing to their side chains properties: simple aliphatic chain (Leu), side chain free (Gly), aromatic side chain (Tyr) and azidyl radical quenching (Trp), respectively. Cyclic peptide c(CRWYDENAC) can target the integrin α_6 receptor, using the sequence RWY (Arg–Trp–Tyr) as binding site.³³ The effect of amino acid methyl esters and peptides conjugated to diazido Pt(IV) complex *trans,trans,trans*-[Pt(py)₂(N₃)₂(OH)₂] (**1**) on the dark stability,

photodecomposition, azidyl radical generation, photoreactions with 5'-GMP and DNA, photocytotoxicity and cellular accumulation of the Pt(IV) complexes was investigated.

3.2. Experimental

Caution! Heavy metal azides can be shock-sensitive detonators. We did not encounter any problems during the work reported here but due care and attention with appropriate precautions should be taken in their synthesis and handling.

All syntheses and purifications were carried out in the dark with minimal light exposure.

3.2.1. Materials

Amino acid methyl esters, 1-ethyl-3-(3-dimethylaminopropyl)carbodiimide (EDC), *N*-hydroxysuccinimide (NHS), 2-(dimethylamino)pyridine (DMAP), and *N,N*-diisopropylethylamine (DIPEA) were purchased from Sigma-Aldrich. Peptide c(CRWYDENAC) was provided by Prof. Musheng Zeng at the Sun Yat-sen University Cancer Centre. *Trans,trans,trans*-[Pt(py)₂(N₃)₂(OH)(succH)] (**2**) was prepared according to the methods described in Chapter 2. All solvents for common use were analytical reagent grade from Fisher Scientific and used as supplied.

3.2.2. Synthesis and characterisation

3.2.2.1. *Trans,trans,trans*-[Pt(py)₂(N₃)₂(OH)(succ-NHS)] (3)

Trans,trans,trans-[Pt(py)₂(N₃)₂(OH)(succH)] (2) (25.0 mg, 43.8 μmol) was stirred with EDC (8.2 mg, 52.8 μmol), NHS (7.6 mg, 66.0 μmol) and DMAP (0.7 mg, 5.7 μmol) in DMF (2 mL) under nitrogen overnight at 298 K. After evaporation to dryness, the oily residue was purified by column chromatography on silica gel (33% acetone + 66% DCM). ¹H NMR (CDCl₃, 400 MHz): 8.91 (d, J = 5.5 Hz, J¹⁹⁵Pt-¹H = 26.7 Hz, 4H, H_α py), 8.12 (t, J = 7.6 Hz, 2H, H_γ py), 7.68 (t, J = 7.0 Hz, 4H, H_β py), 3.45 (s, H, OH), 2.87 (t, J = 6.6 Hz, 2H, CH₂), 2.80 (t, J = 6.6 Hz, 2H, CH₂), 2.70 (s, 4H, CH₂). ESI-MS: [M + Na]⁺ (m/z) Calc., 691.1; Found, 691.1.

3.2.2.2. General synthetic route for *trans,trans,trans*-[Pt(py)₂(N₃)₂(OH)(succ-amino acid methyl ester)]

Freshly prepared *trans,trans,trans*-[Pt(py)₂(N₃)₂(OH)(succ-NHS)] (3) (20 mg, 29.9 μmol) was stirred with 1.2 mol. equiv. of the corresponding amino acid methyl ester and DIPEA (100 μL) in DMF (2 mL) under nitrogen at 298 K for 24 h. After evaporation to dryness, the oily residue was purified by column chromatography on silica gel (methanol + DCM).

Trans,trans,trans-[Pt(py)₂(N₃)₂(OH)(succ-leu-OMe)] (4)

The yellow oily product was purified by column chromatography on silica gel (2% methanol + 98% DCM). ¹H NMR (CDCl₃, 400 MHz): 8.90 (d, J = 5.8 Hz, J¹⁹⁵ Pt-¹ H = 26.8 Hz, 4H, H_α py), 8.06 (t, J = 7.6 Hz, 2H, H_γ py), 7.63 (t, J = 6.9 Hz, 4H, H_β py), 6.25 (d, J = 8.0 Hz, 1H, CONH), 4.49 (dt, 1H, CH), 3.67 (s, 3H, OCH₃), 2.69 (t, J = 6.7 Hz, 2H, CH₂), 2.49-2.35 (m, 2H, CH₂), 1.62-1.43 (m, 3H, CH and CH₂), 0.88 (d, J = 5.4 Hz, 6H, CH₃). ¹³C NMR (CDCl₃,

100 MHz): 176.31 (*COO*), 173.51 (*CONH*), 172.25(*COO*), 149.56 (*C_α py*), 141.24 (*C_γ py*), 125.96 (*C_β py*), 52.04 (*CH*), 50.71 (*CH₃*), 41.30 (*CH₂*), 32.31 (*CH₂*), 32.09 (*CH₂*), 24.75 (*CH*), 22.61(*CH₃*), 21.79 (*CH₃*). ESI-MS: [M + Na]⁺ (*m/z*) Calc., 721.2; Found, 721.3. $\epsilon_{299\text{ nm}} = 17163\text{ M}^{-1}\text{ cm}^{-1}$, $\epsilon_{259\text{ nm}} = 14877\text{ M}^{-1}\text{ cm}^{-1}$ (5% DMSO + 95% RPMI-1640).

***Trans,trans,trans*-[Pt(py)₂(N₃)₂(OH)(succ-gly-OMe)] (5)**

The yellow oily product was purified by column chromatography on silica gel (3% methanol + 97% DCM). ¹H NMR (CDCl₃, 400 MHz): 8.92 (d, J = 5.6 Hz, J¹⁹⁵ Pt–¹H = 26.7 Hz, 4H, *H_α py*), 8.08 (t, J = 7.7 Hz, 2H, *H_γ py*), 7.66 (t, J = 7.0 Hz, 4H, *H_β py*), 6.46 (t, J = 4.4 Hz, 1H, *CONH*), 3.93 (d, J = 5.5 Hz, 2H, *CH₂*), 3.72 (s, 3H, *OCH₃*), 2.75 (t, J = 6.7 Hz, 2H, *CH₂*), 2.47 (t, J = 6.6 Hz, 2H, *CH₂*). ¹³C NMR (CDCl₃, 100 MHz): 176.55 (*COO*), 172.79 (*CONH*), 171.27(*COO*), 149.62 (*C_α py*), 141.27 (*C_γ py*), 126.06 (*C_β py*), 52.24 (*CH₃*), 41.19 (*CH₂*), 32.32 (*CH₂*), 32.22 (*CH₂*). ESI-MS: [M + Na]⁺ (*m/z*) Calc., 665.2; Found, 665.3. $\epsilon_{299\text{ nm}} = 16567\text{ M}^{-1}\text{ cm}^{-1}$, $\epsilon_{259\text{ nm}} = 11189\text{ M}^{-1}\text{ cm}^{-1}$ (5% DMSO + 95% RPMI-1640).

***Trans,trans,trans*-[Pt(py)₂(N₃)₂(OH)(succ-tyr-OMe)] (6)**

The yellow oily product was purified by column chromatography on silica gel (6% methanol + 94% DCM). ¹H NMR (CDCl₃, 400 MHz): 8.89 (d, J = 5.4 Hz, J¹⁹⁵ Pt–¹H = 26.5 Hz, 4H, *H_α py*), 8.01 (t, J = 7.6 Hz, 2H, *H_γ py*), 7.58 (t, J = 7.0 Hz, 4H, *H_β py*), 6.88 (d, J = 8.3 Hz, 1H, *H_{phenyl}*), 6.64 (d, J = 8.3 Hz, 1H, *H_{phenyl}*), 6.39 (d, J = 7.9 Hz, 1H, *CONH*), 4.73 (q, 1H, *CH*), 3.69 (s, 1H, *OH*), 3.68 (s, 3H, *OCH₃*), 3.00-2.87 (m, 2H, *CH₂*), 2.71-2.67 (m, 2H, *CH₂*), 2.39 (t, J = 6.8 Hz, 2H, *CH₂*). ¹³C NMR (CDCl₃, 100 MHz): 176.64 (*COO*), 172.23(*CONH*), 172.11(*COO*), 155.52 (*C_{phenyl}*), 149.50 (*C_α py*), 141.41 (*C_γ py*), 130.32 (*C_{phenyl}*), 127.18 (*C_{phenyl}*), 126.66 (*C_β py*), 115.47 (*C_{phenyl}*), 52.20 (*CH₃*), 36.95(*CH*), 32.17 (*CH₂*), 31.86 (*CH₂*), 25.39

(CH₂). ESI-MS: [M + Na]⁺ (m/z) Calc., 771.2; Found, 771.3. ε_{300 nm} = 17489 M⁻¹ cm⁻¹, ε_{260 nm} = 13023 M⁻¹ cm⁻¹ (5% DMSO + 95% RPMI-1640).

***Trans,trans,trans*-[Pt(py)₂(N₃)₂(OH)(succ-trp-OMe)] (7)**

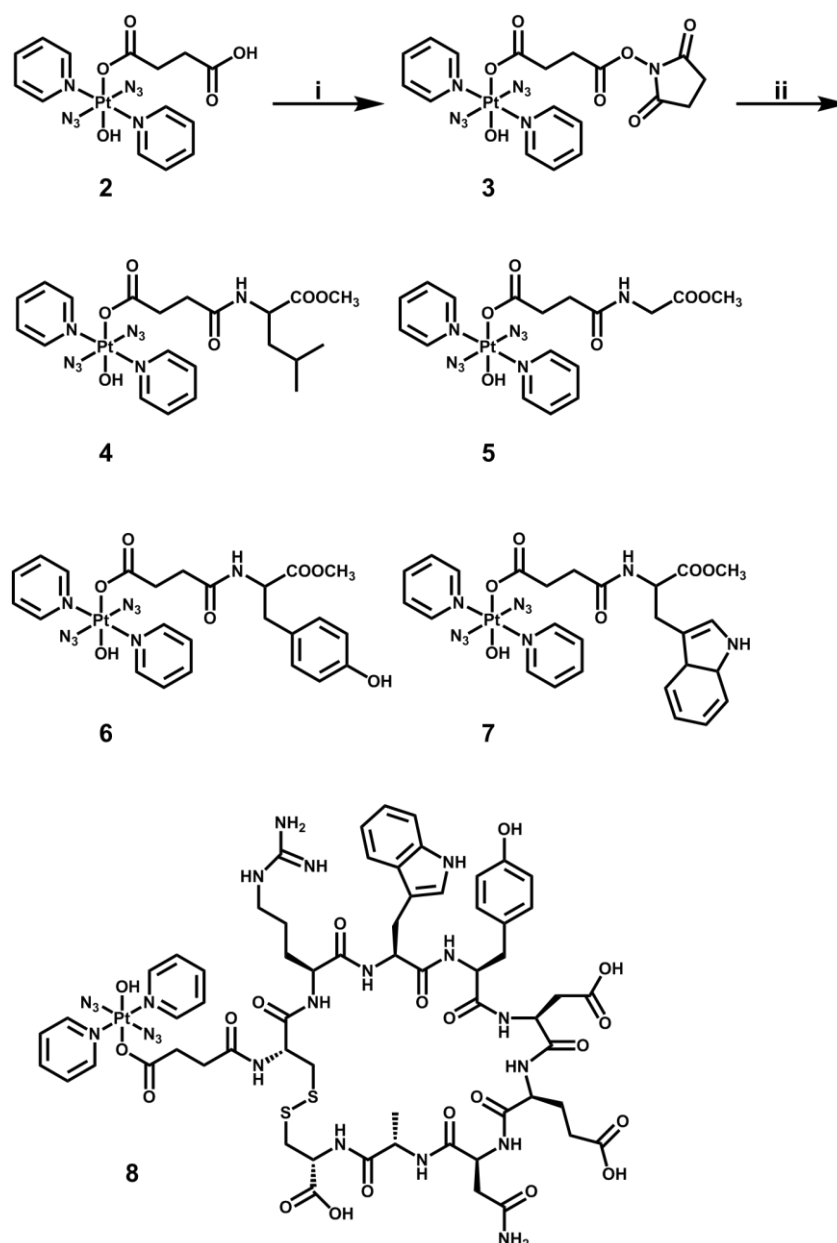
The yellow oily product was purified by column chromatography on silica gel (3% methanol + 97% DCM). ¹H NMR (CDCl₃, 400 MHz): 8.89 (d, J = 5.4 Hz, J¹⁹⁵ Pt–¹H = 26.7 Hz, 4H, H_α py), 8.26 (s, 1H, NH_{indole}), 7.96 (t, J = 7.6 Hz, 2H, H_γ py), 7.55 (t, J = 7.1 Hz, 4H, H_β py), 7.50 (d, J = 7.7 Hz, 1H, H_{indole}), 7.32 (d, J = 8.0 Hz, 1H, H_{indole}), 7.15 (t, J = 7.5 Hz, 1H, H_{indole}), 7.09 (t, J = 7.4 Hz, 1H, H_{indole}), 6.97 (d, J = 2.2 Hz, 1H, H_{indole}), 6.31 (d, J = 7.7 Hz, 1H, CONH), 4.84 (q, 1H, CH), 3.70 (s, 1H, OH), 3.66 (s, 3H, OCH₃), 3.24 (d, J = 5.5 Hz, 2H, CH₂), 2.84-2.65 (m, 2H, CH₂), 2.47-2.35 (m, 2H, CH₂). ¹³C NMR (CDCl₃, 100 MHz): 176.65 (COO), 172.40 (CONH), 172.09 (COO), 155.52 (C_{phenyl}), 149.57 (C_α py), 141.22 (C_γ py), 136.02 (C_{Indole}), 127.56 (C_{Indole}), 126.03 (C_β py), 123.56 (C_{Indole}), 121.97 (C_{Indole}), 119.47 (C_{Indole}), 118.46 (C_{Indole}), 111.35 (C_{Indole}), 109.63 (C_{Indole}), 52.82 (CH), 52.30 (CH₃), 32.29 (CH₂), 31.89 (CH₂), 27.47 (CH₂). ESI-MS: [M + K]⁺ (m/z) Calc., 811.2; Found, 811.2. ε_{290 nm} = 22181 M⁻¹ cm⁻¹, ε_{261 nm} = 19675 M⁻¹ cm⁻¹ (5% DMSO + 95% RPMI-1640).

3.2.2.3. *Trans,trans,trans*-[Pt(py)₂(N₃)₂(OH)(succ-cp)] (8)

Freshly prepared *trans,trans,trans*-[Pt(py)₂(N₃)₂(OH)(succ-NHS)] (3) (14.1 mg, 21.1 μmol) was stirred with c(CRWYDENAC) (9.0 mg, 7.7 μmol) and DIPEA (40 μL) in DMF (2 mL) under nitrogen at 298 K for 36 h. After evaporation to dryness, the excess Pt(IV) precursor and DIPEA were removed by washing with DCM and H₂O. The yellow solid was dried and characterised by LC-MS. ESI-HRMS: [M + 2 H]²⁺ (m/z) Calc., 855.7500; Found, 855.7493

and $[M + H]^+$ (m/z) Calc., 1710.4927; Found, 1710.4919. HPLC purity = 94%. $\epsilon_{290 \text{ nm}} = 30435 \text{ M}^{-1} \text{ cm}^{-1}$, $\epsilon_{260 \text{ nm}} = 27442 \text{ M}^{-1} \text{ cm}^{-1}$ (5% DMSO + 95% RPMI-1640).

Scheme 3.1. The synthetic route for Pt(IV) complexes with amino acid methyl esters (**4–7**) and a peptide (**8**).



(i) EDC, NHS, DMAP, DMF, 298 K, overnight; (ii) amino acid methyl ester or c(CRWYDENAC), DIPEA, DMF, 298 K, 24/36 h.

3.2.3. Methods and instrumentation

3.2.3.1. HPLC purity test

The purity of the complexes was determined on an Agilent 1100 HPLC system with a 100 μL loop and an Agilent ZORBAX Eclipse XDB-C18 column ($250 \times 4.6 \text{ mm}$, $5 \mu\text{m}$). Mobile phases consisted of 0.1% v/v trifluoroacetic acid in HPLC grade H_2O (solvent A) and 0.1% v/v trifluoroacetic acid in HPLC grade CH_3CN (solvent B). The flow rate was set to 1 mL/min and the method used is depicted in Table 3.1. All samples were prepared in HPLC methanol and filtered by syringe filter before injection. The injected volume was 50 μL with needle washing by methanol and water. The detection wavelength was set up at 254 nm using the signal at 360 nm as reference. The percentage of each species was measured by the integration of each peak, assuming the ϵ_{254} for all species are similar.

Table 3.1. Gradient of mobile phases used in HPLC system for purity tests (B = CH_3CN).

Time/min	% B
0	10
30	80
40	80
41	10
55	10

3.2.3.2. Extinction coefficient determination

The extinction coefficient of complexes was estimated in 5% DMSO + 95% RPMI-1640 solution at 298 K. Neat solvent was recorded for reference. The concentrations were set at 100 μM and adjusted by ICP-OES for extinction coefficient determination.

3.2.3.3. Electron paramagnetic resonance

The EPR spectra were recorded on a Bruker EMX (X-band) spectrometer at 298 K. Complexes (5 mM) and radical trap (DMPO, 40 mM) were dissolved in DMSO and diluted in H₂O. 100 μ L samples were transferred using a plastic syringe with metal needle to a standard quality quartz tube with inner diameter of 1.0 mm and outer diameter of 2.0 mm (Wilmad LabGlass) and sealed with parafilm. The EPR tube was placed in a cylindrical T_{M110} mode cavity (Bruker 4103 TM). Using the y-incremental sweep mode of 100 with an accumulation of 5 scans in the X dimension, Typical key EPR spectrometer settings were modulation amplitude 1.0 G, microwave power 6.32 mW, 1.0×10^5 receiver gain, conversion time 5.12 ms, time constant 5.12 ms, sweep width 200 G. The LED465E light was mounted between the EPR magnets with the distance to the EPR cavity being *ca.* 3 cm.

3.2.3.4. DNA melting temperature

The melting curves of *ct*-DNA were recorded by measuring the absorbance at 260 nm. 5% v/v of DMSO and 95% v/v of 1 mM sodium phosphate buffer (pH = 7.9) were used as medium. The nucleotide concentration of *ct*-DNA was determined using a molar extinction coefficient of $6600 \text{ M}^{-1}\text{cm}^{-1}$ at 260 nm.³⁴ The concentration of DNA base pair was 15 μ M with the ratio of drug to base pair being 2. All solutions were prepared in duplicate, one was incubated for 1 h and then irradiated for 1 h, while the other one was incubated for 2 h in the dark. The melting temperature (T_m) was determined as the temperature corresponding to the mid-point absorbance of the melting curves.

3.2.3.5. Photo-dark cytotoxicity testing

The antiproliferative activity of complexes **4–7** was determined in A2780 ovarian cancer cells, and that of **8** was determined in A2780 ovarian, A549 lung, and PC3 prostate carcinoma cell lines. The experiments to determine IC_{50} values were carried out as described in Chapter 2. The concentrations tested range from 100 to 0.01 μM .

3.2.3.6. Cellular accumulation of platinum

For complexes **4–8**, the cellular accumulation was measured in A2780 ovarian cancer cells at the same Pt concentration (10 μM) according to the method described in Chapter 2. The cellular accumulation of **6–8** in A2780 ovarian cancer cells was determined in the absence and presence of light. Independent duplicate plates were exposed to complexes at equipotent concentrations equal to the photoactive IC_{50} values in the corresponding cell line. After 1 h incubation in the dark at 310 K, one of the plates was irradiated by blue light (465 nm) for 1 h, while the other one was left in the dark. The collected cells were treated with concentrated HNO_3 (72%) using the same method described in Chapter 2.

3.3. Results

3.3.1. Synthesis and characterisation

The synthetic route for conjugation of photoactive Pt(IV) complexes with amino acid methyl esters (**4–7**) and cyclic peptide (**8**) is summarised in Scheme 3.1. The coupling of Pt(IV) complexes and amino acid methyl esters was carried out by stirring **3** with corresponding amino acid methyl ester in DMF under nitrogen overnight. The complexes were purified by column

chromatography on silica gel, using DCM and methanol (less than 6%) as mobile phase. The ^1H and ^{13}C NMR spectra of complexes **4–7** contain the anticipated peaks. In the ^1H NMR spectra, the doublets with ^{195}Pt satellites at *ca.* 8.9 ppm ($J = 5.5$ Hz) and the triplets at *ca.* 8.1 ppm ($J = 7.5$ Hz), 7.7 ppm ($J = 7.0$ Hz) are assigned to the α , γ and β proton of pyridine, respectively. The ^{13}C NMR resonances of complexes **4–7** at *ca.* 150, 142 and 126 ppm are attributed to the α , γ and β carbons of pyridine. The peaks for corresponding amino acid can be observed in the spectra. The OCH_3 in amino acid methyl esters give rise to ^1H NMR signal at *ca.* 3.7 ppm. Complex **8** was obtained by coupling **3** with cyclic peptide c(CRWYDENAC). The product was washed with DCM and H_2O to purify the complex. The ions $[\text{M} + 2\text{H}]^{2+}$ (855.7493 *m/z*) and $[\text{M} + \text{H}]^+$ (1710.4919 *m/z*) were detected by HR-MS. The *m/z* values and the isotopic mass distribution pattern of Pt are in good agreement with the calculated spectra. A full assignment of the ^1H NMR peaks for the cyclic peptide in $\text{DMSO-}d_6$ was not attempted, but the doublet at 8.81 ppm ($J = 5.4$ Hz) and the triplets at 8.25 ppm ($J = 7.6$ Hz) and 7.81 ppm ($J = 6.6$ Hz) can be assigned to the α , γ and β protons, respectively, of the pyridine ligands. In addition, in a mixture of 80% $\text{DMSO-}d_6$ and 20% D_2O (v/v), aromatic protons assigned to pyridine, and Trp and Tyr amino acid residues confirm the conjugation of the Pt(IV) fragment to the cyclic peptide.

The purity of Pt(IV) complexes was determined by HPLC chromatography, with the detect wavelength set to 254 nm. Assuming all compounds have the same extinction coefficient, the purity percentage was calculated by the integration of peaks. The HPLC traces for complexes **4–8** were shown in Figure 3.4. Complexes **4–7** exhibit purities higher than 95%, while the purity of complex **8** is 94%.

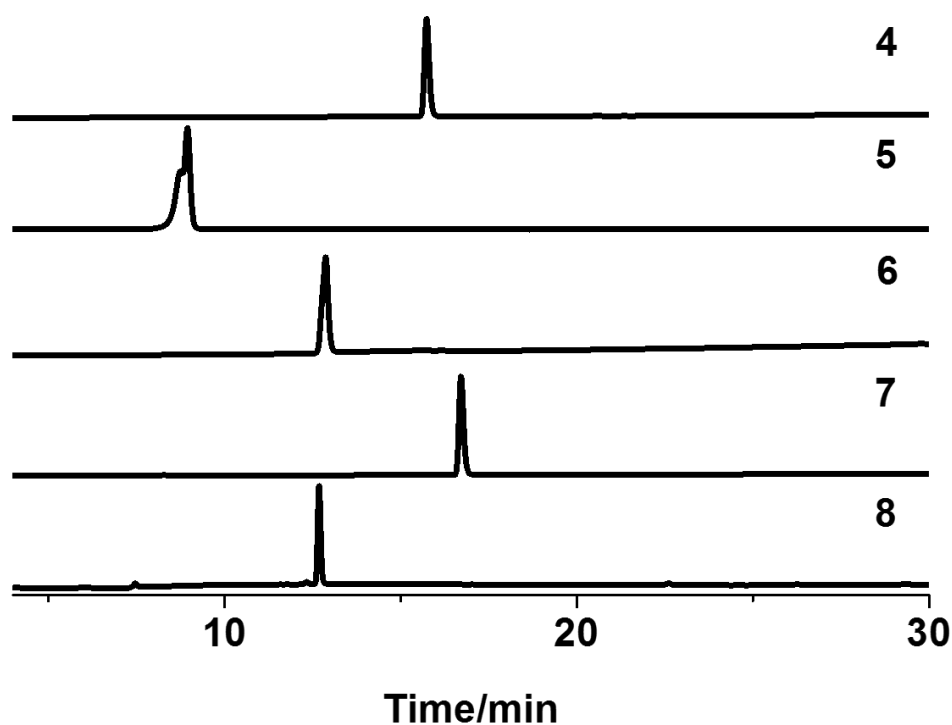


Figure 3.4. HPLC purity of Pt(IV) complexes conjugated to amino acid methyl esters (**4–7**) and cyclic peptide (**8**), detection wavelength 254 nm.

3.3.2. Extinction coefficient studies

The extinction coefficients of complexes **4–8** in phenol red-free RPMI-1640 with 5% DMSO were determined as described in 3.2.3.2. Complexes **4–8** exhibit similar absorption spectra with a high-energy absorbance at *ca.* 260 nm and a maximum absorption band at *ca.* 300 nm ascribed to LMCT ($\text{OH} \rightarrow \text{Pt}$, $\text{N}_3 \rightarrow \text{Pt}$) transition (Figure 3.5). However, due to the effect of side chains in amino acids, different extinction coefficients were founded for these complexes. Among them, complex **8** has much higher extinction coefficients ($\epsilon_{290 \text{ nm}} = 30435 \text{ M}^{-1} \text{ cm}^{-1}$, $\epsilon_{260 \text{ nm}} = 27442 \text{ M}^{-1} \text{ cm}^{-1}$) for both peaks, since it contains 9 amino acids, especially Trp and Tyr. A

specific absorption maximum at 290 nm was observed for complexes **7** and **8**, due to the indole side chain in tryptophan.

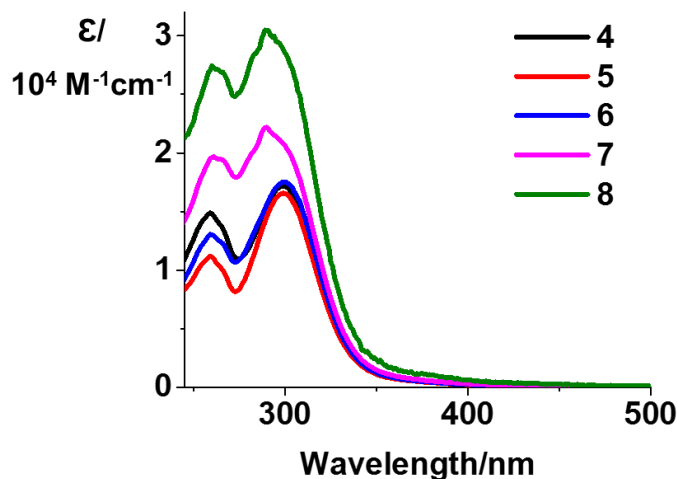


Figure 3.5. UV-vis spectra of the Pt(IV) complexes in phenol red-free RPMI-1640 cell culture medium (100 μ M) at 298 K.

3.3.3. Dark stability

The dark stability is important for photoactive complexes to verify the state of complexes before irradiation and ensure they are relatively non-toxic toward cells in the dark. The standard protocol for Pt(IV) complexes requires 1 h incubation and then 1 h irradiation, thus complexes should be stable in cell culture medium for at least 2 h. The dark stability of complexes **4–8** was assessed by UV-vis spectroscopy (Figure 3.6). Complexes were dissolved in phenol red-free RPMI-1640 with 5% DMSO, their spectra exhibited no apparent change after 2 h, indicating their dark stability in cell culture medium.

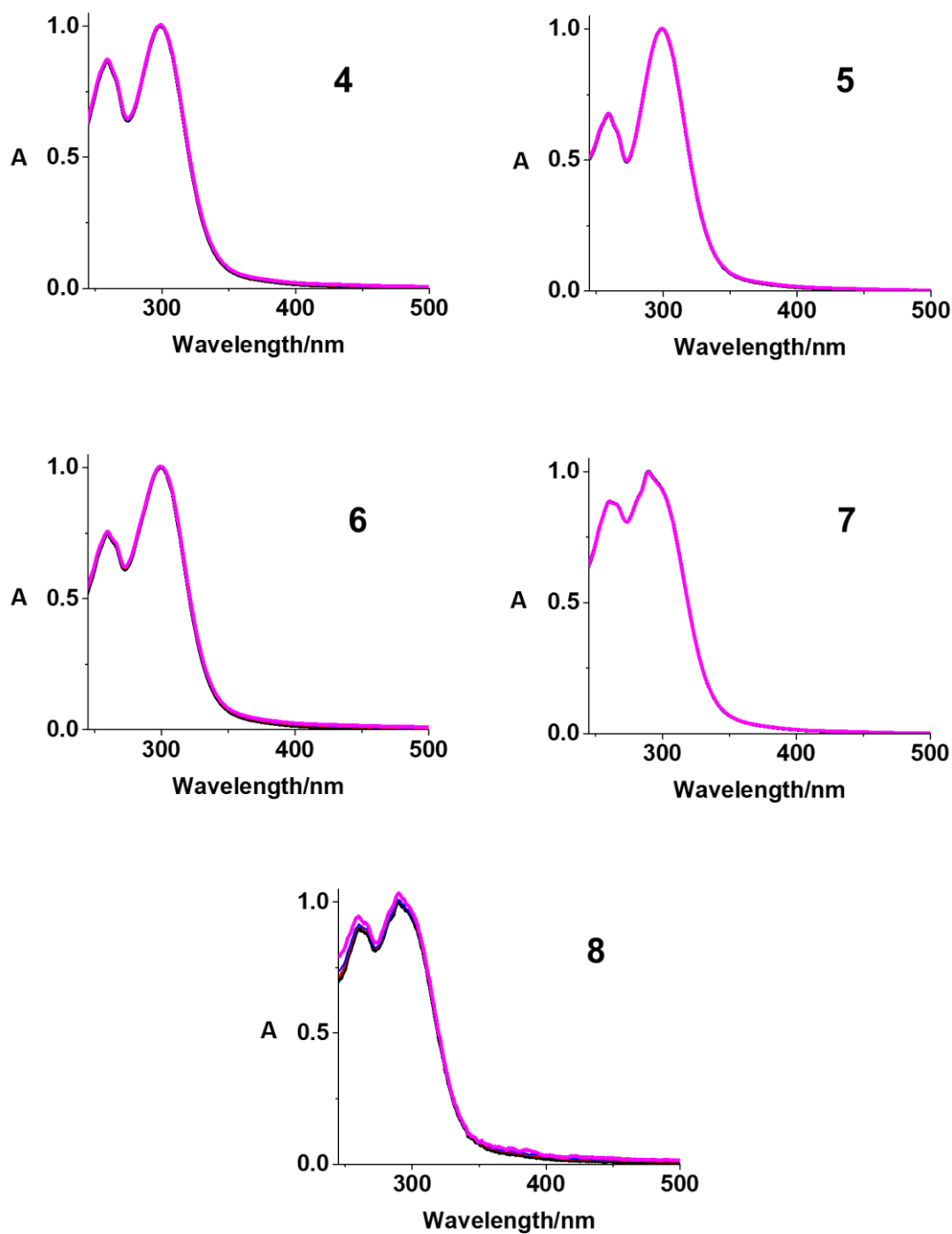


Figure 3.6. Dark stability of complexes 4–8 over 2 h in phenol red-free RPMI-1640 determined by UV-vis spectroscopy.

3.3.4. Photodecomposition followed by UV-vis and EPR

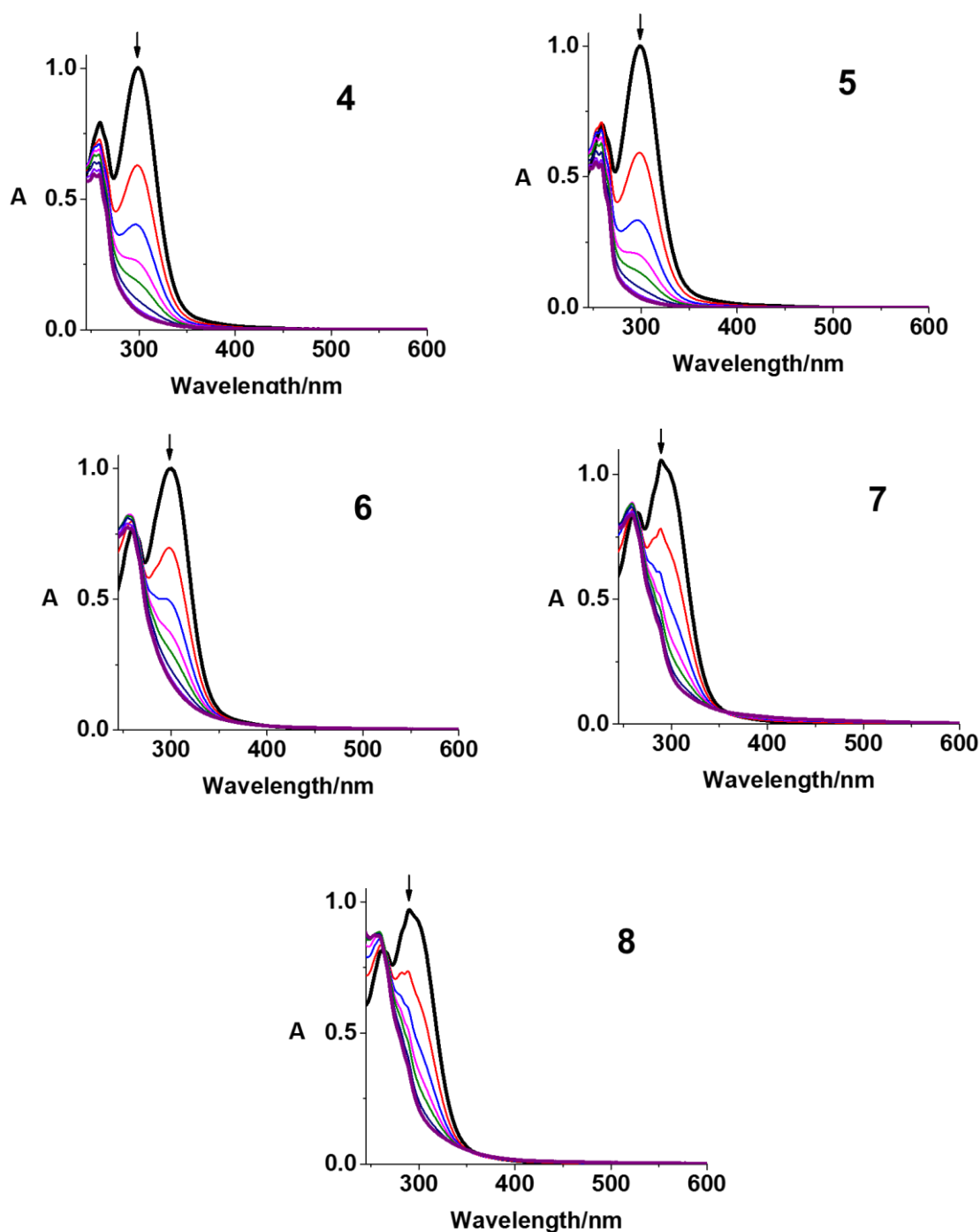


Figure 3.7. UV-vis spectral changes of complexes 4–8 in aqueous solution upon irradiation with indigo light (420 nm, 1 h).

The photodecomposition of complexes **4–8** in aqueous solution was monitored by UV-vis spectroscopy at different time intervals after irradiation with blue light (420 nm) at ambient temperature. A significant decrease in LMCT band ($N_3 \rightarrow Pt$) at *ca.* 300 nm was observed for all of the complexes (Figure 3.7). The decrease was rapid at first and showed no significant change after 30 min. These results were similar to that of the parent complex **1**.

The radicals generated by complexes **4–7** in aqueous solution upon irradiation (465 nm) were trapped by DMPO and measured by EPR (Figure 3.8). The 1 : 2 : 2 : 1 quartet of triplets and the 1 : 2 : 2 : 1 quartet are assigned to the DMPO adducts with azidyl radicals $DMPO-N_3\cdot$ and hydroxyl radicals $DMPO-OH\cdot$, respectively. Both radicals were detected for complexes **4–6** upon irradiation (465 nm). However, for complex **7** with conjugated tryptophan, no EPR signals were observed even after 100 min irradiation.

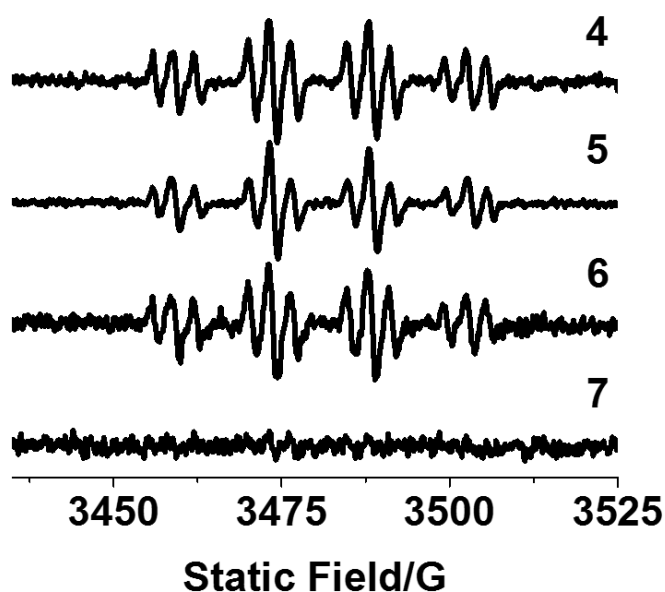


Figure 3.8. EPR spectrum of complexes **4–7** (5 mM) and DMPO (40 mM) in aqueous solution showing the formation of $DMPO-N_3\cdot$ and $DMPO-OH\cdot$ adducts with continues irradiation (465 nm). The experimental trace resulted from the accumulation of 500 scans (conversion time 5.12 ms, time constant 5.12 ms, and sweep time 10.49 s for each scan).

3.3.5. Photoreactions with 5'-GMP

Photoproducts from complexes **4–7** and 5'-GMP were detected. The mixture of complexes and 5'-GMP (1:2) was irradiated by blue light (420 nm) for 1 h and analysed in LC-MS. Complexes **4–6** produced $\{\text{Pt}^{\text{II}}(\text{CH}_3\text{CN})(\text{py})_2(\text{GMP-H})\}^+$ (**G3**) and $\{\text{Pt}^{\text{II}}(\text{N}_3)(\text{py})_2(\text{GMP})\}^+$ (**G4**) as Pt-GMP adducts, while negligible adducts were detected for complex **7** with Trp (Figure 3.9, Table 3.2).

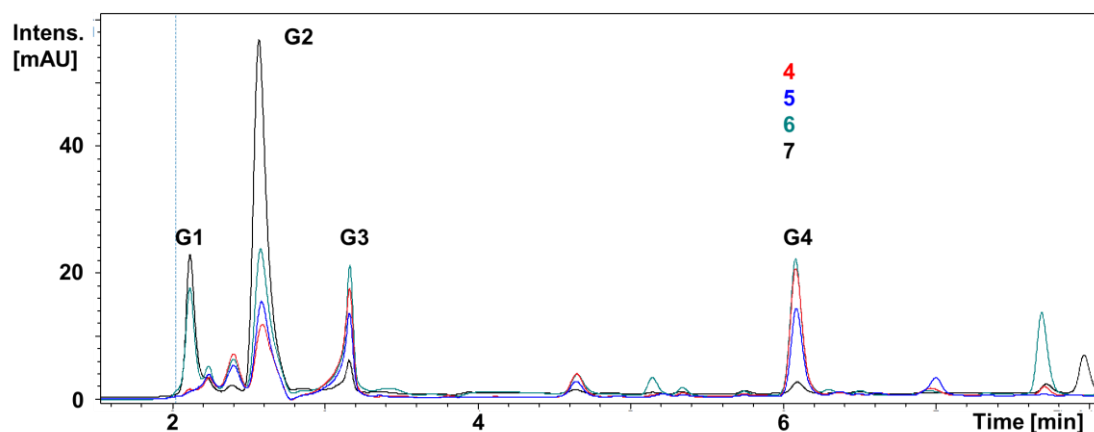


Figure 3.9. Photoproducts between complexes **4–7** and 2 mol. equiv. of 5'-GMP in aqueous solution upon 1h irradiation (420 nm), possible photoproducts **G1–G4** are listed in **Table 3.2**.

Table 3.2. Photoproducts between complexes **4–7** and 2 mol. equiv. of 5'-GMP in aqueous solution in the presence of different amino acids.

Peak	Formula	Structures	Calculated (m/z)	Found (m/z)
G1	$\text{C}_{12}\text{H}_{14}\text{N}_3\text{OPt}$	$\{\text{Pt}^{\text{II}}(\text{py})_2(\text{OH})(\text{CH}_3\text{CN})\}^+$	411.08	411.00
G2	$\text{C}_{10}\text{H}_{15}\text{N}_5\text{O}_8\text{P}$	$[\text{5'-GMP+H}]^+$	364.07	364.09
G3	$\text{C}_{22}\text{H}_{26}\text{N}_8\text{O}_8\text{PPt}$	$\{\text{Pt}^{\text{II}}(\text{py})_2(\text{CH}_3\text{CN})(\text{GMP-H})\}^+$	756.10	756.09
G4	$\text{C}_{20}\text{H}_{24}\text{N}_{10}\text{O}_8\text{PPt}$	$\{\text{Pt}^{\text{II}}(\text{py})_2(\text{N}_3)(\text{GMP})\}^+$	758.12	758.22

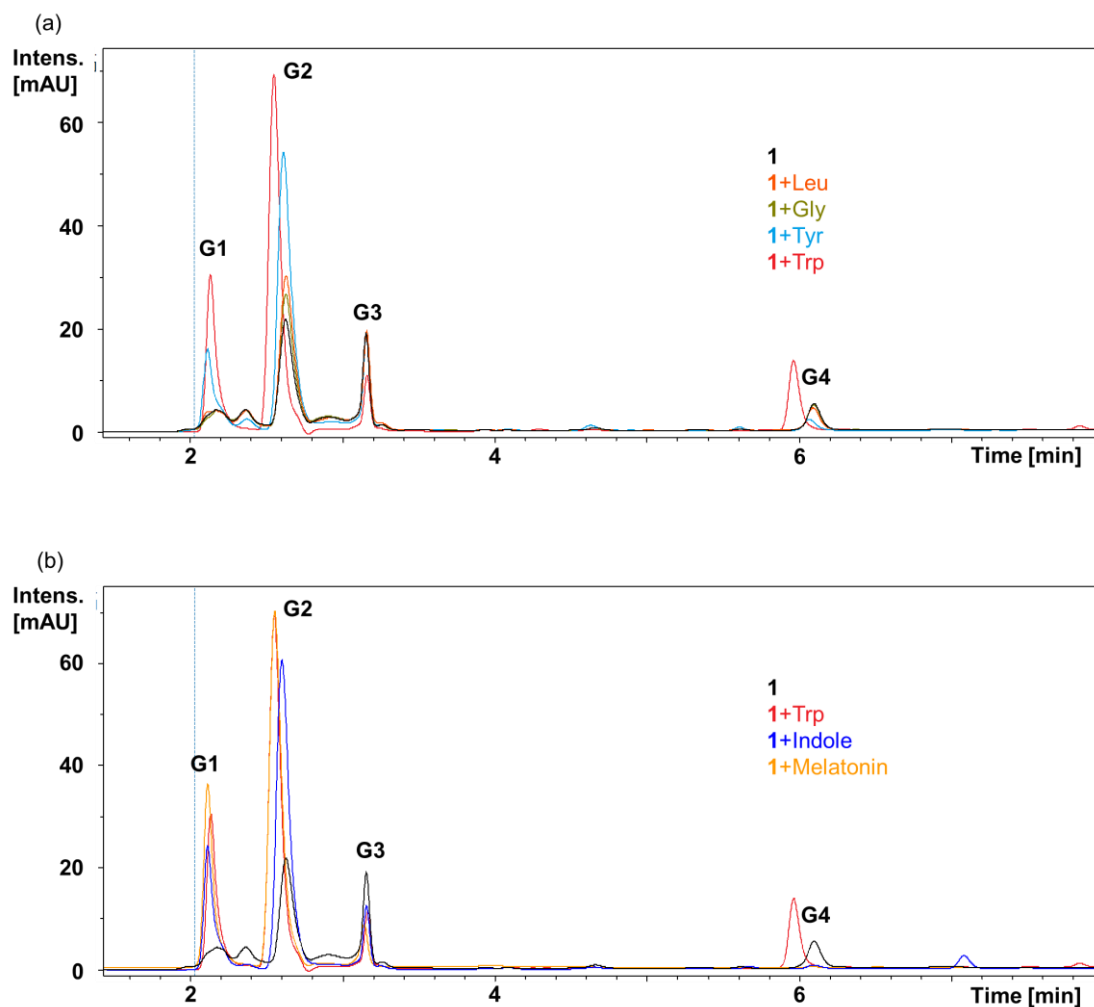


Figure 3.10. Photoproducts between complex **1** and 2 mol. equiv. of 5'-GMP in aqueous solution in the presence of 2 mol. equiv. of amino acids (a); or Trp and its analogues (b) upon 1h irradiation (420 nm).

To confirm the effect of amino acids on DNA platination by Pt(IV) complexes, LC-MS was also employed to investigate the photoinduced reactions between **1** and 5'-GMP in the presence of different amino acids (Figure 3.10). In this experiment, the concentration of **1** and 5'-GMP in different vials were exactly same to ensure that the differences were induced by amino acids. The mixture of **1**, amino acids and 5'-GMP (1:2:2) was irradiated by blue light (420 nm) for 1 h. Upon irradiation, **1** is able to form two major types of adducts with 5'-GMP as detected by

LC-MS, including $\{\text{Pt}^{\text{II}}(\text{CH}_3\text{CN})(\text{py})_2(\text{GMP-H})\}^+$ (G3), and $\{\text{Pt}^{\text{II}}(\text{N}_3)(\text{py})_2(\text{GMP})\}^+$ (G4), in the presence of Leu, Gly and Tyr (Table 3.2). However, negligible formation of Pt-GMP adducts was observed with Trp. To further investigate the effect of Trp, its side chain indole and analogue melatonin were irradiated with **1** and 2 mol. equiv. of 5'-GMP under the same conditions (Figure 3.10b). The LC-MS analysis showed a significant inhibition in the formation of Pt-GMP adducts, only a small amount of $\{\text{Pt}^{\text{II}}(\text{CH}_3\text{CN})(\text{py})_2(\text{GMP-H})\}^+$ (G3) was detected, while no other adduct was found, indicating that the indole structure is the key motif to disrupt the binding of Pt and 5'-GMP. Since no Pt-indole adduct was detected, a possible relationship between the formation of azidyl radicals and Pt-GMP adducts is proposed.

3.3.6. DNA melting temperature

DNA melting experiments were carried out in phosphate buffer (1 mM, pH = 7.9) with the ratio of drug to base pair being 2 to investigate the interaction between DNA and complexes **4–7** in the presence or absence of light. The ΔT_m values for *ct*-DNA with different complexes are summarised in Figure 3.11. Similar to the parental complex **1**, complexes **4–6** exhibited a small effect on DNA melting temperature without light, while were able to increase T_m significantly after irradiation with blue light (420 nm), even though light alone did not induce a notable change in DNA. However, complex **7** with tryptophan that can quench azidyl radicals showed a similar weak effect on DNA melting temperature, regardless of the presence of light.

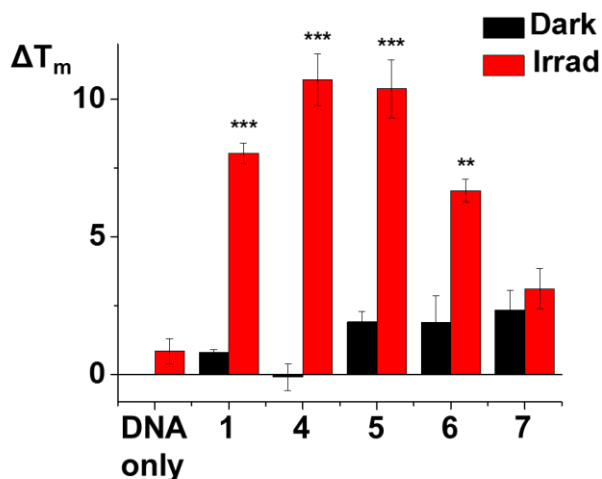


Figure 3.11. DNA melting temperature change (ΔT_m) induced by photoactive complexes containing amino acid methyl esters (**4–7**) with and without irradiation (420 nm, 1 h). All data were determined from triplicate samples, and the irradiated samples were compared with their dark samples by a two-tail t-test with unequal variances. * $p < 0.05$, ** $p < 0.01$, *** $p < 0.005$.

3.3.7. Photocytotoxicity

Satisfactory dark stability of complexes **4–8** was observed in A2780 cells with IC_{50} values higher than 100 μM , similar to parent complex **1** (Table 3.3). Upon 1 h irradiation with blue light (465 nm), all of complexes exhibited similar improved cytotoxicity compared to **1**, and the IC_{50} values followed the order: **1** (7.1 μM) \approx **7** (7.0 μM , Trp) \approx **8** (6.6 μM , cP) $>$ **5** (5.5 μM , Gly) $>$ **4** (4.1 μM , Leu) $>$ **6** (1.4 μM , Tyr).

The cytotoxicity of complex **8** was also determined in A549 lung and PC3 prostate cells in the dark, which gave high IC_{50} values ($> 100 \mu M$). The photocytotoxicity of complex **8** ($IC_{50} = 2.8 \mu M$ for A549, and 22.4 μM for PC3) was more potent than the parent complex **1** ($IC_{50} = 51.9 \mu M$ for A549, and 55.6 μM for PC3) with photocytotoxicity indices (PI) of > 35.7 and 4.5 towards A549 and PC3 cancer cells, respectively (Table 3.4).

Table 3.3. IC₅₀ values and photocytotoxicity indices (PI) for complexes **1** and **4–7** in A2780 ovarian cancer cells obtained after 1 h incubation, 1 h irradiation (465 nm) and 24 h recovery; and cell accumulation of Pt in A2780 cells after exposure to complexes **1** and **4–7**.

Complex	IC ₅₀ (μM) ^a		PI	Pt accumulation (ng/10 ⁶ cells) ^b		
	Dark	Irrad		10 μM, 1 h, dark	IC ₅₀ , 2 h, dark	IC ₅₀ , 1 h dark and 1 h irrad
1	> 100	7.1±0.4	> 14	1.19±0.04***	0.9±0.2**	2.7±0.1***
4	> 100	4.1±0.5	> 23	1.30±0.13***		
5	> 100	5.5±1.2	> 18	0.19±0.03*		
6	> 100	1.4±0.2	> 71	0.32±0.08*	0.14±0.01*	1.81±0.20*
7	> 100	7.0±0.2	> 14	0.75±0.20*	0.66±0.08**	10.1±1.0*

^a Each value is mean of two independent experiments. ^b All data were determined from triplicate samples and compared with the negative control by a two-tail t-test with unequal variances. *p < 0.05, **p < 0.01, ***p < 0.005.

3.3.8. Cellular accumulation

The cellular accumulation of Pt(IV) complexes **4–7** conjugated to amino acid methyl esters was investigated at the same concentration (10 μM) for 1 h in the dark (Table 3.3). Complexes **4–7** displayed 0.19–1.30 ng Pt/10⁶ cells in A2780 cells, which are similar or lower than the parent complex **1** (1.19 ng Pt/10⁶ cells). Complexes **8** exhibited a higher Pt accumulation in A549 compared to A2780 cells. The effect of light on platinum accumulation was also determined for complexes **6–8** in A2780 cells (Table 3.4). Without irradiation, complexes **6–8** exhibited lower platinum accumulation (0.14–0.66 ng Pt/10⁶ cells) than **1** when drugged at IC₅₀ concentrations. However, significant improvement in accumulation was observed for

complexes **6–8** after irradiation (1h, 465 nm), 13×, 15× and 47× for **6**, **7** and **8**, respectively. In contrast, the increase in accumulation of **1** was only 3× after same irradiation.

Table 3.4. IC₅₀ values and photocytotoxicity indices (PI) for complex **8** in cancer cells obtained after 1 h incubation, 1 h irradiation (465 nm) and 24 h recovery; and cellular accumulation of Pt in A2780 cells after exposure to complex **8**.

Complex	Cell	IC ₅₀ (μM) ^a		PI	Pt accumulation (ng/10 ⁶ cells)		
		Dark	Irrad		10 μM, 1 h, in dark	IC ₅₀ , 2 h in dark	IC ₅₀ , 1 h in dark and 1 h irrad
1	A2780	> 100	7.1±0.4	> 14	1.19±0.04 ^{***}	0.9±0.2 ^{**}	2.7±0.1 ^{***}
	A549	> 100	51.9±2.5	> 1.9	1.0±0.2 [*]	n.d.	n.d.
	PC3	> 100	55.6±0.9	> 1.7	1.5±0.3 [*]	n.d.	n.d.
8	A2780	> 100	6.6±0.2	> 15	0.17±0.02 ^{**}	0.20±0.03 [*]	9.41±0.03 ^{***}
	A549	> 100	2.8±0.2	> 35	2.5±0.2 [*]	n.d.	n.d.
	PC3	> 100	22.4±2.2	> 4.4	n.d.	n.d.	n.d.

^a Each value is mean of two independent experiments. ^b 1 h incubation, 1 h irradiation (465 nm). All data were determined from triplicate samples and compared with the negative control by a two-tail t-test with unequal variances. * p < 0.05, ** p < 0.01, *** p < 0.005.

3.4. Discussion

3.4.1. Synthesis and characterisation

The axial hydroxide ligands of diazido Pt(IV) complexes are useful for derivatisation. A fundamental step in the development of Pt(IV) complexes is the carboxylation of the hydroxyl groups, which greatly facilitates subsequent modification. Unlike oxoplatin with a cisplatin

centre, complex **1** tends to form the mono substituted axial derivative **2** with a succinate ligand. The activation of terminal carboxylic acid can be achieved by many methods for amide coupling, such as EDC, TBTU, HATU, T3P, and BOP coupling. Since the succinimidyl esters are relatively stable and can be separated by column chromatography, the combination of EDC, NHS and DMAP was employed to modify the carboxyl acid in **2**, yielding complex **3** with succinimidyl esters. The NHS in the freshly purified **3** was replaced by amino acid methyl esters or cyclic peptide to generate the corresponding complexes. The direct coupling using TBTU resulted in a mixture with impurities that could not be removed by column chromatography on silica gel.

The NMR spectra of complexes **4–7** contained the signals of pyridine bound to Pt and the corresponding amino acid methyl esters. A complicated ^1H NMR spectrum in $\text{DMSO-}d_6$ was observed for complex **8** containing the nona-peptide due to the overlap of the amide, carboxylic acid and aromatic hydrogen signals. The addition of D_2O quenched the amide and carboxylic acid ^1H NMR signals due to the hydrogen–deuterium exchange, giving a simplified ^1H NMR spectrum with only aromatic hydrogen signals that were ascribed to pyridine, indole of Trp and phenol of Tyr. These results indicated that the platinum complex was conjugated to the cyclic peptide.

3.4.2. Dark stability and photodecomposition

The dark stability of complexes **4–8** indicated that the conjugation with amino acid methyl esters and one cyclic peptide did not impair either the aqueous solubility or the kinetic inertness of the Pt(IV) centre. Due to the absorbance of Trp and Tyr at *ca.* 280 nm, complexes **4–8** displayed varied extinction coefficients at *ca.* 260 and 300 nm. The absorption at 300 nm is ascribed to the main LMCT transition ($\text{N}_3 \rightarrow \text{Pt}$) that decreased significantly during

photodecomposition. Different decomposition rates were observed under the same irradiation condition, which indicated the involvement of axial ligands in the photodecomposition. Notably, no EPR signal was observed even after 100 min irradiation of the complex **7** with Trp, which supported the hypothesis that tryptophan was able to quench $N_3\bullet$ and $OH\bullet$ radicals even as part of the platinum complex.

3.4.3. Photoreactions with 5'-GMP and DNA

The nucleotide guanosine monophosphate (5'-GMP) is a RNA monomer and often used as a model for DNA nucleobase guanine that has traditionally been considered as the major target of platinum anticancer drugs. In the presence of Leu, Gly, and Tyr (2 mol. equiv. of amino acid), the photoreaction between diazido Pt(IV) complex **1** and 5'-GMP was not affected significantly, since same types of Pt-GMP adducts were observed. However, Trp, indole, and melatonin quenched the formation of Pt-GMP adducts, indicating that the indole structure is the key motif to disrupt the binding of Pt centre and 5'-GMP. Since no Pt-indole adduct was detected, a possible relationship between the formation of azidyl radicals and Pt-GMP adducts is proposed. Also, the methyl ester of tryptophan conjugated to Pt(IV) complexes can quench the formation of both azidyl radicals and Pt-GMP adducts.

Complexes **4–6** increased the DNA melting temperature only upon irradiation, indicating the stability and lack of interaction of these complexes towards DNA in the dark and their potential to form DNA interstrand cross-link after photodecomposition. Complex **7** containing the methyl ester of Trp quenched the platinum binding to 5'-GMP, which can be related to the lack of DNA binding and negligible increase of T_m upon irradiation.

3.4.4. Photocytotoxicity and cellular accumulation

Complexes **4–7** exhibited improved photocytotoxicity in A2780 cells (up to 5x), but similar dark stability compared with parent complex **1** ($IC_{50} > 100\mu M$). Considering that amino acids are alternative fuel for cancer cells other than glucose, the cellular accumulation of **4–7** was regarded as the main reason for the enhancement in their photocytotoxicity. However, the dark Pt accumulation of **4–7** was similar or less than that of **1**, either in cells treated with drugs at same concentration or equipotent concentration. Thus, the effect of light activation is ascribed as the reason for their high photocytotoxicity. As expected, 1 h irradiation can significantly improve the Pt accumulation in A2780 cancer cells, especially for complex **7** containing the methyl ester of tryptophan. Tryptophan is able to quench the formation of azidyl radicals and Pt-GMP adducts, but complex **7** displayed a similar photocytotoxicity compared with unsubstituted **1**. The reason is tentatively assigned as the high Pt accumulation of photoactivated **7**, which can interact with other biomolecules within cells.

A higher accumulation of **8** in A549 lung cancer than in A2780 ovarian cancer cells was observed, which is consistent with its higher photocytotoxicity in A549 cells. Also, significant improvement in cellular accumulation after irradiation was detected in A2780 for **8**, which is the reason for its similar photocytotoxicity compared with complex **1**.

3.5. Conclusion

In this Chapter, five diazido Pt(IV) complexes conjugated to amino acid methyl esters (**4–7**) or a cyclic peptide (**8**) have been synthesised and characterised by HPLC, NMR, and UV-vis spectra. These complexes exhibited satisfactory dark stability and photodecomposition upon irradiation with indigo light (420 nm). Azidyl and hydroxyl radicals and Pt-GMP adducts were

detected for complexes **4–6** after irradiation, while the methyl ester of tryptophan in complex **7** can quench the formation of azidyl radicals and Pt-GMP adducts. Complexes **4–8** displayed improved photocytotoxicity in A2780 compared with parent complex **1**, while their cellular accumulation in the dark is not as high as that of **1**. Significant enhancement in platinum accumulation was observed for complexes **6–8** after irradiation, which is properly related to their promising photocytotoxicity, especially for complex **7** containing methyl ester of tryptophan. Complex **8** showed higher photocytotoxicity and accumulation in A549 than A2780, which suggests that the cyclic peptide might induce cell selectivity.

3.6. References

1. G. C. Barrett, *Chemistry and Biochemistry of the Amino Acids*, Springer, Netherlands, 1985.
2. A. Ambrogelly, S. Palioura, D. Söll, *Nat. Chem. Biol.*, 2007, **3**, 29–35.
3. H. A. Coller, *Am. J. Pathol.*, 2014, **184**, 4–17.
4. M. Keenan, J. Chi, *Cancer J.*, 2015, **21**, 49–55.
5. O. D. K. Maddocks, C. R. Berkers, S. M. Mason, L. Zheng, K. Blyth, E. Gottlieb, K. H. Vousden, *Nature*, 2012, **493**, 542–546.
6. O. D. K. Maddocks, D. Athineos, E. C. Cheung, P. Lee, T. Zhang, N. J. F. van den Broek, G. M. Mackay, C. F. Labuschagne, D. Gay, F. Kruiswijk, J. Blagih, D. F. Vincent, K. J. Campbell, F. Ceteci, O. J. Sansom, K. Blyth, K. H. Vousden, *Nature*, 2017, **544**, 372–376.

7. S. P. Gravel, L. Hulea, N. Toban, E. Birman, M. J. Blouin, M. Zakikhani, Y. Zhao, I. Topisirovic, J. St-Pierre, M. Pollak, *Cancer Res.*, 2014, **74**, 7521–7533.
8. M. Kwong, L. Fung, G. C. F. Chan, *J. Hematol. Oncol.*, 2017, **10**:144.
9. L. M. Volstein, *Sov. J. Coord. Chem.*, 1975, **1**, 483–509.
10. W. Beck, *Pure Appl. Chem.*, 1988, **60**, 1357–1363.
11. A. Nomoto, N. Sakamoto, Y. Sakai, K. Fukumoto, S. I. Ogura, K. Shouhei, K. Kakiuchi, J. Kikuchi, S. Yano, A. Ogawa, *Res. Chem. Intermed.*, 2019, **45**, 3–12.
12. Z. Kokan, B. Perić, G. Kovačević, A. Brozovic, N. Metzler-Nolte, S. I. Kirin, *Eur. J. Inorg. Chem.*, 2017, 3928–3937.
13. A. Iakovidis, N. Hadjiliadis, *Coord. Chem. Rev.*, 1994, **135–136**, 17–63.
14. E. Bersanetti, A. Pasini, G. Pezzoni, G. Pratesi, G. Savi, R. Supino, F. Zunino, *Inorg. Chim. Acta*, 1984, **93**, 167–172.
15. A. Colombo, R. D. Gioia, A. Pasini, *Inorg. Chim. Acta*, 1986, **125**, L1–L3.
16. A. L. Mellor, D. H. Munn, *Nat. Rev. Immunol.*, 2004, **4**, 762–774.
17. BioMedTracker. *Cancer Immunotherapies*, 2014.
18. S. G. Awuah, Y. R. Zheng, P. M. Bruno, M. T. Hemann, S. J. Lippard, *J. Am. Chem. Soc.*, 2015, **137**, 14854–14857.
19. S. Mukhopadhyay, C. M. Barnés, A. Haskel, S. M. Short, K. R. Barnes, S. J. Lippard, *Bioconjugate Chem.*, 2008, **19**, 39–49.
20. A. Massaguer, A. González-Cantó, E. Escribano, S. Barrabés, G. Artigas, V. Morenoc, V. Marchán, *Dalton Trans.*, 2015, **44**, 202–212.

21. Y. Yuan, R. T. K. Kwok, B. Z. Tang, B. Liu, *J. Am. Chem. Soc.*, 2014, **136**, 2546–2554.
22. A. Gandioso, E. Shaili, A. Massaguer, G. Artigas, A. González-Cantó, J. A. Woods, P. J. Sadler, V. Marchán, *Chem. Commun.*, 2015, **51**, 9169–9172.
23. J. Mayr, P. Heffeter, D. Groza, L. Galvez, G. Koellensperger, A. Roller, B. Alte, M. Haider, W. Berger, C. R. Kowol, B. K. Keppler, *Chem. Sci.*, 2017, **8**, 2241–2250.
24. V. Pichler, J. Mayr, P. Heffeter, O. Dömötör, E. A. Enyedy, G. Hermann, D. Groza, G. Köllensperger, M. Galanksi, W. Berger, B. K. Keppler, C. R. Kowol, *Chem. Commun.*, 2013, **49**, 2249–2251.
25. Y. R. Zheng, K. Suntharalingam, T. C. Johnstone, H. Yoo, W. Lin, J. G. Brooks, S. J. Lippard, *J. Am. Chem. Soc.*, 2014, **136**, 8790–8798.
26. X. Li, J. Mu, F. Liu, E. W. P. Tan, B. Khezri, R. D. Webster, E. K. L. Yeow, B. Xing, *Bioconjugate Chem.*, 2015, **26**, 955–961.
27. B. J. Pages, K. B. Garbutcheon-Singh, J. R. Aldrich-Wright, *Eur. J. Inorg. Chem.*, 2017, 1613–1624.
28. S. J. Berners-Price, L. Ronconi, P. J. Sadler, *Prog. Nucl. Magn. Reson. Spectrosc.*, 2006, **49**, 65–98.
29. C. A. Wootton, C. Sanchez-Cano, A. F. Lopez-Clavijo, E. Shaili, M. P. Barrow, P. J. Sadler, P. B. O'Connor, *Chem. Sci.*, 2018, **9**, 2733–2739.
30. J. Du, Y. Wei, Y. Zhao, F. Xu, Y. Wang, W. Zheng, Q. Luo, M. Wang, F. Wang, *Inorg. Chem.*, 2018, **57**, 5575–5584.
31. J. S. Butler, J. A. Woods, N. J. Farrer, M. E. Newton, P. J. Sadler, *J. Am. Chem. Soc.*, 2012, **134**, 16508–16511.

Chapter 3: Photoactive Pt(IV) Complexes with Amino Acid Methyl Esters and Peptides

32. C. Vallotto, E. Shaili, H. Shi, J. S. Butler, C. J. Wedge, M. E. Newton, P. J. Sadler, *Chem. Commun.*, 2018, **54**, 13845–13848.
33. G. Feng, M. Zhang, H. Wang, J. Cai, S. Chen, Q. Wang, J. Gong, K. W. Leong, J. Wang, X. Zhang, M. Zeng, *Adv. Therap.*, 2019, 1900018.
34. M. F. Reichmann, S. A. Rice, C. A. Thomas, P. Doty, *J. Am. Chem. Soc.*, 1954, **76**, 3047–3053.

Chapter 4

Mono- and Di-substituted Photoactive Pt(IV) Complexes

4.1. Introduction

The kinetic inertness of Pt(IV) complexes allows them to stay intact in the dark, and therefore they are often employed as prodrugs for the corresponding reactive Pt(II) complexes.¹⁻³ The major advantages of Pt(IV) complexes include the reduced side effects and the feasible modification of their axial ligands to improve pharmacological properties.⁴⁻⁶ Not only the axial ligands of Pt(IV) complexes can be released from Pt(IV) during reduction to Pt(II), but they also greatly affect the reduction potential of Pt(IV).^{7,8} In general, Pt(IV) complexes with hydroxide axial ligands exhibit higher dark stability than those with other axial ligands.⁹ However, Pt(IV) complexes with bioactive axial ligands can target several cellular components at the same time as multi-action prodrugs, which results in enhanced selectivity and anticancer potency circumventing cisplatin resistance via combined mechanism of actions.^{3,5}

Two main types of bioactive ligands have been attached to Pt(IV) complexes: (i) cancer-targeting vectors; (ii) anticancer species. In this Chapter, the anticancer drug 3-coumarin carboxylate (cou), pyruvate dehydrogenase kinase (PDK) inhibitor 4-phenylbutyrate (PhB) and dichloroacetate (DCA) and cancer-targeting biotin, were conjugated to diazido Pt(IV) complex **1** to form mono- and di-substituted complexes (Figure 4.1).

Coumarins containing a benzopyrone target a number of pathways in cancer (e.g. kinase inhibition, cell cycle arrest, and angiogenesis inhibition) and have been widely used as anticancer drugs and cellular fluorescence probes.¹⁰⁻¹⁴ Anticancer complexes with coumarin have been reported to show rich photophysical properties (e.g. fluorescence) and high cytotoxicity.^{15,16} Notably, coumarin can act as an antenna for light harvesting when conjugated to metal complexes, therefore enhancing their fluorescence quantum yield and lengthening the life time.¹⁷

PDK inhibitors PhB and DCA suppress aerobic glycolysis and reverse the Warburg effect (according to which cancer cells metabolism trends to be glycolysis rather than oxidative phosphorylation), eventually killing cancer cells.^{3,18} PhB is also a weak extracellular HDAC (histone deacetylase) inhibitor.¹⁹ A series of Pt(IV) complexes with PhB and DCA have been developed, which exhibit significantly improved cytotoxicity.^{3,20-22} Mitaplatin with two DCA ligands can attack both nuclear DNA by Pt(II) species and mitochondria by DCA, thus showing a remarkable selectivity towards cancer cells.

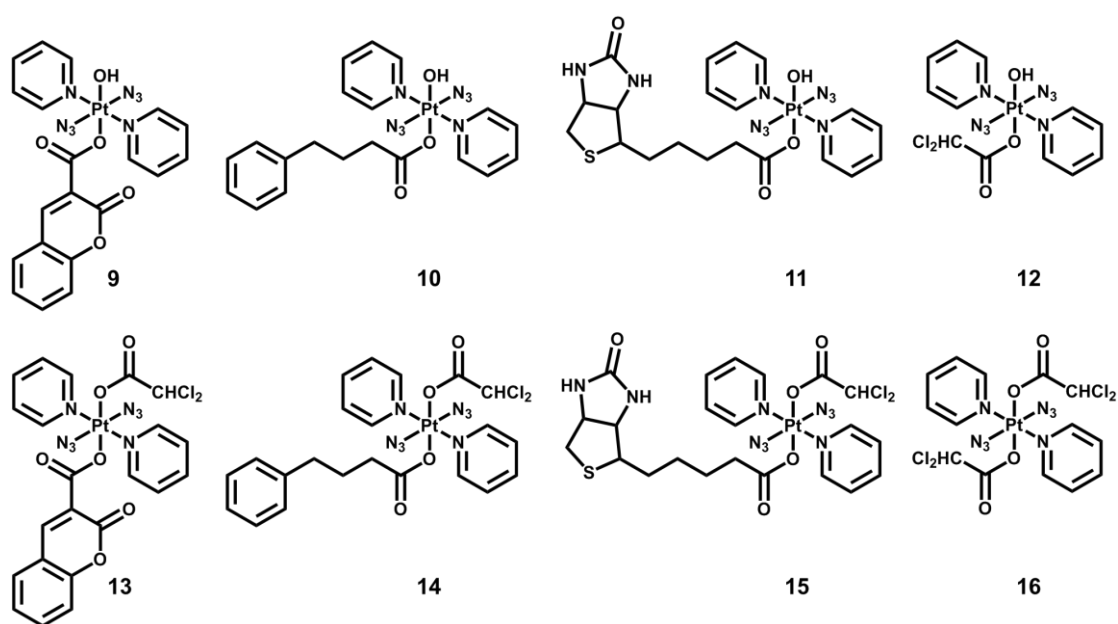


Figure 4.1. Mono-substituted diazido Pt(IV) complexes **9–12** and their di-substituted analogues **13–16**.

Biotin (vitamin H or B7), a vitamin containing an ureido (tetrahydroimidizalone) ring fused with a tetrahydrothiophene ring, plays an important role as a cellular growth promoter and co-enzyme for carboxylase enzymes.²³ Exogenous biotin is taken up via a high-affinity biotin transporter and a sodium-dependent multivitamin transporter (SMVT).^{24,25} Notably, SMVT exhibits higher expression in cancer cells, thus making biotin a tumour-specific vector.²⁶⁻²⁹

Biotin possesses high binding affinity specific to tetrameric egg white avidin (66 kDa) through noncovalent bonds with K_d of 10^{-13} to 10^{-15} M and dissociation half-life ($t_{1/2}$) of *ca.* three months.³⁰ Avidin-biotin complex induces a relatively low immune response *in vivo* and has been widely used in targeted therapy.^{23,31-34} With strong adherence properties to cells *in vitro*, avidin can be administered as a nano-carrier for the delivery of biotinylated drugs.³⁵ Biotinylation of anticancer drugs is therefore a feasible strategy to improve the cellular accumulation of drugs and cancer selectivity.^{14,36, 37}

Previously reported derivatisation of photoactive diazido Pt(IV) complexes has mainly focused on mono-substituted complexes.³⁸⁻⁴⁰ In this Chapter, the synthesis and characterisation of four di-substituted diazido Pt(IV) complexes all bearing a cancer targeting/cytotoxic group and an additional DCA group, along with their mono-substituted analogues are reported. The dark stability and photoactivation with visible light, photoreactions with NADH, 5'-GMP, photocytotoxicity and cellular accumulation, and effect on cellular morphology were also investigated for these complexes.

4.2. Experimental

Caution! Due care and attention should be taken in the synthesis and handling of shock-sensitive heavy azido metal complexes in the dark with minimal light exposure although we encountered no problems during the work reported here.

4.2.1. Materials

Coumarin-3-carboxylic acid (cou), biotin, dichloroacetic anhydride (DCA anhydride), 4'-hydroxyazobenzene-2-carboxylic acid (HABA) and *N, N*-Diisopropylethylamine (DIPEA)

were purchased from Sigma-Aldrich, *o*-(Benzotriazol-1-yl)-*N,N,N',N'*-tetramethyluronium tetrafluoroborate (TBTU) was purchased from Merck. 4-Phenylbutyric acid (PhB) was from Acros Organics. ***Trans,trans,trans*-[Pt(py)₂(N₃)₂(OH)₂] (1)** was prepared according to the method described in Chapter 2. All solvents for common use were analytical reagent grade from Fisher Scientific and were used as supplied.

4.2.2. Synthesis and characterisation

***Trans,trans,trans*-[Pt(py)₂(N₃)₂(cou)(OH)] (9)**

To the solution of complex **1** (40.0 mg, 85 μ mol), 3-coumarin carboxylic acid (16.2 mg, 85 μ mol), and TBTU (27.3 mg, 85 μ mol) in DMF solution (2 mL), DIPEA (100 μ L) was added. The reaction mixture was stirred overnight at 298 K under a nitrogen atmosphere. After evaporation to dryness, the oily residue was collected and purified by column chromatography on silica gel (3% methanol + 97% DCM). ¹H NMR (CDCl₃, 400 MHz): 9.09 (d, J = 5.8 Hz, J¹⁹⁵ Pt–¹H = 27.5 Hz, 4H, *H_α py*), 8.33 (s, 1H, *CH_{coumarin}*), 8.12 (t, J = 7.7 Hz, 2H, *H_γ py*), 7.61 (t, J = 6.9 Hz, 4H, *H_β py*), 7.49 (t, J = 7.9 Hz, 1H, *H_{phenyl}*), 7.42 (d, J = 7.4 Hz, 1H, *H_{phenyl}*), 7.24 (d, J = 8.4 Hz, 1H, *H_{phenyl}*), 7.18 (t, J = 7.6 Hz, 1H, *H_{phenyl}*), 3.38 (s, 1H, *OH*). ¹³C NMR (CDCl₃, 125 MHz): 167.10 (*COO*), 158.10 (*COO*), 154.90 (=C–), 149.87 (*C_α py*), 146.97 (*CH*), 141.27 (*C_γ py*), 133.17 (*CH*), 129.11 (*CH*), 125.95 (*C_β py*), 124.43 (*CH*), 121.51 (=C–), 118.45 (=C–), 116.47 (*CH*). ESI-MS: [M + Na]⁺ (*m/z*) Calc., 666.1; Found, 666.1. $\epsilon_{298\text{ nm}} = 31660\text{ M}^{-1}\text{ cm}^{-1}$, $\epsilon_{266\text{ nm}} = 16358\text{ M}^{-1}\text{ cm}^{-1}$ (5% DMSO + 95% RPMI-1640).

***Trans,trans,trans*-[Pt(py)₂(N₃)₂(PhB)(OH)] (10)**

To the solution of complex **1** (40.0 mg, 85 μ mol), 4-phenylbutyric acid (14.0 mg, 85 μ mol), and TBTU (27.3 mg, 85 μ mol) in DMF solution (2 mL), DIPEA (100 μ L) was added. The reaction mixture was stirred overnight at 298 K under a nitrogen atmosphere. After evaporation to dryness, the oily residue was collected and purified by column chromatography on silica gel (2% methanol + 98% DCM). ¹H NMR (CDCl₃, 400 MHz): 8.95 (d, J = 5.3 Hz, J¹⁹⁵ Pt–¹H = 27.3 Hz, 4H, *H_α* py), 8.06 (t, J = 7.6 Hz, 2H, *H_γ* py), 7.62 (t, J = 7.1 Hz, 4H, *H_β* py), 7.23 (d, J = 7.6 Hz, 2H, *H_{phenyl}*), 7.18-7.13 (m, 3H, *H_{phenyl}*), 3.46 (s, 1H, *OH*), 2.60 (t, J = 7.8 Hz, 2H, *CH₂*), 2.43 (t, J = 7.5 Hz, 2H, *CH₂*), 1.89 (m, 2H, *CH₂*). ¹³C NMR (CDCl₃, 100 MHz): 177.13 (*COO*), 149.65 (*C_α* py), 142.08 (*C_{phenyl}*), 141.26 (*C_γ* py), 128.51 (*C_{phenyl}*), 128.24 (*C_{phenyl}*), 125.92 (*C_β* py), 125.71 (*C_{phenyl}*), 36.37 (*CH₂*), 35.24 (*CH₂*), 27.79 (*CH₂*). ESI-MS: [M + H]⁺ (*m/z*) Calc., 618.2; Found, 618.2. $\epsilon_{297\text{ nm}} = 19187\text{ M}^{-1}\text{ cm}^{-1}$, $\epsilon_{259\text{ nm}} = 15895\text{ M}^{-1}\text{ cm}^{-1}$ (5% DMSO + 95% RPMI-1640).

***Trans,trans,trans*-[Pt(py)₂(N₃)₂(biotin)(OH)] (11)**

To the solution of complex **1** (40 mg, 85 μ mol), biotin (21 mg, 86 μ mol), and TBTU (27 mg, 85 μ mol) in DMF solution (2 mL), N, N-diisopropylethylamine (DIPEA) (100 μ L) was added. The reaction mixture was stirred overnight at 298 K under a nitrogen atmosphere. After evaporation to dryness, the oily residue was collected and purified by column chromatography on silica gel (8% methanol + 92% DCM). ¹H NMR (DMSO-*d*₆, 400 MHz): 8.82 (d, J = 5.5 Hz, J¹⁹⁵Pt-¹H = 26.8 Hz, 4H, *H_{ortho}* py), 8.28 (t, J = 7.6 Hz, 2H, *H_{para}* py), 7.85 (t, J = 6.9 Hz, 4H, *H_{meta}* py), 6.39 (s, 1H, *NHC(O)NH*), 6.35 (s, 1H, *NHC(O)NH*), 4.31-4.28 (m, 1H, *CH*), 4.11-4.08 (m, 1H, *CH*), 3.51 (s, 1H, *OH*), 3.06-3.01 (m, 1H, *CH*), 2.81 (dd, J = 12.4, 5.1 Hz, 1H, *CH₂*), 2.59 (s, 1H, *CH₂*), 2.23 (t, J = 7.3 Hz, 2H, *CH₂*), 1.62-1.24 (m, 6H, *CH₂*). ¹³C NMR

(DMSO-*d*₆, 100 MHz): 175.92 (*NHC(O)NH*), 163.18 (*COO*), 149.75 (*C_{ortho} py*), 142.45 (*C_{para} py*), 126.68 (*C_{meta} py*), 61.55 (*CH*), 59.64 (*CH*), 55.98 (*CH*), 55.38 (*CH*₂), 36.74 (*CH*₂), 28.72 (*CH*₂), 28.58 (*CH*₂), 26.34 (*CH*₂). ESI-HRMS: [M + Na]⁺ (*m/z*) calcd 720.1405, found 720.1398. Anal. Calcd: C₂₀H₂₆N₁₀O₄PtS•(CH₂Cl₂)_{0.5}: C 33.27, H 3.68, N 18.93. Found: C 33.67, H 3.70, N 18.59. ε_{299 nm} = 19330 M⁻¹ cm⁻¹, ε_{260 nm} = 12188 M⁻¹ cm⁻¹ (5% DMSO + 95% RPMI-1640).

***Trans,trans,trans*-[Pt(py)₂(N₃)₂(cou)(DCA)] (13)**

Three mol. equiv. of dichloroacetic anhydride was stirred with complex **9** in DMF solution overnight at 298 K under a nitrogen atmosphere. After evaporation to dryness, the oily residue was collected and purified by column chromatography on silica gel (1% methanol + 99% DCM). ¹H NMR (CDCl₃, 400 MHz): 9.15 (d, J = 5.6 Hz, J¹⁹⁵ Pt–¹ H = 24.9 Hz, 4H, *H_α py*), 8.25 (s, 1H, *CH_{coumarin}*), 8.02 (t, J = 7.8 Hz, 2H, *H_γ py*), 7.71 (t, J = 7.0 Hz, 4H, *H_β py*), 7.59 (t, J = 7.8 Hz, 1H, *H_{phenyl}*), 7.49 (d, J = 7.4 Hz, 1H, *H_{phenyl}*), 7.32 (d, J = 8.4 Hz, 1H, *H_{phenyl}*), 7.26 (t, J = 7.3 Hz, 1H, *H_{phenyl}*), 5.86 (s, 1H, *CHCl₂*). ¹³C NMR (CDCl₃, 125 MHz): 167.46 (*COO*), 166.72 (*COO*), 157.68 (*COO*), 155.03 (=C–), 150.06 (*C_α py*), 147.72 (*CH*), 141.76 (*C_γ py*), 133.66 (*CH*), 129.28 (*CH*), 126.08 (*C_β py*), 124.60 (*CH*), 119.63 (=C–), 118.14 (=C–), 116.55 (*CH*), 65.42 (*CHCl₂*). ESI-MS: [M + Na]⁺ (*m/z*) Calc., 777.0; Found, 777.1. ε_{306 nm} = 30650 M⁻¹ cm⁻¹ (DMSO).

***Trans,trans,trans*-[Pt(py)₂(N₃)₂(PhB)(DCA)] (14)**

Three mol. equiv. of dichloroacetic anhydride was stirred with complex **10** in DMF solution overnight at 298 K under a nitrogen atmosphere. After evaporation to dryness, the oily residue was collected and purified by column chromatography on silica gel (1% methanol + 99%

DCM). ^1H NMR (CDCl_3 , 400 MHz): 8.92 (d, $J = 6.0$ Hz, $J^{195}\text{Pt}-^1\text{H} = 24.8$ Hz, 4H, H_α py), 8.10 (t, $J = 7.5$ Hz, 2H, H_γ py), 7.65 (t, $J = 6.8$ Hz, 4H, H_β py), 7.24 (d, $J = 7.5$ Hz, 2H, H_{phenyl}), 7.19-7.09 (m, 3H, H_{phenyl}), 5.83 (s, 2H, CHCl_2), 2.56 (t, $J = 7.6$ Hz, 2H, CH_2), 2.42 (t, $J = 7.6$ Hz, 2H, CH_2), 1.83 (m, 2H, CH_2). ^{13}C NMR (CDCl_3 , 100 MHz): 178.26 (COO), 166.89 (COO), 149.59 (C_α py), 141.87 (C_γ py), 141.50 (C_{phenyl}), 128.44 (C_{phenyl}), 128.34 (C_{phenyl}), 126.23 (C_β py), 125.91 (C_{phenyl}), 65.50 (CHCl_2), 35.64 (CH_2), 35.00 (CH_2), 27.46 (CH_2). ESI-MS: $[\text{M} + \text{Na}]^+$ (m/z) Calc., 751.1; Found, 751.1. $\epsilon_{313\text{ nm}} = 17654\text{ M}^{-1}\text{ cm}^{-1}$ (DMSO).

***Trans,trans,trans*-[Pt(py)₂(N₃)₂(biotin)(DCA)] (15)**

Three mol. equiv. of dichloroacetic anhydride (DCA anhydride) was stirred with complex **11** in DMF solution overnight at 298 K under a nitrogen atmosphere. After evaporation to dryness, the oily residue was collected and purified by column chromatography on silica gel (3% methanol + 97% DCM). ^1H NMR (CDCl_3 , 400 MHz): 8.77 (d, $J = 5.6$ Hz, $J^{195}\text{Pt}-^1\text{H} = 26.2$ Hz, 4H, H_{ortho} py), 8.34 (t, $J = 7.6$ Hz, 2H, H_{para} py), 7.90 (t, $J = 7.0$ Hz, 4H, H_{meta} py), 6.61 (s, 1H, CHCl_2), 6.38 (s, 1H, $\text{NHC}(\text{O})\text{NH}$), 6.35 (s, 1H, $\text{NHC}(\text{O})\text{NH}$), 4.31-4.28 (m, 1H, CH), 4.10-4.09 (m, 2H, CH), 3.04-2.99 (m, 1H, CH), 2.81 (dd, $J = 12.4, 5.1$ Hz, 1H, CH_2), 2.58 (d, $J = 12.5$ Hz, 1H, CH_2), 2.30 (t, $J = 4.9$ Hz, 2H, CH_2), 1.59-1.23 (m, 6H, CH_2). ^{13}C NMR ($\text{DMSO-}d_6$, 100 MHz): 175.71 ($\text{NHC}(\text{O})\text{NH}$), 163.16 (COO), 149.57 (C_{ortho} py), 143.24 (C_{para} py), 127.26 (C_{meta} py), 66.32 (CHCl_2), 61.52 (CH), 59.64 (CH), 55.90 (CH), 55.36 (CH_2), 49.07 (CH_2), 35.52 (CH_2), 28.47 (CH_2), 26.12 (CH_2). COO in DCA is too weak to detect. ESI-HR MS: $[\text{M} + \text{Na}]^+$ (m/z) calcd 830.0731, found 830.0738. Anal. Calcd: $\text{C}_{22}\text{H}_{26}\text{Cl}_2\text{N}_{10}\text{O}_5\text{PtS}\cdot(\text{CH}_2\text{Cl}_2)_{0.8}$: C 31.24, H 3.17, N 15.98. Found: C 31.49, H 3.20, N 15.31. $\epsilon_{308\text{ nm}} = 20983\text{ M}^{-1}\text{ cm}^{-1}$, $\epsilon_{260\text{ nm}} = 17827\text{ M}^{-1}\text{ cm}^{-1}$ (5% DMSO + 95% RPMI-1640).

***Trans,trans,trans*-[Pt(py)₂(N₃)₂(DCA)(OH)]** (12) and ***trans,trans,trans*-[Pt(py)₂(N₃)₂(DCA)₂** (16)

Three mol. equiv. of dichloroacetic anhydride was stirred with complex **1** in DMF solution overnight at 298 K under a nitrogen atmosphere. After evaporation to dryness, the oily residue was collected and purified by column chromatography on silica gel (1% methanol + 99% DCM).

12. ¹H NMR (CDCl₃, 400 MHz): 8.96 (d, J = 6.1 Hz, J¹⁹⁵ Pt⁻¹ H = 27.0 Hz, 4H, *H_α* py), 8.16 (t, J = 7.6 Hz, 2H, *H_γ* py), 7.72 (t, J = 7.0 Hz, 4H, *H_β* py), 5.96 (s, 1H, CHCl₂). ¹³C NMR (CDCl₃, 100 MHz): 167.76 (COO), 149.30 (*C_α* py), 141.63 (*C_γ* py), 126.23 (*C_β* py), 66.80 (CHCl₂). ESI-MS: [M + Na]⁺ (*m/z*) Calc., 605.0; Found, 605.0. ε_{299 nm} = 16575 M⁻¹ cm⁻¹, ε_{259 nm} = 12514 M⁻¹ cm⁻¹ (5% DMSO + 95% RPMI-1640).

16. ¹H NMR (CDCl₃, 400 MHz): 8.96 (d, J = 5.3 Hz, J¹⁹⁵ Pt⁻¹ H = 25.6 Hz, 4H, *H_α* py), 8.14 (t, J = 7.6 Hz, 2H, *H_γ* py), 7.70 (t, J = 7.2 Hz, 4H, *H_β* py), 5.84 (s, 2H, CHCl₂). ¹³C NMR (CDCl₃, 125 MHz): 167.46 (COO), 149.52 (*C_α* py), 142.10 (*C_γ* py), 126.37 (*C_β* py), 65.05 (CHCl₂). ESI-MS: [M + Na]⁺ (*m/z*) Calc., 715.9; Found, 715.1. ε_{319 nm} = 16257 M⁻¹ cm⁻¹ (DMSO).

4.2.3. Methods and instrumentation

4.2.3.1. HPLC purity test

Purity tests for complexes **9–16** were carried out using the same HPLC instruments and methods as described for **4–8** in Chapter 3.

4.2.3.2. X-ray crystallography

Single crystals of **9** and **13** were obtained by diffusion of diethyl ether into their DCM/MeOH solution, and single crystals of **14** and **16** were obtained by evaporation of their DCM/MeOH solution at 298 K. The crystal structures were determined using the method described in Chapter 2.

4.2.3.3. Cyclic voltammetry

All cyclic voltammetry (CV) experiments were carried out using a CH Instrument model 600D Electrochemical Analyser/Workstation (Austin, TX). The solution was prepared in DMF containing tetrabutylammonium hexafluorophosphate (0.1 M) as supporting electrolyte and degassed under nitrogen. A typical three-electrode system was used to scan the cyclic voltammogram traces: a glassy carbon electrode as the working electrode, Ag/AgCl in 3.0 M KCl as the reference electrode (0.21 V versus NHE), and platinum wire as the counter electrode. The scan rate was set to 100 mV/s.

4.2.3.4. Interaction with avidin

To a mixture of avidin (8 μM) and HABA (160 μM) in phosphate-buffered saline (PBS) solution (500 μL), aliquots of a biotin or biotinylated complexes solution (1.6 mM) in DMSO were added. The concentration of avidin was calibrated by titration with biotin, since the concentration of avidin should be 0.25 \times as that of standard biotin solution at the end titration point. UV-vis spectra were recorded in a quartz cell ($l = 1 \text{ cm}$) after 1 min equilibration.

4.2.3.5. Photo-dark cytotoxicity testing

The antiproliferative activity of complexes **9–16** was determined in A2780 ovarian, A549 lung, and PC3 prostate carcinoma, as well as MRC-5 fibroblast cell lines. The experiments to determine IC₅₀ values were carried out as described in Chapter 2.

4.2.3.6. Cellular accumulation of platinum

The cellular accumulation was measured in A549 lung and A2780 ovarian cancer cells at the same concentration (2 or 10 μM) according to the method described in Chapter 2.

4.2.3.7. Cellular morphological change

A2780 cells were seeded in two glass-bottom cell culture dishes (CELLview, 2×10^5 cells, 24 h for attachment) and exposed to complexes for 1 h in the dark. One dish was irradiated by blue light (465 nm) for 1 h, while the other was kept in the dark for comparison. Supernatants of both plates were removed by suction and cells were washed with PBS. Cells were left in full cell culture medium for 24 h for recovery and stained by SYTOTM 17 Red Fluorescent Nucleic Acid Stain (2.5 μM) for 30 min. The fluorescence images were recorded on a confocal microscope (LSM 880, AxioObserver, $\lambda_{\text{ex}} = 633 \text{ nm}$, $\lambda_{\text{em}} = 638\text{--}759 \text{ nm}$).

4.3. Results

4.3.1. Synthesis and characterisation

Mono-substituted complexes **9–11** were obtained by combining parent complex **1** with corresponding acid using TBTU as amide coupling agent, and the bi-substituted **13–15** were synthesised by stirring **9–11** with dichloroacetic anhydride, while **12** and **16** were made by directly reacting **1** with dichloroacetic anhydride.

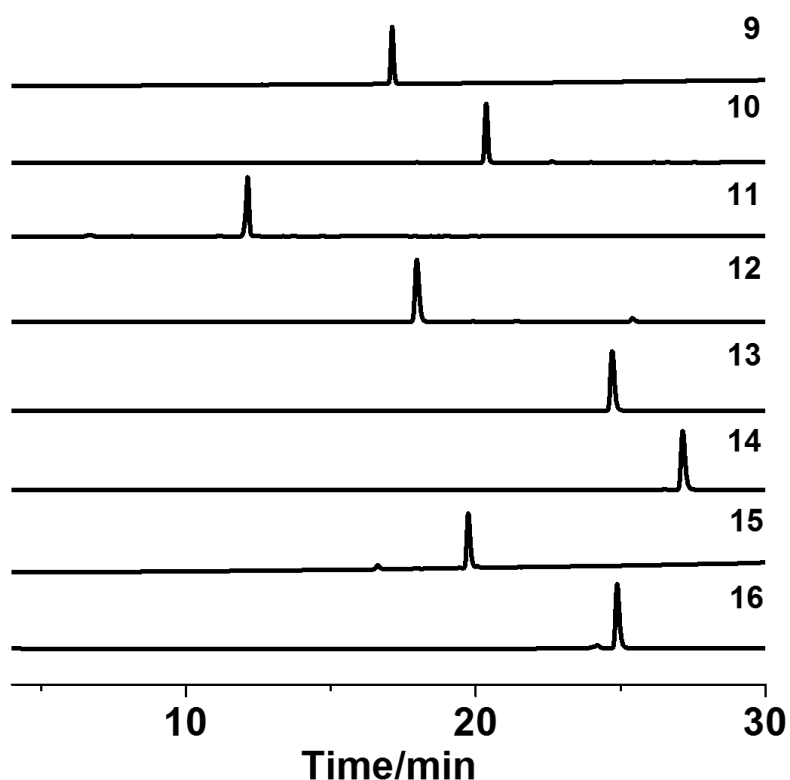


Figure 4.2. HPLC purity of mono-substituted diazido Pt(IV) complexes **9–12** and their di-substituted analogues **13–16**, detection wavelength 254 nm.

All the ^1H and ^{13}C NMR spectra support the proposed structures for the complexes. The Pt coordinated pyridine can be identified by the doublets with ^{195}Pt satellites at *ca.* 9.0 ppm, and

the triplets at *ca.* 8.1 and 7.7 ppm in the ^1H NMR spectra and the ^{13}C NMR resonance at *ca.* 150, 142 and 126 ppm, which are attributed to the α , γ and β CH of pyridine, respectively. The purity of Pt(IV) complexes **9–16** determined by HPLC chromatography was higher than 95% (Figure 4.2). Notably, the di-substituted complexes exhibited *ca.* 7 min longer HPLC retention times than their corresponding mono-substituted analogues, suggesting a higher lipophilicity.

4.3.2. X-ray crystallography

Crystals of complexes **9** and **13** suitable for X-ray diffraction studies were obtained through diffusion of diethyl ether into the corresponding solutions in DCM/MeOH, while those of **14** and **16** were obtained by evaporation of their DCM/MeOH solutions at 298 K. The perspective drawings of complexes **9**, **13**, **14** and **16** are shown in Figure 4.3. The crystallographic data are summarised in Table 4.1 and selected bond distances and angles are listed in Table 4.2 and 4.3. Complexes **9**, **14** and **16** crystallised in the triclinic P-1 space group with two molecules in the unit cell of **9** and **14**, but only one molecule in the unit cell of **16**, while complex **13** crystallised in the trigonal R-3 space group with eighteen molecules in the unit cell.

Complexes **9**, **13**, **14** and **16** are neutral mononuclear Pt(IV) complexes. All structures adopt an octahedral geometry similar to that of parental complex **1**. The Pt(IV) centre with a $[\text{N}_4\text{O}_2]$ hexacoordinated environment is slightly distorted in the structures of **9**, **13** and **14**, while it is fully symmetrical in that of **16**. These complexes show similarities in the equatorial plane defined by four nitrogen atoms, two from the *trans* pyridine and the others from the *trans* azide ligands, and resemble typical equatorial planes in their analogues.¹ The difference lies in the axial ligands. Complex **9** is mono-substituted, while the others are di-substituted. The bond angles between Pt(IV) ion and two axial *trans* oxygen atoms can be used to determine the

distortion from ideal octahedral geometry, which follow the order: **16** (180°) > **14** ($178.76(10)^\circ$) > **9** ($175.13(6)^\circ$) > **13** ($171.97(12)^\circ$).

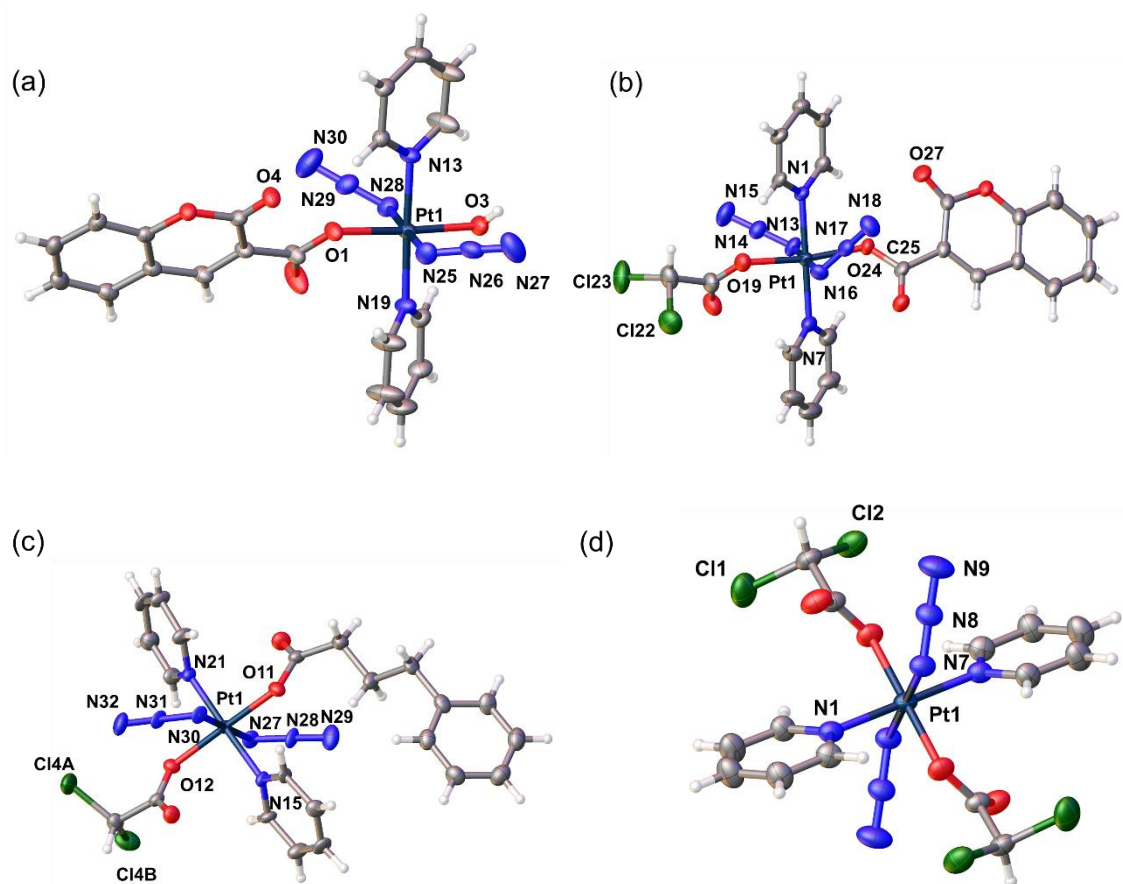


Figure 4.3. X-ray crystal structures of (a) **9**, (b) **13**, (c) **14**, and (d) **16**, with key atoms labeled and thermal ellipsoids drawn at 50% probability level.

Complex **9** is mono-substituted with a coumarin and ligand, and the free hydroxide ligand can form a moderate hydrogen bond with hydroxide ligand in an adjacent molecule ($O3-H3B \cdots O3$, $2.013(11)$ Å, Table 4.4). Complexes **13** and **14** are di-substituted with a dichloroacetic acid ligand and another axial ligand (3-coumarin carboxylic acid for **13** and 4-phenylbutyric acid for **14**). The axial bond angle between Pt(IV) ion and two oxygen atoms in *trans* of **14** ($178.76(10)^\circ$) is larger than that of **13** ($171.97(12)^\circ$), indicating that 3-coumarin carboxylic acid has more effect on the distortion of platinum centre than 4-phenylbutyric acid, which might be

due to the larger steric hindrance of 3-coumarin carboxylic acid. Complex **16** is fully symmetric with two dichloroacetate ligands and the platinum ion sits on an inversion centre. Interactions are observed between CHCl_2 and $\text{O}=\text{C}$ in an adjacent molecule ($\text{Cl}_2\text{C}-\text{H}\cdots\text{O}=\text{C}$, 2.209 Å), which can be regarded as weak hydrogen bond.

Table 4.1. Crystal data and structure refinement for **9**, **13**, **14** and **16**.

Complex	9	13	14	16
Empirical formula	$\text{C}_{20}\text{H}_{16}\text{N}_8\text{O}_5\text{Pt}$	$\text{C}_{22.5}\text{H}_{16.75}\text{Cl}_2\text{N}_8$ $.25\text{O}_{6.08}\text{Pt}$	$\text{C}_{22}\text{H}_{22}\text{Cl}_2\text{N}_8\text{O}_4$ Pt	$\text{C}_{14}\text{H}_{12}\text{Cl}_4\text{N}_8\text{O}_4$ Pt
Formula weight	643.50	766.01	728.46	693.21
Temperature/K	150(2)	150(2)	150(2)	150(2)
Crystal system	triclinic	trigonal	triclinic	triclinic
Space group	P-1	R-3	P-1	P-1
$a/\text{Å}$	7.6941(3)	37.7424(3)	9.5857(2)	7.2235(2)
$b/\text{Å}$	9.2101(3)	37.7424(3)	9.73231(19)	8.4944(2)
$c/\text{Å}$	16.4767(6)	9.84140(10)	15.2124(2)	10.0233(3)
$\alpha/^\circ$	86.004(3)	90	98.1190(14)	105.343(3)
$\beta/^\circ$	84.751(3)	90	103.9082(15)	95.673(3)
$\gamma/^\circ$	67.335(4)	120	104.4649(18)	108.477(3)
Volume/ Å^3	1072.15(7)	12140.8(2)	1302.96(4)	551.19(3)
Z	2	18	2	1
$\rho_{\text{calc}}/\text{g/cm}^3$	1.993	1.886	1.857	2.088
μ/mm^{-1}	6.596	12.037	12.352	6.888
F(000)	620.0	6663.0	708.0	330.0
Crystal size/ mm^3	$0.2 \times 0.1 \times 0.04$ yellow block	$0.3 \times 0.1 \times 0.08$ yellow block	$0.16 \times 0.06 \times 0.01$ colourless block	$0.3 \times 0.18 \times 0.005$ colourless block
Radiation	MoK α ($\lambda = 0.71073$)	CuK α ($\lambda = 1.54184$)	CuK α ($\lambda = 1.54184$)	MoK α ($\lambda = 0.71073$)

2 θ range for data collection/ $^{\circ}$	4.796 to 62.186	8.114 to 146.702	9.608 to 156.79	5.324 to 62.12
Index ranges	-11 \leq h \leq 11, -12 \leq k \leq 13, -23 \leq l \leq 23	-46 \leq h \leq 46, -46 \leq k \leq 42, -10 \leq l \leq 12	-12 \leq h \leq 12, -11 \leq k \leq 12, -19 \leq l \leq 19	-10 \leq h \leq 10, -12 \leq k \leq 12, -13 \leq l \leq 14
Reflections collected	62932	49969	47810	33847
Independent reflections	6486 [R _{int} = 0.0564, R _{sigma} = 0.0292]	5410 [R _{int} = 0.0711, R _{sigma} = 0.0284]	5513 [R _{int} = 0.0596, R _{sigma} = 0.0267]	3261 [R _{int} = 0.0678, R _{sigma} = 0.0338]
Data/restraints/parameters	6486/4/313	5410/4/366	5513/12/334	3261/0/142
Goodness-of-fit on F ²	1.046	1.082	1.136	1.023
Final R indexes [I \geq 2 σ (I)]	R ₁ = 0.0225, wR ₂ = 0.0475	R ₁ = 0.0314, wR ₂ = 0.0814	R ₁ = 0.0309, wR ₂ = 0.0751	R ₁ = 0.0303, wR ₂ = 0.0731
Final R indexes [all data]	R ₁ = 0.0261, wR ₂ = 0.0492	R ₁ = 0.0317, wR ₂ = 0.0817	R ₁ = 0.0329, wR ₂ = 0.0760	R ₁ = 0.0308, wR ₂ = 0.0737
Largest diff. peak/hole/e \AA^{-3}	1.17/-1.33	1.51/-1.10	3.50/-1.55	1.66/-1.63

Table 4.2. Selected bond lengths (\AA) and bond angles ($^{\circ}$) for **9** and **13**.

9		13	
Pt1–O3	1.9753(17)	Pt1–O19	2.020(3)
Pt1–N25	2.049(2)	Pt1–N13	2.045(4)
Pt1–N28	2.044(2)	Pt1–N16	2.058(4)
Pt1–O1	2.0289(16)	Pt1–O24	2.005(3)
Pt1–N13	2.033(2)	Pt1–N1	2.040(3)
Pt1–N19	2.025(2)	Pt1–N7	2.028(3)
N25–N26	1.212(3)	N13–N14	1.211(5)
N26–N27	1.139(3)	N14–N15	1.147(5)
N28–N29	1.209(3)	N16–N17	1.222(5)

N29–N30	1.147(3)	N17–N18	1.148(6)
O1–Pt1–O3	175.13(6)	O19–Pt1–O24	171.97(12)
N13–Pt1–N19	178.33(8)	N1–Pt1–N7	179.26(15)
N25–Pt1–N28	179.07(8)	N13–Pt1–N16	178.49(14)
N26–N25–Pt1	116.89(17)	N14–N13–Pt1	116.0(3)
N25–N26–N27	174.3(3)	N13–N14–N15	175.2(5)
N29–N28–Pt1	117.37(18)	N17–N16–Pt1	114.9(3)
N28–N29–N30	174.6(3)	N16–N17–N18	175.2(4)
		Cl23–C21–Cl22	112.1(3)

Table 4.3. Selected bond lengths (Å) and bond angles (°) for **14** and **16**.

14		16	
Pt1–O12	2.016(3)	Pt1–O10	2.006(3)
Pt1–N30	2.054(3)	Pt1–N1	2.034(3)
Pt1–N27	2.061(3)	Pt1–N7	2.047(3)
Pt1–O11	1.992(3)	N7–N8	1.223(5)
Pt1–N21	2.031(3)	N8–N9	1.141(5)
Pt1–N15	2.035(3)	O10–Pt1–O10 ¹	180.0(3)
N27–N28	1.220(6)	N1–Pt1–N1 ¹	180.0
N28–N29	1.143(6)	N7–Pt1–N7 ¹	180.0
N31–N30	1.227(5)	N8–N7–Pt1	117.8(3)
N31–N32	1.132(6)	N7–N8–N9	174.1(4)
O11–Pt1–O12	178.76(10)	Cl12–C12–Cl11	110.1(2)
N21–Pt1–N15	177.79(13)		
N30–Pt1–N27	179.44(14)		
N28–N27–Pt1	112.7(3)		
N29–N28–N27	177.0(5)		
N31–N30–Pt1	115.2(3)		
N32–N31–N30	176.4(4)		
Cl4A–C14–Cl4B	111.5(2)		

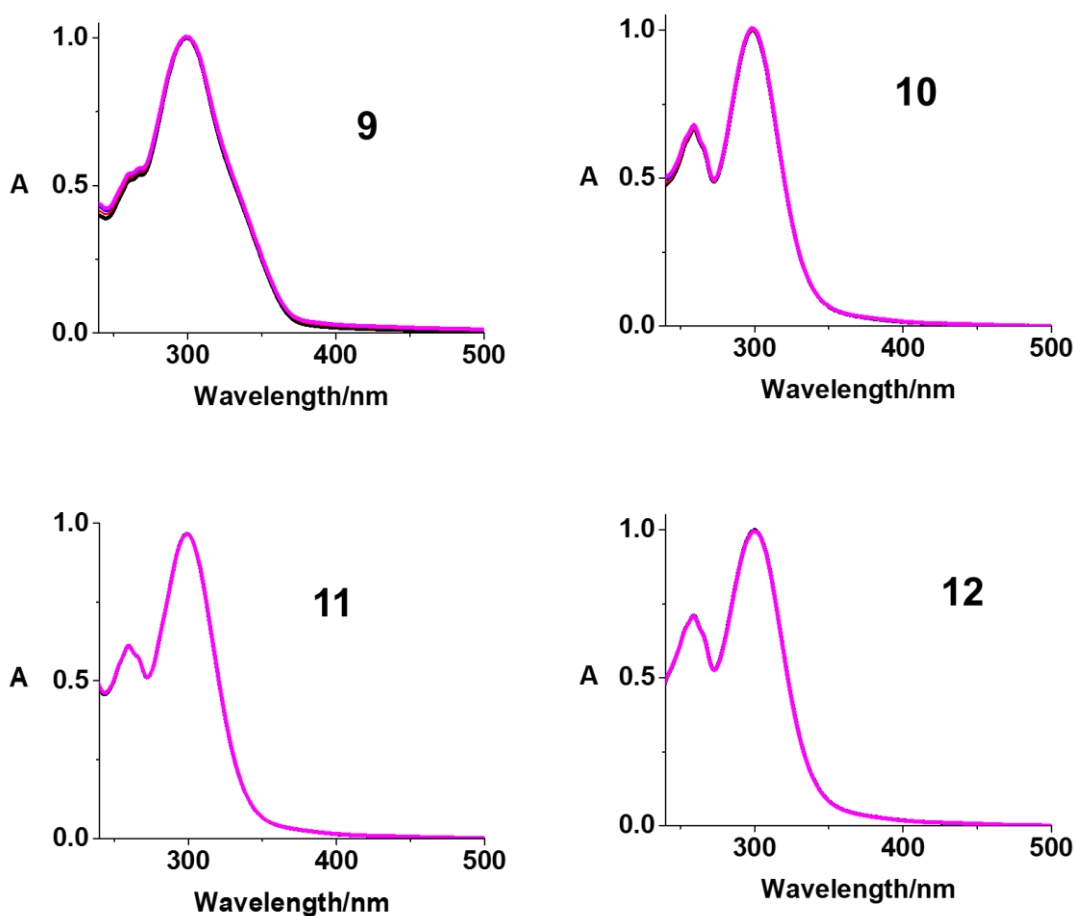
¹1-X, 1-Y, 1-Z

Table 4.4. Selected hydrogen bond parameters for **9**.

D	H	A	d(D-H)/Å	d(H-A)/Å	d(D-A)/Å	D-H-A/°
O3	H3B	O3	0.852(4)	2.013(11)	2.854(4)	169(6)

4.3.3. Dark stability

The dark stability of complexes **9–12** and **15** was tested in phenol red-free RPMI-1640 described in Chapter 3. The results confirmed their good dark stability, since no noticeable spectral change was observed (Figure 4.4). Due to the poor aqueous solubility of complex **13**, **14** and **16**, their dark stability was investigated only in DMSO and no apparent change was detected (Figure 4.5).



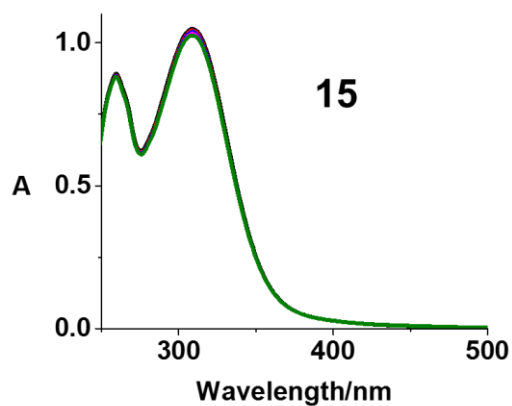


Figure 4.4. Dark stability test of mono-substituted Pt(IV) complexes **9–12** and di-substituted Pt(IV) complex **15** in phenol red-free RPMI-1640 with 5% DMSO for 2 h monitored by UV-vis spectroscopy.

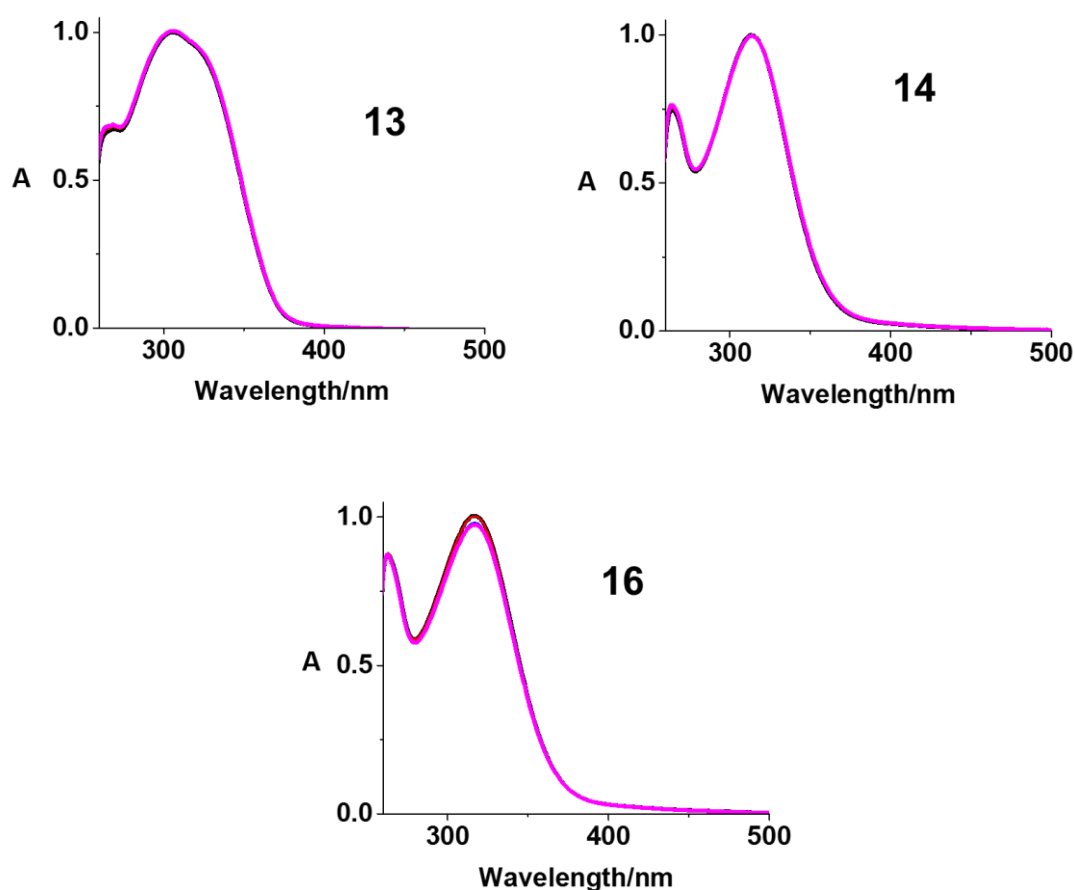


Figure 4.5. Dark stability test for di-substituted Pt(IV) complexes **13**, **14** and **16** in DMSO for 2 h monitored by UV-vis spectroscopy.

4.3.4. Extinction coefficient studies

The extinction coefficients of mono-substituted Pt(IV) complexes **9–12** and di-substituted Pt(IV) complex **15** were determined in phenol red-free RPMI-1640 with 5% DMSO, while those of di-substituted Pt(IV) complexes **13**, **14** and **16** were determined in DMSO due to their poor aqueous solubility. Due to the presence of coumarin, the extinction coefficient of **9** and **13** at their absorption maxima (*ca.* 300 nm) are larger than their analogues. Biotin contributed slightly to the absorption maximum, while 4-phenylbutyric acid showed a negligible effect on the UV-vis spectra. The substitution with dichloroacetic acid in the second axial ligand position resulted in a red-shifted absorption maximum for Pt(IV) complexes (8 nm between **11** and **15**).

4.3.5. Cyclic voltammetry

Pt(IV) complexes with more negative reduction potential are more stable towards reductants. Cyclic voltammogram traces for **1**, **9** and **13** were acquired in the potential range -1.8 – 0.0 V in DMF at 298 K, using 0.1 M NBu₄PF₆ as supporting electrolyte. An irreversible reduction wave assigned to Pt^{IV}/ Pt^{II} was observed with E_{pc} being -1.699, -1.285 and -0.886 V for **1**, **9** and **13**, respectively (Figure 4.6).

4.3.6. Photodecomposition

The photodecomposition of complexes **9–12** and **15**, **16** in aqueous solution with 5% DMSO was monitored by UV-vis spectroscopy (Figure 4.7). Upon irradiation with indigo light (420 nm), a rapid decrease at the LMCT absorption peak was observed for all of the complexes. Notably, the di-substituted complexes **15** and **16** displayed a faster decomposition rate than their mono-substituted analogues under the same conditions. The photodecomposition of

complexes **13**, **14** and **16** in DMSO was also determined using UV-vis spectroscopy (Figure 4.8). All of the di-substituted complexes decomposed within 10 min irradiation in DMSO and no spectral change was observed with longer irradiation times. The comparison between the photodecompositions of **16** in aqueous solution and DMSO under same irradiation condition showed that pure DMSO solution accelerated the decomposition of **16** significantly. The photodecomposition of complex **9** with longer wavelength excitation was also observed due to the presence of the coumarin moiety. Similar to indigo light (420 nm), exposure to blue light (463 nm) resulted in the complete decomposition of **9** in aqueous solution within 1 h. However, green light (517 nm) took a longer time for the photodecomposition (Figure 4.9).

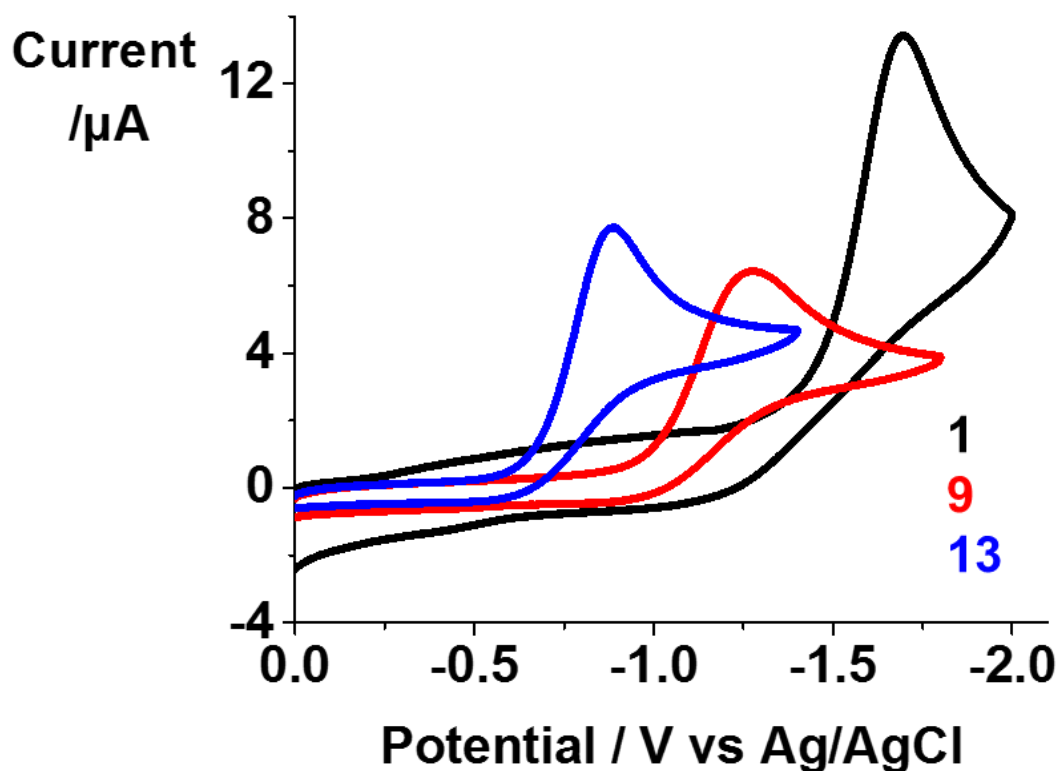


Figure 4.6. The cyclic voltammogram traces of complexes **1**, **9** and **13** (1 mM) in 0.1 M $\text{NBu}_4\text{PF}_6\text{-DMF}$ (degassed under N_2).

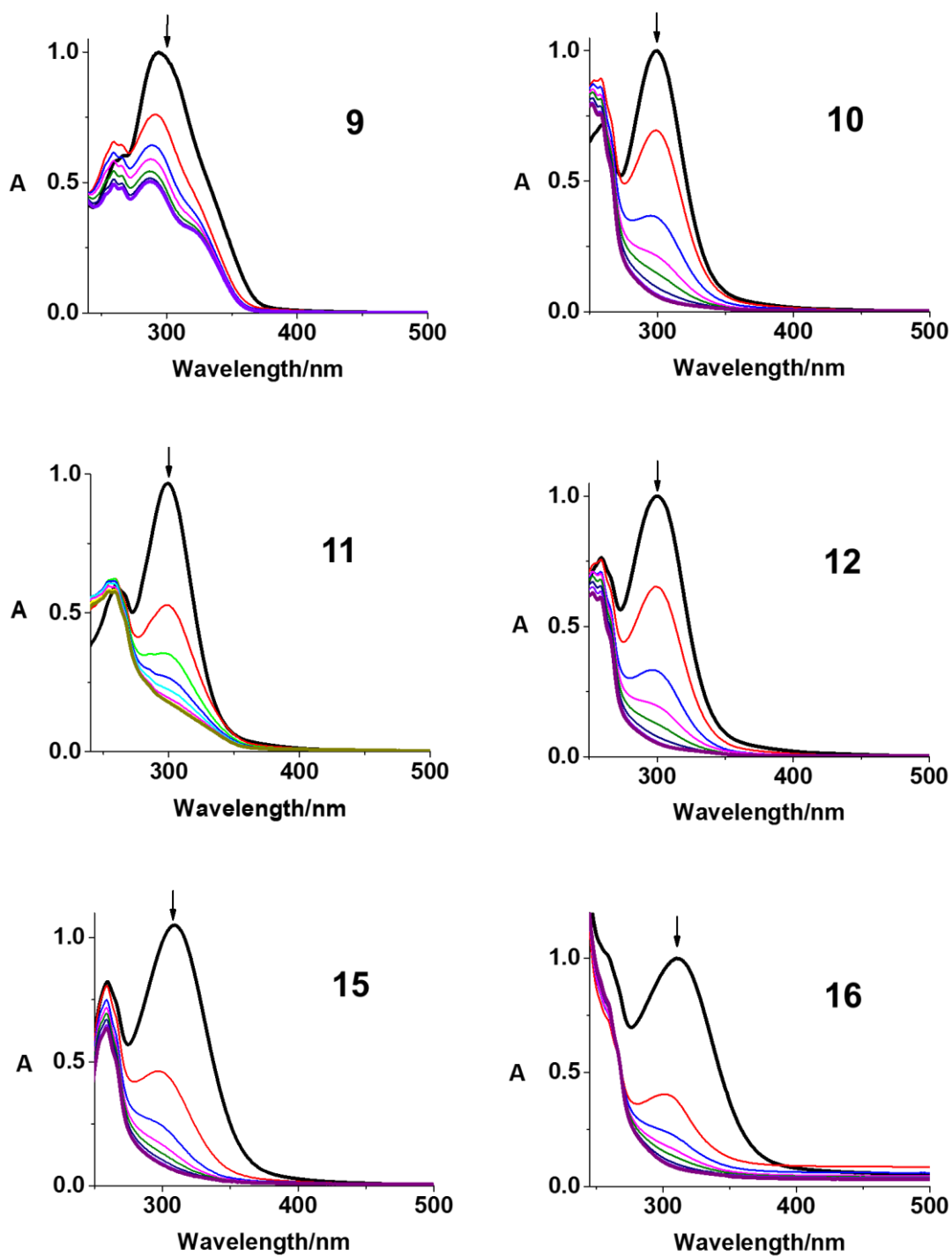


Figure 4.7. UV-vis spectral changes of mono-substituted Pt(IV) complexes **9–12** and di-substituted Pt(IV) complexes **15** and **16** in aqueous solution upon irradiation with indigo light (420 nm, 1 h).

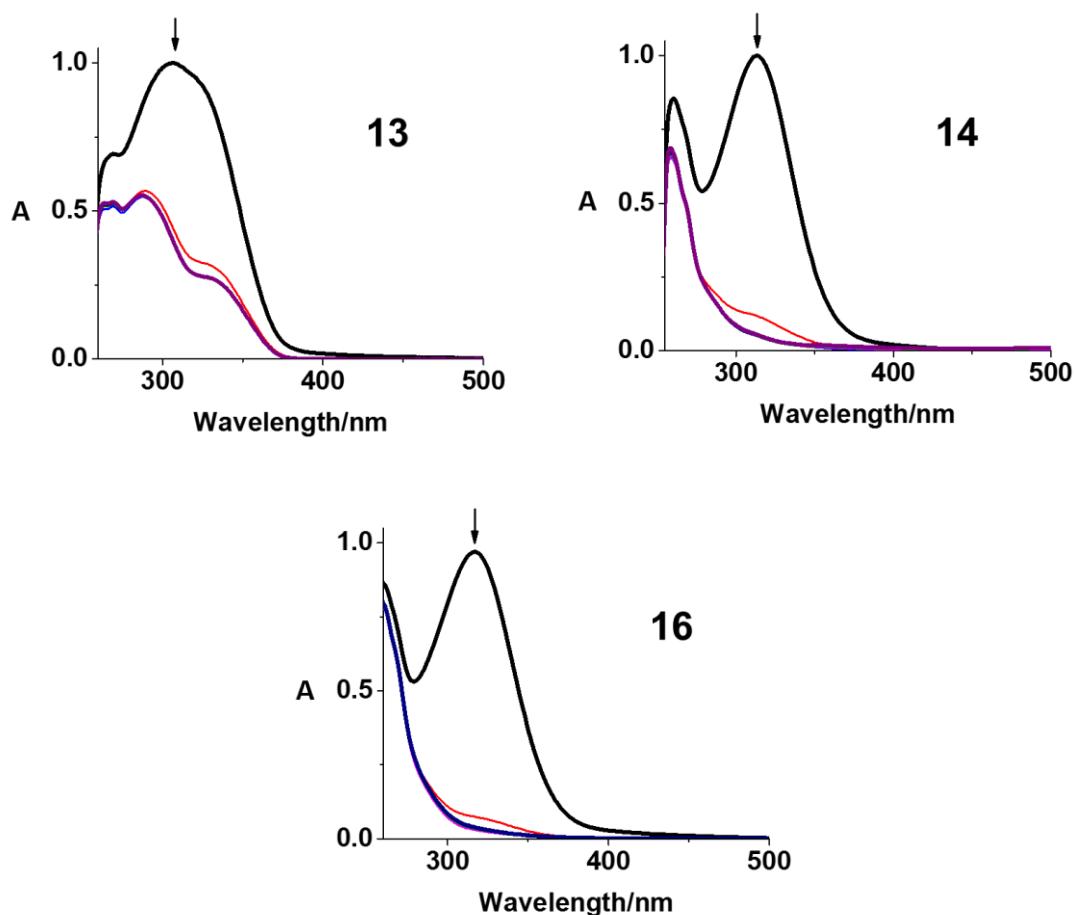


Figure 4.8. UV-vis spectral changes of di-substituted Pt(IV) complexes **15–16** in DMSO solution upon irradiation with indigo light (420 nm, 1 h).

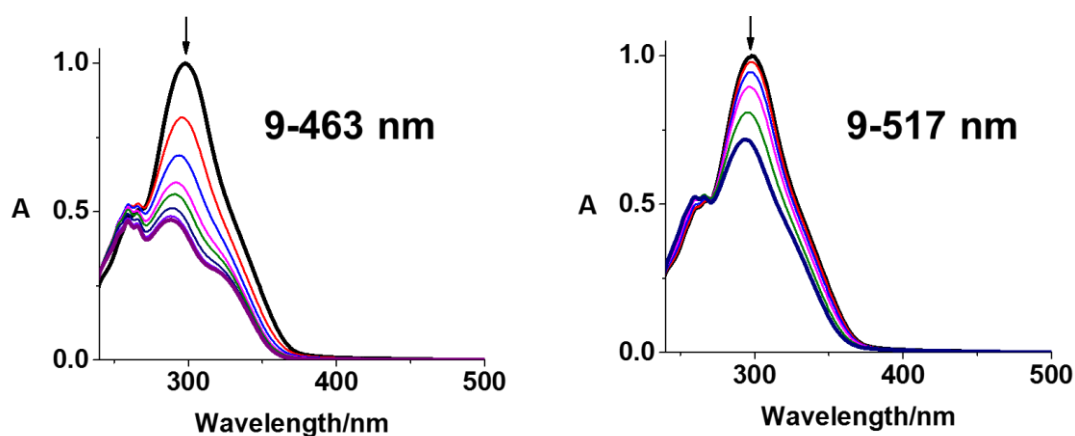


Figure 4.9. UV-vis spectral changes of complex **9** in aqueous solution upon irradiation with blue (463 nm, 1 h) and green light (517 nm, 1.5 h).

Different methods were used to monitor the decomposition of complex **9**. Fluorescence is another indicator that can be used to track the photodecomposition of **9**. In fact, the fluorescence of the coumarin motif switches on after its photoinduced release due to the formation of fluorescent 7-hydroxycoumarin-3-carboxylic acid in the presence of $\text{OH}\cdot$. No apparent fluorescence was observed before irradiation, while blue fluorescence with $\lambda_{\text{max}} = 450$ nm appeared during first 5 min irradiation with indigo light (420 nm) and increased slowly afterwards (Figure 4.10).

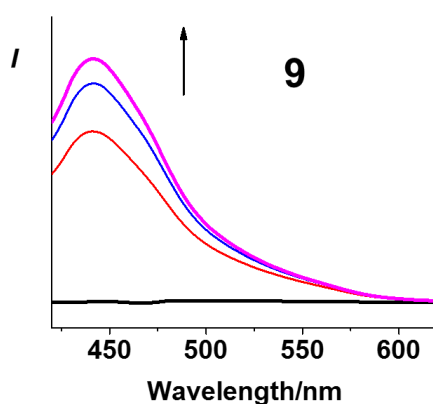


Figure 4.10. Fluorescence change during photochemical decomposition of complex **9** in aqueous solution upon irradiation with indigo light (420 nm, 20 min).

LC-MS was employed to monitor the photoactivation of **9** in aqueous solution (Figure 4.11 and Table 4.5). Only a HPLC peak assigned to complex **9** was observed before irradiation, indicating the purity of the complex, which disappeared within 20 min of irradiation with indigo light (420 nm). The peak assigned to $\{\text{Pt}^{\text{IV}}(\text{py})_2(\text{N}_3)(\text{OH})(\text{cou})\}^+$ (601.18 m/z) increased gradually and peaked after 5 min, and thereafter started to decrease in 5-30 min with a concomitant increase of the Pt(II) photoproducts $[2\{\text{Pt}^{\text{II}}(\text{py})(\text{N}_3)(\text{OH})(\text{HCOO})\} + \text{H}]^+$ (756.80 m/z), $[\{\text{Pt}^{\text{II}}(\text{py})_2(\text{N}_3)_2\} + \text{Na}]^+$ (460.08 m/z), $[\{\text{Pt}^{\text{II}}(\text{py})(\text{cou})(\text{HCOOH})(\text{N}_3)\} + \text{H}]^+$ (552.05 m/z), $\{\text{Pt}^{\text{III}}(\text{py})_2(\text{HCOO})(\text{N}_3)\}^+$ (440.07 m/z), $\{\text{Pt}^{\text{II}}(\text{py})_2(\text{N}_3)(\text{CH}_3\text{CN})\}^+$ (436.08 m/z),

$\{\text{Pt}^{\text{II}}(\text{py})(\text{cou})(\text{CH}_3\text{CN})_2\}^+$ (545.10 m/z), and 3-coumarin carboxylic acid. The ^1H NMR spectra of **9** suggested a complicated mixture formed after irradiation (420 nm), which is consistent with the results obtained by LC-MS. Upon irradiation with green light (517 nm) for 1 h, about 28% of **9** decomposed, producing $[\{\text{Pt}^{\text{II}}(\text{py})_2(\text{N}_3)(\text{OH})\}+\text{CH}_3\text{CN}+\text{Na}]^+$ (476.03 m/z), $\{\text{Pt}^{\text{II}}(\text{py})_2(\text{N}_3)(\text{CH}_3\text{CN})\}^+$ (436.26 m/z), $\{\text{Pt}^{\text{III}}(\text{py})_2(\text{N}_3)_2\}^+$ (437.26 m/z), $\{\text{Pt}^{\text{IV}}(\text{py})_2(\text{N}_3)(\text{OH})(\text{cou})\}^+$ (601.22 m/z), and the released axial ligand coumarin-3-carboxylic acid ($\text{cou}+\text{H}^+$, 191.29 m/z).

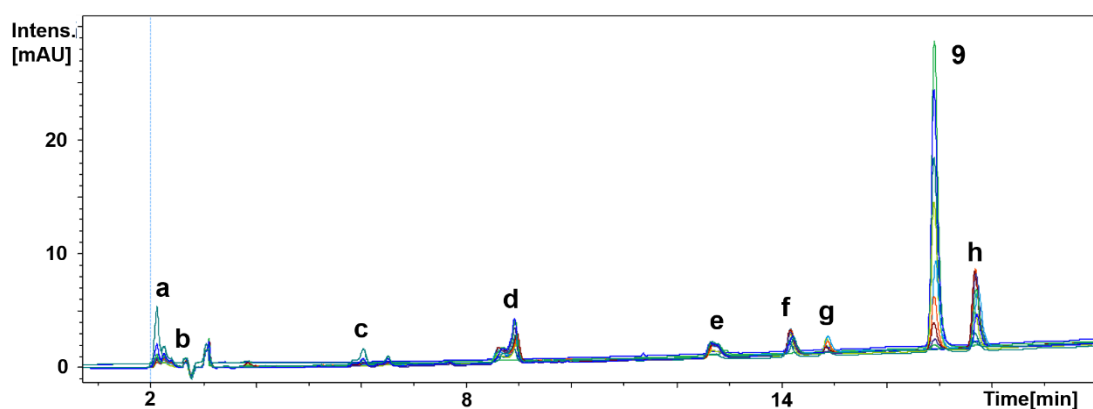


Figure 4.11. Photochemical decomposition of **9** determined by HPLC upon 1 h irradiation with indigo light (420 nm), possible photoproducts **a–h** are listed in **Table 4.5**.

Table 4.5. Photochemical decomposition products of **9** detected by LC-MS (positive ion mode).

Peak	Formula	Structure	Calculated	Found
a	$\text{C}_{12}\text{H}_{15}\text{N}_8\text{O}_6\text{Pt}_2$	$[2\{\text{Pt}^{\text{II}}(\text{py})(\text{N}_3)(\text{OH})(\text{HCOO})\}+\text{H}]^+$	757.04	756.80
b	$\text{C}_{19}\text{H}_{16}\text{N}_3\text{O}_4\text{Pt}$	$\{\text{Pt}^{\text{II}}(\text{py})(\text{cou})(\text{CH}_3\text{CN})_2\}^+$	545.08	545.10
c	$\text{C}_{11}\text{H}_{11}\text{N}_5\text{O}_2\text{Pt}$	$\{\text{Pt}^{\text{III}}(\text{py})_2(\text{HCOO})(\text{N}_3)\}^+$	440.06	440.07
d	$\text{C}_{12}\text{H}_{13}\text{N}_6\text{Pt}$	$\{\text{Pt}^{\text{II}}(\text{py})_2(\text{N}_3)(\text{CH}_3\text{CN})\}^+$	436.08	436.08
e	$\text{C}_{10}\text{H}_7\text{O}_4$	3-coumarin carboxylic acid+ H^+	191.03	191.29
f	$\text{C}_{20}\text{H}_{16}\text{N}_5\text{O}_5\text{Pt}$	$\{\text{Pt}^{\text{IV}}(\text{py})_2(\text{N}_3)(\text{OH})(\text{cou})\}^+$	601.08	601.18
g	$\text{C}_{10}\text{H}_{10}\text{N}_8\text{NaPt}$	$[\{\text{Pt}^{\text{II}}(\text{py})_2(\text{N}_3)_2\}+\text{Na}]^+$	460.06	460.08
h	$\text{C}_{16}\text{H}_{13}\text{N}_4\text{O}_6\text{Pt}$	$[\{\text{Pt}^{\text{II}}(\text{py})(\text{cou})(\text{HCOOH})(\text{N}_3)\}+\text{H}]^+$	552.05	552.10

The EPR spectra of **9** showed no signal in the absence of irradiation, while a 1 : 2 : 2 : 1 quartet of triplets signal assigned as DMPO–N₃• and a quartet signal for DMPO–OH• were detected after irradiation (463 nm) (Figure 4.12).

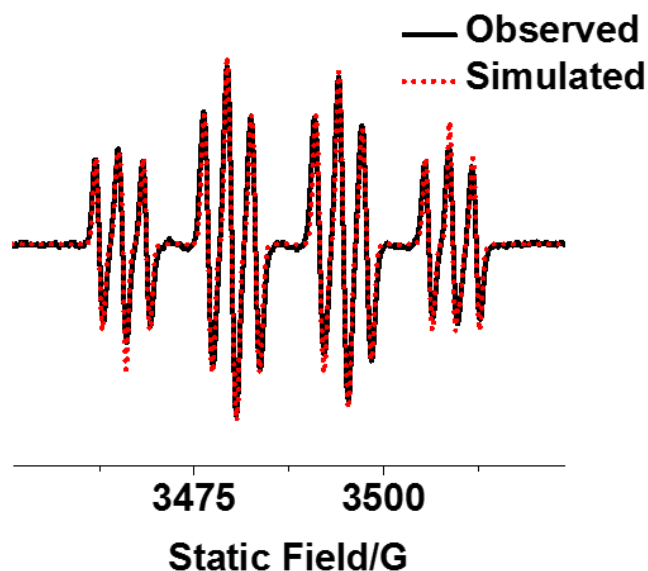


Figure 4.12. EPR spectrum of complex **9** (2.5 mM) in aqueous solution with 5% DMSO showing the formation of DMPO–N₃• and DMPO–OH• adducts after irradiation (465 nm; observed, black; simulated, red). The experimental trace shows the accumulation of 300 scans (conversion time 5.12 ms, time constant 5.12 ms, and sweep time 10.49 s for each scan) with continuous irradiation (463 nm). Parameters for simulation: DMPO–N₃• ($g = 2.00595$, $a_{\text{NO}}^{\text{N}} = 1.43$ mT, $a_{\beta}^{\text{H}} = 1.45$ mT, and $a_{\text{N}\alpha}^{\text{N}} = 0.29$ mT); DMPO–OH• ($g = 2.00592$, $a_{\text{NO}}^{\text{N}} = 1.43$ mT, and $a_{\beta}^{\text{H}} = 1.45$ mT).

4.3.7. Photoreactions with 5'-GMP followed by LC-MS

A mixture of 30 μM **9** and 2 equiv. of 5'-GMP in aqueous solution was irradiated by indigo light (420 nm) then studied by LC-MS at different time intervals (Figure 4.13).

$\{\text{Pt}^{\text{II}}(\text{CH}_3\text{CN})(\text{py})_2(\text{GMP-H})\}^+$ (756.16 m/z, G1), $\{\text{Pt}^{\text{II}}(\text{OC}(\text{O})\text{H})(\text{py})_2(\text{GMP})\}^+$ (762.10 m/z, G2) and $\{\text{Pt}^{\text{II}}(\text{N}_3)(\text{py})_2(\text{GMP})\}^+$ (758.16 m/z, G3) were detected as the major photoproducts between **9** and 5'-GMP, and their presence increased with irradiation time. Similar photoproducts were observed for other Pt(IV) complexes in this Chapter.

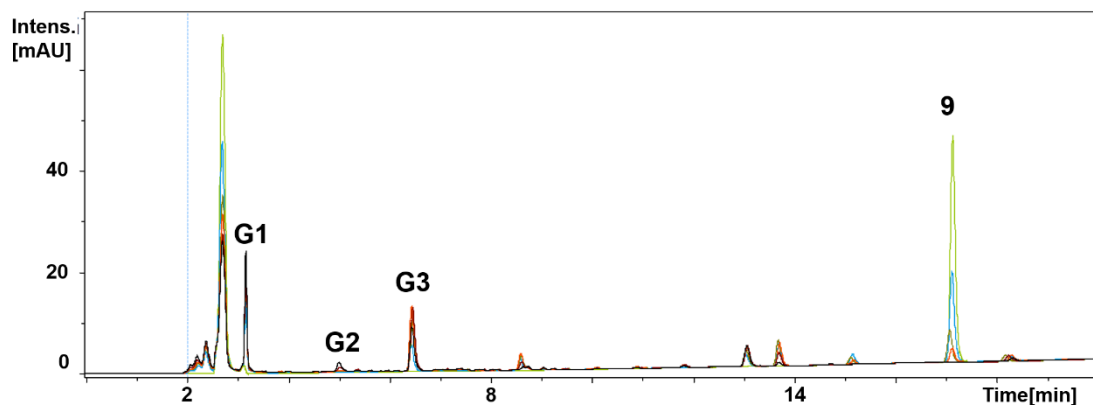


Figure 4.13. Photoreactions between of **9** and 5'-GMP over 1 h irradiation monitored by HPLC.

4.3.8. Interaction with avidin

The binding affinity of avidin towards complexes **11** and **15** in PBS was assessed by a displacement titration using HABA, a weakly binding biotin analogue, and monitored by UV-vis spectroscopy (Figure 4.14). HABA displays a band at 496 nm in absorption spectra when bound to avidin.⁴¹ When HABA is replaced by biotinylated complexes, the signal at 496 nm will decrease. HABA (160 μM) was mixed with avidin (8 μM) beforehand and biotinylated complex was added into the system. A gradual decrease of the absorbance at 496 nm was observed upon addition of both complexes, which indicates their stronger binding to avidin compared with HABA (dissociation constant $K_d = 10^{-6}$ M).⁴² Only when K_d of avidin and the biotinylated complex is $< 10^{-9}$ M, does the titration plot give sharp end points.⁴² At the end point, the absorbance change for biotinylated complexes is the same as that of biotin with ΔA

= 1.01 (496 nm). The titration results indicate that **11** and **15** exhibit similar affinity towards avidin as unmodified biotin.

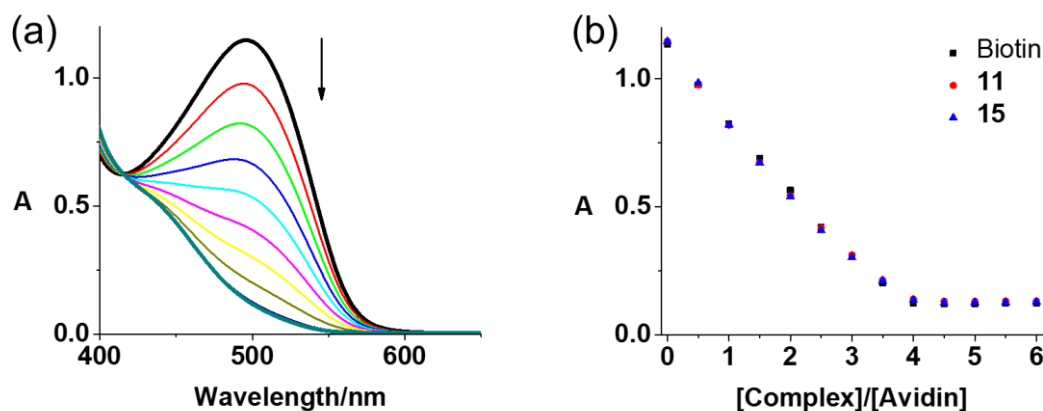


Figure 4.14. (a) UV-vis spectral changes of avidin-HABA in PBS solution upon addition of complex **11** in DMSO, (b) absorbance change at 496 nm in HABA displacement titrations of biotin and biotinylated complexes.

4.3.9. Photocytotoxicity

The dark-photocytotoxicity of complexes **9–11** was determined in A2780 ovarian, A549 lung and PC3 prostate cancer cells, and MRC-5 lung normal fibroblast and the IC_{50} values are summarised in Table 4.6. Mono-substituted Pt(IV) complexes **9–12** and di-substituted Pt(IV) complex **15** displayed significant dark stability with IC_{50} values $> 100 \mu\text{M}$, while those for di-substituted Pt(IV) complexes **13**, **14** and **16** were not as high as **15** due to their poor aqueous solubility and relatively lower dark stability. Notably, di-substituted Pt(IV) complexes showed at least $2\times$ enhanced photocytotoxicity compared with their mono-substituted analogues in all of cancer cells tested. In contrast, low cytotoxicity was observed for all of complexes in the normal MRC-5 cells.

In order to investigate the effect of its strong binding to avidin on cytotoxicity, the biotin tagged photoactive Pt(IV) complex, **11** was mixed with avidin (**11**: avidin = 4:1) prior to addition to A2780 cells following the same protocol used for **11** alone. It was notable that the adduct of **11** and avidin exhibited good dark stability, while being potently photocytotoxic with an IC₅₀ value of 4.4 μM, which is 2.7× lower than that of **11**, and 1.6× more toxic than parent complex **1**.

Table 4.6. IC₅₀ values and photocytotoxicity indices (PI) for complexes **9–11** obtained after 1 h incubation, 1 h irradiation (465 nm) and 24 h recovery.

Complex	IC ₅₀ (μM) ^a			
	A2780	A549	PC3	MRC-5
9	Dark	> 100	> 100	> 100
	Irrad	2.9±0.2	7.8±0.1	6.5±0.8
	PI	> 34	> 12	> 15
10	Dark	> 100		> 100
	Irrad	0.92±0.07	5.44±0.05	
	PI	> 108	> 18	
11	Dark	> 100	> 100	> 100
	Irrad	11.7±0.3	13.3±0.7	21.1±0.4
	PI	> 8	> 7	> 4
11- avidin^b	Dark	> 100		
	Irrad	4.4±0.3		
	PI	> 22		
12	Dark	> 100		> 100
	Irrad	1.2±0.2	6.6±1.1	
	PI	> 83	> 15	
13	Dark	1.9±0.1	>50	> 50
	Irrad	0.11±0.02	2.6±0.3	
	PI	17.3	> 19	

14	Dark	1.3±0.2	>20		> 20
	Irrad	0.15±0.01	1.2±0.1		
	PI	8.7	> 16		
15	Dark	> 50	> 100	> 100	> 100
	Irrad	1.3±0.2	5.9±0.6	3.0±0.1	
	PI	> 38	> 16	> 33	
16	Dark	1.9±0.3	>20		> 20
	Irrad	0.39±0.01	1.9±0.1		
	PI	4.9	> 10		

^a Each value is the mean of two independent experiments; b the IC₅₀ value is based on Pt concentration.

4.3.10. Cellular accumulation

The cellular accumulation of biotinylated complexes **11** and **15** with high aqueous solubility at 10 µM were investigated, while the accumulation of other di-substituted complexes was studied at 2 µM due to their poor aqueous solubility and high dark cytotoxicity.

A2780 and A549 cells were exposed to Pt(IV) complexes (10 µM) in the dark for 1 h (Table 4.7). Complex **9** exhibited *ca.* 30× enhanced Pt accumulation compared to the parent complex **1** in A549 cells. The mono-substituted **11** exhibits lower Pt accumulation (0.4 ng/10⁶ cells) than **1** (1.2 ng/10⁶ cells) after 1 h incubation, while the accumulation of di-substituted **15** (19.1 ng/10⁶ cells) is 16× higher than that of **1** and 47× higher than **11**. Since the avidin-**11** complex exhibited improved photocytotoxicity, the effect of avidin in the uptake of **11** was also investigated. The accumulation of Pt in A2780 after exposure to the mixture of **11** and avidin (4: 1) is 10× higher than **11** alone, which correlates with the higher photocytotoxicity of **11**-avidin complex and suggests the potential role of avidin as a carrier for **11**.

Table 4.7. Cellular accumulation of Pt in A549 cells after exposure to complexes **1** and **9**, and A2780 cells to complexes **1** and **11**, **15** (10 μ M, 1 h, in the dark).

Cell	Complex	Pt accumulation (ng/10 ⁶ cells) ^a
A549	1	1.0±0.2*
	9	30.9±5.7
A2780	1	1.19±0.04***
	11	0.40±0.04*
	11-avidin	4.1±0.7*
	15	19.1±2.8*

^a All data were determined from triplicate samples and compared with the negative control by a two-tail t-test with unequal variances. * p < 0.05, ** p < 0.01, *** p < 0.005.

Table 4.8. Cellular accumulation of Pt in A2780 cells and A549 cells after exposure to **1**, mono- and di-substituted complexes (2 μ M, 1 h, in the dark).

Cell	Complex	Pt accumulation (ng/10 ⁶ cells) ^a
A549	1	0.51±0.05***
	9	9.8±2.1***
	13	71.8±5.2***
A2780	1	0.16±0.02*
	9	6.5±0.4***
	10	3.5±0.4***
	12	10.8±0.3***
	13	90.9±12.0***
	14	61.4±4.0***
	16	53.8±1.9***

^a All data were determined from triplicate samples and compared with the negative control by a two-tail t-test with unequal variances. * p < 0.05, ** p < 0.01, *** p < 0.005.

The cellular accumulation for complexes at 2 μM was also determined in A2780 and A549 cells due to the high dark cytotoxicity and low aqueous solubility of di-substituted complexes. Mono-substituted complexes exhibited improved cellular accumulation than unsubstituted **1**, and significantly higher cellular accumulation was observed for di-substituted complexes compared to the corresponding mono-substituted analogues (*ca.* 5–18 \times , Table 4.8).

4.3.11. Cellular morphological change

The photocytotoxicity of complexes is reflected in their cellular morphological change upon irradiation. Ovarian A2780 cancer cells were treated with **11** ($2 \times$ photo IC_{50} concentration) with and without light to investigate changes in their cellular morphology (Figure 4.15). The cell permeant dye SYTOTM 17 was used to stain the nuclei. Without irradiation, **11** exhibited low cytotoxicity ($\text{IC}_{50} > 100 \mu\text{M}$) and, accordingly, no changes in cellular morphology were observed when cells were treated with **11** for 2 h in the dark. In these conditions, the cells appeared healthy with well-defined plasma membranes and intact nuclei. On the contrary, A2780 cells treated with **11** exhibit dramatic morphology change after 1 h irradiation with blue light (465 nm). The cells rounded up and the nuclei were fragmented into pieces. Damaged membranes and copious cell debris were observed (Figure 4.15). Light (465 nm) alone shows no significant effect on cellular morphology.

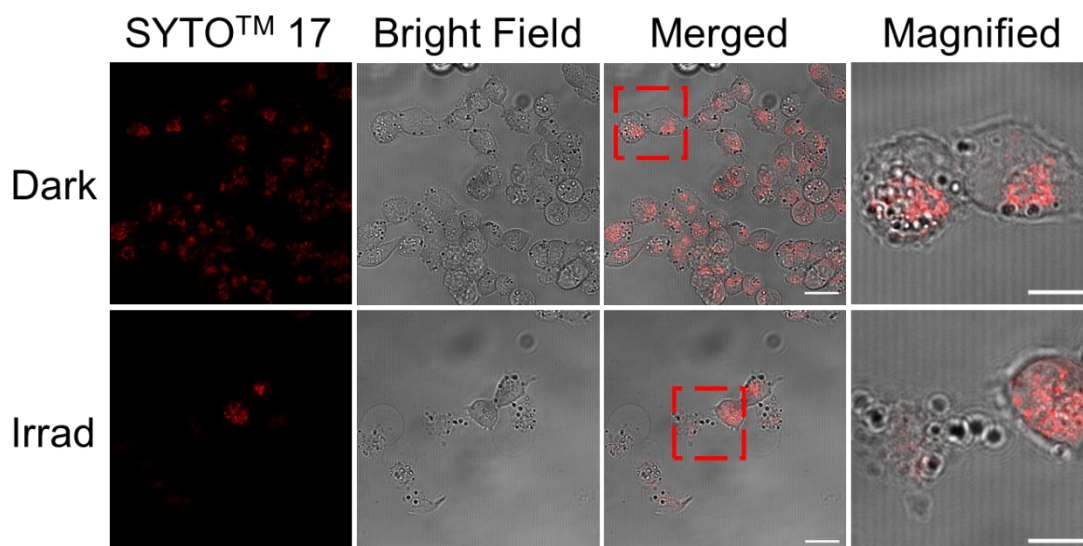


Figure 4.15. Fluorescence images of A2780 cells treated with **11** in the dark and after irradiation with blue light ($\lambda = 463$ nm, 1 h). Cells were stained by SYTO™ 17 (2.5 μ M) for 30 min showing the location and morphology of nuclei. Scale bar = 20 μ m (10 μ m in magnification).

4.4. Discussion

4.4.1. Synthesis and characterisation

Two major agents employed for the modification of axial ligands in Pt(IV) complexes are acid anhydrides and ester coupling reagents. In this Chapter, cou, PhB and biotin were conjugated to Pt(IV) complex using TBTU, while dichloroacetic anhydride was used as the source for DCA ligand. Generally, the coupling using TBTU resulted in only mono-substituted products, while coupling with dichloroacetic anhydride gave a mixture of mono- and di-substituted products. Therefore, to synthesise di-substituted diazido Pt(IV) complexes with different axial ligands, the coupling requires TBTU should be the first step followed by the coupling with anhydride.

4.4.2. Dark stability, photodecomposition and photoproducts

Axial hydroxide ligands are thought to be able to stabilise the Pt(IV) centre and improve the aqueous solubility, and therefore enhances the dark stability of Pt(IV) complexes. Thus, mono-substituted complexes **9–12** displayed promising dark stability in RPMI-1640 cell culture medium. The biotin ligand in complex **15** enables its good aqueous solubility and dark stability in RPMI-1640, even if it is di-substituted. Due to the poor aqueous solubility, the dark stability of other di-substituted **13**, **14** and **16** was measured in DMSO. The substitution of the second axial ligand can increase the reduction potential of Pt(IV) complexes and reduce their stability towards reduction. However, despite the presence of the two axial substituents, the reduction potential of **13** is still negative, indicating its resistance to reduction. Di-substituted **13**, **14** and **16** displayed satisfactory dark stability towards GSH in aqueous solution as monitored by LC-MS.

The photodecomposition of mono-substituted complexes **9–12** in aqueous solution is similar to that of their parent complex **1** upon irradiation with indigo light (420 nm). The less negative reduction potential of di-substituted complexes, on the other hand, can favour their photoreduction. Complex **15** exhibited a larger decrease at the absorption maximum than **11**, which might result from the release of DCA ligand. In addition, the photodecomposition of **16** in DMSO is faster than that in aqueous solution, which might be ascribed to the high affinity of DMSO to Pt(II) species that can accelerate the decomposition.

The photoproducts of **9** were also investigated by fluorescence, LC-MS, and EPR. The release of Pt(II) species, azidyl and hydroxyl radicals, and coumarin-3-carboxylic acid was detected. Upon excitation with $\lambda = 405$ nm, both coumarin-3-carboxylic acid and **9** exhibited no detectable emission. However, an emission peak at $\lambda_{\text{max}} = 450$ nm was observed for **9** after

irradiation ($\lambda = 420$ nm), which is tentatively ascribed to coumarin derivatives oxidised by hydroxyl radicals.

The photoreactions between 5'-GMP and complexes **9–16** are similar to those of **1**, since their axial ligands were released during the photodecomposition and exhibited no apparent effects on the active Pt(II) species.

4.4.3. Photocytotoxicity, cellular accumulation and morphological change

Mono-substituted Pt(IV) complexes exhibited satisfactory dark stability towards bio-reductants maintaining a negative reduction potential. Furthermore, they displayed improved photocytotoxicity towards cancer cells compared with the parent complexes **1**, owing to their ability to release bioactive species other than Pt(II) species and azidyl radicals. The second substituted axial ligand in **15** did not decrease its dark stability, but enhanced its photocytotoxicity, since the axial biotin ligand can maintain the aqueous solubility of the complex **15** even in the presence of lipophilic DCA ligand. These results also suggest the synergic effect of the bioactive axial ligands. Due to the limitation of other di-substituted complexes in aqueous solubility and the relatively weak dark stability, they exhibited low dark IC₅₀ values to cancer cells. On the other hand, all di-substituted complexes showed significantly enhanced photocytotoxicity with blue light irradiation. Notably, similar to the parent complex **1**, these Pt(IV) complexes were relatively non-toxic to normal MRC-5 lung cells.

The Pt accumulation in A549 cells of complex **9** is *ca.* 30× higher than **1**, which is consistent with its higher photocytotoxicity. The higher lipophilicity of **9**, as seen from the long HPLC retention time (17.1 min), is regarded as an important reason for its high cellular accumulation.

The mono-substituted **11** exhibits lower Pt accumulation (0.4 ng/10⁶ cells) than **1** (1.2 ng/10⁶ cells) after 1 h incubation, while the accumulation of di-substituted **15** (19.1 ng/10⁶ cells) is 16× higher than that of **1** and 47× higher than **11**. These results suggest that the conjugation with biotin alone did not increase the accumulation of diazido Pt(IV) complexes in A2780, while the substitution of the second axial ligand with DCA resulted in a significant increase in platinum cellular accumulation, perhaps due to the improved lipophilicity as seen from its longer HPLC retention time. The amount of platinum taken up by A2780 cells incubated with **1**, **11** and **15** was directly proportional to their photocytotoxicity. These results suggest that cellular accumulation of Pt(IV) prodrugs plays an important role in their antiproliferative activity. Complexes **11** and **15** with biotin can bind to avidin with high affinity, which allows avidin to act as nano-carrier to delivery biotinylated complexes. The avidin-**11** complex exhibited improved photocytotoxicity, and the effect of avidin on the uptake of **11** was also investigated. The accumulation of platinum after exposure of A2780 to the mixture of **11** and avidin (4: 1) is 10× higher than **11** alone, which correlates with the higher photocytotoxicity of **11**-avidin complex. For other complexes in this Chapter, the cellular accumulation follows the trend: di-substituted complexes > mono-substituted complexes > **1**, which resulted from their relative lipophilicity and contributed to their cytotoxicity.

A2780 cells treated with **11** and 1 h irradiation displayed fragmented nuclei and damaged membranes. Since DNA is usually regarded as the major target of platinum anticancer drugs, the ability of **11** to fragment the cell nuclei exclusively upon irradiation, is indicative of the potential of this complex as a photoactive prodrug with a novel mechanism of action.

4.5. Conclusion

In this Chapter, mono-substituted diazido Pt(IV) complexes **9–12** and their di-substituted analogues **13–16** were synthesised and characterised by NMR, ESI-MS, UV-vis spectroscopy, and X-ray crystallography. The purities of complexes were confirmed by HPLC. Di-substituted complexes displayed longer HPLC retention times and therefore lower aqueous solubility and higher lipophilicity. The reduction potential of Pt^{IV}/Pt^{II} followed the trend: di-substituted complexes > mono-substituted complexes > parent complex **1**. Mono-substituted diazido Pt(IV) complexes **9–12** and di-substituted complex **15** displayed satisfactory dark stability in RPMI-1640, while other di-substituted complexes with lower aqueous solubility were stable in DMSO. The photodecomposition of complexes **9–12** and **15, 16** in aqueous solution upon irradiation with indigo light (420 nm) was similar to that of **1**, and di-substituted complexes **13, 14**, and **16** can decompose at a faster rate in DMSO under same irradiation condition. Pt(II) species, 3-coumarin-carboxylic acid, and azidyl and hydroxyl radicals were detected as the photoproducts of **9**. Diazido Pt(IV) complexes form Pt-GMP adducts only after irradiation.

Mono-substituted diazido Pt(IV) complexes **9–12** and di-substituted complex **15** exhibited good dark stability with IC₅₀ values > 50 µM, and enhanced photocytotoxicity than **1**. The dark IC₅₀ values of other di-substituted complexes are relatively lower, but they also displayed much higher photocytotoxicity compared with their mono-substituted analogues. Complex **11** has high affinity to avidin, and the avidin-**11** complex displayed a photocytotoxicity higher than that of **11** alone.

Complex **9** displayed a *ca.* 30× Pt accumulation in A549 cells than **1** in the dark under the same condition. The di-substituted complexes exhibited much cellular Pt accumulation in A2780 and A549, compared with mono-substituted complexes and unsubstituted **1**. When A2780 cells were incubated with avidin-**11** complex, cellular accumulation was enhanced significantly.

Dramatic morphological changes in A2780 cells were observed after irradiation with **11**, consistent with the photocytotoxicity caused by azidyl radicals and Pt(II) species.

In summary, promising di-substituted diazido Pt(IV) complexes and their mono-substituted analogues are reported in this Chapter. They exhibited high photo-selectivity and cellular accumulation, and the ability to fragment cell nuclei on irradiation, which provide a novel design concept for multi-action photoactive Pt(IV) complexes with diverse functional axial ligands.

4.6. References

1. C. M. Giandomenico, M. J. Abrams, B. A. Murrer, J. F. Vollano, M. I. Rheinheimer, S. B. Wyer, G. E. Bossard, J. D. Higgins, *Inorg. Chem.*, 1995, **34**, 1015–1021.
2. T. C. Johnstone, K. Suntharalingam, S. J. Lippard, *Chem. Rev.*, 2016, **116**, 3436–3486.
3. D. Gibson, *J. Inorg. Biochem.*, 2019, **191**, 77–84.
4. X. Li, Y. Liu, H. Tian, *Bioinorg. Chem. Appl.*, 2018: 8276139.
5. Z. Wang, Z. Deng, G. Zhu, *Dalton Trans.*, 2019, **48**, 2536–2544.
6. K. M. Deo, D. L. Ang, B. McGhie, A. Rajamanickam, A. Dhiman, A. Khoury, J. Holland, A. Bjelosevic, B. Pages, C. Gordon, J. R. Aldrich-Wright, *Coord. Chem. Rev.*, 2018, **375**, 148–163.
7. N. A. Kratochwil, P. J. Bednarski, *Arch. Pharm. Pharm. Med. Chem.*, 1999, **332**, 279–285.
8. L. T. Ellis, H. Meng Er, T. W. Hambley, *Aust. J. Chem.*, 1995, **48**, 793–806.
9. M. D. Hall, T. W. Hambley, *Coord. Chem. Rev.*, 2002, **232**, 49–267.
10. A. Thakur, R. Singla, V. Jaitak, *Eur. J. Med. Chem.*, 2015, **101**, 476–495.
11. O. M. Hafez, M. I. Nassar, S. M. El-Kousy, A. F. Abdel-Razik, M. M. Sherien, M. M.

- El-Ghonemy, *Acta Pol. Pharm.*, 2014, **71**, 594–601.
12. M. H. Lina, C. H. Cheng, K. C. Chen, W. T. Lee, Y. F. Wang, C. Q. Xiao, C. W. Lin, *Chem.-Biol. Interact.*, 2014, **218**, 42–49.
 13. L. Long, Y. Wu, L. Wang, A. Gong, F. Hu, C. Zhang, *Chem. Commun.*, 2015, **51**, 10435–10438.
 14. S. Maiti, N. Park, J. H. Han, H. M. Jeon, J. H. Lee, S. Bhuniya, C. Kang, J. S. Kim, *J. Am. Chem. Soc.*, 2013, **135**, 4567–4572.
 15. R. Ye, C. Tan, L. Ji, Z. Mao, *Dalton Trans.*, 2016, **45**, 13042–13051.
 16. R. Nomula, X. Wu, J. Zhao, N. R. Munirathnam, *Mater. Sci. Eng. C*, 2017, **79**, 710–719.
 17. D. S. Tyson, F. N. Castellano, *Inorg. Chem.*, 1999, **38**, 4382–4383.
 18. M. G. Vander Heiden, L. C. Cantley, C. B. Thompson, *Science*, 2009, **324**, 1029–1033.
 19. G. S. Kaiser, S. M. Germann, T. Westergaard, M. Lisby, *Mutat. Res.*, 2011, **713**, 64–75.
 20. R. Raveendran, J. P. Braude, E. Wexselblatt, V. Novohradsky, O. Stuchlikova, V. Brabec, V. Gandin, D. Gibson, *Chem. Sci.*, 2016, **7**, 2381–2391.
 21. E. Petruzzella, J. P. Braude, J. R. Aldrich-Wright, V. Gandin, D. Gibson, *Angew. Chem. Int. Ed.*, 2017, **56**, 11539–11544.
 22. S. Dhar, S. J. Lippard, *Proc. Natl. Acad. Sci. U. S. A.*, 2009, **106**, 22199–22204.
 23. W. X. Ren, J. Han, S. Uhm, Y. J. Jang, C. Kang, J. H. Kim, J. S. Kim, *Chem. Commun.*, 2015, **51**, 10403–10418.
 24. J. Zempleni, D. M. Mock, *Am. J. Physiol.*, 1998, **275**, C382–C388.
 25. H. M. Said, *J. Nutr.*, 1999, **129**, 490S–493S.
 26. J. F. Shi, P. Wu, Z. H. Jiang, X. Y. Wei, *Eur. J. Med. Chem.*, 2014, **71**, 219–228.
 27. P. D. Prasad, H. Wang, W. Huang, Y. J. Fei, F. H. Leibach, L. D. Devoe, V. Ganapathy, *Arch. Biochem. Biophys.*, 1999, **366**, 95–106.
 28. S. Luo, V. S. Kansara, X. Zhu, D. Pal, A. K. Mitra, *Mol. Pharm.*, 2006, **3**, 329–339.

29. H. Wang, W. Huang, W. Fei, H. Xia, T. L. Y. Feng, F. H. Leibac, L. D. Devoe, V. Ganapathy, P. D. Prasad, *J. Biol. Chem.*, 1999, **274**, 14875–14883.
30. N. M. Green, *Adv. Protein Chem.*, 1975, **29**, 85–133.
31. H. P. Lesch, M. U. Kaikkonen, J. T. Pikkarainen, S. Ylä-Herttuala, *Expert Opin. Drug Deliv.*, 2010, **7**, 551–564.
32. X. Zeng, Y. Sun, X. Zhang, R. Zhuo, *Org. Biomol. Chem.*, 2009, **7**, 4201–4210.
33. A. Jain, K. Cheng, *J. Control. Release*, 2017, **245**, 27–40.
34. S. C. Park, Y. M. Kim, N. H. Kim, E. J. Kim, Y. H. Park, J. R. Lee, M. K. Jang, *Macromol. Res.*, 2017, **25**, 882–889.
35. L. Chen, B. Schechter, R. Arnon, M. Wilchek, *Drug Dev. Res.*, 2000, **50**, 258–271.
36. N. Muhammad, N. Sadia, C. Zhu, C. Luo, Z. Guo, X. Wang, *Chem. Commun.*, 2017, **53**, 9971–9974.
37. K. Mitra, A. Shettar, P. Kondaiah, A. R. Chakravarty, *Inorg. Chem.*, 2016, **55**, 5612–5622.
38. A. Gandioso, E. Shaili, A. Massaguer, G. Artigas, A. González-Cantó, J. A. Woods, P. J. Sadler, V. Marchán, *Chem. Commun.*, 2015, **51**, 9169–9172.
39. E. Shaili, M. Fernández-Giménez, S. Rodríguez-Astor, A. Gandioso, L. Sandín, C. García-Vélez, A. Massaguer, G. J. Clarkson, J. A. Woods, P. J. Sadler, V. Marchán, *Chem. Eur. J.*, 2015, **21**, 18474–18486.
40. V. Venkatesh, C. J. Wedge, I. Romero-Canelón, A. Habtemariam, P. J. Sadler, *Dalton Trans.*, 2016, **45**, 13034–13037.
41. N. M. Green, *Biochem. J.*, 1965, **94**, 23c–24c.
42. N. M. Green, *Methods Enzymol.*, 1970, **18**, 418–424.

Chapter 5

Photoactive Pt(IV)

**Complexes with Fluorescent
and Photo-switchable Tags**

5.1. Introduction

Fluorescence imaging provides a promising strategy to probe dynamic processes within live cells.¹⁻³ Fluorescent organic dyes have been widely used in cellular imaging to indicate the location of cellular components, monitor the level of important biomolecules (e.g. ROS, GSH, NADH) and the state of cells (e.g. apoptosis).¹ Conjugates of anticancer drugs and fluorescent tags are potential theranostic (i.e. combining therapy and diagnostics) systems in which the localisation and activation of drugs can be monitored by fluorescence.⁴⁻⁶

Different from photosensitive ruthenium and iridium complexes used in PDT,⁷⁻⁹ photoactive Pt(IV) complexes are non-fluorescent and need to be conjugated to fluorescent tags for cellular imaging. Due to fluorescence resonance energy transfer (FRET) and the heavy metal effect, the fluorescence of the tags is quenched when they are attached to platinum.^{10,11} However, the fluorescence can be restored when the tags are released from the complexes.¹² A nano-system with photoactive Pt(IV) complexes and a FRET pair (a far-red fluorescence donor Cy5 and a NIR quencher Qsy21) linked by apoptosis sensitive peptide exhibited fluorescence when the peptide was cleaved by apoptosis induced by platinum complexes upon irradiation has been reported.^{13,14} Fluorescent tags can also be used as photosensitisers that transfer energy from light to generate ROS in PDT, therefore enable the conjugates to be dual-action drugs and improve the photocytotoxicity.¹⁵

Fluorescein, BODIPY, porphyrin, coumarin, dansyl, and 1,8-naphthalimides are often attached to platinum complexes as fluorescent tags.^{12,16-25} They exhibit promising photophysical properties, including high quantum yield and long excitation wavelengths, and thus are potent candidates as fluorescent cellular probes. Pt(IV) complexes with two fluorescein ligands have displayed a 5-fold increase in fluorescence in the presence of GSH due to the reduction of Pt(IV) and release of fluorescein.¹² The released fluorescein can accumulate in lysosomes. A glucose-

appended Pt(II)-BODIPY conjugate is reported to generate singlet oxygen and exhibited remarkable photocytotoxicity upon red light (600–720 nm) irradiation with mitochondrial localisation.¹⁶ A series of porphyrin-Pt(II) conjugates have been developed as a novel type of photosensitisers that are photocytotoxic with red light (600–730 nm).^{17,18} Even though the non-substituted coumarin shows very weak fluorescence, its derivatives, especially those with electron-donating substituents, are important fluorescence probes.^{19,20} Pt(II) complexes with aniline containing coumarin 120 as a non-leaving ligand showed high DNA binding affinity and moderate cytotoxicity.²¹ When it was oxidised to Pt(IV), a 7-fold decrease in fluorescence was detected. Dansyl-bearing Pt(IV) complex [Pt(edDs)Cl₂] showed a 6.3-fold emission increase upon addition of reducing agents, therefore has the potential to monitor the reduction of Pt(IV) complex within cells.²² Pt(II) complex [Pt(Ds-dpm)Cl₂] (dpm = di-2-pyridylmethane) with dansyl motif can undergo photodecomposition and form a new Pt(II) species.²³ *Trans*-Pt(BODIPY)(4-ethynyl-1,8-naphthalimide)(PR₃)₂ (R = Et or Ph) contains two dyes connected to Pt(II) *via* a direct σ bond and exhibits high quantum yield.²⁴ Fast and efficient energy transfer from naphthalimide to BODIPY demonstrated an antenna effect. Pt(II) bisacetylide complex with two naphthalenediimide (NDI) displayed intense absorption centred at 581 nm and near-IR emission at 784 nm.²⁵

Azo ligands are photo-switchable, which is ascribed as a reason for their non-fluorescence.^{26,27} The flat *trans* azobenzene is thermodynamically more stable than its bent *cis* isomer.²⁸ Vorinostat (SAHA) analogues with azobenzene in cap moieties or linkers exhibit enhanced HDAC inhibition and therefore higher cytotoxicity in their *cis* form.²⁸ The photo-isomerisation of the N=N bond remains when the azo ligands are attached to platinum without using the N=N bond.²⁹ The metal-bound azo group in complex 2-(phenylazo)pyridine Pt(II) catecholates can be reduced by GSH, which results in the release of catecholates and active bifunctional Pt(II)

species.³⁰ Its anthracenyl analogue can form azo bound platinum–GSH adducts with excess GSH.³¹

Despite of the notable progress in the development of platinum complexes with fluorescent and photo-switchable azo tags, the conjugation between photoactive diazido Pt(IV) complexes and fluorescent or photo-switchable azo tags is less explored.¹³⁻¹⁵ In this Chapter, diazido Pt(IV) complexes with coumarin, dansyl, 1,8-naphthalimide and azo ligands have been prepared (Figure 5.1). Their dark stability and photoactivation with visible light, photoreactions with NADH and 5'-GMP, photocytotoxicity and cellular accumulation were investigated.

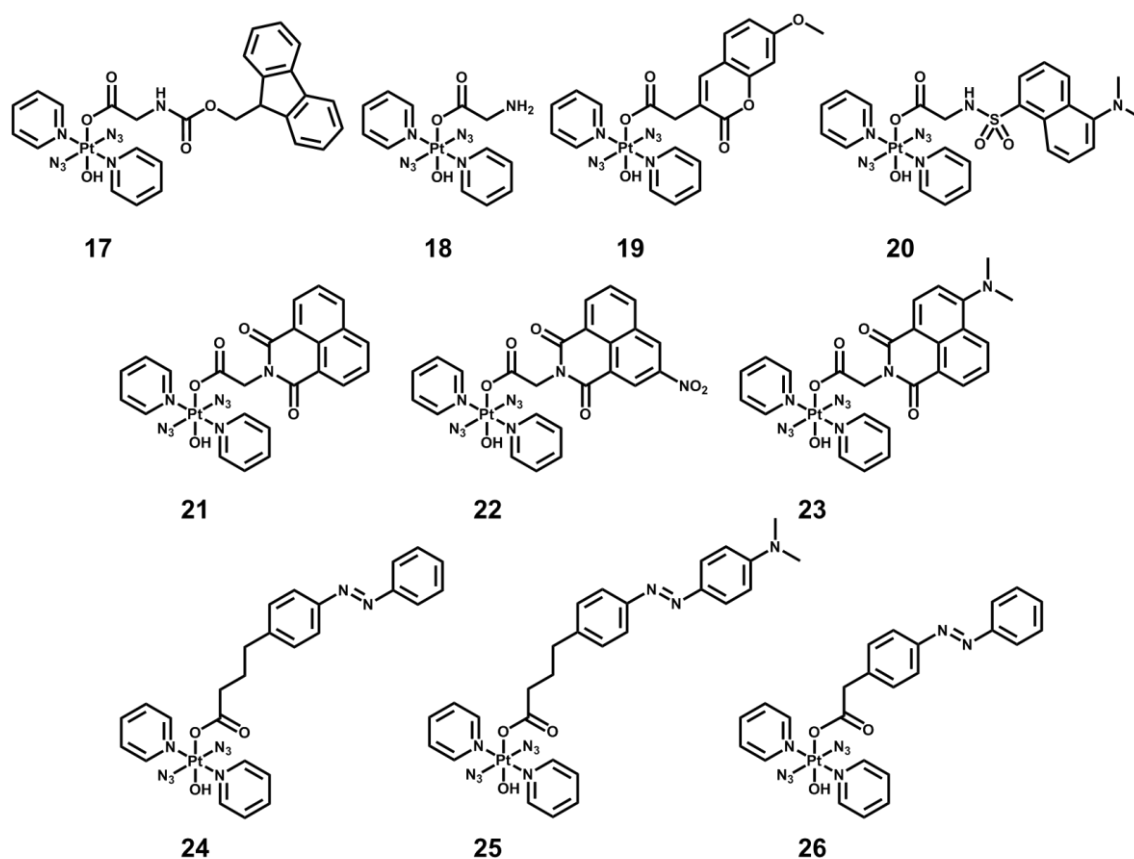


Figure 5.1. Synthesis precursors **17** and **18**, diazido Pt(IV) complexes with fluorescence tags **19–23** and those with azo dyes **24–26**.

5.2. Experimental

Caution! The synthesis and handling of heavy metal azides should be carried out in the dark with minimal light exposure with attention and appropriate precautions since they can be shock-sensitive detonators, even though we did not encounter any problems during the work reported here.

5.2.1. Materials

Dansyl chloride, naphthalic anhydride, 3-nitro-1,8-naphthalic anhydride, nitrosobenzene, 4-(4-aminophenyl)butyric acid, 4-aminophenylacetic acid, 7-methoxycoumarin-4-acetic acid and Human Serum Albumin (HSA) were purchased from Sigma-Aldrich, *o*-(benzotriazol-1-yl)-*N,N,N',N'*-tetramethyluronium tetrafluoroborate (TBTU) was purchased from Merck. ***Trans,trans,trans*-[Pt(py)₂(N₃)₂(OH)₂] (1)** was prepared according to the method described in Chapter 2. 4-Dimethylamino-1,8-naphthalic anhydride, (*E*)-4-(4-(phenyldiazenyl)phenyl)butanoic acid, (*E*)-4-(4-((4-(dimethylamino)phenyl)diazenyl)phenyl)butanoic acid and (*E*)-2-(4-(phenyldiazenyl)phenyl)acetic acid were synthesised according to the reported method.^{32,33} All solvents for common use were analytical reagent grade from Fisher Scientific and used as supplied.

5.2.2. Synthesis and characterisation

***Trans,trans,trans*-[Pt(py)₂(N₃)₂(OH)(gly)] (18)**. To the solution of complex **1** (50.0 mg, 106 μmol), Fmoc-gly-OH (31.6 mg, 106 μmol), and TBTU (34.2 mg, 106 μmol) in DMF solution (3 mL), DIPEA (100 μL) was added. The reaction mixture was stirred overnight at 298 K under

a nitrogen atmosphere. After evaporation to dryness, the oily residue was collected and purified by column chromatography on silica gel (2% methanol + 98% DCM) to get *trans,trans,trans*-[Pt(py)₂(N₃)₂(OH)(gly-Fmoc)] (**17**, ESI-MS: [M + Na]⁺ (*m/z*) Calc., 773.2; Found, 773.3.). The yellow solid was re-dissolved in piperidine/DMF (20:80) and stirred overnight at 298 K under a nitrogen atmosphere. After evaporation to dryness, the oily residue was dissolved in a small amount of DCM and a precipitate was formed immediately upon addition of excess diethyl ether. The solid was collected and used directly without purification in the next step of the synthesis. ¹H NMR (CDCl₃, 400 MHz): 8.92 (d, J = 6.2 Hz, J¹⁹⁵Pt-¹H = 26.8 Hz, 4H, H_α py), 8.26 (t, J = 7.5 Hz, 2H, H_γ py), 7.79 (t, J = 6.4 Hz, 4H, H_β py), 3.74 (s, 2H, CH₂), 3.36 (s, 1H, OH), 3.32 (s, 2H, NH₂). ESI-MS: [M + H]⁺ (*m/z*) Calc., 529.1; Found, 529.3.

Trans,trans,trans-[Pt(py)₂(N₃)₂(cou-OMe)(OH)] (**19**). To the solution of complex **1** (40.0 mg, 85 μmol), 7-methoxycoumarin-3-carboxylic acid (18.7 mg, 85 μmol), and TBTU (27.3 mg, 85 μmol) in DMF solution (2 mL), DIPEA (100 μL) was added. The reaction mixture was stirred overnight at 298 K under a nitrogen atmosphere. After evaporation to dryness, the oily residue was collected and purified by column chromatography on silica gel (3% methanol + 97% DCM). ¹H NMR (CDCl₃, 400 MHz): 8.71 (d, J = 6.0 Hz, J¹⁹⁵Pt-¹H = 26.9 Hz, 4H, H_α py), 8.03 (t, J = 7.5 Hz, 2H, H_γ py), 7.55 (d, J = 9.6 Hz, 1H, CH_{coumarin}), 7.52 (t, J = 6.1 Hz, 4H, H_β py), 6.80 (s, 1H, CH_{coumarin}), 6.75 (d, J = 8.9 Hz, 1H, CH_{coumarin}), 6.18 (s, 1H, CH_{coumarin}), 3.86 (s, 3H, CH₃), 3.74 (s, 2H, CH₂), 3.68 (s, 1H, OH). ¹³C NMR (CDCl₃, 100 MHz): 162.73 (COO), 161.34 (COO), 155.47 (=C-), 150.72 (=C-), 149.18 (C_α py), 141.46 (C_γ py), 126.56 (CH), 126.47 (CH), 125.99 (C_β py), 113.19 (CH), 112.21 (CH), 55.82 (CH₃), 43.31 (CH₂). ESI-MS: [M + Na]⁺ (*m/z*) Calc., 710.1; Found, 710.2. ε_{306 nm} = 27184 M⁻¹ cm⁻¹, ε_{260 nm} = 15493 M⁻¹ cm⁻¹, ε_{253 nm} = 15339 M⁻¹ cm⁻¹ (5% DMSO + 95% RPMI-1640).

***Trans,trans,trans*-[Pt(py)₂(N₃)₂(OH)(gly-Dan)]** (20). ***Trans,trans,trans*-[Pt(py)₂(N₃)₂(OH)(gly)]** (18, 40.0 mg, 76 μmol) and dansyl chloride (24.5 mg, 91 μmol) were suspended in DCM (3 mL) and DIPEA (100 μL) was added. The reaction mixture was stirred overnight at 298 K under a nitrogen atmosphere. After evaporation to dryness, the oily residue was collected and purified by column chromatography on silica gel (4% methanol + 96% DCM). ¹H NMR (CDCl₃, 400 MHz): 8.81 (d, J = 5.4 Hz, J¹⁹⁵Pt-¹H = 27.1 Hz, 4H, H_α py), 8.53 (d, J = 8.5 Hz, 1H, H_{phenyl}), 8.27 (d, J = 8.7 Hz, 1H, H_{phenyl}), 8.21 (d, J = 7.3 Hz, 1H, H_{phenyl}), 8.03 (t, J = 7.6 Hz, 2H, H_γ py), 7.58 (t, J = 7.2 Hz, 4H, H_β py), 7.50 (q, J = 8.8 Hz, 2H, H_{phenyl}), 7.17 (d, J = 7.4 Hz, 1H, H_{phenyl}), 3.74 (d, J = 5.0 Hz, 2H, CH₂), 3.46 (s, 1H, OH), 2.88 (s, 6H, CH₃). ¹³C NMR (CDCl₃, 100 MHz): 171.99 (COO), 151.82 (C_{phenyl}), 149.42 (C_α py), 141.41 (C_γ py), 134.61 (C_{phenyl}), 130.42 (CH_{phenyl}), 129.91 (C_{phenyl}), 129.71 (C_{phenyl}), 129.45 (CH_{phenyl}), 128.37 (CH_{phenyl}), 126.13 (C_β py), 123.19 (CH_{phenyl}), 119.22 (CH_{phenyl}), 115.20 (CH_{phenyl}), 45.86 (CH₂), 45.45 (CH₃). ESI-MS: [M + Na]⁺ (m/z) Calc., 784.2; Found, 784.3.

***Trans,trans,trans*-[Pt(py)₂(N₃)₂(OH)(gly-NA)]** (21). ***Trans,trans,trans*-[Pt(py)₂(N₃)₂(OH)(gly)]** (18, 20.0 mg, 38 μmol) and 1,8-naphthalic anhydride (7.5 mg, 38 μmol) were suspended in DMF and the reaction mixture was stirred overnight at 353 K under a nitrogen atmosphere. After evaporation to dryness, the oily residue was collected and purified by column chromatography on silica gel (4% methanol + 96% DCM). ¹H NMR (DMSO-*d*₆, 400 MHz): 8.75 (d, J = 6.0 Hz, J¹⁹⁵Pt-¹H = 25.8 Hz, 4H, H_α py), 8.54 (d, J = 7.1 Hz, 2H, H_{na}), 8.47 (d, J = 8.1 Hz, 2H, H_{na}), 8.24 (t, J = 7.0 Hz, 2H, H_γ py), 7.88 (d, J = 7.7 Hz, 2H, H_{na}), 7.76 (t, J = 6.9 Hz, 4H, H_β py), 4.74 (s, 2H, CH₂), 3.40 (s, 1H, OH). ¹³C NMR (DMSO-*d*₆, 100 MHz): 169.69 (COO), 163.69 (C(O)NC(O)), 149.63 (C_α py), 142.51 (C_γ py), 135.00 (C_{na}), 131.80 (C_{na}), 131.35 (C_{na}), 127.85 (C_{na}), 127.68 (C_{na}), 126.62 (C_β py), 122.31 (C_{na}), 43.46 (CH₂). ESI-MS: [M + Na]⁺ (m/z) Calc., 731.1; Found, 731.2.

***Trans,trans,trans*-[Pt(py)₂(N₃)₂(OH)(gly-NANO₂)]** (22). ***Trans,trans,trans*-**

[Pt(py)₂(N₃)₂(OH)(gly)] (18, 40.0 mg, 76 μmol) and 3-nitro-1,8-naphthalic anhydride (21 mg, 76 μmol) were suspended in ethanol and the reaction mixture was stirred overnight at 353 K under a nitrogen atmosphere. After evaporation to dryness, the oily residue was collected and purified by column chromatography on silica gel (5% methanol + 95% DCM). ¹H NMR (DMSO-*d*₆, 400 MHz): 9.52 (s, 1H, *H_{na}*), 8.99 (s, 1H, *H_{na}*), 8.82-8.72 (m, 6H, *H_{na}* and *H_α* *py*), 8.26 (t, *J* = 7.4 Hz, 2H, *H_γ* *py*), 8.08 (t, *J* = 8.0 Hz, 1H, *H_{na}*), 7.80 (t, *J* = 5.9 Hz, 4H, *H_β* *py*), 4.75 (s, 2H, *CH*₂), 4.0 (s, 1H, *OH*). ¹³C NMR (DMSO-*d*₆, 100 MHz): 170.32 (*COO*), 163.02 (*C(O)NC(O)*), 162.51 (*C(O)NC(O)*), 149.64 (*C_α* *py*), 146.43 (*C_{na}*), 142.62 (*C_γ* *py*), 137.14 (*C_{na}*), 134.66 (*C_{na}*), 131.40 (*C_{na}*), 130.54 (*C_{na}*), 129.95 (*C_{na}*), 129.79 (*C_{na}*), 126.75 (*C_β* *py*), 124.10 (*C_{na}*), 123.64 (*C_{na}*), 122.72 (*C_{na}*), 43.74 (*CH*₂). ESI-MS: [M + Na]⁺ (*m/z*) Calc., 776.1; Found, 776.2.

***Trans,trans,trans*-[Pt(py)₂(N₃)₂(OH)(gly-NADM)]** (23). ***Trans,trans,trans*-**

[Pt(py)₂(N₃)₂(OH)(gly)] (18, 33.0 mg, 63 μmol) and 4-dimethylamino-1,8-naphthalic anhydride (16.7 mg, 69 μmol) were suspended in ethanol and the reaction mixture was stirred overnight at 353 K under a nitrogen atmosphere. After evaporation to dryness, the oily residue was collected and purified by column chromatography on silica gel (3% methanol + 97% DCM). ¹H NMR (CDCl₃, 400 MHz): 8.91 (d, *J* = 5.9 Hz, *J*¹⁹⁵Pt-¹H = 26.5 Hz, 4H, *H_α* *py*), 8.55 (d, *J* = 7.2 Hz, 1H, *H_{na}*), 8.46 (d, *J* = 8.2 Hz, 1H, *H_{na}*), 8.42 (d, *J* = 8.5 Hz, 1H, *H_{na}*), 8.01 (t, *J* = 7.6 Hz, 2H, *H_γ* *py*), 7.64 (t, *J* = 7.6 Hz, 1H, *H_{na}*), 7.59 (t, *J* = 6.8 Hz, 4H, *H_β* *py*), 7.10 (d, *J* = 8.2 Hz, 1H, *H_{na}*), 4.95 (s, 2H, *CH*₂), 3.48 (s, 1H, *OH*), 3.10 (s, 6H, *N(CH*₃)₂). ¹³C NMR (CDCl₃, 125 MHz): 171.68 (*COO*), 164.47 (*C(O)NC(O)*), 163.87 (*C(O)NC(O)*), 157.0 (*C_{na}*), 149.70 (*C_α* *py*), 141.09 (*C_γ* *py*), 132.59 (*C_{na}*), 131.22 (*C_{na}*), 130.96 (*C_{na}*), 130.50 (*C_{na}*),

125.97 (C_{β} py), 125.35 (C_{na}), 124.78 (C_{na}), 123.19 (C_{na}), 115.13 (C_{na}), 113.24 (C_{na}), 44.80 (CH_3), 43.30 (CH_2). ESI-MS: $[M + Na]^+$ (m/z) Calc., 774.3; Found, 774.1.

***Trans,trans,trans*-[Pt(py)₂(N₃)₂(OH)(b-azo)] (24).** To the solution of complex **1** (30.0 mg, 64 μ mol), (*E*)-4-(4-(phenyldiazenyl)phenyl)butanoic acid (18.8 mg, 70 μ mol), and TBTU (20.5 mg, 64 μ mol) in DMF solution (2 mL), DIPEA (100 μ L) was added. The reaction mixture was stirred overnight at 298 K under a nitrogen atmosphere. After evaporation to dryness, the oily residue was collected and purified by column chromatography on silica gel (3% methanol + 97% DCM). ¹H NMR (CDCl₃, 400 MHz): 8.94 (d, $J = 5.5$ Hz, $J^{195}\text{Pt}-^1\text{H} = 26.5$ Hz, 4H, H_{α} py), 8.05 (t, $J = 7.6$ Hz, 2H, H_{γ} py), 7.90 (d, $J = 7.4$ Hz, 2H, H_{phenyl}), 7.81 (d, $J = 8.3$ Hz, 2H, H_{phenyl}), 7.61 (t, $J = 7.0$ Hz, 4H, H_{β} py), 7.53-7.44 (m, 3H, H_{phenyl}), 7.28 (d, $J = 8.6$ Hz, 2H, H_{phenyl}), 2.68 (t, $J = 7.6$ Hz, 2H, CH_2), 2.46 (t, $J = 7.4$ Hz, 2H, CH_2), 1.99-1.88 (m, 2H, CH_2). ¹³C NMR (CDCl₃, 100 MHz): 177.00 (COO), 152.72 (C_{phenyl}), 151.00 (C_{phenyl}), 149.43 (C_{α} py), 145.72 (C_{phenyl}), 141.33 (C_{γ} py), 130.76 (C_{phenyl}), 129.23 (C_{phenyl}), 129.07 (C_{phenyl}), 126.09 (C_{β} py), 122.83 (C_{phenyl}), 122.70 (C_{phenyl}), 36.20 (CH_2), 35.07 (CH_2), 27.53 (CH_2). ESI-MS: $[M + Na]^+$ (m/z) Calc., 744.2; Found, 744.3. Anal. calcd for C₂₆H₂₆N₁₀O₃Pt: C 43.27, H 3.63, N 19.41; found C 43.26, H 3.58, N 19.26.

***Trans,trans,trans*-[Pt(py)₂(N₃)₂(OH)(b-azo-NMe₂)] (25).** To the solution of complex **1** (30.0 mg, 64 μ mol), (*E*)-4-(4-((4-(dimethylamino)phenyl)diazenyl)phenyl)butanoic acid (23.8 mg, 77 μ mol), and TBTU (20.5 mg, 64 μ mol) in DMF solution (2 mL), DIPEA (100 μ L) was added. The reaction mixture was stirred overnight at 298 K under a nitrogen atmosphere. After evaporation to dryness, the oily residue was collected and purified by column chromatography on silica gel (3% methanol + 97% DCM). ¹H NMR (CDCl₃, 400 MHz): 8.95 (d, $J = 5.8$ Hz,

$J^{195}\text{Pt-}^1\text{H} = 27.2$ Hz, 4H, H_α py), 8.05 (t, $J = 7.0$ Hz, 2H, H_γ py), 7.86 (d, $J = 9.0$ Hz, 2H, H_{phenyl}), 7.72 (d, $J = 8.2$ Hz, 2H, H_{phenyl}), 7.62 (t, $J = 6.7$ Hz, 4H, H_β py), 7.23 (d, $J = 8.1$ Hz, 2H, H_{phenyl}), 6.76 (d, $J = 8.1$ Hz, 2H, H_{phenyl}), 3.08 (s, 6H, CH_3), 2.67 (t, $J = 7.5$ Hz, 2H, CH_2), 2.44 (t, $J = 7.2$ Hz, 2H, CH_2), 1.97-1.91 (m, 2H, CH_2). ^{13}C NMR (CDCl_3 , 100 MHz): 177.14 (COO), 152.29 (C_{phenyl}), 151.54 (C_{phenyl}), 149.48 (C_α py), 143.80 (C_{phenyl}), 143.72 (C_{phenyl}), 141.23 (C_γ py), 129.09 (C_{phenyl}), 125.98 (C_β py), 124.78 (C_{phenyl}), 122.16 (C_{phenyl}), 40.34 ($\text{N}(\text{CH}_3)_2$), 36.21 (CH_2), 35.00 (CH_2), 27.55 (CH_2). ESI-MS: $[\text{M} + \text{Na}]^+$ (m/z) Calc., 787.7; Found, 786.4. Anal. calcd for $\text{C}_{28}\text{H}_{31}\text{N}_{11}\text{O}_3\text{Pt}$: C 43.98, H 4.09, N 20.15; found C 44.21, H 4.08, N 19.69.

***Trans,trans,trans*-[Pt(py)₂(N₃)₂(OH)(a-azo)] (26).** To the solution of complex **1** (30.0 mg, 64 μmol), (*E*)-2-(4-(phenyldiazenyl)phenyl)acetic acid (18.4 mg, 77 μmol), and TBTU (20.5 mg, 64 μmol) in DMF solution (2 mL), DIPEA (100 μL) was added. The reaction mixture was stirred overnight at 298 K under a nitrogen atmosphere. After evaporation to dryness, the oily residue was collected and purified by column chromatography on silica gel (3% methanol + 97% DCM). ^1H NMR (CDCl_3 , 400 MHz): 8.76 (d, $J = 6.0$ Hz, $J^{195}\text{Pt-}^1\text{H} = 27.4$ Hz, 4H, H_α py), 8.01-7.96 (m, 4H, H_γ py and H_{phenyl}), 7.88 (d, $J = 7.7$ Hz, 2H, H_{phenyl}), 7.59-7.47 (m, 9H, H_β py and H_{phenyl}), 1.56 (s, 2H, CH_2). ^{13}C NMR (CDCl_3 , 100 MHz): 174.68 (COO), 152.69 (C_{phenyl}), 151.36 (C_{phenyl}), 149.27 (C_α py), 141.13 (C_γ py), 140.11 (C_{phenyl}), 131.02 (C_{phenyl}), 130.55 (C_{phenyl}), 130.18 (C_{phenyl}), 129.16 (C_{phenyl}), 125.84 (C_β py), 122.84 (C_{phenyl}), 53.44 (CH_2). ESI-MS: $[\text{M} + \text{Na}]^+$ (m/z) Calc., 716.1; Found, 716.3. Anal. calcd for $\text{C}_{24}\text{H}_{22}\text{N}_{10}\text{O}_3\text{Pt}$: C 41.56, H 3.20, N 20.19; found C 41.62, H 3.16, N 19.75.

5.2.3. Methods and instrumentation

5.2.3.1. HPLC purity test

Purity tests for complexes **19–26** were carried out in the same manner as that for **4–8** described in Chapter 3.

5.2.3.2. Extinction coefficient determination

Extinction coefficients of complexes **19–26** were determined as what described in Chapter 3.

5.2.3.3. Interaction with HSA

To a solution of HSA (10 μ M, 800 μ L) in PBS, aliquots of an azo-complexes solution (1.6 mM) in DMSO were added. The fluorescence spectra were recorded at the same excitation wavelength after 1 min equilibration. The binding constant was determined by applying equation (1):³⁴

$$\log[(I_0-I)/I] = \log K + n \log [Q] \quad (1)$$

Where I_0 and I are the fluorescence intensity of HSA without and with complex, respectively; $[Q]$ is complex concentration. Plot of $\log[(I_0-I)/I]$ versus $\log [Q]$ gave the y-intercept equalling to $\log K$, and the binding constant can be obtained accordingly.

The concentration of HSA was determined by UV-vis spectroscopy using the extinction coefficient of 35700 $M^{-1} \text{ cm}^{-1}$ at 280 nm.³⁵

5.2.3.4. Photo-dark cytotoxicity testing

The antiproliferative activity of complexes **19–26** was determined in A2780 ovarian, A549 lung, and PC3 prostate carcinoma cell lines.

5.2.3.5. Cellular accumulation of platinum

The cellular accumulation of complexes **19, 21–23** in A549 lung cancer cells was determined as described in Chapter 2.

5.3. Results

5.3.1. Synthesis and characterisation

Complexes **19** and **24–26** were obtained by combining parent complex **1** with corresponding acid using TBTU as amide coupling agent (Figure 5.1). Complexes **20–23** were synthesised by coupling complex **20** with corresponding acyl chloride or anhydride (Figure 5.1). The ^1H and ^{13}C NMR spectra are supportive of the supposed structures for the complexes. In the NMR spectra, Pt coordinated pyridine can be certificated by the doublets with ^{195}Pt satellites at *ca.* 8.8 ppm, and the triplets at *ca.* 8.1 and 7.7 ppm in the ^1H NMR spectra and the resonance at *ca.* 149, 142 and 126 ppm in the ^{13}C NMR. The purities of Pt(IV) complexes **19–26** determined by HPLC chromatography were higher than 95% (Figures 5.2 and 5.3).

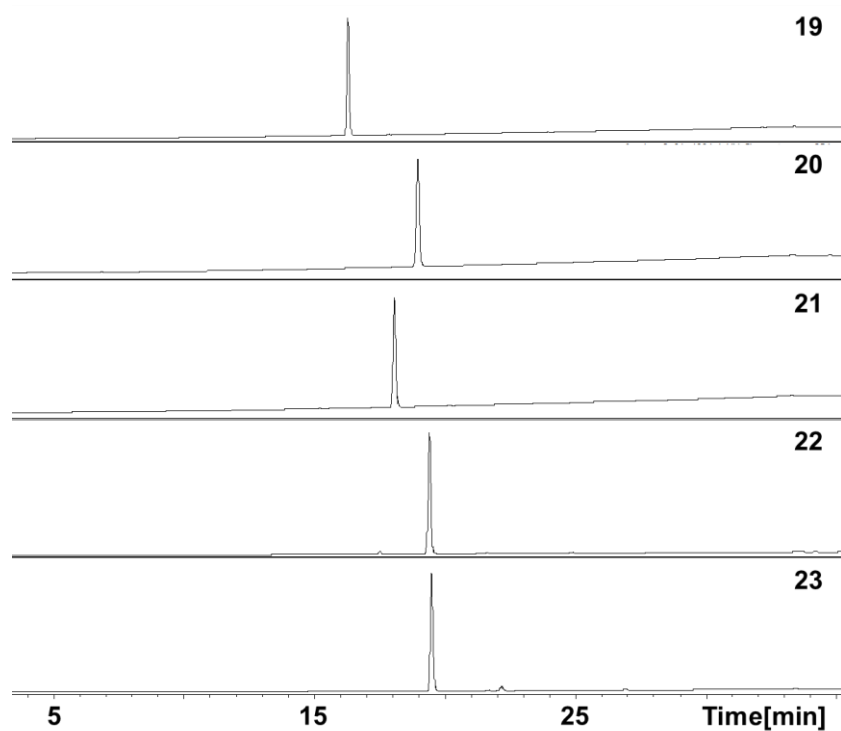


Figure 5.2. HPLC purity of Pt(IV) complexes with fluorescence tags (**19–23**), detection wavelength 254 nm.

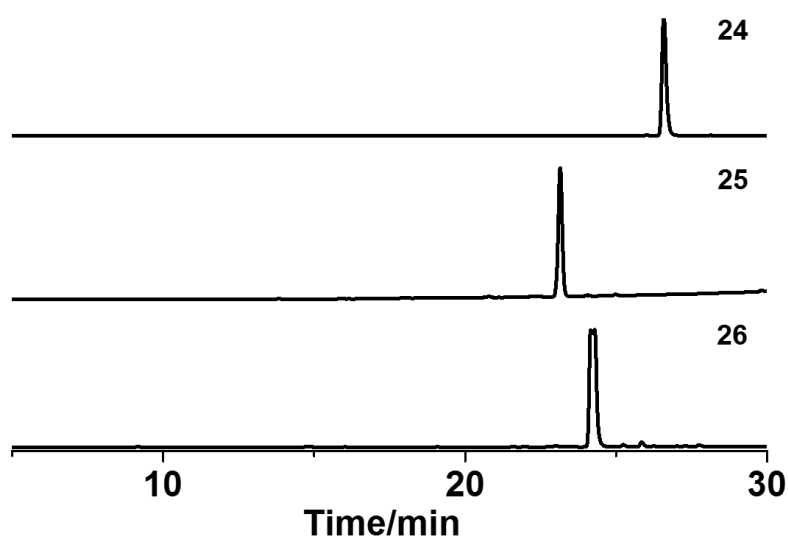


Figure 5.3. HPLC purity of Pt(IV) complexes with azo dyes (**24–26**), detection wavelength 254 nm.

5.3.2. X-ray crystallography

Crystals suitable for X-ray diffraction studies of complexes **19**, **22–24** were obtained through diffusion of diethyl ether into the corresponding solution in DCM/MeOH, while that of **21** was obtained by diffusion into its solution in DMSO and DMF. The perspective drawings of complexes **19**, **21–24** are shown in Figure 5.4. The crystallographic data are summarised in Table 5.1 and 5.3, and selected bond distances and angles are listed in Table 5.2 and 5.4. Complexes **19**, **21** and **24** crystallised in the triclinic space group P-1 with two molecules within the unit cell, complex **22** crystallised in the monoclinic space group P2₁/n with four molecules within the unit cell while complex **23** crystallised in the monoclinic space group I2/a with eight molecules within the unit cell. The platinum centres in complexes **19** and **21–24** exhibit slight distortion from ideal octahedral geometry with the O–Pt–O angle less than 180° (**19** (178.8(2)°), **21** (177.17(7)°), **22** (175.53(10)°), **23** (170.01(9)°) and **24** (178.2(2)°)).

The coumarin rings of complex **19** are antiparallel with their adjacent rings, the distance between adjacent planes is 3.189 or 3.275 Å. The hydrogen bonds formed between axial O–H and terminal N in azide ligand of adjacent molecule (O1–H1···N6) build an antiparallel double chain with the coumarin rings between them.

Table 5.1. Crystal data and structure refinement for **19** and **24**.

Complex	19	24
Empirical formula	C ₂₂ H ₂₀ N ₈ O ₆ Pt	C ₂₆ H ₂₆ N ₁₀ O ₃ Pt
Formula weight	687.55	721.66
Temperature/K	150(2)	150(2)
Crystal system	triclinic	triclinic
Space group	P-1	P-1
<i>a</i> /Å	7.6674(2)	8.45220(10)

Chapter 5: Photoactive Pt(IV) Complexes with Fluorescent and Photo-switchable Tags

$b/\text{\AA}$	10.0346(2)	9.1920(2)
$c/\text{\AA}$	15.9728(4)	18.0599(6)
$\alpha/^\circ$	81.038(2)	81.350(2)
$\beta/^\circ$	79.373(2)	89.870(2)
$\gamma/^\circ$	76.664(2)	72.125(2)
Volume/ \AA^3	1167.02(5)	1318.76(6)
Z	2	2
$\rho_{\text{calc}}/\text{g/cm}^3$	1.957	1.817
μ/mm^{-1}	6.070	5.370
$F(000)$	668.0	708.0
Crystal size/ mm^3	0.18 × 0.12 × 0.04 colorless (very faintly yellow) block	0.2 × 0.2 × 0.01 orange plate
Radiation	MoK α ($\lambda = 0.71073$)	MoK α ($\lambda = 0.71073$)
2 Θ range for data collection/ $^\circ$	6.47 to 60.34	4.906 to 60.468
Index ranges	-10 ≤ h ≤ 10, -14 ≤ k ≤ 14, -22 ≤ l ≤ 22	-11 ≤ h ≤ 11, -12 ≤ k ≤ 12, -25 ≤ l ≤ 25
Reflections collected	16157	16222
Independent reflections	16157 [$R_{\text{int}} = ?$, $R_{\text{sigma}} = 0.0457$]	16222 [$R_{\text{int}} = ?$, $R_{\text{sigma}} = 0.0659$]
Data/restraints/parameters	16157/0/336	16222/0/363
Goodness-of-fit on F^2	1.054	1.041
Final R indexes [$I \geq 2\sigma(I)$]	$R_1 = 0.0437$, $wR_2 = 0.1126$	$R_1 = 0.0434$, $wR_2 = 0.1053$
Final R indexes [all data]	$R_1 = 0.0469$, $wR_2 = 0.1136$	$R_1 = 0.0484$, $wR_2 = 0.1066$
Largest diff. peak/hole / e \AA^{-3}	2.94/-3.10	1.72/-1.61

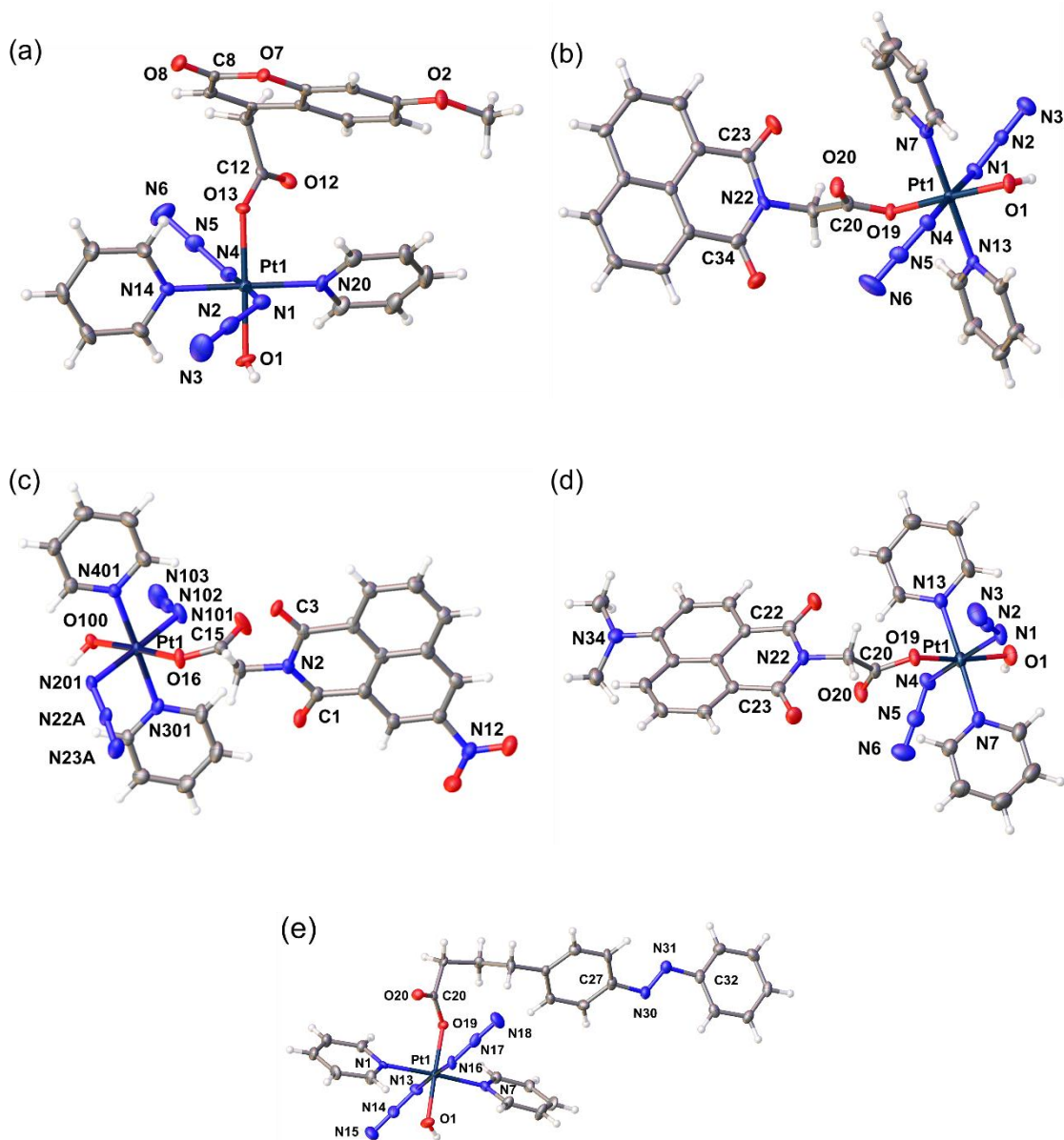


Figure 5.4. Crystal structures of (a) **19**, (b) **21**, (c) **22**, (d) **23**, and (e) **24**, with key atoms labeled and thermal ellipsoids drawn at 50% probability level.

Table 5.2. Selected bond lengths (Å) and bond angles (°) for **19** and **24**.

19		24	
Pt1–N14	2.042(6)	Pt1–N1	2.030(6)
Pt1–N20	2.026(6)	Pt1–N7	2.030(6)
Pt1–O13	2.053(5)	Pt1–N13	2.061(6)

Pt1–O1	1.973(5)	Pt1–N16	2.039(7)
Pt1–N1	2.046(6)	Pt1–O1	1.974(5)
Pt1–N4	2.052(7)	Pt1–O19	2.033(5)
N1–N2	1.211(10)	N13–N14	1.198(9)
N2–N3	1.145(11)	N17–N16	1.219(9)
N4–N5	1.210(9)	N14–N15	1.154(9)
N5–N6	1.146(10)	N17–N18	1.146(10)
O8–C8	1.209(9)	N31–N30	1.238(9)
O12–C12	1.213(9)	N30–C27	1.434(10)
O1–Pt1–O13	178.8(2)	N31–C32	1.425(10)
N1–Pt1–N4	176.6(3)	O1–Pt1–O19	178.2(2)
N20–Pt1–N14	179.0(2)	C20–O19–Pt1	123.1(4)
O13–C12–C11	112.0(7)	O19–C20–C21	114.1(6)
C12–O13–Pt1	122.7(5)	N31–N30–C27	113.2(7)
C10–C11–C12	116.2(6)	N30–N31–C32	113.7(7)

Table 5.3. Crystal data and structure refinement for **21–23**.

Complex	21	22	23
Empirical formula	C ₂₄ H ₁₉ N ₉ O ₅ Pt	C ₂₄ H ₁₈ N ₁₀ O ₇ Pt	C ₂₆ H ₂₄ N ₁₀ O ₅ Pt
Formula weight	708.57	753.57	751.64
Temperature/K	150(2)	150(2)	150(2)
Crystal system	triclinic	monoclinic	monoclinic
Space group	P-1	P2 ₁ /n	I2/a
<i>a</i> /Å	7.40510(12)	8.6649(3)	15.6369(3)
<i>b</i> /Å	8.24493(17)	22.7275(5)	7.99463(15)
<i>c</i> /Å	21.2074(4)	13.1568(4)	42.5857(7)
<i>α</i> /°	92.7868(16)	90	90
<i>β</i> /°	90.0429(14)	104.556(3)	95.8821(17)
<i>γ</i> /°	106.8637(16)	90	90
Volume/Å ³	1237.51(4)	2507.82(13)	5295.67(18)
<i>Z</i>	2	4	8

$\rho_{\text{calc}}/\text{cm}^3$	1.902	1.996	1.886
μ/mm^{-1}	5.725	5.664	5.359
F(000)	688.0	1464.0	2944.0
Crystal size/ mm^3	$0.32 \times 0.12 \times 0.06$	$0.4 \times 0.18 \times 0.1$	$0.35 \times 0.2 \times 0.06$
	light yellow block	yellow block	yellow block
Radiation	MoK α ($\lambda =$ 0.71073)	MoK α ($\lambda =$ 0.71073)	MoK α ($\lambda =$ 0.71073)
2 Θ range for data collection/ $^\circ$	5.17 to 60.054	6.646 to 59.794	5.186 to 60.814
Index ranges	$-10 \leq h \leq 10, -11 \leq$ $k \leq 11, -28 \leq l \leq 29$	$-11 \leq h \leq 11, -31 \leq$ $k \leq 31, -16 \leq l \leq 17$	$-21 \leq h \leq 19, -11 \leq$ $k \leq 10, -58 \leq l \leq 60$
Reflections collected	59521	30200	33072
Independent reflections	6820 [$R_{\text{int}} =$ 0.0512, $R_{\text{sigma}} =$ 0.0322]	6663 [$R_{\text{int}} =$ 0.0346, $R_{\text{sigma}} =$ 0.0323]	7190 [$R_{\text{int}} =$ 0.0340, $R_{\text{sigma}} =$ 0.0307]
Data/restraints/parameters	6820/84/480	6663/272/513	7190/0/382
Goodness-of-fit on F^2	1.035	1.193	1.085
Final R indexes [$I \geq 2\sigma$ (I)]	$R_1 = 0.0223, wR_2 =$ 0.0424	$R_1 = 0.0320,$ $wR_2 = 0.0550$	$R_1 = 0.0274, wR_2 =$ 0.0573
Final R indexes [all data]	$R_1 = 0.0265, wR_2 =$ 0.0439	$R_1 = 0.0384,$ $wR_2 = 0.0565$	$R_1 = 0.0389, wR_2 =$ 0.0618
Largest diff. peak/hole / e \AA^{-3}	1.20/-1.13	0.96/-0.98	1.22/-1.18

Table 5.4. Selected bond lengths (\AA) and bond angles ($^\circ$) for **21**, **22** and **23**.

	21	22	23
Pt1–N1	2.060(2)	Pt1–N201	2.055(3)
Pt1–N4	2.042(2)	Pt1–N401	2.037(3)
Pt1–N7	2.035(2)	Pt1–N101	2.051(3)
Pt1–N13	2.0372(19)	Pt1–N301	2.035(3)
Pt1–O1	1.9814(16)	Pt1–O100	1.970(2)
Pt1–O19	2.0333(16)	Pt1–O16	2.056(2)

N1–N2	1.210(3)	N101–N102	1.210(5)	N1–N2	1.201(4)
N2–N3	1.145(3)	N102–N103	1.147(5)	N2–N3	1.139(4)
N4–N5	1.219(3)	N201–N22A	1.231(8)	N4–N5	1.222(4)
N5–N6	1.145(3)	N22A–N23A	1.133(11)	N5–N6	1.133(4)
O1–Pt1–O19	177.17(7)	O100–Pt1– O16	175.53(10)	O1–Pt1–O19	170.01(9)
C20–O19–Pt1	123.32(14)	C15–O16–Pt1	131.2(2)	C20–O19–Pt1	126.29(18)
O19–C20–C21	109.8(5)	O15–C15–C14	122.1(3)	O19–C20–C21	111.3(3)
N22–C21–C20	111.1(8)	N2–C14–C15	113(2)	N22–C21–C20	111.5(2)
C23–N22–C34	126.6(13)	C3–N2–C1	123(3)	C23–N22–C22	125.2(2)

The naphthalimide ring of **21** was modelled as disordered over two positions related by a small twist about the N22–C21 bond. The occupancy was linked to a free variable which refined to 48:52. The naphthalimide rings form infinite stacks by π stacking along the *a* axis of the cell. Naphthalimide rings are antiparallel with their adjacent rings, and the distance between closest naphthalimide rings is 3.516 Å. The large planar structure of the naphthalimide ring allows it to intercalate between DNA bases. Two hydrogen bonds (O1–H1 \cdots N3) can be found between two adjacent **21** molecules (Table 5.5). The hydrogen bond formed between axial O–H and terminal N in azide ligand made these two molecules antiparallel to each other. Due to the π stacking and hydrogen bond, an infinite chain was formed with all adjacent molecules within antiparallel to each other. The substituent NMe₂ causes distortion of naphthalimide ring in complex **23**, which reduces its ability to form π stacking. No infinite stacks can be found in this crystal, but the distance between two closest naphthalimide rings is *ca.* 3.324 Å. A hydrogen bond between axial O–H and terminal N in azide ligand of adjacent molecule (O1–H1 \cdots N3) was observed in complex **23**. The complex **22** with substituent NO₂ displays no apparent π stacking in the crystal, but a hydrogen bond between the axial O–H and O in carbonyl group close to platinum in adjacent molecule (O100–H100 \cdots O15).

Table 5.5. Selected hydrogen bond parameters for **19** and **21–24**.

	D	H	A	d(D-H)/Å	d(H-A)/Å	d(D-A)/Å	D-H-A/°
19	O1	H1	N6 ¹	0.84	2.19	3.001(9)	161.9
21	O1	H1	N3 ²	0.84	2.31	3.039(3)	145.4
22	O100	H100	O15 ³	0.84	2.03	2.864(4)	170.7
23	O1	H1	N3 ⁴	0.84	2.24	3.012(4)	153.6
24	O1	H1	N15 ⁵	0.84	2.20	3.020(10)	166.8

¹-1+X,+Y,+Z; ²1-X,-Y,-Z; ³-0.5+X,0.5-Y,-0.5+Z; ⁴+X,-1+Y,+Z; ⁵-X, 2-Y, 1-Z

Two parallel hydrogen bonds between axial O–H and terminal N in azide ligand of adjacent molecule (O1–H1⋯N15) was observed in complex **24** (Table 5.5). The axial azo ligand is in its *trans* form and the dihedral angle between two phenyl rings is 48.79°. No noticeable π stacking can be found in the crystal of **24**.

5.3.3. Dark stability

The dark stability of complexes **19** and **23** was tested in RPMI-1640 cell culture medium (Figure 5.5). The negligible spectral change of **19** indicated its dark stability. The spectral change of **23** in RPMI-1640 (Figure 5.5) was ascribed to its poor aqueous solubility which causes precipitation, since it displayed stable absorption spectra in DMSO, which is similar to those of complexes **24–26** (Figure 5.6). In addition, the dark stability of complexes **20–26** were investigated by LC-MS in the presence of 2.4 mM GSH. All of these complexes exhibited good dark stability towards GSH for 2 h.

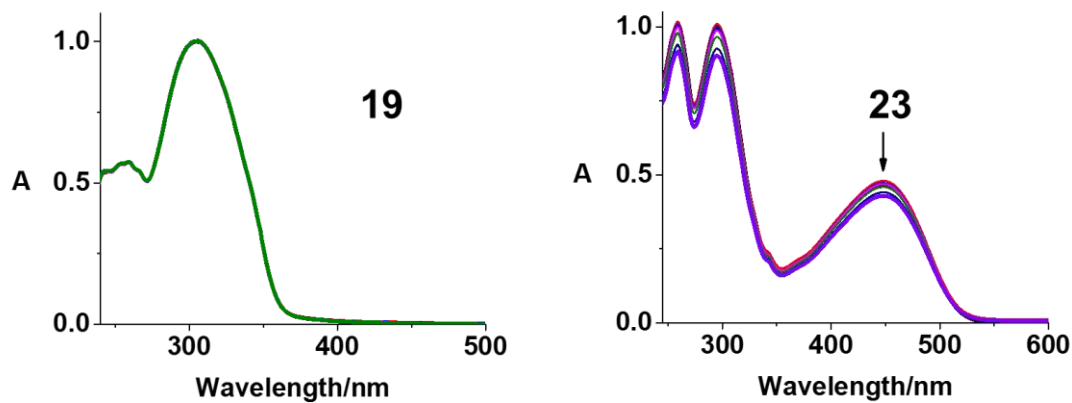


Figure 5.5. Dark stability test of **19** and **23** in phenol red-free RPMI-1640 with 5% DMSO for 2 h monitored by UV-vis spectroscopy.

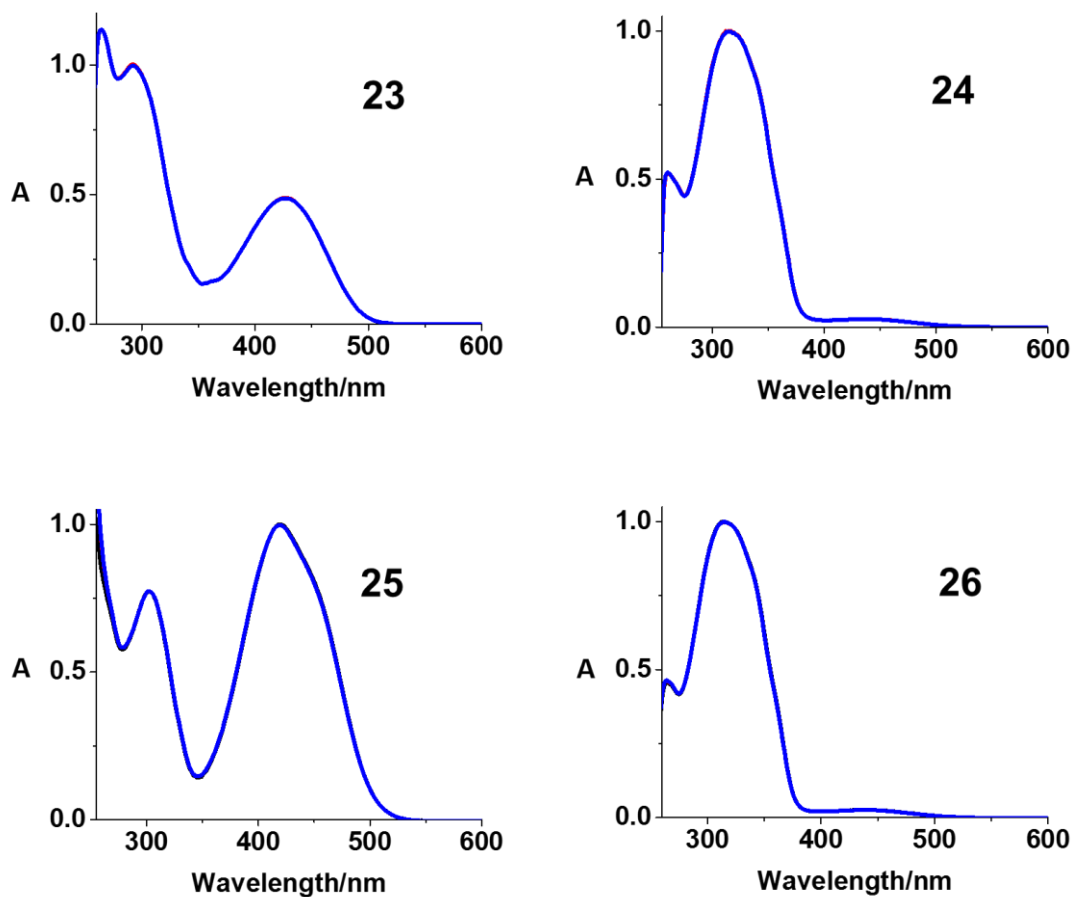


Figure 5.6. Dark stability test of **23–26** in DMSO for 2 h monitored by UV-vis spectroscopy.

5.3.4. Extinction coefficient studies

Extinction coefficients for **19** in RPMI-1640, and **21–23** in PBS were determined using UV-vis spectroscopy and calibrated by ICP-OES (Figure 5.7a). Due to the presence of different fluorescent tags, the absorption spectra of the Pt(IV) complexes were significantly affected. The UV-vis spectrum of **19** is similar to **9** (Figure 4.1), but a slight red-shift (8 nm) at the absorption maximum (*ca.* 300 nm) was observed, owing to the electron-donating OMe substituent in coumarin. The absorption of Pt(IV) complexes with naphthalimide rings was also influenced by the substituents (Figure 5.7a). Complex **23** with a strong electron-donating NMe₂ group displayed a strong absorbance at 450 nm (14095 M⁻¹ cm⁻¹), which might allow the photoactivation with longer wavelengths. Upon excitation at $\lambda = 355$ nm, complex **21** exhibited purple emission ($\lambda_{\text{max}} = 395$ nm), while complex **23** exhibited green-yellow emission ($\lambda_{\text{max}} = 550$ nm) upon excitation at $\lambda = 450$ nm in PBS (Figure 5.7b).

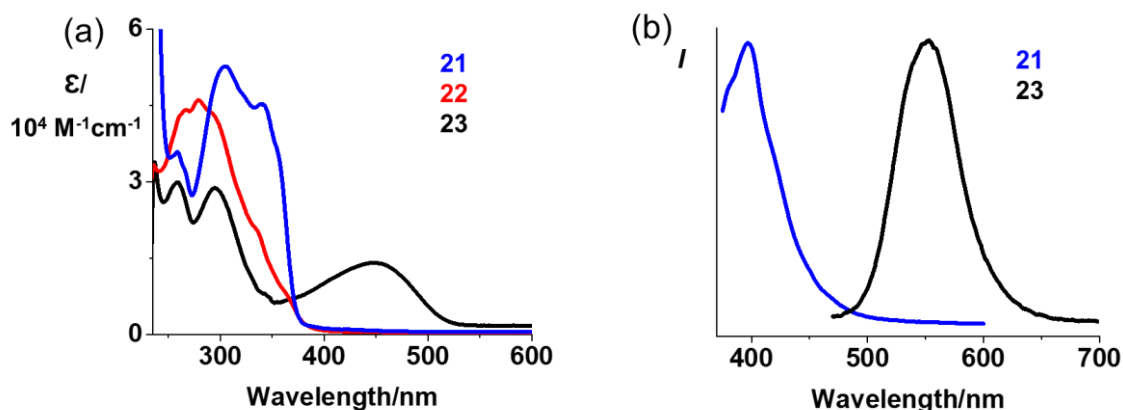


Figure 5.7. (a) UV-vis and (b) fluorescence spectra of Pt(IV) complexes **21–23** with 1,8-naphthalimide rings in PBS with 5% DMSO at 298 K.

5.3.5. Cyclic Voltammetry

An irreversible reduction wave assigned to Pt^{IV}/Pt^{II} was detected with $E_{pc} = -1.296$ V for **19** in DMF at 298 K, using 0.1 M NBu₄PF₆ as supporting electrolyte (Figure 5.8). Its analogues **9** and parent complex **1** displayed irreversible reduction waves at -1.285 and -1.699, respectively.

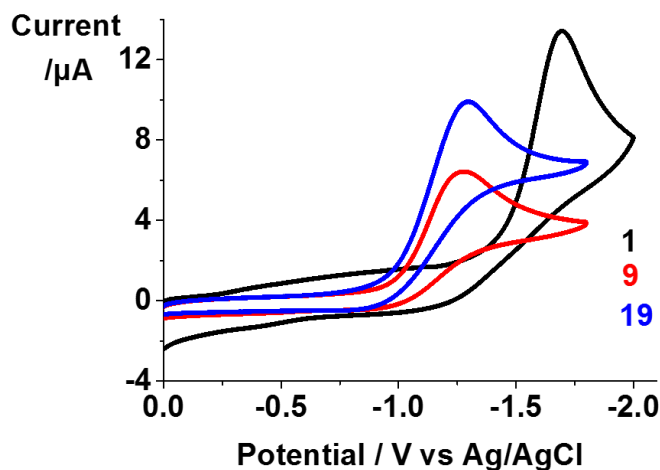


Figure 5.8. The cyclic voltammogram traces of complexes **1**, **9** and **19** (1 mM) in 0.1 M NBu₄PF₆-DMF (degassed under N₂).

5.3.6. Photodecomposition

The photodecomposition of complexes **19–26** was monitored by UV-vis and fluorescence spectroscopy, as well as LC-MS upon irradiation with indigo (420 nm), blue (463 nm) and green (517 nm) light. Similar to its analogue **9**, coumarin-containing complex **19** in aqueous solution displayed a decrease in its LMCT band upon irradiation with visible light (420–517 nm), and an increased fluorescence peak at *ca.* 450 nm with indigo irradiation (Figure 5.9).

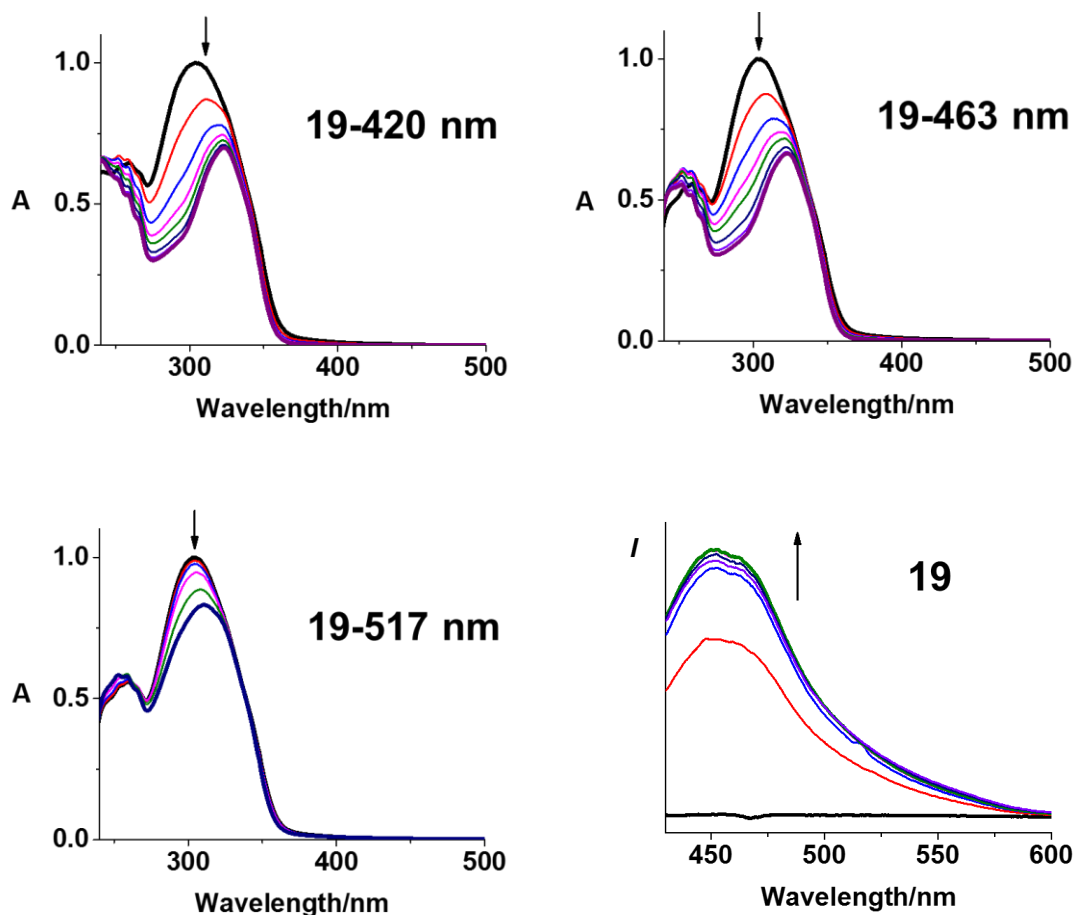


Figure 5.9. Photochemical decomposition of **19** in H₂O with 5% DMSO with indigo (420 nm), blue (463 nm), and green (517 nm) light monitored by UV-vis spectroscopy, and fluorescence spectroscopy (420 nm) for 1 h.

Approximate 22% of **9** decomposed with 1 h green irradiation as monitored by LC-MS (Figure 5.10). Azidyl and hydroxyl radicals released from **19** were trapped by DMPO upon irradiation with blue light (Figure 5.11a). The infrared phosphorescence singlet oxygen peak at *ca.* 1265 nm was detected for **19** when the excitation wavelength was set to 420 nm (Figure 5.11b).³⁶

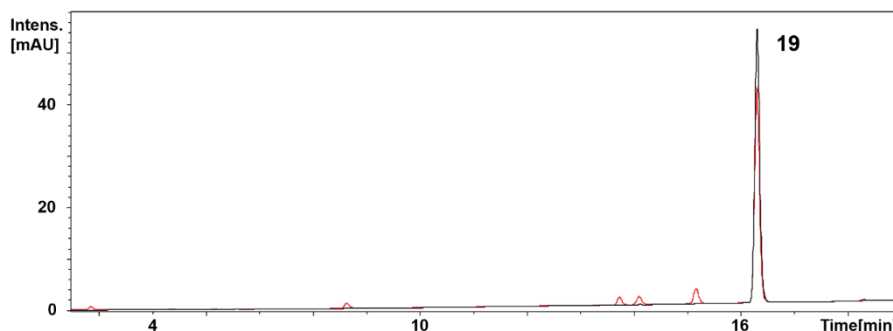


Figure 5.10. Photochemical decomposition of **19** determined by HPLC upon 1 h irradiation with green light (517 nm, —, dark; —, irradiated).

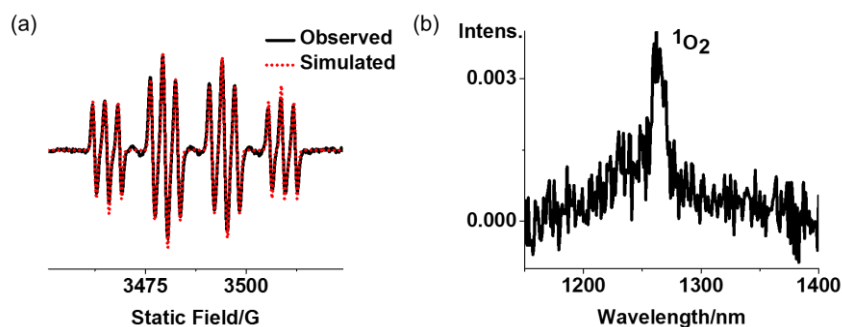
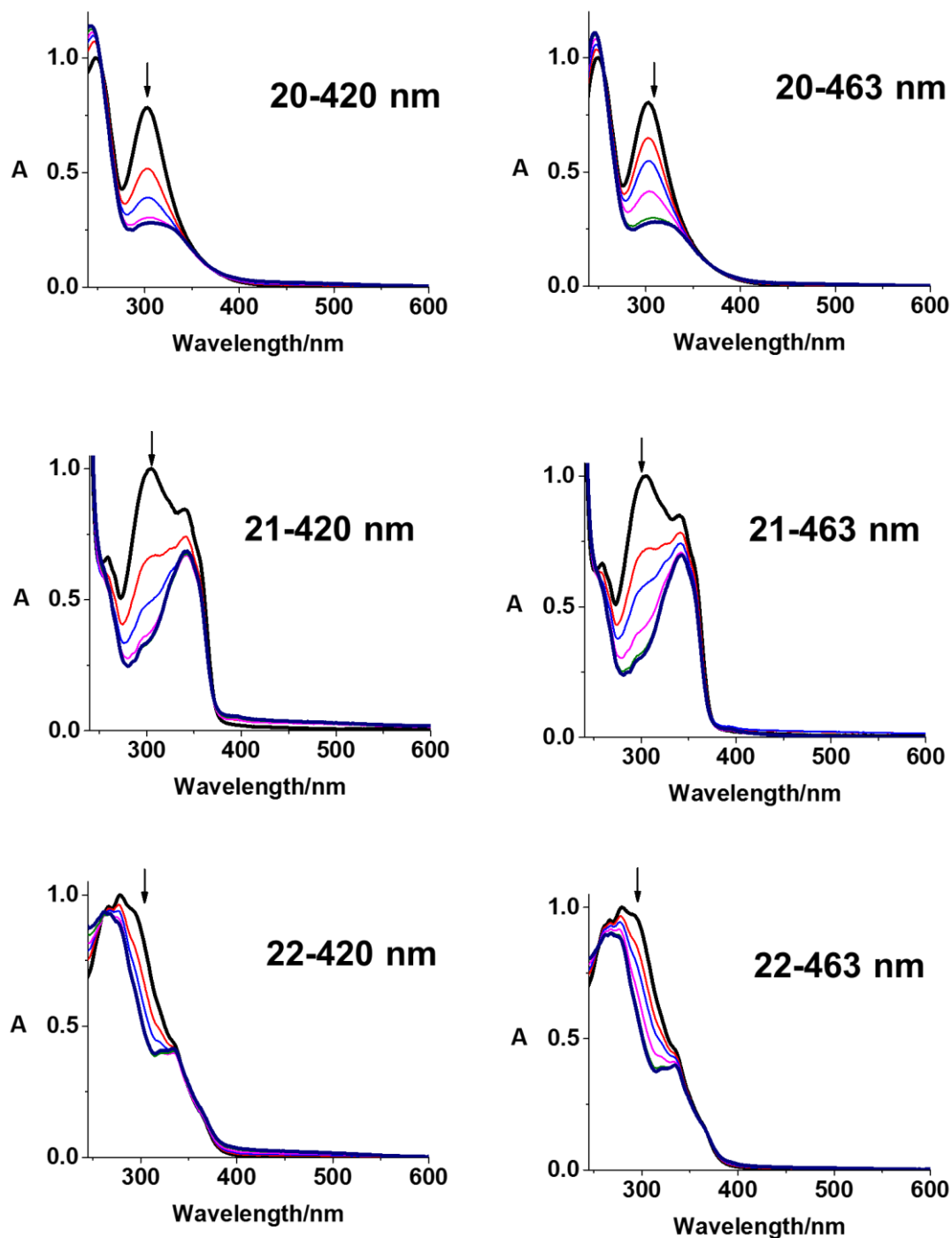


Figure 5.11. (a) EPR spectrum of complex **19** (2.5 mM) after irradiation (463 nm) in the presence of DMPO (40 mM) in aqueous solution with 5% DMSO showing the formation of DMPO–N₃• and DMPO–OH• adducts. The experimental trace results from the accumulation of 300 scans (conversion time 5.12 ms, time constant 5.12 ms, and sweep time 10.49 s for each scan) with continuous irradiation (463 nm). Parameters for simulation: DMPO–N₃• ($g = 2.00595$, $a_{\text{NO}}^{\text{N}} = 1.43$ mT, $a_{\beta}^{\text{H}} = 1.43$ mT, and $a_{\text{N}\alpha}^{\text{N}} = 0.29$ mT); DMPO–OH• ($g = 2.00592$, $a_{\text{NO}}^{\text{N}} = 1.43$ mT, and $a_{\beta}^{\text{H}} = 1.43$ mT); (b) infrared phosphorescence at 1265 nm indicates ¹O₂ formation when complex **19** (200 μM) in acetonitrile was excited by blue light (420 nm, 1 mW).

Dansyl-containing complex **20** also showed a decreased LMCT band upon irradiation with visible light (Figure 5.12). The photodecomposition of complexes **21–23** with naphthalimide rings was observed upon irradiation with indigo and blue light as the decreased LMCT band (Figure 5.12). The photodecomposition of **23** with green light was also observed due to its red-shifted absorption (Figure 5.12).



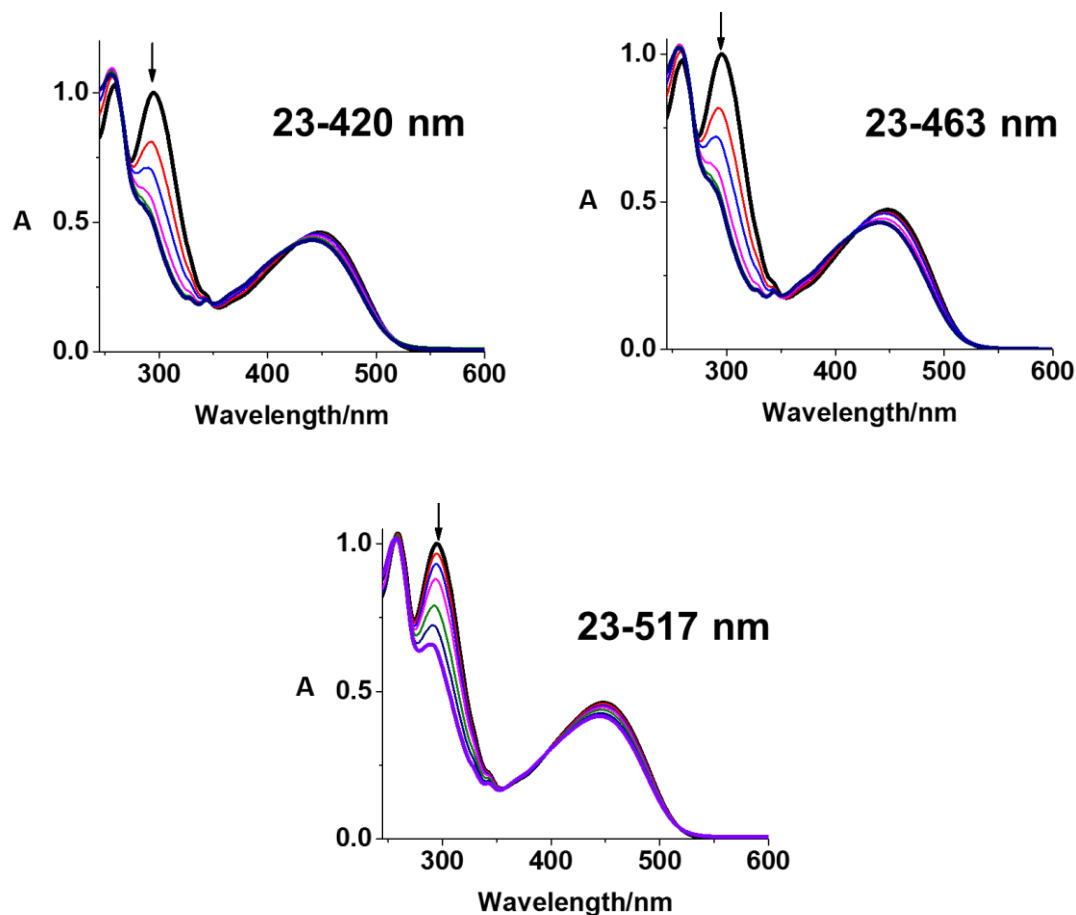


Figure 5.12. UV-vis spectral changes of **20–23** in RPMI-1640 with 5% DMSO with 1 h indigo (420 nm), blue (463 nm), and green (517 nm) light irradiation.

The emission of **21** and **23** increased gradually with irradiation (463 nm), indicating the release of axial ligand with naphthalimide (Figure 5.13). However, no emission change was observed for **22**. Singlet oxygen was also detected for complex **23** in acetonitrile (200 μM) directly by infrared fluorescence spectroscopy. Upon irradiation with indigo light, the peak assigned to complex **23** decreased gradually and disappeared within 30 min, in accompany with the formation of Pt(IV) species $\{\text{Pt}^{\text{IV}}(\text{py})_2(\text{N}_3)(\text{OH})(\text{gly-NADM})\}^+$ (708.81 m/z, b), Pt(II) species $\{\text{Pt}^{\text{II}}(\text{py})_2(\text{CH}_3\text{CN})(\text{N}_3)\}^+$ (436.00 m/z, a) and released axial ligand gly-NADM (c) (Figure

5.14a). 95% of complex **21**, 54% of complex **22** and 66% of complex **23** decomposed after 1 h irradiation with green light (Figure 5.14b).

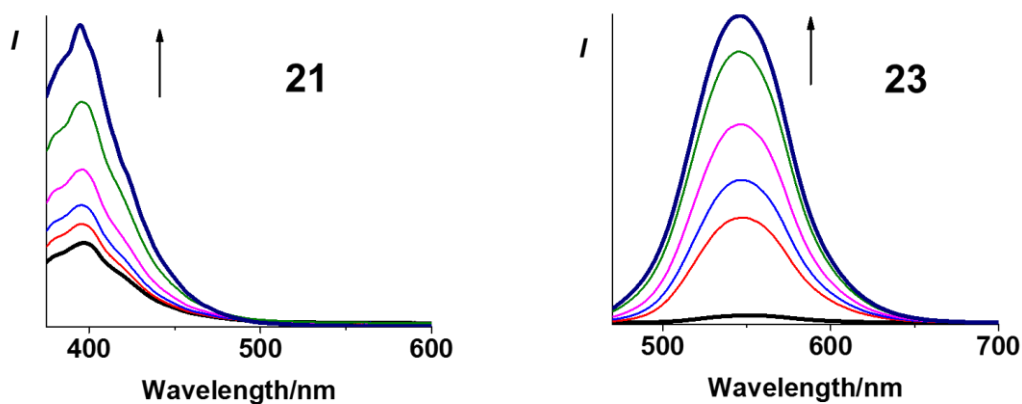


Figure 5.13. Fluorescence changes during photochemical decomposition of complexes **21** and **23** in PBS solution with 5% DMSO upon irradiation with blue light (463 nm, 1 h).

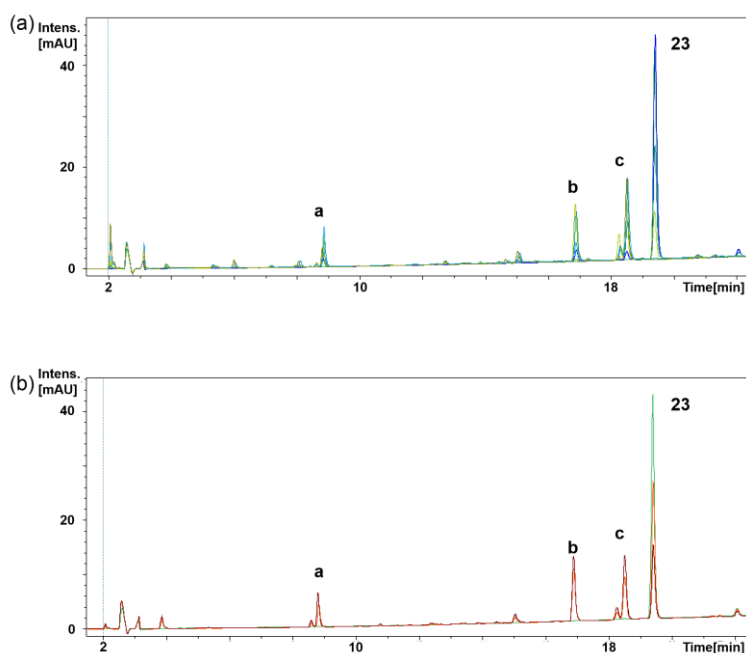


Figure 5.14. Photochemical decomposition of **23** determined by HPLC upon 1 h irradiation with (a) indigo (420 nm) and (b) green (517 nm) light. a, $\{\text{Pt}^{\text{II}}(\text{py})_2(\text{CH}_3\text{CN})(\text{N}_3)\}^+$ (436.00 m/z); b, $\{\text{Pt}^{\text{IV}}(\text{py})_2(\text{N}_3)(\text{OH})(\text{gly-NADM})\}^+$ (708.81 m/z); c, Glycine-4-dimethylamino-1,8-naphthalimide+ H^+ (298.48 m/z).

The photodecomposition of complexes **24–26** was carried out in DMSO and monitored by UV-vis spectroscopy (Figure 5.15). Complexes **24** and **26** showed a decreased absorbance at 314 nm upon irradiation, which is similar to their parent complexes. Notably, complex **25** with an NMe₂ substituent exhibited a decrease at both 300 and 420 nm.

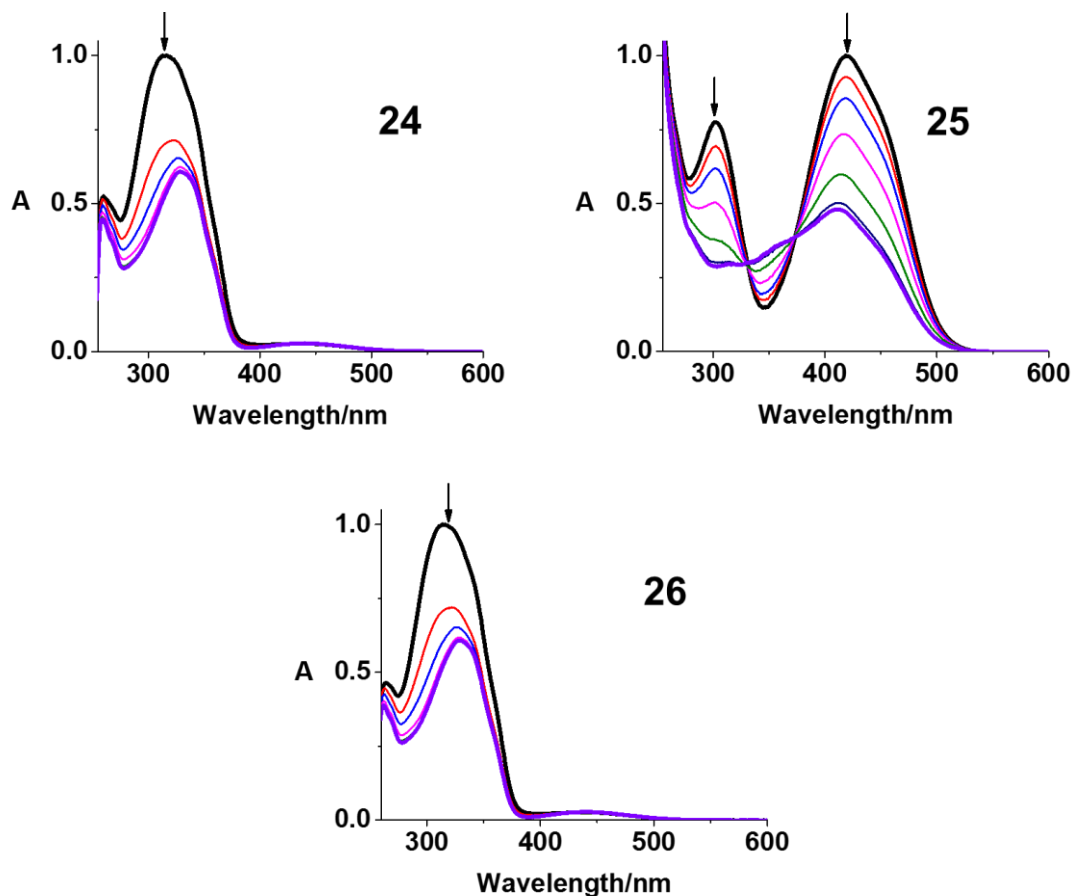


Figure 5.15. UV-vis spectral changes of **24–26** in DMSO with indigo (420 nm) light irradiation for 1 h.

The photoproducts of **24** in aqueous solution were analysed by LC-MS (Figure 5.16, Table 5.6). Before irradiation, the single peak for complex **24** indicated the high purity of the complex. After 10 min irradiation, a new peak with shorter retention time (21.4 min) was detected with same mass spectrum as complex **24**, which was assigned as the complex with axial azo ligand

in its *cis* form. Also, two peaks assigned as *cis*-azo ligand (268.96 m/z, f) and *trans*-azo ligand (268.97 m/z, h) were observed. In addition, two small peaks assigned as *trans,trans,trans*-[Pt(N₃)(py)₂(OH)(*cis*-b-azo)]⁺ (679.25 m/z, e) and *trans,trans,trans*-[Pt(N₃)(py)₂(OH)(*trans*-b-azo)]⁺ (679.25 m/z, g) appeared. With increased irradiation time, Pt(II) species {Pt^{IV}(py)₂(OC(O)H)₃}⁺ (488.04 m/z, a) [Pt^{II}(CH₃CN)(N₃)(py)₂]⁺ (436.02 m/z, b), [Pt(HCOO)(py)₂(b-azo)]+H⁺ (666.23 m/z, c), and [Pt(N₃)(py)₂(b-azo)]+H⁺ (663.25 m/z, d) appeared, and the majority of *trans* complex **24** disappeared. The photodecomposition induced by green light (517 nm) was investigated as well. After 1 h irradiation, released *cis*- and *trans*-azo ligands and *cis*-**24** were detected as photodecomposition products of complex **24**.

Table 5.6. Photochemical decomposition products of complex **24** detected by LC-MS (positive ion mode).

Peak	Formula	Structure	Calculated (m/z)	Found (m/z)
a	C ₁₃ H ₁₃ N ₂ O ₆ Pt	{Pt ^{IV} (py) ₂ (OC(O)H) ₃ } ⁺	488.04	488.03
b	C ₁₂ H ₁₃ N ₆ Pt	[Pt ^{II} (CH ₃ CN)(N ₃)(py) ₂] ⁺	436.08	436.02
c	C ₂₇ H ₂₇ N ₄ O ₄ Pt	[Pt(HCOO)(py) ₂ (b-azo)]+H ⁺	666.17	666.23
d	C ₂₆ H ₂₆ N ₇ O ₂ Pt	[Pt(N ₃)(py) ₂ (b-azo)]+H ⁺	663.18	663.25
e	C ₂₆ H ₂₆ N ₇ O ₃ Pt	[Pt(N ₃)(py) ₂ (OH)(<i>cis</i> -b-azo)] ⁺	679.17	679.25
f	C ₁₆ H ₁₇ N ₂ O ₂	<i>Cis</i> -b-azo+H ⁺	269.13	268.96
g	C ₂₆ H ₂₆ N ₇ O ₃ Pt	[Pt(N ₃)(py) ₂ (OH)(<i>trans</i> -b-azo)] ⁺	679.17	679.25
h	C ₁₆ H ₁₇ N ₂ O ₂	<i>Trans</i> -b-azo+H ⁺	269.13	268.97

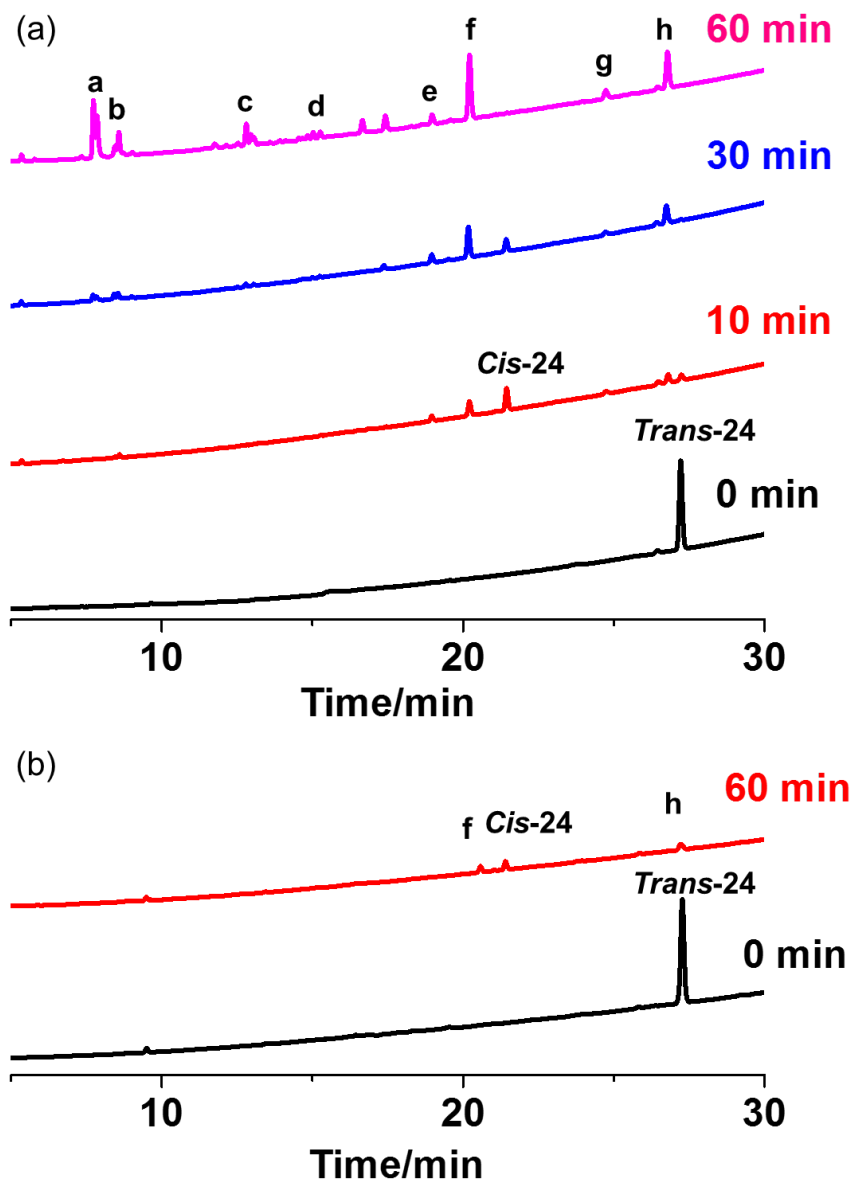


Figure 5.16. Photochemical decomposition of **24** determined by HPLC upon 1 h irradiation with (a) indigo (420 nm) and (b) green (517 nm) light. Species **a–h** are listed in **Table 5.6**.

5.3.7. Photoreactions with 5'-GMP followed by LC-MS

Similar to parent complex **1**, complexes **21–23** with naphthalimide rings and complex **24** with azo ligand on reaction with 5'-GMP and irradiation at 420 nm in aqueous solution were able

to form $\{\text{Pt}^{\text{II}}(\text{py})_2(\text{OH})(\text{CH}_3\text{CN})\}^+$ (755.73 m/z, G1) and $\{\text{Pt}^{\text{II}}(\text{py})_2(\text{N}_3)(\text{GMP})\}^+$ (757.74 m/z, G2) as the major photoproducts (Figure 5.17). In addition, complex **23** formed the same Pt-GMP adducts, but in a less amount with green light irradiation (517 nm).

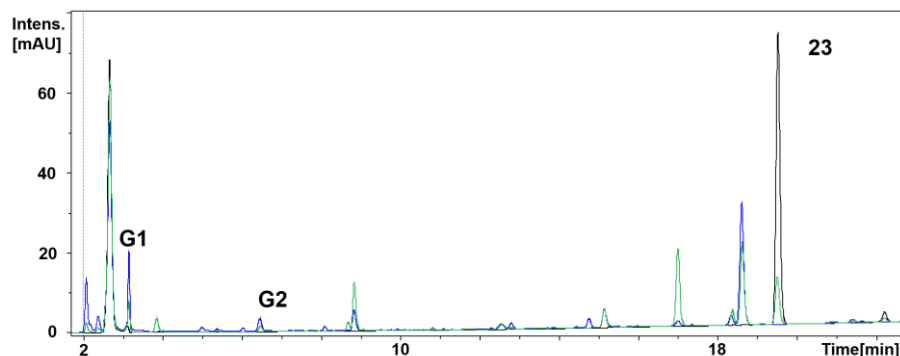


Figure 5.17. Photoreactions between of **23** and 5'-GMP after 1 h irradiation monitored by HPLC, dark (—), blue light (—), green light (—). G1: $\{\text{Pt}^{\text{II}}(\text{py})_2(\text{OH})(\text{CH}_3\text{CN})\}^+$; G2: $\{\text{Pt}^{\text{II}}(\text{py})_2(\text{N}_3)(\text{GMP})\}^+$.

5.3.8. Photoreactions with NADH

The photooxidations of NADH by complexes **1**, **9**, **19** and **23** were investigated by LC-MS (Figure 5.18). The decrease of the peak assigned as NADH (665.61 m/z) and the appearance of a new peak for NAD^+ (663.62 m/z) were observed after 1 h irradiation (420 nm). The amount of NAD^+ produced by **20** and **23** is *ca.* 1.3 \times and 1.9 \times as much as that produced by **1**, respectively, while the formation of NAD^+ by coumarin complexes **9** and **19** are similar to that by **1**.

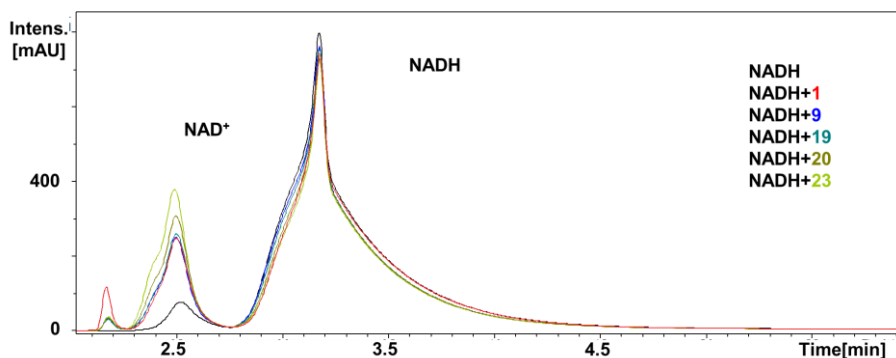


Figure 5.18. Photooxidation of NADH by complexes after 1 h irradiation with indigo light (420 nm), NADH alone (—) was used as reference.

5.3.9. Interaction between Pt(IV) complexes and HSA

HSA is the most abundant protein in human blood plasma and can be used as nano-carrier to deliver drugs, since it contains multiple hydrophobic binding pockets.³⁷ Upon addition of azo-complexes, the fluorescence of HSA was quenched. The binding constant of azo-Pt(IV) complexes with HSA was determined to be 1.9×10^5 (**24**), 2.9×10^5 (**25**), 1.7×10^6 (**26**) M^{-1} , respectively (Figure 5.19).

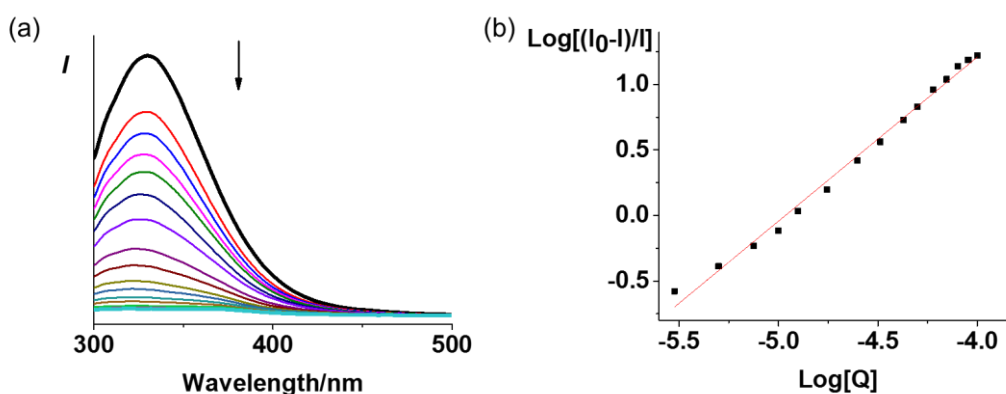


Figure 5.19. (a) Changes in the fluorescent of HSA upon addition of complex **26** in PBS solution with increasing ratio of $[Pt]/[HSA] = 0-10.00$ at 298 K; and (b) plots of absorbance change at 330 nm.

5.3.10. Photocytotoxicity

Due to the extremely poor aqueous solubility of complexes **20–22**, their biological tests were not carried out. Complexes **19** and **23** displayed low dark cytotoxicity to A2780 ovarian, A549 lung and PC3 prostate cancer cells in the dark, but significant photocytotoxicity upon irradiation (465 nm, 1 h) with IC₅₀ values of 4.3–36.4 and 1.2–13.5 μM, respectively (Table 5.7). Notably, photocytotoxicity with green light (520 nm, 1 h) was also detected for **23** (IC₅₀ = 32.7–92.8 μM). The photocytotoxicity of Pt(IV) complexes **24–26** with azo ligands was detected in A2780 ovarian cancer cells with low IC₅₀ values (0.12–0.35 μM) and high photocytotoxic indices.

Table 5.7. IC₅₀ values and photocytotoxicity indices (PI) for complexes **19** and **23–26** obtained after 1 h incubation, 1 h irradiation (465 nm for all and 520 nm for **23**) and 24 h recovery using **1** as a reference.

Complex		IC ₅₀ (μM) ^a		
		A2780	A549	PC3
19	Dark	> 100	> 100	> 100
	Irrad	4.3±0.5	36.4±1.1	23.5±3.1
	PI	> 23.2	> 2.7	> 4.2
23	Dark	>100	> 100	> 100
	465 nm	1.243±0.004	13.5±1.3	10.1±0.2
	520 nm	35.3±2.2	92.8±13.5	32.7±0.5
	PI Blue	>80.5	>7.4	>9.8
	Green	>2.8	>1.0	>3.0
24	Dark	>20		
	Irrad	0.35±0.04		
	PI	>57.1		
25	Dark	>20		

26	Irrad	0.31±0.04		
	PI	>64.5		
	Dark	>20		
1	Irrad	0.12±0.01		
	PI	>166.6		
	Dark	> 100	> 100	> 100
	Irrad	7.1±0.4	51.9±2.5	55.6±0.9
	PI	> 14	> 1.9	> 1.7

^a Each value is mean of two independent experiments.

5.3.11. Cellular accumulation

To investigate the reasons behind the promising photocytotoxicity of **19** and **23**, their cellular accumulation was determined. Complex **19** displayed a 5× higher cellular accumulation (5.6 ± 0.4 ng/ 10^6 cells) in A549 cells than its parent complex **1** under the same conditions (10 μ M, 1 h, dark). The cellular accumulations of **23** (10 μ M) in A2780 ovarian, A549 lung and PC3 prostate cancer cells in the dark are > 15× higher than **1** (Table 5.8).

Table 5.8. Cellular accumulation of Pt (ng/ 10^6 cells) in cancer cells after exposure to complexes **1**, **19** and **23** (10 μ M, 1 h, in the dark).

Complex	Pt accumulation (ng/ 10^6 cells)		
	A2780	A549	PC3
19	-	5.6 ± 0.4 ***	-
23	18.4 ± 3.5 *	20.7 ± 1.3 **	23.2 ± 1.4 *
1	1.19 ± 0.04 ***	1.0 ± 0.2 *	1.5 ± 0.3 *

^a All data were determined from triplicate samples and compared with the negative control by a two-tail t-test with unequal variances. * $p < 0.05$, ** $p < 0.01$, *** $p < 0.005$.

5.4. Discussion

5.4.1. Synthesis and characterisation

The axial hydroxide ligand in diazido Pt(IV) complexes can not only be modified to give a terminal carboxylic acid, but also a free amine. Glycine with a carboxylic acid and an amine group is an ideal agent for amination due to its simple structure. The amine group in glycine exhibits better reactivity to carboxylic acid than the hydroxide bound to platinum directly. The combination of acyl chloride or naphthalic anhydride and axial hydroxide ligand was not successful, therefore glycine was introduced for the synthesis of complexes **20–23**. However, the axial hydroxide ligand can react with some carboxylic acids in the presence of TBTU (**19** and **24–26**).

5.4.2. Dark stability and photodecomposition

In general, diazido Pt(IV) complexes with one hydroxide ligand should be stable in solution since they exhibit negative reduction potentials in DMF. The dark stability of complex **19** was satisfactory in RPMI-1640 cell culture medium due to its good aqueous solubility. However, the absorption spectra of Pt(IV) complexes with hydrophobic axial ligands changed over time, owing to the poor aqueous solubility as well as tendency to aggregate and precipitate. Thus, their stability could only be tested in DMSO. The stable spectra suggested their substitution inertness in contrast to their Pt(II) counterparts.

Complexes **19–26** photodecomposed upon irradiation with visible light, even those with long wavelength (517 nm). The conjugated fluorescent tags red-shifted the absorption of the complexes and behaved as the light antennas. Notably, complexes **24–26** with photo-

switchable azo ligands released both *cis*- and *trans*-azo ligands upon irradiation, and also formed Pt(IV) complexes with *cis*-azo ligands.

5.4.3. Photoreactions with 5'-GMP and NADH

The LC-MS results showed the release of Pt(II) species from complexes **19–26** upon irradiation with visible light and the formation of Pt-GMP adducts, which suggested that 5'-GMP reacted with platinum species only after they were released and the course of the reaction was not affected by the axial functionalisation.

Complexes **20** and **23** displayed improved NADH photooxidation compared with the parent complex **1**. It is envisaged that the dansyl and 4-dimethylamino-1,8-naphthalimide in axial ligand might act as PDT photosensitisers to transfer energy from light to oxygen then oxidise NADH.

5.4.4. Photocytotoxicity and cellular accumulation

In spite of the similarity between **19** and **9** (Figure 4.1) in chemical properties, complex **9** showed a higher cellular accumulation and therefore increased photocytotoxicity to cancer cells.

Complex **23** displayed significant photocytotoxicity with high photocytotoxicity indices. Compared with its unsubstituted analogues **21** and **22** with an electron-withdrawing substituent, **23** exhibited better aqueous solubility and moderate lipophilicity, which contributed to its highly improved cellular accumulation. The photodecomposition with visible light and the high cellular accumulation are regarded as the main reasons for the low photo IC₅₀ values of **23** (465 nm: 1.2–13.5 μM) even upon irradiation with green light (520 nm: 32.7–92.8 μM).

Complexes **24–26** showed significant photocytotoxicity, since they can release Pt(II) species, azidyl radicals and also *cis*-azo ligands. Different conformations of azo ligands result in different cytotoxicity and should be investigated in the future.

5.5. Conclusions

In this Chapter, diazido Pt(IV) complexes with coumarin **19**, dansyl **20**, 1,8-naphthalimide **21–23**, and *trans*-azo ligand **24–26** have been synthesised and characterised NMR, ESI-MS, UV-vis and fluorescence spectroscopy, and X-ray crystallography. They exhibited satisfactory HPLC purity (> 95%). The fluorescence tags red-shifted the absorption spectra of Pt(IV) complexes and make the complexes fluorescent. Dark stability and photoactivation with visible light (420–517 nm) were observed for these complexes. Pt(II) species, azidyl and hydroxyl radicals, and corresponding fluorescent ligands can be released by **19–23** upon irradiation. Notably, the increased fluorescence can also be used to monitor the photodecomposition of complexes **19**, **21** and **23**, which indicates the release of fluorescent axial ligands. The *trans*-azo ligands attached to or released from Pt(IV) complex **24** can undergo photoswitching to form the *cis*-azo ligands. Pt-GMP adducts were detected when Pt(IV) complexes **19–26** were irradiated with 5'-GMP, and NADH can be photooxidised by these complexes, which indicates the dual-mode action of these complexes by DNA platination and redox balance disturbance. Pt(IV) complexes **24–26** showed binding affinity to HSA, which might be used as a nano-carrier to stabilise and deliver the complexes.

Significant photocytotoxicity with low dark cytotoxicity were detected for complexes **19**, **23** and **24–26** in cancer cells upon irradiation with blue light (465 nm), and even green light (520 nm) for **23**. The high cellular accumulation was regarded as an important reason for their

promising photocytotoxicity, which was ascribed to their higher lipophilicity than the parent complex **1**.

In conclusion, the conjugation of diazido Pt(IV) complexes with fluorescent and photo-switchable tags does not affect their photoreactions with biomolecules, but allows photodecomposition with light of longer wavelength (517 nm) and enhances their cellular accumulation and photocytotoxicity.

5.6. References

1. K. Singh, A. M. Rotaru, A. A. Beharry, *ACS Chem. Biol.*, 2018, **13**, 1785–1798.
2. L. D. Lavis, R. T. Raines, *ACS Chem. Biol.*, 2008, **3**, 142–155.
3. G. E. Carver, S. A. Locknar, D. L. Weaver, J. L. Stein, G. S. Stein, *J. Cell Physiol.*, 2019, **234**, 5413–5419.
4. S. Maiti, N. Park, J. H. Han, H. M. Jeon, J. H. Lee, S. Bhuniya, C. Kang, J. S. Kim, *J. Am. Chem. Soc.*, 2013, **135**, 4567–4572.
5. T. Etrych, H. Lucas, O. Janoušková, P. Chytil, T. Mueller, K. Mäder, *J. Control. Release*, 2016, **226**, 168–181.
6. E. Bodio, P. Le Gendre, F. Denat, C. Goze, *Adv. Inorg. Chem.*, 2016, **68**, 253–299.
7. G. Shi, S. Monro, R. Hennigar, J. Colpitts, J. Fong, K. Kasimova, H. Yin, R. DeCoste, C. Spencer, L. Chamberlain, A. Mandel, L. Lilge, S. A. McFarland, *Coord. Chem. Rev.*, 2015, **282–283**, 127–138.
8. H. Huang, S. Banerjee, P. J. Sadler, *ChemBioChem*, 2018, **19**, 1574–1589.

9. F. Heinemann, J. Karges, G. Gasser, *Acc. Chem. Res.*, 2017, **50**, 2727–2736.
10. J. R. Lakowicz, *Principles of Fluorescent Spectroscopy*, Springer, Berlin, 2006.
11. J. Hernando, M. van der Schaaf, E. M. H. P. van Dijk, M. Sauer, M. F. García-Parajó, N. F. van Hulst, *J. Phys. Chem.*, 2003, **A107**, 43–52.
12. Y. Song, K. Suntharalingam, J. S. Yeung, M. Royzen, S. J. Lippard, *Bioconjugate Chem.*, 2013, **24**, 1733–1740.
13. Y. Min, J. Li, F. Liu, E.K.L. Yeow, B. Xing, *Angew. Chem. Int. Ed.*, 2014, **53**, 1012–1016.
14. X. Li, J. Mu, F. Liu, E. W. P. Tan, B. Khezri, R. D. Webster, E. K. L. Yeow, B. Xing, *Bioconjugate Chem.*, 2015, **26**, 955–961.
15. S. Xu, X. Zhu, C. Zhang, W. Huang, Y. Zhou, D. Yan, *Nature Commun.*, 2018, **9**:2053.
16. V. Ramu, S. Gautam, A. Garai, P. Kondaiah, A. R. Chakravarty, *Inorg. Chem.*, 2018, **57**, 1717–1726.
17. C. Lottner, K. C. Bart, G. Bernhardt, H. Brunner, *J. Med. Chem.*, 2002, **45**, 2064–2078.
18. C. Lottner, K. C. Bart, G. Bernhardt, H. Brunner, *J. Med. Chem.*, 2002, **45**, 2079–2089.
19. A. Thakur, R. Singla, V. Jaitak, *Eur. J. Med. Chem.*, 2015, **101**, 476–495.
20. J. Donovalová, M. Cigáň, H. Stankovičová, J. Gašpar, M. Danko, A. Gáplovský, P. Hrdlovič, *Molecules*, 2012, **17**, 3259–3276.
21. E. J. New, R. Duan, J. Z. Zhang, T. W. Hambley, *Dalton Trans.*, 2009, 3092–3101.
22. J. J. Wilson, S. J. Lippard, *Inorg. Chim. Acta.*, 2012, **389**, 77–84.
23. J. J. Wilson, J. F. Lopes, S. J. Lippard, *Inorg. Chem.*, 2010, **49**, 5303–5315.

24. F. Geist, A. Jackel, P. Irmeler, M. Linseis, S. Malzkuhn, M. Kuss-Petermann, O. S. Wenger, R. F. Winter, *Inorg. Chem.*, 2017, **56**, 914–930.
25. Y. Liu, W. Wu, J. Zhao, X. Zhang, H. Guo, *Dalton Trans.*, 2011, **40**, 9085–9089.
26. H. Rau, *Angew. Chem., Int. Ed.*, 1973, **12**, 224–235.
27. A. Cembran, F. Bernardi, M. Garavelli, L. Gagliardi, G. Orlandi, *J. Am. Chem. Soc.*, 2004, **126**, 3234–3243.
28. W. Szymanski, M. E. Ourailidou, W. A. Velema, F. J. Dekker, B. L. Feringa, *Chem. Eur. J.*, 2015, **21**, 16517–16524.
29. M. E. Moustafa, M. S. McCready, P. D. Boylea, R. J. Puddephatt, *Dalton Trans.*, 2017, **46**, 8405–8414.
30. K. Mitra, S. Patil, P. Kondaiah, A. R. Chakravarty, *Inorg. Chem.*, 2015, **54**, 253–264.
31. M. K. Raza, K. Mitra, A. Shettar, U. Basu, P. Kondaiah, A. R. Chakravarty, *Dalton Trans.*, 2016, **45**, 13234–13243.
32. P. Prasad, I. Pant, I. Khan, P. Kondaiah, A. R. Chakravarty, *Eur. J. Inorg. Chem.*, 2014, **2014**, 2420–2431.
33. M. E. Moustafa, R. H. E. Hudson, *Nucleos. Nucleot. Nucl.*, 2011, **30**, 740–751.
34. F. Samari, B. Hemmateenejad, M. Shamsipur, M. Rashidi, H. Samouei, *Inorg. Chem.*, 2012, **51**, 3454–3464.
35. E. L. Gelamo, M. Tabak, *Spectrochim. Acta, Part A*, 2000, **56**, 2255–2271.
36. A. A. Gorman, W. A. J. Rodgers, *CRC Handbook of Organic Photochemistry*, CRC Press, Boca Raton, 1989.

37. T. Peters, *All about albumin: biochemistry, genetics, and medical applications*, Calif: Academic, San Diego, 1996.

Chapter 6

Heteronuclear Photoactive

Complexes

6.1. Introduction

Heteronuclear complexes with platinum centres provide a feasible strategy to improve the photocytotoxicity and photoselectivity.¹⁻⁵ Two main types of photoactive heteronuclear complexes have been reported so far. An antenna complex has been attached to photoactive Pt(II) complexes to allow photoactivation at longer wavelength and enhanced photocytotoxicity.¹⁻³ In contrast, the photostable Pt(II) complexes can be conjugated to other photoactive metal complexes.^{4,5} Upon irradiation, the photoactive metal complexes can generate singlet oxygen, while the platinum centres can bind to DNA, which leads to cell death with a synergistic mechanism. Re and Ru motifs have been reported as the photosensitiser in the heterobimetallic complexes.^{4,5}

In this Chapter, two heteronuclear complexes *trans,trans,trans*-[Pt(py)₂(N₃)₂(OH)(gly-Fe)] (**27**) and *trans,trans,trans*-[Pt(py)₂(N₃)₂(OH)(succ-Ir)]Cl (**28**) were prepared as photoactive prodrugs (Figure 6.1). Ferrocene (Fe(η⁵-C₅H₅)₂) is a well-known organometallic compound with chronic toxicity in animals,⁶ and the ferrocenium cation, [Fe(η⁵-C₅H₅)₂]⁺, exhibits *in vivo* cytotoxicity by generating hydroxyl radicals that damage DNA and cell membranes.⁷ Ferrocene can be used as an antenna, since it is able to initiate ROS generation from Pt(II) complexes by a Fenton-type pathway.⁸ The ability of ferrocene to catalyse the decomposition of hydrogen peroxide plays an important role in the generation of anticancer active radicals. H₂O₂ is a photoproduct of diazido platinum complexes and is not itself very reactive towards DNA.^{9,10} Cyclometalated Ir(III) complexes are regarded as efficient photosensitisers for the production of singlet oxygen and probes for cellular imaging, owing to their outstanding photophysical properties.¹¹⁻¹⁴ Notably, the oxygen gas released during the photodecomposition of Pt(IV) complexes can also be excited by the photosensitiser to generate ROS, which allows the photosensitiser to overcome the hypoxic condition within tumours.¹⁵

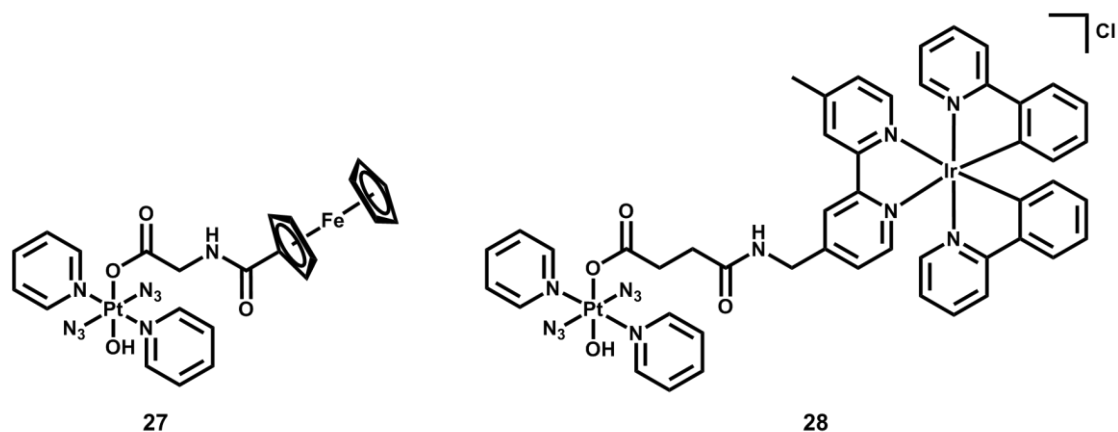


Figure 6.1. Heteronuclear complexes with diazido Pt(IV) motifs **27** and **28**, containing a ferrocene and a cyclometallated Ir(III) photosensitiser, respectively.

Both the ferrocene and Ir(III) motifs are expected to red-shift the absorption of the photoactive prodrugs and improve the ROS production efficiency. Herein, the dark stability and photoactivation with visible light of **27** and **28**, their photoreactions with NADH and 5'-GMP, photocytotoxicity and cellular accumulation, generation of ROS and radicals are investigated.

6.2. Experimental

Caution! No problems were encountered in this work, but due care and attention should be taken in the synthesis and handling of shock-sensitive heavy metal azides in the dark with minimal light exposure.

6.2.1. Materials

Ferrocenoyl chloride and CYPMPO (5-(2,2-Dimethyl-1,3-propoxy cyclophosphoryl)-5-methyl-1-pyrroline *N*-oxide) were purchased from Sigma-Aldrich. *Trans,trans,trans-*

[Pt(py)₂(N₃)₂(OH)(succ-NHS)] (**3**) was prepared according to the method described in Chapter 3. *Trans,trans,trans*-**[Pt(py)₂(N₃)₂(OH)(gly)]** (**18**) was prepared according to the method described in Chapter 5. [Ir(ppy)₂(bpy-CH₂NH₂)]Cl was provided by Dr. Huaiyi Huang.

6.2.2. Synthesis and characterisation

Trans,trans,trans-**[Pt(py)₂(N₃)₂(OH)(gly-Fe)]** (**27**). *Trans,trans,trans*-**[Pt(py)₂(N₃)₂(OH)(gly)]** (**18**, 50 mg, 95 μmol) and ferrocenoyl chloride (28.2 mg, 113 μmol) were suspended in DCM and DIPEA (100 μL) was added. The reaction mixture was stirred overnight at 298 K under a nitrogen atmosphere. After evaporation to dryness, the oily residue was collected and purified by column chromatography on silica gel (6% methanol + 94% DCM). HPLC purity = 99%. ¹H NMR (CDCl₃, 400 MHz): 8.95 (d, J = 5.3 Hz, J¹⁹⁵Pt-¹H = 27.2 Hz, 4H, H_α py), 8.08 (t, J = 7.4 Hz, 2H, H_γ py), 7.66 (t, J = 6.8 Hz, 4H, H_β py), 6.36 (s, 1 H, CONH), 4.65 (s, 2H, CH), 4.29 (s, 2H, CH), 4.25 (s, 1H, OH), 4.22 (d, J = 4.6 Hz, 2H, CH₂), 4.14 (s, 5H, CH). ¹³C NMR (CDCl₃, 100 MHz): 173.64 (COO), 170.35 (CONH), 149.46 (C_α py), 141.49 (C_γ py), 126.19 (C_β py), 70.4 (CH), 69.77 (CH), 68.23 (CH), 43.19 (CH₂). ESI-MS: [M + Na]⁺ (m/z) Calc., 763.0764; Found, 763.0758. Anal. Calcd: C₂₃H₂₃FeN₉O₄Pt: C 37.31, H 3.13, N 17.03. Found: C 37.28, H 3.04, N 17.00. ε_{436 nm} = 623 M⁻¹ cm⁻¹, ε_{300 nm} = 20490 M⁻¹ cm⁻¹, ε_{260 nm} = 21837 M⁻¹ cm⁻¹ (5% DMSO + 95% RPMI-1640).

Trans,trans,trans-**[Pt(py)₂(N₃)₂(OH)(succ-Ir)]Cl** (**28**). *Trans,trans,trans*-**[Pt(py)₂(N₃)₂(OH)(succ-NHS)]** (**3**, 10.4 mg, 15.5 μmol) was stirred with [Ir(ppy)₂(bpy-CH₂NH₂)]Cl (11.0 mg, 15.0 μmol) in DMF (2 mL) in the presence of DIPEA (20 μL, 114.8 μmol) under nitrogen at room temperature overnight. The mixture was dried by evaporation and purified by column chromatography on alumina (6% methanol + 94% DCM). HPLC purity

= 95%. ^1H NMR (CDCl_3 , 600 MHz): 9.66 (t, $J = 6.3$ Hz, 1H, $C(O)NH$), 9.46 (s, 1H, H bpy), 9.08 (s, 1H, H bpy), 8.96 (d, $J = 5.8$ Hz, $J^{195}\text{Pt}-^1\text{H} = 26.4$ Hz, 4H, H_α py), 8.02 (t, $J = 7.6$ Hz, 2H, H_γ py), 7.91 (t, $J = 8.6$ Hz, 2H, H ppy), 7.78-7.72 (m, 8H, H_β py and H ppy), 7.68 (d, $J = 7.8$ Hz, 2H, H ppy), 7.51 (d, $J = 5.8$ Hz, 1H, H bpy), 7.45 (d, $J = 5.8$ Hz, 1H, H bpy), 7.37 (d, $J = 5.6$ Hz, 1H, H bpy), 7.15 (d, $J = 5.6$ Hz, 1H, H bpy), 7.03 (t, $J = 7.9$ Hz, 2H, H ppy), 7.01 (d, $J = 7.0$ Hz, 2H, H ppy), 6.96 (t, $J = 6.6$ Hz, 1H, H ppy), 6.91 (t, $J = 7.4$ Hz, 2H, H ppy), 6.29 (dd, $J = 13.6, 7.6$ Hz, 2H, H ppy), 4.69 (d, $J = 6.2$ Hz, 2H, CH_2), 2.84 (t, $J = 7.5$ Hz, 2H, CH_2), 2.70 (t, $J = 7.8$ Hz, 2H, CH_2), 2.61 (s, 3H, CH_3). ^{13}C NMR (CDCl_3 , 150 MHz): 176.12, 173.69, 167.97, 167.84, 155.95, 155.83, 153.69, 152.08, 150.79, 150.51, 149.64, 149.54, 149.23, 148.67, 148.31, 143.51, 143.43, 141.06, 137.97, 137.87, 131.74, 131.70, 130.79, 130.69, 128.52, 127.01, 126.90, 126.26, 124.94, 124.79, 124.70, 123.23, 123.10, 122.56, 122.44, 119.64, 119.44, 41.90, 32.45, 32.23, 21.61. ^{195}Pt NMR (CDCl_3 , 129 MHz): 961.07. ESI-HRMS: $[\text{M}]^+$ (m/z) Calc., 1253.2833; Found, 1253.2838. $\epsilon_{411\text{ nm}} = 2587\text{ M}^{-1}\text{ cm}^{-1}$, $\epsilon_{381\text{ nm}} = 3987\text{ M}^{-1}\text{ cm}^{-1}$, $\epsilon_{296\text{ nm}} = 23087\text{ M}^{-1}\text{ cm}^{-1}$, $\epsilon_{257\text{ nm}} = 33438\text{ M}^{-1}\text{ cm}^{-1}$ (5% DMSO + 95% PBS).

6.2.3. Methods and instrumentation

6.2.3.1. Purity test

HPLC purity tests for complexes **27** and **28** were carried out in the same manner as that for **4–8** described in Chapter 3. The purity of **27** was also confirmed by elemental analysis on a CE-440 elemental analyser.

6.2.3.2. X-ray crystallography

A suitable crystal of complex **27** was obtained through the diffusion of diethyl ether into corresponding solution in DCM/methanol and the X-ray diffraction data were collected and solved as the method described in Chapter 2.

6.2.3.3. Radical trapping

A solution of each complex (2.5 mM) and DMPO (40 mM) was prepared for azidyl radical trapping; complex (2.5 mM), NADH (50 mM) and CYPMPO (10 mM) for NAD radical; complex (2.5 mM) and TEMP (20 mM) for singlet oxygen. The solutions were irradiated by blue light (463 nm) and EPR spectra were recorded with the methods given in Chapter 2.

6.2.3.4. Photo-dark cytotoxicity testing

The antiproliferative activity of complexes **27** and **28** was determined in A2780 ovarian, A549 lung, and PC3 prostate carcinoma cell lines, using a protocol similar to that described in Chapter 2, while the LED light sources used in this Chapter were blue (465 nm) or green (520 nm) light, and the irradiation times varied from 10 min, 30 min to 1 h.

6.2.3.5. Cellular accumulation of platinum

The cellular accumulation experiments were carried out as described in Chapter 2 with modification. (i) Cells were exposed to complexes at equipotent concentrations equal to the photoactive IC₅₀ values (for irradiation at 465 nm) in corresponding cell lines (ovarian A2780, lung A549, and prostate PC3 cancer cells), incubated in the dark for 1 h then irradiated with

blue light (465 nm) for 1 h. The control plates were incubated in the dark for 1 h for comparison.

(ii) Cells were exposed to complexes at 10 μM for 1 h.

6.2.3.6. Singlet oxygen ($^1\text{O}_2$) detection

Singlet oxygen generation was detected using both infrared phosphorescence and SOSG sensibilisation. **Infrared phosphorescence.** Infrared phosphorescence of **27** and **28** was measured on a Fluorolog-3 spectrofluorometer (Jobin Yvon Horiba, Model FL3-11) with a 450 W Xenon lamp light source and a solid state Liquid nitrogen cooled Indium Gallium Arsenide detector. The excitation light power at 420 nm was *ca.* 1 mW. The 850 nm longpass glass filter from Thorlabs (FGL850S) was used between the light source and detector. **SOSG sensibilisation.** An aqueous solution of **27** (50 μM) and SOSG (1 μM) was irradiated with blue light (463 nm) and its fluorescent spectrum was recorded every 10 s with $\lambda_{\text{ex}} = 504 \text{ nm}$, $\lambda_{\text{em}} = 525 \text{ nm}$.

6.2.3.7. Detection of H_2O_2

Pt(IV) complexes (5 mM, 10 μL) in aqueous solution was dropped on a peroxide test stick (Quantofix[®] Peroxide 25). One stick was kept in the dark while the other one was irradiated with blue light (463 nm) for 30 s. The concentration of H_2O_2 was semi-quantitatively measured by comparing to the colour scale.

6.2.3.8. ROS production in cell

2',7'-Dichlorofluorescein diacetate (DCFH-DA, Sigma-Aldrich) was used to determine the intracellular ROS production in the dark and after irradiation when A549 cells were exposed

to Pt(IV) complexes. DCFH-DA is a cell permeable non-fluorescent probe that turn into the highly fluorescent dye DCF upon oxidation by ROS in cells. A549 cells were seeded in 96-well plates (*ca.* 1×10^4 cells per well) then exposed to complexes at various concentration for 1 h. One plate was irradiated for 1 h with blue light (465 nm), while the other was kept in the dark. Drugs were removed and DCFH-DA (20 μ M) was added to the cells and incubated for 40 min. Cells were washed in Hank's Balanced Salt Solution (HBSS) and incubated in serum-free medium. The fluorescence intensity was measured on a Promega microplate reader with comparison to a negative control.

6.2.3.9. Confocal fluorescence microscopy

The fluorescence images were recorded on a fluorescence confocal microscope (LSM 880, AxioObserver). A549 cells (*ca.* 1×10^5) were seeded in glass-bottom cell culture dishes (CELLview) and allowed 24 h for attachment.

Cellular colocalisation. A549 cells were treated with complexes (10 μ M) 1 h in the dark, followed by 1 h blue light (465 nm) irradiation. Cells were washed by PBS and stained by SYTOTM 17 (2.5 μ M, $\lambda_{\text{ex}}/\lambda_{\text{em}} = 633/637\text{--}753$ nm), LysoTrackerTM Deep Red (0.5 μ M, $\lambda_{\text{ex}}/\lambda_{\text{em}} = 633/637\text{--}753$ nm) and MitoTrackerTM Red (0.5 μ M, $\lambda_{\text{ex}}/\lambda_{\text{em}} = 561/567\text{--}620$ nm) for 30 min, respectively. Cells were washed by PBS before measurement.

ROS generation. A549 cells were exposed to complexes (10 μ M) in the absence and presence of NAC (N-acetyl-L-cysteine, 10 mM) for 1 h in the dark then 1 h irradiation with blue light (465 nm). Samples kept in the dark for 2 h were prepared for comparison. Drugs were removed and cells were incubated with DCFH-DA (20 μ M, 488/502–532 nm) for 40 min. Cells were washed with Hank's Balanced Salt Solution (HBSS) before measurement.

Singlet oxygen generation. A549 cells were exposed to a mixture of complexes (10 μM) and SOSG (1 μM , 488/517–559 nm) for 1 h in the dark, followed by 1 h irradiation with blue light (465 nm) or another 1 h in the dark. Cells were washed by HBSS before measurement.

6.3. Results

6.3.1. Synthesis and characterisation

Complex **27** was synthesised by coupling complex **18** with ferrocenoyl chloride, while complex **28** was obtained by stirring **3** with $[\text{Ir}(\text{ppy})_2(\text{bpy}-\text{CH}_2\text{NH}_2)]\text{Cl}$. Both complexes gave satisfactory HPLC purity ($> 95\%$, Figure 6.2) and were characterised by ESI-HRMS and NMR.

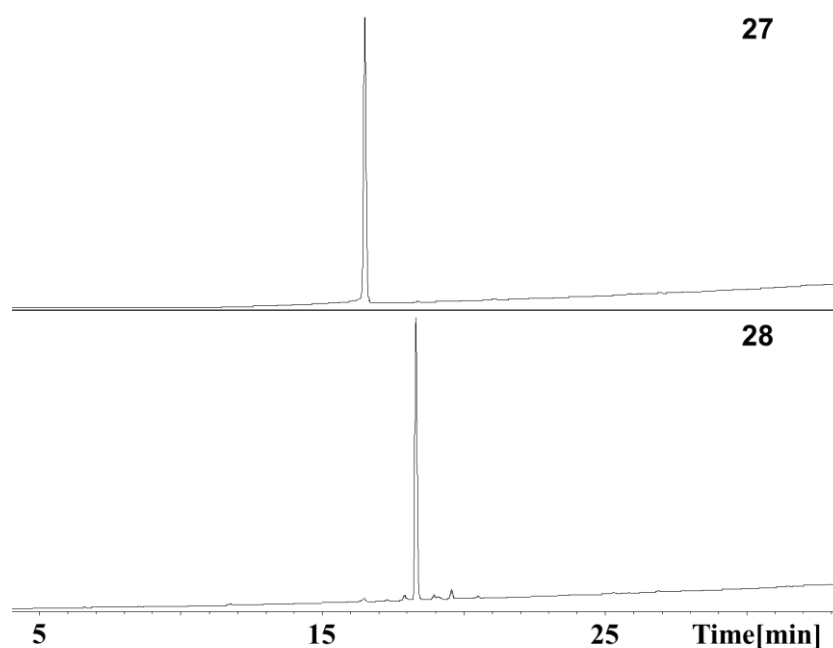


Figure 6.2. HPLC chromatogram of complex **27** and **28** confirming their purity (wavelength: 254 nm).

The Pt coordinated pyridines have characteristic ^1H NMR doublets with ^{195}Pt satellites at *ca.* 8.8 ppm, and the triplets at *ca.* 8.0 and *ca.* 7.6 ppm and ^{13}C NMR resonances at *ca.* 149, 141 and 126 ppm in the. The ^1H NMR singlets at 4.65, 4.29 and 4.14 ppm and ^{13}C NMR peaks at 70.4, 69.77 and 68.23 ppm were assigned to the protons in ferrocene fragment of **27**. Complex **28** gave a ^{195}Pt NMR signal at 961.07 ppm.

6.3.2. X-ray crystallography

Crystal suitable for X-ray diffraction studies of complex **27** were obtained through the diffusion of diethyl ether into corresponding solution in DCM/methanol. The perspective drawing of complex **27** is shown in Figure 6.3. The crystallographic data are summarised in Table 6.1 and selected bond distances and angles are listed in Table 6.2. Complex **27** crystallised in the monoclinic space group $P2_{1/c}$ with four molecules within a unit cell. **27** is a neutral hetero-dinuclear complex with a Pt(IV) and an Fe(II) centres. The platinum motif is similar to its parental complex **1**,¹⁶ which shows a symmetric octahedral geometry with a $[\text{N}_4\text{O}_2]$ hexacoordinated environment around the Pt(IV) with slight distortion due to the presence of the gly-fer ligand in one axial position. In the iron motif, the cyclopentadienyl (Cp) rings are symmetrically η^5 -bonded to iron with an average Fe-C distances of 2.04 Å (range 2.036(3)–2.059(3) Å). The distance between to metal centres within one molecule is 6.070 Å.

Hydrogen bonds are observed for complex **27** (Table 6.3). One is between axial O–H from platinum motif and the carbonyl group on the Cp ring (O1–H1 \cdots O23, 2.704(3) Å), and the other one is between the amide N–H and the ester group coordinated to platinum centre (N22–H22 \cdots O20, 2.819(3) Å).

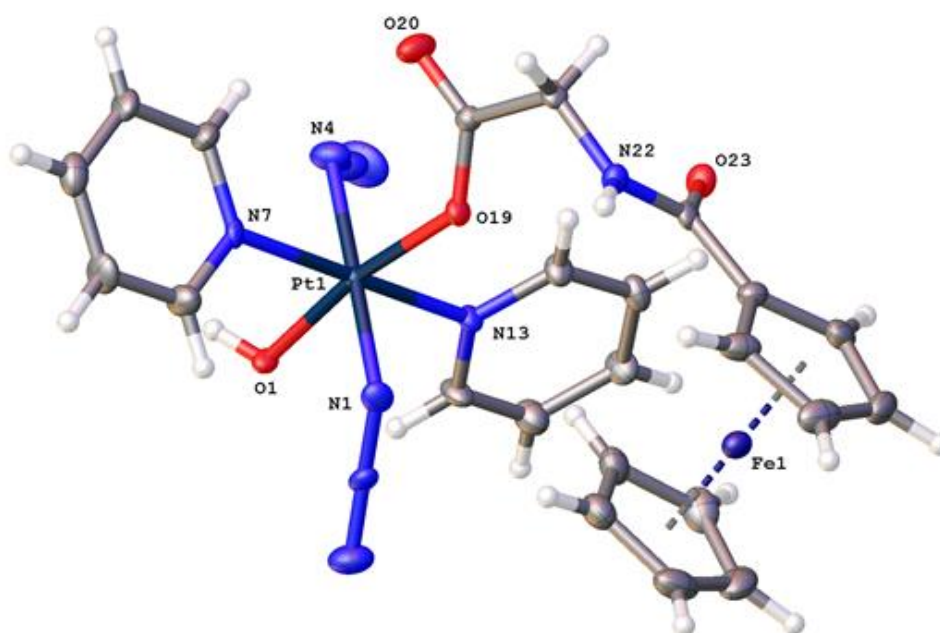


Figure 6.3. Crystal structure of **27** with key atoms labeled and thermal ellipsoids drawn at 50% probability level.

Table 6.1. Crystallographic data and structure refinement for **27**.

Empirical formula	$C_{23}H_{23}FeN_9O_4Pt$
Formula weight	740.44
Temperature/K	150(2)
Crystal system	monoclinic
Space group	$P2_1/c$
$a/\text{\AA}$	15.1269(3)
$b/\text{\AA}$	10.50172(17)
$c/\text{\AA}$	16.1559(3)
$\alpha/^\circ$	90
$\beta/^\circ$	101.4247(19)

$\gamma/^\circ$	90
Volume/ \AA^3	2515.64(8)
Z	4
$\rho_{\text{calc}}/\text{cm}^3$	1.955
μ/mm^{-1}	6.181
F(000)	1440.0
Crystal size/ mm^3	$0.32 \times 0.3 \times 0.22$ orange block
Radiation	MoK α ($\lambda = 0.71073$)
2Θ range for data collection/ $^\circ$	4.754 to 60.628
Index ranges	$-19 \leq h \leq 19$, $-14 \leq k \leq 14$, $-22 \leq l \leq 21$
Reflections collected	24793
Independent reflections	6758 [$R_{\text{int}} = 0.0362$, $R_{\text{sigma}} = 0.0399$]
Data/restraints/parameters	6758/0/344
Goodness-of-fit on F^2	1.047
Final R indexes [$I \geq 2\sigma(I)$]	$R_1 = 0.0251$, $wR_2 = 0.0461$
Final R indexes [all data]	$R_1 = 0.0320$, $wR_2 = 0.0487$
Largest diff. peak/hole/ $e \text{\AA}^{-3}$	0.71/-1.06

Table 6.2. Selected bond lengths (\AA) and bond angles ($^\circ$) for **27**.

Pt1–O1	1.9660(19)	O1–Pt1–O19	170.63(7)
Pt1–O19	2.0622(18)	N13–Pt1–N7	177.32(8)
Pt1–N13	2.047(2)	N4–Pt1–N1	178.53(10)
Pt1–N1	2.059(2)	C24–Fe1–C30	107.69(12)

Pt1–N7	2.051(2)	C24–Fe1–C28	40.91(12)
Pt1–N4	2.042(2)	C24–Fe1–C33	156.53(15)
Fe1–C30	2.042(3)	C24–Fe1–C26	68.83(12)
Fe1–C24	2.037(3)	C24–Fe1–C29	120.93(13)
Fe1–C28	2.040(3)	C24–Fe1–C31	124.90(13)
Fe1–C33	2.041(3)	C24–Fe1–C32	161.51(14)
Fe1–C26	2.046(3)	C24–Fe1–C27	68.27(12)
Fe1–C29	2.039(3)	C25–Fe1–C24	41.55(11)
Fe1–C25	2.036(3)	C26–C25–C24	107.2(3)
Fe1–C31	2.043(3)	O19–C20–C21	115.3(2)
Fe1–C32	2.045(3)	O20–C20–O19	127.2(3)
Fe1–C27	2.059(3)	N22–C23–C24	117.1(2)
N1–N2	1.215(3)	C23–N22–C21	121.1(2)
N2–N3	1.148(3)		
N4–N5	1.203(3)		
N5–N6	1.141(4)		

Table 6.3. Selected hydrogen bond parameters for **27**.

D	H	A	d(D-H)/Å	d(H-A)/Å	d(D-A)/Å	D-H-A/°
O1	H1	O23 ¹	0.84	1.87	2.704(3)	169.6
N22	H22	O20 ²	0.88	2.05	2.819(3)	145.7

¹+X, 3/2-Y, -1/2+Z; ²1-X, -1/2+Y, 3/2-Z

6.3.3. Dark stability

The dark stability of complexes **27** and **28** was tested in phenol red-free RPMI-1640 with 5% DMSO. Both complexes exhibited good dark stability since no significant spectral change was observed over 2 h (Figure 6.4).

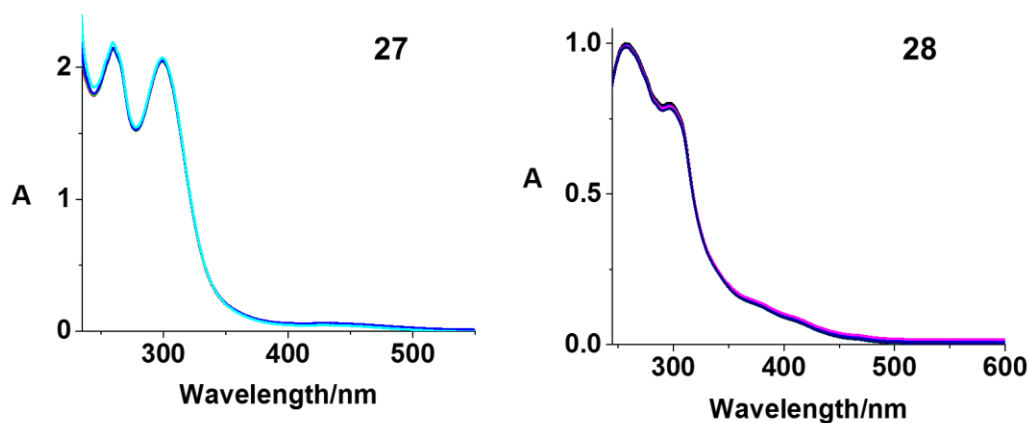


Figure 6.4. Dark stability tests for **27** and **28** in phenol red-free RPMI-1640 with 5% DMSO for 2 h monitored by UV-vis spectroscopy.

6.3.4. Extinction coefficient studies

The extinction coefficients in RPMI medium of **27** were mainly based on the platinum centre and ferrocene motif. The absorption spectrum was in a similar pattern as the parent complex **1** with an absorption maximum at 300 nm ($20490 \text{ M}^{-1} \text{ cm}^{-1}$) ascribed to LMCT transition, but the extinction coefficient at 260 nm ($21837 \text{ M}^{-1} \text{ cm}^{-1}$) was higher and a weak new peak at 436 nm ($623 \text{ M}^{-1} \text{ cm}^{-1}$) appeared due to the ferrocene motif. Both platinum and iridium centres contributed to the extinction coefficients of **28**, thus resulted in a new absorption pattern with an absorption maximum at 257 nm ($33438 \text{ M}^{-1} \text{ cm}^{-1}$), a shoulder at 296 nm ($23087 \text{ M}^{-1} \text{ cm}^{-1}$) ascribed to LMCT transition, and a tail extended into 500 nm ($\epsilon_{411 \text{ nm}} = 2587 \text{ M}^{-1} \text{ cm}^{-1}$).

6.3.5. Cyclic voltammetry

Ferrocene undergoes a reversible one-electron oxidation and is often used as standard for electrochemical measurements.¹⁷ A cyclic voltammogram trace for **27** was acquired in the potential range -1.8 – 1.0 V in DMF at 298 K, using 0.1 M NBu₄PF₆ as supporting electrolyte (Figure 6.5). This complex exhibited a reversible oxidation wave assigned to Fc⁺/Fc with $E_{pa} = 0.247$ V and $E^{\circ} = 0.211$ V, and an irreversible reduction wave assigned to Pt^{IV}/ Pt^{II} with $E_{pc} = -1.466$ V. The cyclic voltammogram trace for parental complex **1** was obtained as reference, in which the irreversible reduction wave assigned to Pt^{IV}/ Pt^{II} was determined as $E_{pc} = -1.699$ V.

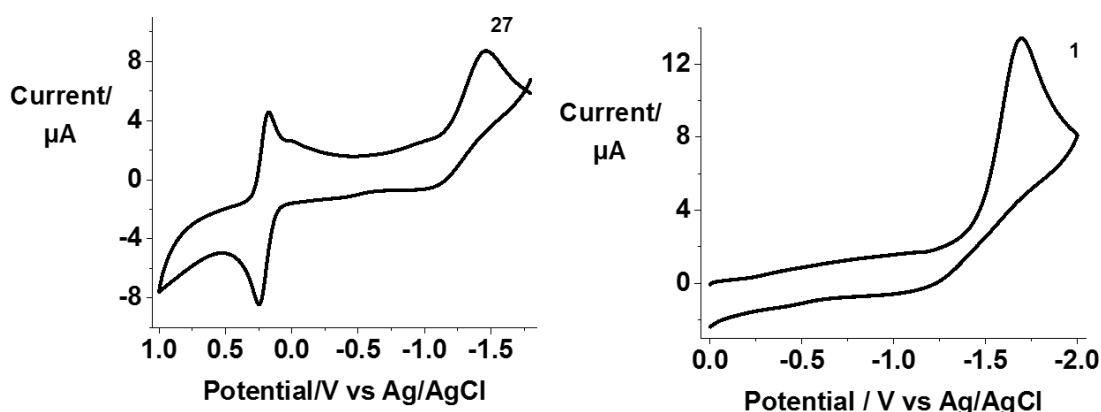


Figure 6.5. The cyclic voltammogram traces of complexes **27** and **1** (1 mM) in 0.1 M NBu₄PF₆-DMF (degassed under N₂).

6.3.6. Photodecomposition

The photodecomposition of **27** in RPMI-1640 cell culture medium was monitored by UV-vis spectroscopy at different time intervals after irradiation with indigo (420 nm), blue (463 nm), green (517 nm), and orange (593 nm) light at 298 K (Figure 6.6). Irradiation with indigo, blue and green light, decreased the intensity at the absorbance maximum of **27** at 300 nm, indicating

the release of the azide ligands. In the meantime, an apparent increase in intensity of the high-energy band at 260 nm and the absorbance at > 350 nm was observed.

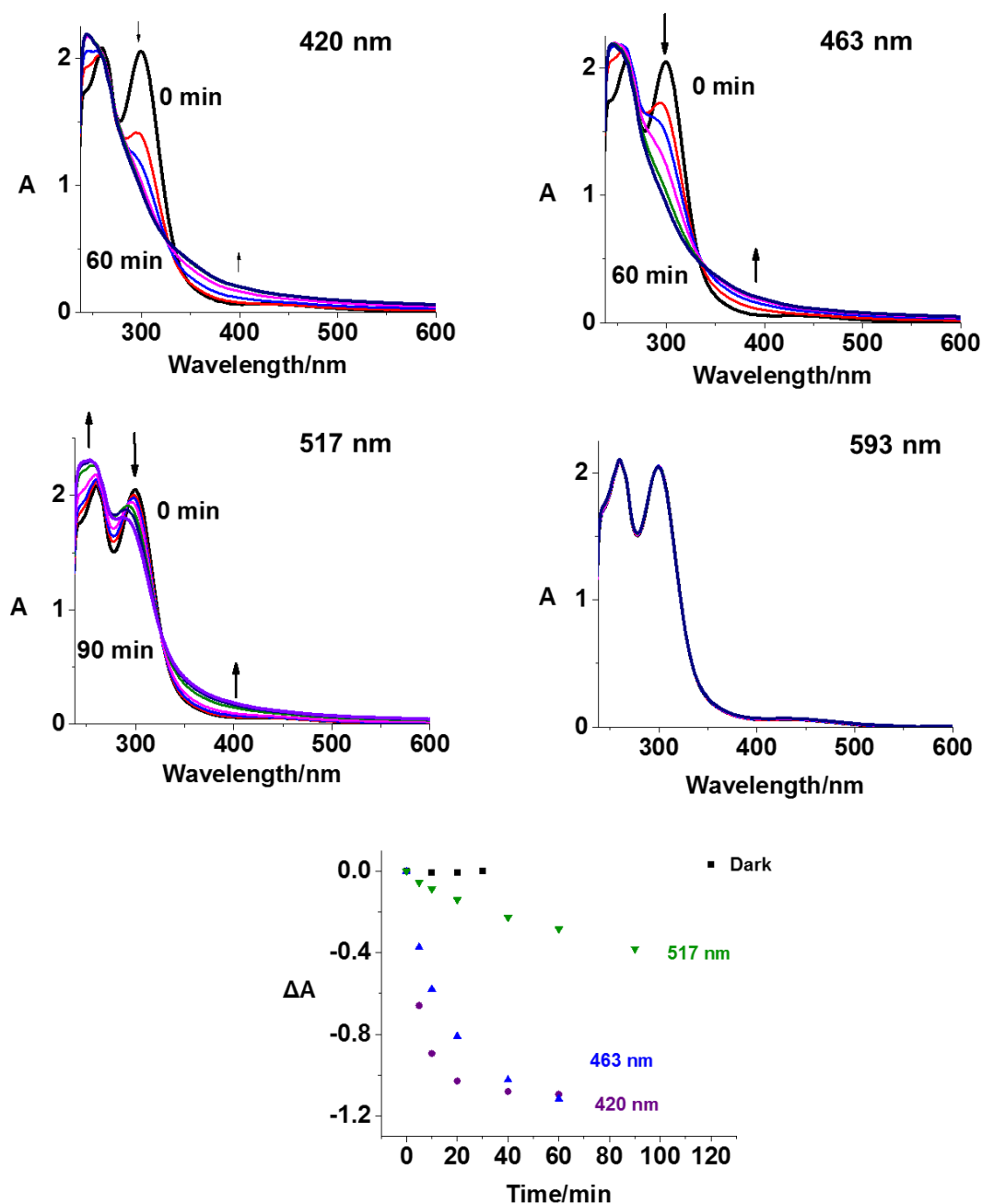


Figure 6.6. UV-vis spectral changes of **27** (phenol red-free RPMI-1640 with 5% DMSO) with 1 h indigo (420 nm), blue (463 nm), green (517 nm) and orange (593 nm) light irradiation, and time dependent absorbance change of **27** at 300 nm upon irradiation with light at different wavelengths.

Notably, the decrease in absorbance of **27** at 300 nm with green light irradiation, though not as large as that with blue light, is about 4× as high as that detected for complex **1** under same irradiation conditions (Figure 6.7). However, when irradiated by orange light, no apparent decrease at 300 nm was observed. (Figure 6.6).

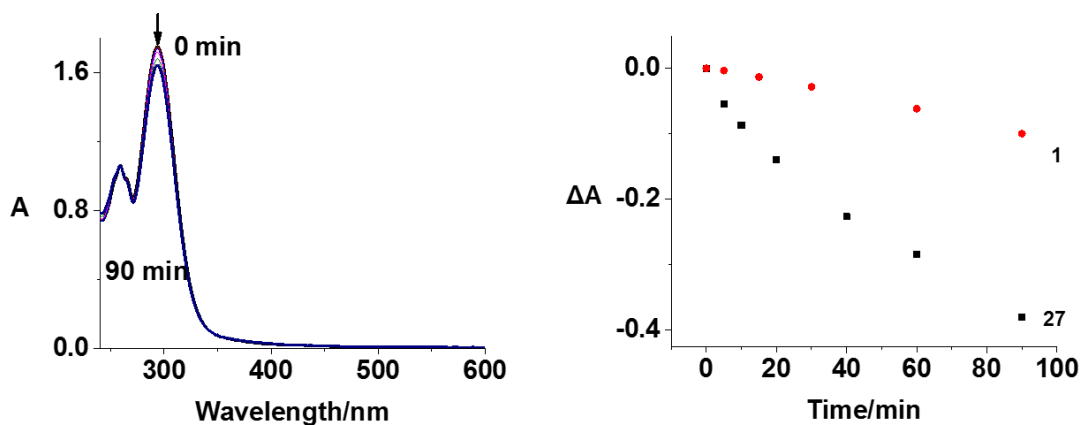


Figure 6.7. UV-vis spectral changes of **1** (phenol red-free RPMI-1640 with 5% DMSO) with 1 h green light (517 nm) irradiation, and time dependent absorbance change of **27** and **1** at 300 nm upon irradiation with green light (517 nm).

Upon irradiation with indigo (420 nm) or blue (463 nm) light, a decreased absorption of **28** at 298 nm was observed, which indicates the release of azide ligand, together with an increase at the high-energy band at 258 nm and the absorbance at the range > 350 nm (Figure 6.8). Notably, an apparent spectral change was only observed during the first 5 min, and the spectra recorded later exhibited relatively small changes even with longer irradiation.

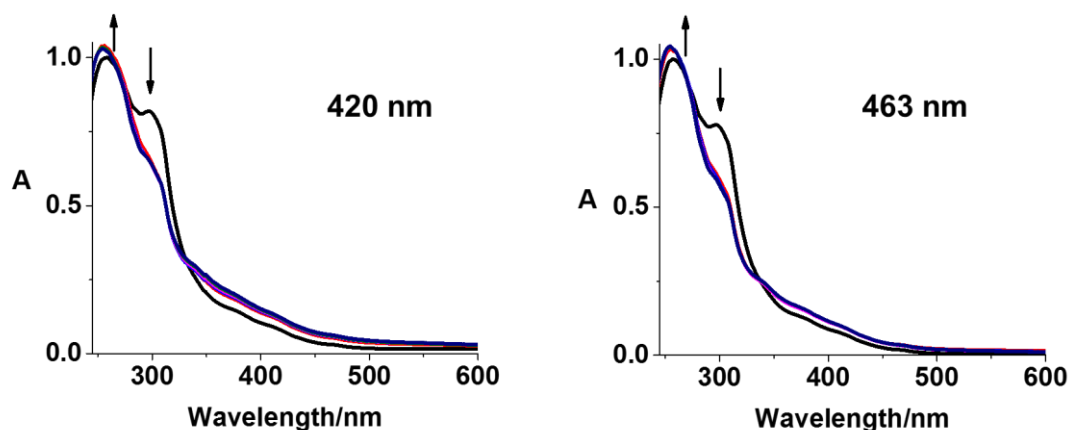


Figure 6.8. UV-vis spectral changes of **28** (phenol red-free RPMI-1640 with 5% DMSO) with indigo (420 nm) and blue (463 nm) light irradiation.

In order to investigate the species formed upon irradiation, LC-MS was employed to monitor the photoactivation of **27** and **28** with indigo, green and orange light irradiation. The HPLC peak assigned to **27** (retention time = 16.5 min) decreased gradually with indigo light (420 nm) exposure time, and disappeared within 15 min, more than 2× as fast as that observed for the parent complex **1** (Figure 6.9a and Table 6.4). The major photodecomposition products detected after 1 h irradiation included $[2\{\text{Pt}^{\text{II}}(\text{N}_3)_2(\text{py})(\text{OH}_2)\}+\text{Na}]^+$ (774.70 m/z), $\{\text{Pt}^{\text{IV}}(\text{py})_2(\text{N}_3)_2(\text{ONa})\}^+$ (475.74 m/z), $\{\text{Pt}^{\text{II}}(\text{py})_2(\text{CH}_3\text{CN})(\text{HCOO})\}^+$ (439.36 m/z), and $\{\text{Pt}^{\text{II}}(\text{CH}_3\text{CN})(\text{N}_3)(\text{py})_2\}^+$ (436.28 m/z). Intermediates $[\{\text{Pt}^{\text{II}}(\text{gly-Fc})(\text{N}_3)(\text{py})(\text{HCOOH})\}+\text{Na}]^+$ (671.62 m/z), $\{\text{Pt}^{\text{IV}}(\text{gly-Fc})(\text{py})_2(\text{N}_3)_2\}^+$ (722.88 m/z) and $\{\text{Pt}^{\text{IV}}(\text{gly-Fc})(\text{py})_2(\text{CH}_3\text{CN})(\text{OH})_2\}^+$ (697.60 m/z) formed but then decomposed after 1 h irradiation. The HPLC peak assigned as **28** disappeared with 5 min irradiation with indigo light (420 nm), and the photodecomposed products Pt(II) species $[2\{\text{Pt}^{\text{II}}(\text{N}_3)_2(\text{py})(\text{OH}_2)\}+\text{Na}]^+$ (774.74 m/z), $\{\text{Pt}^{\text{II}}(\text{CH}_3\text{CN})(\text{HCOO})(\text{py})_2\}^+$ (439.50 m/z), $\{\text{Pt}^{\text{II}}(\text{CH}_3\text{CN})(\text{N}_3)(\text{py})_2\}^+$ (436.28 m/z), and the released iridium complex $\{\text{Ir}^{\text{III}}(\text{ppy})_2(\text{bpy-CH}_2\text{NHCO}(\text{CH}_2)_2\text{COOH})\}^+$ (799.85 m/z) were detected (Figure 6.9b and Table 6.5).

Table 6.5. Photochemical decomposition products of **27** detected by LC-MS (positive ion mode). For peak labels, see Figure 6.9a.

Peak	Formula	Structure	Calculated	Found
a	C ₁₀ H ₁₄ N ₁₄ O ₂ Pt ₂ Na	[2{Pt ^{II} (N ₃) ₂ (py)(OH ₂)}+Na] ⁺	775.06	774.70
b	C ₁₀ H ₁₀ N ₈ ONaPt	{Pt ^{IV} (py) ₂ (N ₃) ₂ (ONa)} ⁺	476.05	475.72
c	C ₁₃ H ₁₄ N ₃ O ₂ Pt	{Pt ^{II} (py) ₂ (CH ₃ CN)(HCOO)} ⁺	439.07	439.40
d	C ₁₉ H ₁₉ N ₅ O ₅ NaFePt	{Pt ^{II} (gly-Fc)(py)(N ₃)(HCOO)} ⁺	671.03	671.62
e	C ₁₈ H ₁₈ N ₉ O ₄ FePt	{Pt ^{IV} (gly-Cp-Fe)(py) ₂ (N ₃) ₂ (OH)} ⁺	675.05	675.21
f	C ₁₂ H ₁₃ N ₆ Pt	{Pt ^{II} (py) ₂ (N ₃)(CH ₃ CN)} ⁺	436.08	436.28
g	C ₂₃ H ₂₄ N ₃ O ₄ FePt	[{Pt ^{II} (gly-Fc)(py) ₂ (OH)}+H] ⁺	657.08	657.94
h	C ₂₃ H ₂₃ N ₃ O ₄ NaFePt	[{Pt ^{II} (gly-Fc)(py) ₂ (OH)}+Na] ⁺	679.06	679.67
i	C ₂₃ H ₂₄ N ₃ O ₅ FePt	{Pt ^{IV} (gly-Fc)(py) ₂ (OH) ₂ } ⁺	673.07	673.84
j	C ₁₃ H ₁₄ NO ₃ Fe	[gly-Fc+H] ⁺	288.03	287.63
k	C ₂₅ H ₂₆ N ₄ O ₄ FePt	{Pt ^{IV} (gly-Fc)(py) ₂ (CH ₃ CN)(OH) ₂ } ⁺	697.10	697.60
l	C ₂₃ H ₂₂ N ₉ O ₃ FePt	{Pt ^{IV} (gly-Fc)(py) ₂ (N ₃) ₂ } ⁺	723.08	722.88

Table 6.6. Photochemical decomposition products of **28** detected by LC-MS (positive ion mode). For peak labels, see Figure 6.9b.

Peak	Formula	Structure	Calculated	Found
a	C ₁₀ H ₁₄ N ₁₄ O ₂ Pt ₂ Na	[2{Pt ^{II} (N ₃) ₂ (py)(OH ₂)}+Na] ⁺	775.06	774.74
b	C ₁₃ H ₁₄ N ₃ O ₂ Pt	{Pt ^{II} (CH ₃ CN)(HCOO)(py) ₂ } ⁺	439.07	439.50
c	C ₁₂ H ₁₃ N ₆ Pt	{Pt ^{II} (CH ₃ CN)(N ₃)(py) ₂ } ⁺	436.08	436.28
d	C ₃₈ H ₃₃ N ₅ O ₃ Ir	{Ir ^{III} (ppy) ₂ (bpy- CH ₂ NHCO(CH ₂) ₂ COOH)} ⁺	800.22	799.85

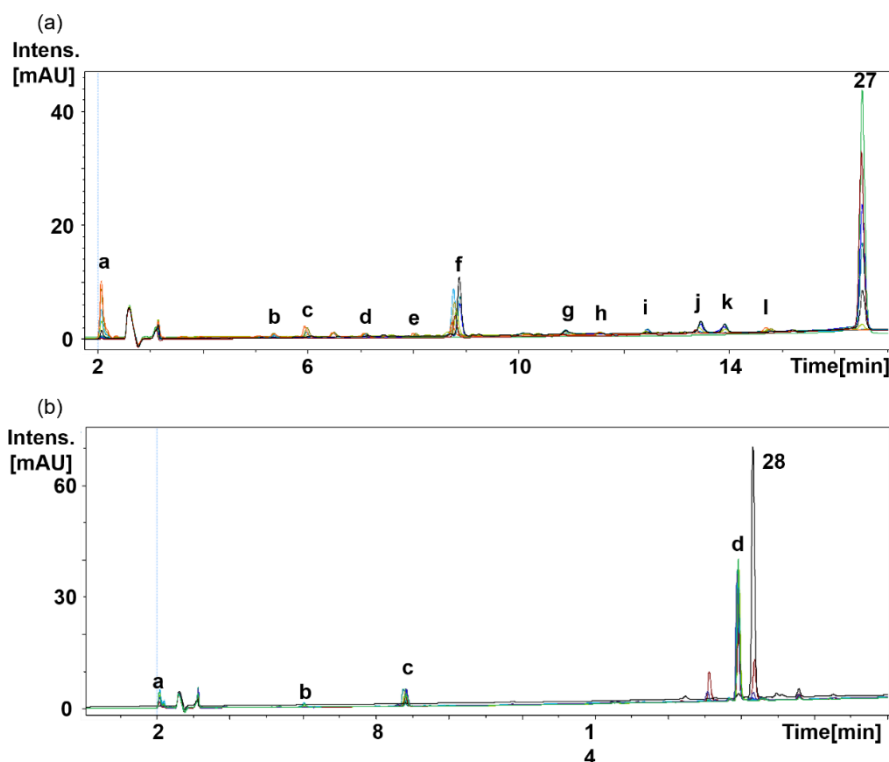


Figure 6.9. (a) Photochemical decomposition of **27** and (b) **28** determined by HPLC upon 1 h irradiation with indigo light (420 nm), possible assignments of species **a–l** for **27** and **a–d** for **28** are listed in **Tables 6.5** and **6.6**, respectively.

More than 80% of **27** decomposed after 1 h irradiation with green light (517 nm) yielding three main peaks (Figure 6.10a). These peaks can be assigned to the Pt(II) species $\{\text{Pt}^{\text{II}}(\text{CH}_3\text{CN})(\text{N}_3)(\text{py})_2\}^+$ (436.28 m/z, β) and $[\{\text{Pt}^{\text{II}}(\text{gly-Fc})(\text{N}_3)(\text{py})(\text{H}_2\text{O})\} + \text{Na}]^+$ (643.25 m/z, γ), and Pt(IV) species $\{\text{Pt}^{\text{IV}}(\text{N}_3)_2(\text{OH})(\text{gly-Cp-Fe})(\text{py})_2\}^+$ (675.21 m/z, α) resulting from the release of a Cp ring from ferrocene. The formation of Pt(II) species and generation of free binding sites on Fe(II) might allow interaction with DNA and other biomolecules. Upon irradiation with green light (517 nm) for 1 h, more than 65% of **28** decomposed with formation of $\{\text{Pt}^{\text{II}}(\text{CH}_3\text{CN})(\text{N}_3)(\text{py})_2\}^+$ (436.28 m/z, β) and released Ir(III) complex (799.69 m/z, δ , Figure 6.10b). In contrast, complex **1** showed negligible decomposition (< 2.5%) after the same

irradiation, and no apparent photodecomposition could be detected by LC-MS (Figure 6.10c). Upon irradiation with orange light (593 nm), only about 2 % of complex **27** decomposed after 2 h irradiation. However, Pt(II) species $\{\text{Pt}^{\text{II}}(\text{CH}_3\text{CN})(\text{N}_3)(\text{py})_2\}^+$ (436.28 m/z) and $[\{\text{Pt}^{\text{II}}(\text{gly-Fc})(\text{N}_3)(\text{py})(\text{H}_2\text{O})\}+\text{Na}]^+$ (643.25 m/z) were detectable despite their low intensity.

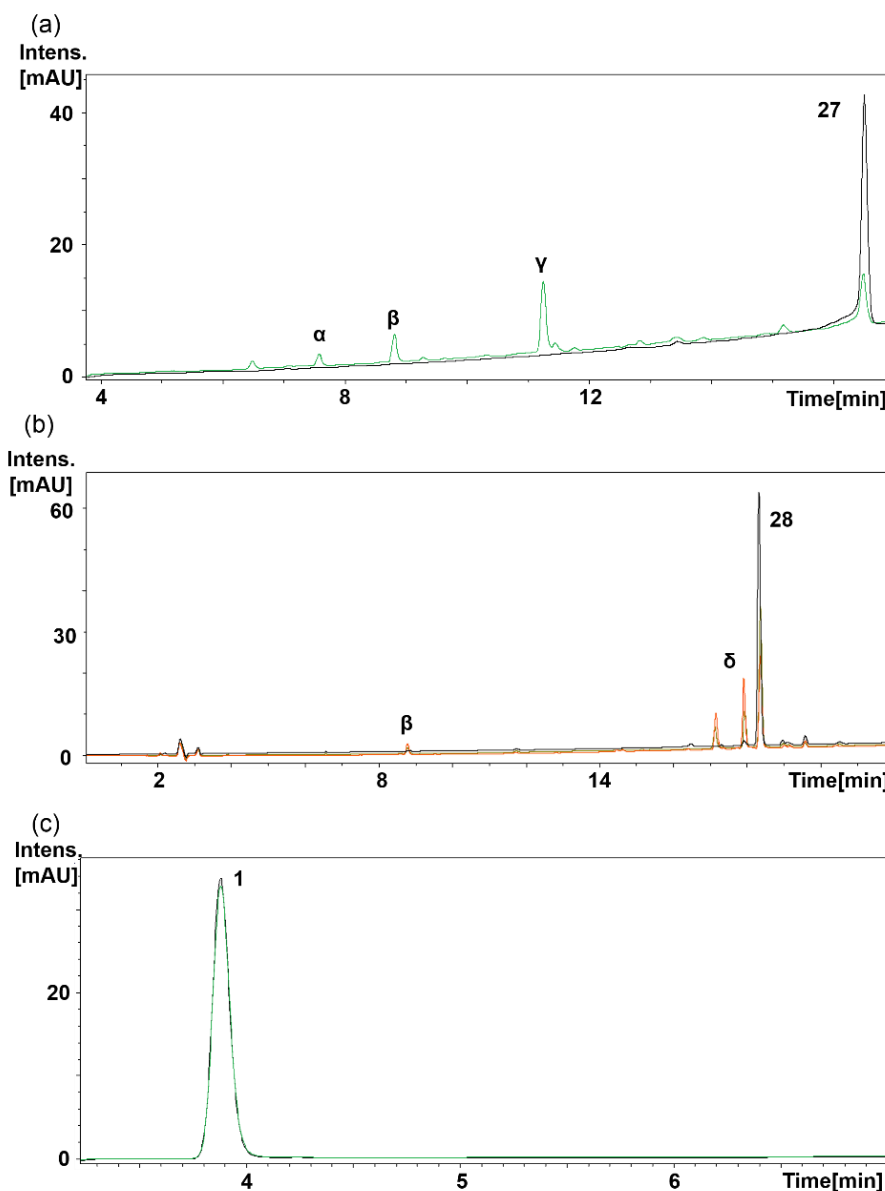


Figure 6.10. HPLC chromatograms of (a) **27**, (b) **28** and (c) **1** upon 1 h irradiation with green light (517 nm). α , $\{\text{Pt}^{\text{IV}}(\text{N}_3)_2(\text{OH})(\text{gly-Cp-Fe})(\text{py})_2\}^+$ (675.21 m/z); β , $\{\text{Pt}^{\text{II}}(\text{CH}_3\text{CN})(\text{N}_3)(\text{py})_2\}^+$ (436.28 m/z); γ , $[\{\text{Pt}^{\text{II}}(\text{gly-Fc})(\text{N}_3)(\text{py})(\text{H}_2\text{O})\}+\text{Na}]^+$ (643.25 m/z); δ , $\{\text{Ir}^{\text{III}}(\text{ppy})_2(\text{bpy-CH}_2\text{NHCO}(\text{CH}_2)_2\text{COOH})\}^+$ (799.85 m/z).

6.3.7. Photoreactions with 5'-GMP

The interaction of dinuclear complexes and 5'-GMP as a model nucleotide upon irradiation was investigated using LC-MS as described in Chapter 2. For both of complexes, the major Pt-GMP adducts were assigned as $\{\text{Pt}^{\text{II}}(\text{CH}_3\text{CN})(\text{py})_2(\text{GMP-H})\}^+$ (755.66 m/z, G1), $\{\text{Pt}^{\text{II}}(\text{HCOO})(\text{py})_2(\text{GMP})\}^+$ (761.68 m/z, G2) and $\{\text{Pt}^{\text{II}}(\text{N}_3)(\text{py})_2(\text{GMP})\}^+$ (757.68 m/z, G3) after irradiation with indigo light (420 nm, Figure 6.11). However, with green light (517 nm) irradiation, $\{\text{Pt}^{\text{II}}(\text{N}_3)(\text{py})_2(\text{GMP})\}^+$ (757.68 m/z, G3) was detected as the major adduct, while the other two adducts were too weak to be detected (Figure 6.11).

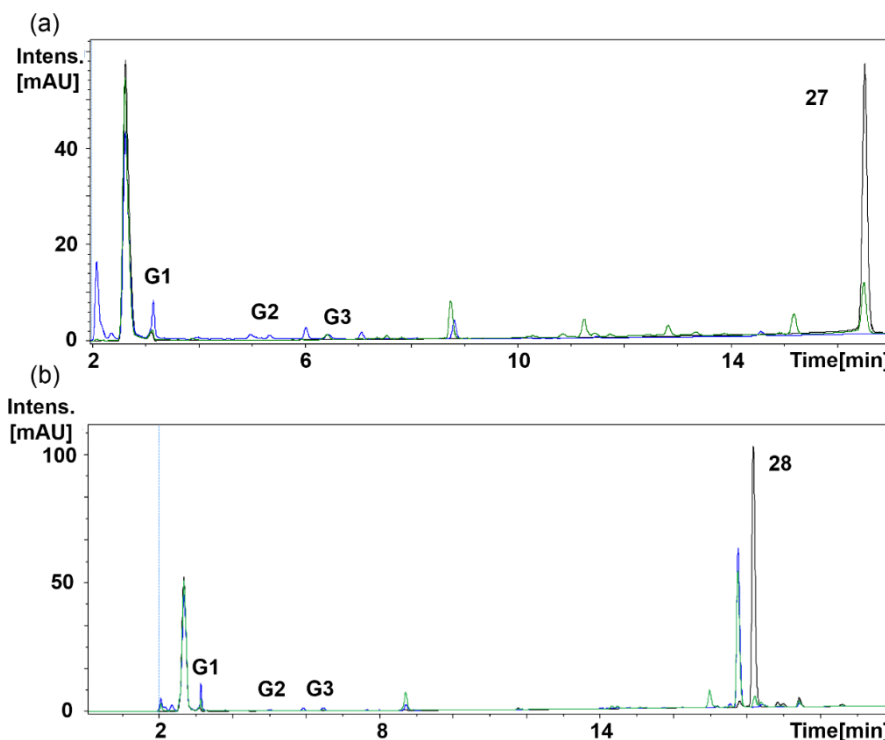


Figure 6.11. Photoreactions between (a) **27** and (b) **28** with 5'-GMP in aqueous solution after 1 h irradiation monitored by HPLC, dark (—), blue light (—), green light (—). G1, $\{\text{Pt}^{\text{II}}(\text{CH}_3\text{CN})(\text{py})_2(\text{GMP-H})\}^+$ (755.66 m/z); G2, $\{\text{Pt}^{\text{II}}(\text{HCOO})(\text{py})_2(\text{GMP})\}^+$ (761.68 m/z); G3, $\{\text{Pt}^{\text{II}}(\text{N}_3)(\text{py})_2(\text{GMP})\}^+$ (757.68 m/z).

6.3.8. Photoreactions with NADH

NAD is a coenzyme found in all living cells, and exists in two forms: NAD^+ and NADH. The balance between NAD^+ and NADH plays an important role in cell metabolism, which provides a novel avenue to design anticancer drugs since the redox metabolism of cancer cells is distinctly different from normal cells.¹⁸⁻²⁰ The photooxidation of NADH was observed for **27** and **28** as investigated by LC-MS with a decrease in intensity of peaks assigned as NADH (665.61 m/z) and the appearance of a new peak for NAD^+ (663.62 m/z). 55%, 15% and 12% of NADH was photooxidised by **28**, **27** and **1**, respectively, after 1 h irradiation with indigo light (Figure 6.12).

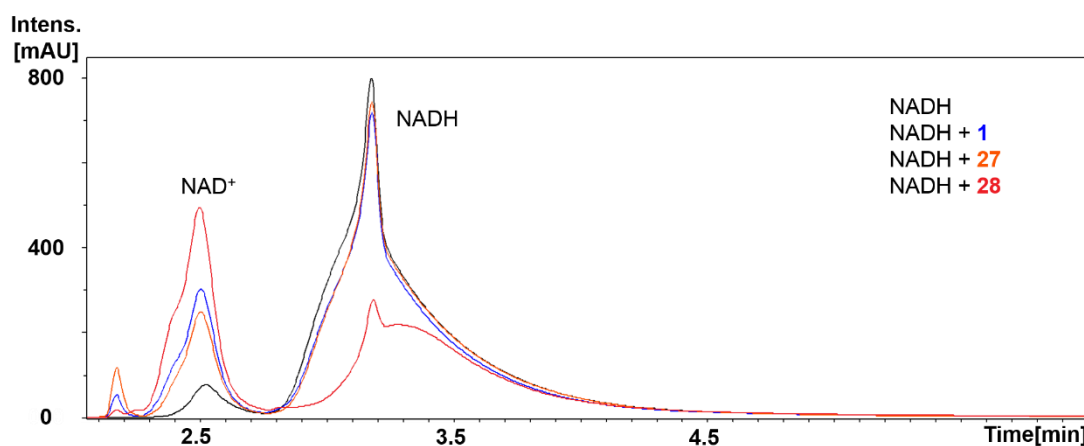


Figure 6.12. Photooxidation of NADH by complexes after 1 h irradiation with indigo light (420 nm) monitored by LC-MS, NADH alone (—) was used as reference.

To further investigate the pathway for the oxidation of NADH by **27** and **28** with light, the EPR spectra of a mixture of complex, CYPMPO and NADH in aqueous solution were recorded after 10 min irradiation (463 nm). The signal ascribed to CYPMPO– NAD^\bullet was observed for both complexes, the spectral parameters match well with reported values (Figure 6.13).²¹ In the

presence of NADH, the azidyl radical signal generated by **28** was quenched and not trapped by DMPO.

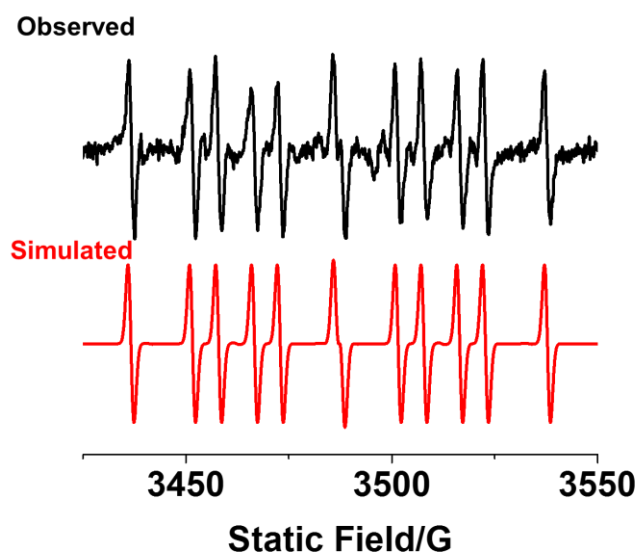


Figure 6.13. EPR spectrum of complex **27** (3 mM) and CYPMPO (10 mM) mixture in aqueous solution showing the formation of CYPMPO–NAD• adduct after irradiation (463 nm). The experimental trace resulted from the accumulation of 500 scans (conversion time 5.12 ms, time constant 5.12 ms, and sweep time 10.49 s for each scan) after 10 min irradiation (463 nm). Parameters for simulation: CYPMPO–NAD• ($g = 2.00442$, $\alpha_N = 1.49$ mT, $\alpha_H = 2.13$ mT, and $\alpha_P = 4.99$ mT).

6.3.9. Photocytotoxicity

Complexes **27** and **28** had little effect on the viability of human A2780 ovarian, A549 lung and PC3 prostate cancer cells, as well as healthy MRC-5 lung cells in the dark ($IC_{50} > 60$ μ M, Table 6.7). Upon irradiation with blue light (465 nm, 4.8 mW/cm²) for 1 h, the cytotoxicity of **27** and **28** was significantly improved with high photocytotoxicity indices (IC_{50} 1.5–26.9 μ M for **27**, 1.3–9.7 μ M for **28**, Table 6.7). The dependence of the photocytotoxicity of **27** and **28** on

irradiation times was investigated in A2780 cells. The IC₅₀ value of **27** was 15.4 μM with 30 min irradiation, and the IC₅₀ values of **28** were 23.5 and 6.2 μM after 10- and 30-min irradiation, respectively. In contrast, parent complex **1** displayed no significant photocytotoxicity with short irradiation times (< 30 min). The cytotoxicity of **27** were also enhanced by green light (60 min) irradiation giving IC₅₀ values of 3.8–41.3 μM (Table 6.7).

Table 6.7. IC₅₀ values and photocytotoxic indices (PI) for complexes **27** and **28** obtained after 1 h incubation, 1 h irradiation (465/520 nm) and 24 h recovery. CDDP (cisplatin) and complex **1** were used as references.

Cell		IC ₅₀ (μM) ^a			
		27	28	1	CDDP
A2780	Dark	> 60	> 100	> 100	> 100
	465 nm (10 min <i>hν</i>)	n.d.	23.5±0.5	> 100	n.d.
	465 nm (30 min <i>hν</i>)	15.4±1.2	6.2±0.2	> 60	n.d.
	465 nm	1.5±0.1	1.3±0.1	7.1±0.4	> 100
	520 nm	3.8±0.3	n.d.	> 100	n.d.
	PI Blue	> 33	> 76.9	> 14	-
	Green	> 13	-	-	-
A549	Dark	> 100	> 100	> 100	> 100
	465 nm	26.9±0.9	3.5±0.1	51.9±2.5	> 100
	520 nm	41.3±1.8	n.d.	> 100	n.d.

	PI	Blue	> 3.7	> 28.5	> 1.9	-
		Green	> 2.4	-	-	-
PC3	Dark		> 100	> 100	> 100	> 100
	465 nm		4.2±0.4	9.7±2.3	55.6±0.9	> 100
	520 nm		9.0±0.1	n.d.	> 100	n.d.
	PI	Blue	> 24	> 10.3	> 1.7	-
		Green	> 11	-	-	-
MRC-5	Dark		> 100	> 100	> 100	> 100

^a Each value is mean of two independent experiments. n.d. = not determined.

6.3.10. Cellular accumulation

When cells were treated with 10 μ M complex in the dark for 1 h, **27** gave platinum accumulation of 3.4–8.3 ng/10⁶ cells in cancer cell lines, and **28** gave the values of 2.8–3.8 ng/10⁶ cells (Table 6.8).

Irradiation promoted platinum accumulation in A2780 cells for **27**. Cells treated with **27** at IC₅₀ concentration accumulated 1.1 ng Pt/10⁶ cells for 1 h in the dark, which increased to 3.7 ng Pt/10⁶ cells after 1 h irradiation with blue light (Table 6.9). Similar results were obtained for **1**, 1 h irradiation enhanced the platinum accumulation from 0.8 to 2.7 ng Pt/10⁶ cells.

Table 6.8. Accumulation of Pt (ng/10⁶ cells) in cancer cells after exposure to complexes **1**, **27** and **28** (10 μM, 1 h, in the dark).

Complex	Pt accumulation (ng/10 ⁶ cells)		
	A2780	A549	PC3
27	3.4±0.5**	4.9±1.0*	8.3±1.6*
28	3.53±0.03***	2.8±0.1***	3.8±0.6**
1	1.19±0.04***	1.0±0.2*	1.5±0.3*

^a All data were determined from triplicate samples and compared with the negative control by a two-tail t-test with unequal variances. * p < 0.05, ** p < 0.01, *** p < 0.005.

Table 6.9. Accumulation of Pt (ng/10⁶ cells) in cancer cell treated with complexes **1** and **27** (equipotent IC₅₀ concentration) before and after irradiation (1 h, 465 nm).

Complex	Pt accumulation (ng/10 ⁶ cells)			
		Dark (1 h)	Irrad ^a	PI
27	A2780	1.1±0.1**	3.7±0.1***	3.4
	A549	11.7±3.0*	n.d.	-
	PC3	6.0±0.8**	n.d.	-
1	A2780	0.8±0.2*	2.7±0.3***	3.4
	A549	10.8±1.4***	n.d.	-
	PC3	13.2±1.1*	n.d.	-

^a 1 h incubation, 1 h irradiation (465 nm). All data were determined from triplicate samples and compared with the negative control by a two-tail t-test with unequal variances. * p < 0.05, ** p < 0.01, *** p < 0.005.

6.3.11. Singlet oxygen ($^1\text{O}_2$), hydrogen peroxide and radical generation

Singlet oxygen can be detected using three different methods, including direct measurement of the infrared phosphorescence of $^1\text{O}_2$, trapping $^1\text{O}_2$ by TEMP to give an EPR signal, and monitoring the fluorescence variation of a $^1\text{O}_2$ probe: Singlet Oxygen Sensor Green (SOSG[®]).

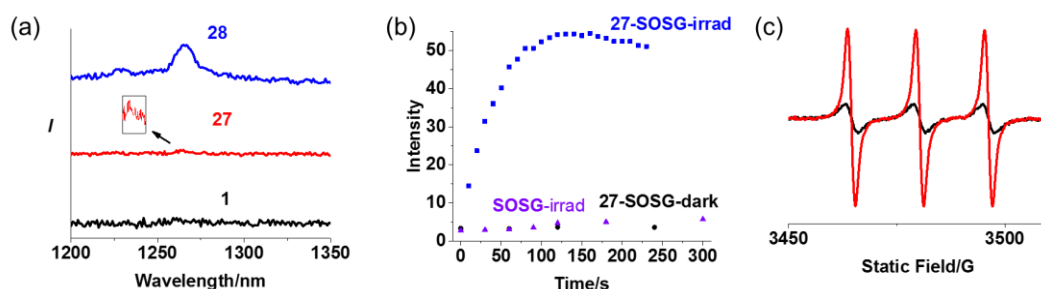


Figure 6.14. (a) Infrared phosphorescence indicates $^1\text{O}_2$ formation when complexes (200 μM) in acetonitrile were excited by blue light (420 nm, 1 mW); (b) The time dependent intensity of the fluorescence ($\lambda_{\text{ex}} = 504$ nm, $\lambda_{\text{em}} = 525$ nm) of complex **27** (50 μM) and SOSG (1 μM) in aqueous solution with 5% DMSO and 1% MeOH upon irradiation at 463 nm; (c) EPR spectra of **28** (2.5 mM) upon irradiation with blue light using TEMP to trap singlet oxygen (red: dark; blue: irrad; $a_{\text{N}\alpha}^{\text{N}} = 15.8$ G).

Singlet oxygen generated by **27** and **28** (200 μM) in acetonitrile solution was measured using infrared phosphorescence at *ca.* 1270 nm with excitation at 420 nm. Emission at 1265 nm detected for both **27** and **28** indicated the generation of singlet oxygen, and the signal detected for **28** is much more intense (Figure 6.14a). Complex **1** produced a peak for emission from $^1\text{O}_2$ under the same condition, but very weak. The $^1\text{O}_2$ produced by **27** in H_2O was also detected using SOSG. SOSG emits strong green fluorescence in the presence of $^1\text{O}_2$ ($\lambda_{\text{ex}} = 504$ nm, $\lambda_{\text{em}} = 525$ nm). An aqueous solution of **27** (50 μM) and SOSG (1 μM) was irradiated with blue light (463 nm) and its fluorescence was measured every 10 s. The emission at 525 nm increased

rapidly and reached a plateau after 90 s irradiation (Figure 6.14b). No apparent change in the intensity of fluorescence was detected for the solution without **27** or irradiation. The $^1\text{O}_2$ produced by **28** in H_2O was trapped by TEMP (Figure 6.14c). The intense triplets EPR signal of **28** and TEMP mixture in acetonitrile solution after irradiation (463 nm) indicates the formation of TEMPO caused by $^1\text{O}_2$.

To test hydrogen peroxide generation, 10 μL of Pt(IV) complexes in aqueous solution was dropped on a peroxide test stick (Quantofix[®] Peroxide 25, Figure 6.15). No colour change was observed for both **27** and **1** in the dark, but the area stained with **1** turned blue after 30 s irradiation with blue light (463 nm), and the H_2O_2 concentration was semi-quantitatively measured as 5 mg/L by comparison with the colour scale. However, the paper zone stained with **27** remained colourless even after irradiation.

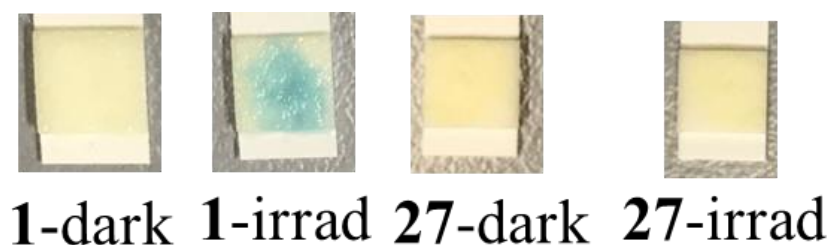


Figure 6.15. Colour change in the aqueous solution of complex **1** or **27** (5 mM) stained area on the paper zone of the Peroxide 25 Test Sticks (Quantofix[®]) in the absence or presence of irradiation.

The adducts with azidyl radicals $\text{DMPO-N}_3\cdot$ and hydroxyl radicals $\text{DMPO-OH}\cdot$ were detected as a 1 : 2 : 2 : 1 quartet of triplets and a 1 : 2 : 2 : 1 quartet, respectively when **27** was irradiated

with blue light in the presence of DMPO (Figure 6.16), and DMPO–N₃• can also be detected for **28** in the same condition.

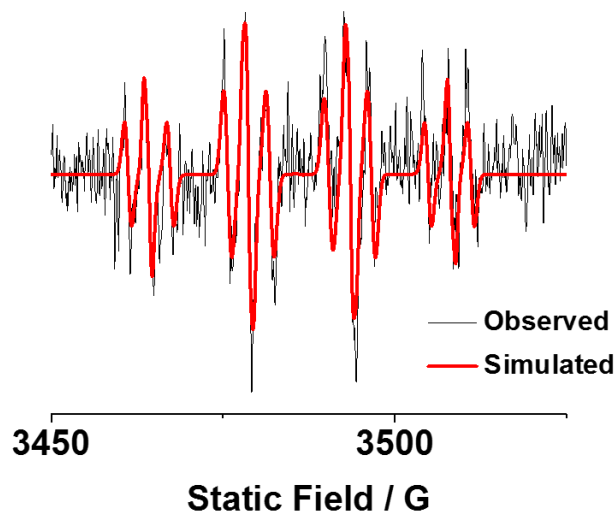


Figure 6.16. Observed (black) and simulated (red) EPR spectra of complex **27** (2.5 mM) in RPMI-1640 medium with 5% DMSO showing the formation of DMPO–N₃• and DMPO–OH• adducts after irradiation (465 nm). The experimental trace is the accumulation of 200 scans (conversion time 5.12 ms, time constant 5.12 ms, and sweep time 10.48 s for each scan) with continuous irradiation (465 nm). Parameters for simulation: DMPO–N₃• ($g = 2.0054$, $a_{\text{NO}}^{\text{N}} = 1.46$ mT, $a_{\beta}^{\text{H}} = 1.46$ mT, and $a_{\text{N}\alpha}^{\text{N}} = 0.29$ mT); DMPO–OH• ($g = 2.0054$, $a_{\text{NO}}^{\text{N}} = 1.46$ mT, and $a_{\beta}^{\text{H}} = 1.46$ mT).

6.3.12. ROS production in cells

Cumulative ROS can result in cellular damage, known as oxidative stress that can eventually lead to apoptosis.²²⁻²⁴ The ROS levels of A549 cells affected by platinum complexes were analysed by DCFH-DA assay using a Promega microplate reader (for **27**) and fluorescence confocal microscopy (for **27** and **28**). A significant increase in fluorescence was observed for

irradiated cells treated with **27** (Figure 6.17), which increased with drug concentration. On the contrary, for the dark plates, fluorescence intensity of cells treated with **27** exhibited no apparent difference with the control cells. In the presence of the ROS inhibitor NAC (10 mM), fluorescence was significantly quenched for cells treated with **27** after irradiation (Figure 6.17c). Same results were observed for **28**.

SOSG was used to detect singlet oxygen generated in A549 cells by **27** and **28**. Green fluorescence observed in A549 cells treated with **27/28** and SOSG (1 μ M) after 1 h irradiation, but no fluorescence was detected for the dark control (Figure 6.18).

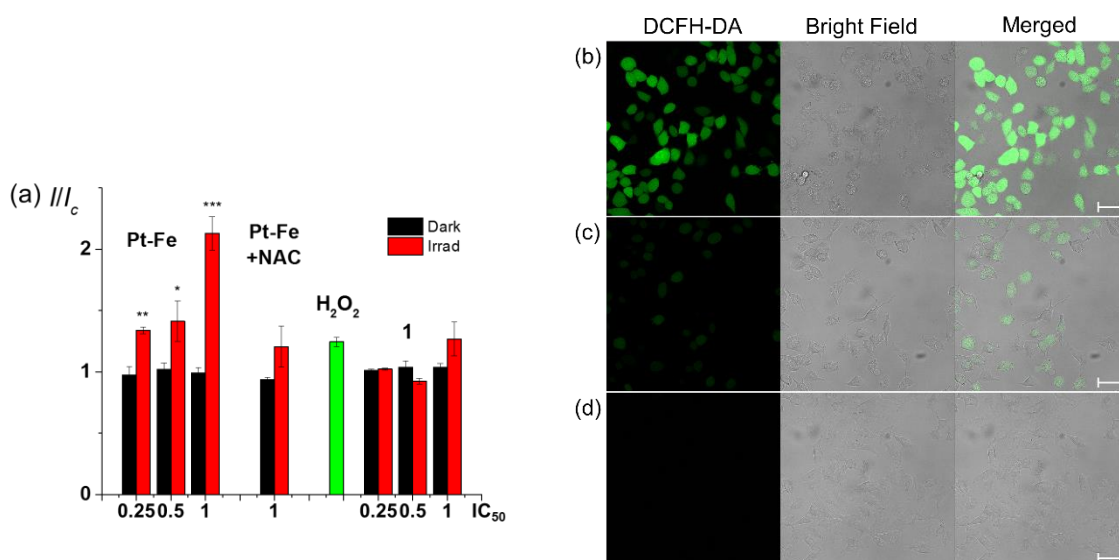


Figure 6.17. (a) Relative fluorescence intensity of A549 cells treated with **27** (2 h in the dark or 1 h in the dark and 1 h irradiation, 465 nm) then probed by DCFH-DA. H_2O_2 (5 mM) was used as a positive control; Confocal fluorescence microscopy images of ROS generation of A549 cells treated with **27** (1 h in the dark and 1 h irradiation, 465 nm) then probed by DCFH-DA in the absence (b) and presence (c) of antioxidant N-acetyl-L-cysteine (NAC). A549 cells irradiated without **27** (d) were used as a negative control. Scale bar: 50 μ m.

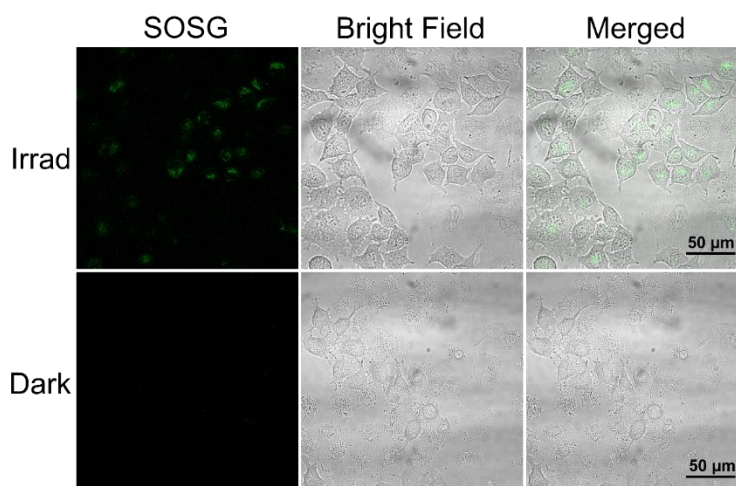


Figure 6.18. Singlet oxygen detection in A549 cells treat with **28** (10 μM) after 1 h incubation and 1 h irradiation (465 nm, 4.8 mW/cm^2) using SOSG as a singlet oxygen fluorescence indicator.

6.3.13. Cellular localisation and morphology

Since complex **28** is fluorescent in aqueous solution, its cellular localisation was investigated in A549 cells using SYTOTM 17, LysoTrackerTM Deep Red and MitoTrackerTM Red to stain nuclei, lysosomes and mitochondria, respectively (Figure 6.19). A549 cells were exposed to **28** (10 μM) for 1 h then irradiated by blue light (465 nm) for another 1 h, with control plate kept in the dark. Without irradiation, **28** is distributed mainly in cytoplasm, especially in mitochondria. The nuclei are intact with an elliptical shape. However, upon irradiation the nuclei are broken and chromosomes are released. **28** can be found in the whole cell, including the nucleus.

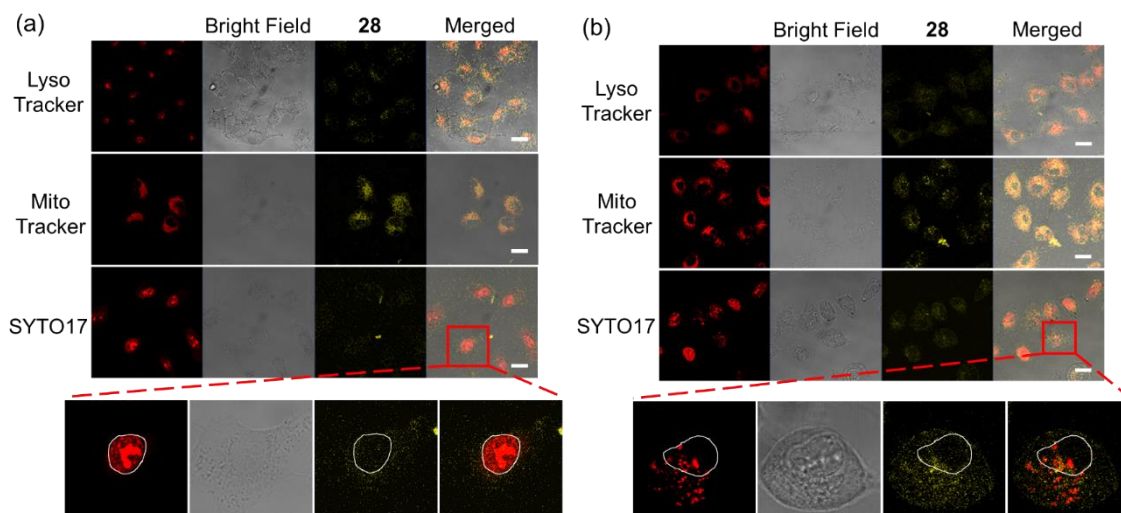


Figure 6.19. Colocalisation fluorescence images of A549 cells treat with **28** ($10\ \mu\text{M}$) upon 2 h dark incubation (a) or 1 h incubation and 1 h irradiation ($465\ \text{nm}$, $4.8\ \text{mW}/\text{cm}^2$, b), then stained by LysoTrackerTM Deep Red, MitoTrackerTM Red and SYTOTM 17 to indicate nuclei, lysosomes and mitochondria, respectively. Scale bar: $20\ \mu\text{m}$.

6.4. Discussion

6.4.1. Dark stability and photodecomposition

Heteronuclear complexes **27** and **28** were stable in the dark in RPMI-1640 medium due to the kinetic inertness of diazido Pt(IV) complexes. The axial OH ligand can enhance aqueous solubility of Pt(IV) complexes and stabilise the Pt^{IV} oxidation state.²⁵ Although reduction potential (Pt^{IV}/Pt^{II}) of **27** ($E_{\text{pc}} = -1.466\ \text{V}$) is not as negative as that of parental complex **1** ($E_{\text{pc}} = -1.699\ \text{V}$), **27** exhibited dark stability towards bio-reductants.

Photodecomposition upon irradiation with indigo ($420\ \text{nm}$) and blue ($463\ \text{nm}$) light are feasible for parental complex **1**, owing to the mixed ¹LMCT/¹IL transitions at $414\ \text{nm}$. Therefore, the photodecomposition of **27** and **28** were observed with these light wavelengths. Rapid

photodecomposition of **28** compared with the parent complex indicated the importance of **Ir** motif to transfer energy from light and promote the decomposition of Pt(IV) centre. The absorption peak at 436 nm and the tail extended to 500 nm allowed the photodecomposition of **27** and **28** at longer excitation wavelength, respectively. Complex **27** decomposed upon green (517 nm) and even orange (593 nm) light irradiation, which might result from intra-molecule reduction with electron transfer from the photoactivation initiator ferrocene motif to the Pt(IV) centre.

6.4.2. Photoreactions with 5'-GMP and NADH

The photoproducts of **27/28** and 5'-GMP were similar to that of **1** upon indigo (420 nm) light irradiation, which was expected since axial derivation did not affect the Pt(II) species released by photodecomposition. However, **27** and **28** were able to form more Pt-GMP adducts with green (517 nm) light than complex **1**, because the conjugation with other metal centre red-shifted the absorption of Pt(IV) complexes and therefore allowed them to photodecompose with longer excitation wavelengths.

Complexes **1**, **27** and **28** were capable of oxidising NADH *via* an initial one-electron oxidation, as demonstrated by trapping of NAD• radicals by the spin-trap CYPMPO. In particular, complex **28** with a photosensitive **Ir** motif displayed a significant improved NADH oxidation ability, since the **Ir** motif can act as a photo-catalyst that transfer energy from light to oxidise NADH.

6.1.1. Photocytotoxicity and cellular accumulation

Significantly enhanced photocytotoxicity of **27** and **28** was determined with a longer excitation wavelength and shorter irradiation time. These improvements were attributed to the following reasons: (i) Red-shifted absorbance allowed photodecomposition at longer wavelength; (ii) higher lipophilicity resulted in promoted cellular accumulation; (iii) higher photodecomposition rate shortened the required irradiation time; (iv) and the synergic effect of the two metal centres with different mechanisms of action.

When cells were exposed to Pt(IV) complexes at the same concentration (10 μ M), the Pt accumulation of **27** and **28** was at least 3 \times and 2 \times higher than mononuclear **1**, respectively. The higher lipophilicity as seen from reversed-phase HPLC retention times (**1**: 3.9 min; **27**: 16.5 min; **28**: 18.3 min) correlates with the higher cellular accumulation of **27** and **28**. The positive charge of **28** might also enhance its uptake. Light can promote the cellular accumulation of **1** and **27**, which might be caused by the positive charge of the photoreleased Pt(II) species and certificate the photoactivation of diazido Pt(IV) complexes.

6.1.2. Singlet oxygen ($^1\text{O}_2$) detection and ROS production in cell

ROS and other radicals play a key role in the phototherapy.²⁶ Complexes **27** and **28** generated azidyl and hydroxyl radicals, singlet oxygen and other ROS upon irradiation both in aqueous solution and in cancer cells upon irradiation. Hydrogen peroxide was not detected when **27** was irradiated since ferrocene is likely to catalyse the decomposition of hydrogen peroxide to hydroxyl radicals. In addition, due to the catalytic ability of the iron in ferrocene, more ROS was produced by **27** in cells upon irradiation. Larger amount of $^1\text{O}_2$ was generated by **28** than **1**, since the **Ir** motif is a photosensitiser and plays a major role in oxygen excitation in this complex.

6.1.3. Cellular localisation and morphology

The fluorescence of **28** allowed its monitoring within cells by confocal microscope using specific dyes to indicate the different cellular components. The irradiation of **28** *in vitro* resulted in the ruptured nuclear membranes and released chromosomes. Part of photodecomposed **28** in cytoplasm entered nuclei, bound to DNA, and led to cell death eventually. These studies suggested the synergic effect of Pt(II) species and ROS, azidyl radicals, in which ROS and azidyl radicals attack the nuclear membrane then Pt(II) species interact with DNA.

6.2. Conclusions

In this Chapter, heteronuclear complexes *trans,trans,trans*-[Pt(py)₂(N₃)₂(OH)(gly-Fe)] (**27**) with ferrocene and *trans,trans,trans*-[Pt(py)₂(N₃)₂(OH)(succ-Ir)]Cl (**28**) with [Ir(ppy)₂(bpy-CH₂NH₂)]Cl were synthesised and characterised by NMR, ESI-HRMS, UV-vis and fluorescence spectroscopy, and X-ray crystallography. These appear to be the first reported heteronuclear complexes containing diazido Pt(IV) fragments. The purity of complexes were confirmed by elemental analysis and HPLC. The presence of an additional metal centre red-shifted the absorption of Pt(IV) complexes and made the reduction potential of Pt^{IV}/Pt^{II} less negative. Both complexes displayed satisfactory dark stability and photodecomposition with indigo (420 nm), blue (463 nm), green (517 nm), and even orange (593 nm, for **27**) light in RPMI-1640 medium, which allows the light penetration from 1 to 4 mm in tissue and hence treatment of more types of tumours. The LC-MS studies revealed the formation of Pt(II) species and EPR studies indicated the generation of azidyl and hydroxyl radicals during the photodecomposition of these complexes. Singlet oxygen was detected directly by infrared phosphorescence and indirectly by SOSG indicator and TEMP EPR radical trapping after

irradiation. No H₂O₂ was detected for **27** with and without light, since iron can catalyse the decomposition of H₂O₂.

Upon irradiation, photoactivated **27** and **28** bound to 5'-GMP and produced {Pt^{II}(CH₃CN)(py)₂(GMP-H)}⁺ as the major Pt-GMP adducts. The photooxidation of NADH was also observed during the photoactivation of **27** and **28** with NAD• radicals formed as intermediate. The results suggest the dual-mode action of these complexes by DNA platination and disturbance of the redox balance in cells.

Low dark cytotoxicity and significantly enhanced photocytotoxicity of **27** and **28** were determined with longer excitation wavelength and shorter irradiation time. The higher cellular accumulation of **27** and **28** was ascribed to the higher lipophilicity as determined from HPLC retention time. The positive charge of **28** might also enhance its uptake and light can promote the cellular accumulation of **27**.

Complexes **27** and **28** generated high levels of cellular ROS and singlet oxygen as detected by DCFH-DA and SOSG in A549 lung cells upon irradiation. Ruptured nuclear membrane and released chromosomes were observed when A549 cells were exposed to **28** with light, indicating its promising photocytotoxicity with potential synergistic effect of the two different metal centres.

6.3. References

1. B. Maity, S. Gadhadar, T. K. Goswami, A. A. Karande and A. R. Chakravarty, *Eur. J. Inorg. Chem.*, 2012, **57**, 250–258.
2. K. Mitra, U. Basu, I. Khan, B. Maity, P. Kondaiiah and A. R. Chakravarty, *Dalton Trans.*, 2014, **43**, 751–763.

3. K. Mitra, A. Shettar, P. Kondaiah and A. R. Chakravarty, *Inorg. Chem.*, 2016, **55**, 5612–5622.
4. L. Quental, P. Raposinho, F. Mendes, I. Santos, C. Navarro-Ranninger, A. Alvarez-Valdes, H. Huang, H. Chao, R. Rubbiani, G. Gasser, A. G. Quiroga, A. Paulo, *Dalton Trans.*, 2017, **46**, 14523–14536.
5. Y. Zheng, D. Zhang, H. Zhang, J. Cao, C. Tan, L. Ji, Z. Mao, *Chem. Eur. J.*, 2018, **24**, 18971–18980.
6. R. A. Yeary, *Toxicol. Appl. Pharmacol.* 1969, **15**, 666–676.
7. P. Köpf-Maier, H. Köpf, E. W. Neuse, *Angew. Chem. Int. Ed.* 1984, **23**, 456–457.
8. M. Patra, G. Gasser, *Nat. Rev. Chem.*, 2017, 1.
9. J. A. Imlay, S. M. Chin, S. Linn, *Science*, 1988, **240**, 640–642.
10. G.Y. Liou, P. Storz, *Free Radic. Res.*, 2010, **44**, doi:10.3109/10715761003667554.
11. H. Huang, S. Banerjee, P. J. Sadler, *ChemBioChem*, **2018**, *19*, 1574–1589.
12. M. Martínez-Alonso, N. Busto, L. D. Aguirre, L. Berlanga, M. C. Carriijn, J. V. Cuevas, A. M. Rodríguez, A. Carbayo, B. R. Manzano, E. Ortí, F. A. Jalón, B. García, G. Espino, *Chem. Eur. J.*, **2018**, *24*, 17523–17537.
13. L. He, C. Tan, R. Ye, Y. Zhao, Y. Liu, Q. Zhao, L. Ji, Z. Mao, *Angew. Chem. Int. Ed.*, **2014**, *53*, 12137–12141.
14. K. Qiu, H. Huang, B. Liu, Y. Liu, Z. Huang, Y. Chen, L. Ji, H. Chao, *ACS Appl. Mater. Interfaces*, **2016**, *8*, 12702–12710.
15. S. Xu, X. Zhu, C. Zhang, W. Huang, Y. Zhou, D. Yan, *Nat. Commun.* **2018**, *9*, 2053.

16. N. J. Farrer, J. A. Woods, L. Salassa, Y. Zhao, K. S. Robinson, G. Clarkson, F. S. Mackay, P. J. Sadler, *Angew. Chem., Int. Ed.*, **2010**, *49*, 8905–8908.
17. R. R. Gagne, C. A. Koval, G. C. Lisensky, *Inorg. Chem.*, 1980, **19**, 92854–2855.
18. Z. Liu, R. J. Deeth, J. S. Butler, A. Habtemariam, M. E. Newton, P. J. Sadler, *Angew. Chem. Int. Ed.*, **2013**, *52*, 4194–4197.
19. Z. Liu, I. Romero-Caneln, B. Qamar, J. M. Hearn, A. Habtemariam, N. P. E. Barry, A. M. Pizarro, G. J. Clarkson, P. J. Sadler, *Angew. Chem. Int. Ed.*, **2014**, *53*, 3941–3946.
20. Y. Fu, M. J. Romero, A. Habtemariam, M. E. Snowden, L. Song, G. J. Clarkson, B. Qamar, A. M. Pizarro, P. R. Unwin, P. J. Sadler, *Chem. Sci.*, **2012**, *3*, 2485–2494.
21. S. Matsuzaki, Y. Kotake, *Biochemistry*, 2011, **50**, 10792–10803.
22. J. M. Dąbrowski, *Adv. Inorg. Chem.*, 2017, **70**, 343–394.
23. B. Halliwell, *Biochem. J.*, **2007**, *401*, 1–11.
24. Z. Zhou, J. Song, L. Nie, X. Chen, *Chem. Soc. Rev.*, **2016**, *45*, 6597–6626.
25. M. D. Hall, T. W. Hambley, *Coord. Chem. Rev.*, 2002, **232**, 49–267.
26. J. M. Dąbrowski, B. Pucelik, A. Regiel-Futyra, M. Brindell, O. Mazuryk, A. Kyzioł, G. Stochel, W. Macyk, L. G. Arnaut, *Coord. Chem. Rev.*, 2016, **325**, 67–101.

Chapter 7

Conclusions

7.1. Conclusions

In this thesis, the development of a series of novel photoactive diazido Pt(IV) complexes has been investigated, including the synthesis and characterisation by NMR, HPLC, ESI-MS, UV-vis and fluorescence spectroscopy, cyclic voltammetry, and X-ray crystallography. The dark stability and photodecomposition in aqueous solution, the photoreactions with biomolecules, the photocytotoxicity, cellular accumulation and mechanism of action were studied.

The parent complex *trans,trans,trans*-[Pt(py)₂(N₃)₂(OH)₂] (**1**) with two axial hydroxide ligands, two azide ligands and two pyridines at *trans* position is stable in the dark and able to undergo photodecomposition to release cytotoxic Pt(II) species and azidyl radicals upon irradiation with blue light.^{1,2} This thesis is concerned with the photoactivation with longer wavelength; improvement in the cancer selectivity, photocytotoxicity, and cellular accumulation; and investigation of the mechanism of action.

The modification of the axial hydroxide ligands is the main focus of this thesis. Bioactive vectors have been attached to diazido Pt(IV) complexes directly or through an organic linker, such as succinic acid and glycine. The effect of amino acids and peptides in diazido Pt(IV) complexes was investigated in Chapter 3; mono- and di-substituted complexes were compared in Chapter 4; fluorescent tags were conjugated to Pt(IV) complexes in Chapter 5, and heteronuclear complexes with diazido Pt(IV) motifs were developed in Chapter 6.

Amino acids and a cyclic peptide were attached to diazido Pt(IV) complex **1** using a bridge linker succinic acid to generate complexes **4–8** (Scheme 3.1). Complexes **4–6** released cytotoxic azidyl and hydroxyl radicals and Pt(II) species that bind to guanine base upon irradiation (420 nm). However, in the presence of Trp, the azidyl and hydroxyl radicals were quenched and the Pt-GMP adducts were not detected as the photoproducts of complex **7**. These complexes exhibited dark stability and promising photocytotoxicity in cancer cells. However,

their cellular accumulation in the dark is not as high as that of **1**. Significant enhancement in Pt accumulation was observed for complexes **6–8** after irradiation, which is properly related to their promising photocytotoxicity, especially for complex **7** containing the methyl ester of tryptophan. Complex **8** showed higher photocytotoxicity and accumulation in A549 than A2780, which suggests that the cyclic peptide might induce cell selectivity.

Mono-substituted diazido Pt(IV) complexes **9–12** and their di-substituted analogues **13–16** (Figure 4.1) displayed similarities in the photodecomposition and photoreactions, but differences in aqueous solubility, reduction potential, photocytotoxicity and cellular accumulation. Di-substituted complexes displayed longer HPLC retention times and therefore lower aqueous solubility and higher lipophilicity. Also, less negative reduction potentials were observed for di-substituted complexes. Thus, the dark stability of di-substituted complexes is not as high as that of mon-substituted complexes. But more potent photocytotoxicity and much higher cellular accumulation were detected for di-substituted complexes. Dramatic morphological changes in A2780 cells, including fragmented nuclei and damaged membranes, were observed after irradiation with **11**, consistent with the photocytotoxicity caused by azidyl radicals and Pt(II) species. Notably, the biotinylated complex **11** can form non-covalent adduct with avidin. This adduct displayed improved photocytotoxicity and cellular accumulation compared with the complex alone, since avidin can act as a nano-carrier to deliver biotinylated complexes.

The fluorescent tags red-shifted the absorption spectra of diazido Pt(IV) complexes with coumarin **19**, dansyl **20**, 1,8-naphthalimides **21–23**, and *trans*-azo ligands **24–26** and might make the complexes fluorescent (Figure 5.1). The red-shifted absorption band of diazido Pt(IV) complexes and the absorbance of the fluorescent tags in the visible range allowed the photoactivation of these complexes upon green light irradiation. Pt(II) species, azidyl and hydroxyl radicals, and corresponding fluorescent ligands can be released from these complexes,

thus the LC-MS, EPR and fluorescence spectroscopy can also be used to monitor the photodecomposition. The *trans*-azo ligands attached to or released from Pt(IV) complexes can undergo photoswitching to form the *cis*-azo ligands. Photoreactions with 5'-GMP and photooxidation of NADH were observed for these complexes. Significant photocytotoxicity with low dark cytotoxicity was detected for complexes **19**, **23** and **24–26** in cancer cells upon irradiation with blue light (465 nm), and even green light (520 nm) for **23**. The high cellular accumulation was regarded as an important reason for their promising photocytotoxicity, which was attributed to their higher lipophilicity than the parent complex **1**.

Heteronuclear complexes **27** with ferrocene and **28** with [Ir(ppy)₂(bpy-CH₂NH₂)]Cl were synthesised and characterised (Figure 6.1). A red-shifted absorption band and less negative reduction potential of Pt^{IV}/ Pt^{II} for Pt(IV) complexes were observed due to the effect of the other metal centre. Satisfactory dark stability and photodecomposition with indigo (420 nm), blue (463 nm), green (517 nm, for **27**), and orange (593 nm, for **27**) light in RPMI-1640 medium were monitored by UV-vis. The LC-MS studies revealed the formation of Pt(II) species and EPR studies indicated the generation of azidyl and hydroxyl radicals during the photodecomposition of these complexes. Singlet oxygen was detected directly by infrared fluorescence and indirectly by SOSG indicator and TEMP radical trapper after irradiation. No H₂O₂ was detected for **27** with and without light, since iron can catalyse the decomposition of H₂O₂. {Pt^{II}(CH₃CN)(py)₂(GMP-H)}⁺ was detected as the major Pt-GMP adduct, and photooxidation of NADH was observed during the photoactivation with NAD• radicals formed as intermediate. Low dark cytotoxicity and significantly enhanced photocytotoxicity were determined with longer excitation wavelength and shorter irradiation time. The higher lipophilicity of **27** and positive charge of **28** are regarded as the main reason for their high cellular accumulation. The generation of ROS and singlet oxygen were also detected by DCFH-DA and SOSG *in vitro* for A549 lung cells treated with **27/28** and irradiation. Ruptured nuclear

membrane and released chromosomes were observed in A549 cells exposed to **28** with light, indicating its promising photocytotoxicity with the synergetic effect of the two different metal centres.

7.2. Future work

Based on the work reported in this thesis, future work to improve the potential of photoactive diazido Pt(IV) complexes and investigate the mechanism of action can be proposed.

Firstly, diazido Pt(IV) complexes are the second generation of photoactive Pt(IV) complexes following the diiodo Pt(IV) complexes.³ Also, chloride,⁴⁻⁶ curcumin,⁷ o-nitrobenzyl alcohol,⁸ and MOPEP⁹ ligands have been used as leaving ligands of platinum complexes. Diazido Pt(IV) complexes have an advantage over other complexes due to their excellent dark stability.¹ However, the main LMCT band of *trans* diazido Pt(IV) complexes locates at *ca.* 300 nm,¹⁰ and the photodecomposition of these complexes with longer wavelength (> 500 nm) is limited. Therefore, new leaving ligands, such as acetylide and NO, might be introduced to develop a new generation of photoactive Pt(IV) complexes.

Secondly, the modification of non-leaving ligands has been carried out previously by our group,^{11,12} but most of them are N-donor ligands, thus did not exhibit significant difference from pyridine. π -Conjugated substituents on non-leaving pyridine attached to Pt(IV) may be able to red-shift the absorption of Pt(IV) complexes, therefore allow photoactivation at longer wavelength. In another way, C-, P- and S-donor can be considered to replace the N-donor, which may produce diazido Pt(IV) complexes with new mechanism of action.

Thirdly, the almost simultaneous absorption of two photons to excite one molecule to a higher energy state equivalent to the absorption of the single photon of twice the energy is a strategy

to activate complexes with longer wavelength, namely two-photon excitation.¹³ However, a large two-photon absorption cross section (δ) is required for complexes to be excited by two-photons.¹⁴ Our attempt to activate complex **23** with 4-dimethylamino-1,8-naphthalimide using two-photon excitation did not work. Well-designed complexes with large π -conjugated system and proper donor and acceptor groups might exhibit two-photon absorption. Porphyrin derivatives should be good candidates for conjugation and generation of two-photon active diazido Pt(IV) complexes.

Fourthly, drug delivery with nanoparticles,^{15,16} hydrogels,¹⁷ and proteins^{18,19} have been reported with enhanced photocytotoxicity and cellular accumulation. In this thesis, avidin has been used to deliver biotinylated complex **11**. However, the mechanism of action of this adduct was not investigated in detail. The elucidation of the pathway of these adducts with radio-labelled Pt within cells can be useful for the design of new nano-carriers.

Fifthly, a fluorescent tag is an important tool to monitor the drugs within cells using confocal microscopy.²⁰ I have prepared some fluorescent diazido Pt(IV) complexes in this thesis, but the investigation of their localisation, activation and pathway in cancer cells is limited due to the low emission quantum yield. Novel fluorescent tags, such as organic luminophores with aggregation induced emission, could be conjugated to diazido Pt(IV) complexes for higher resolution imaging.

Sixthly, complex **1** exhibited relatively low cytotoxicity towards normal MRC-5 lung cells even after irradiation. The higher ROS level required to kill normal cells is tentatively considered as the major reason, since azidyl and hydroxyl radicals and singlet oxygen are important cytotoxic species of diazido Pt(IV) complexes.² Thus, the mechanism of action for **1** in healthy cells could be investigated by determining the cellular ROS level and the cellular Pt distribution changes after irradiation.

Finally, *in vivo* experiments, an important step towards clinical trials, could be carried out in a bladder tumour model in mice that is accessible for extraneous light source.^{21,22} *Trans,trans,trans*-[Pt(py)(NH₃)(N₃)₂(OH)₂] is the only simple diazido Pt(IV) prodrug that has been tested *in vivo*. Two of seven nude mice bearing OE19 oesophageal cancer xenograft treated with *trans,trans,trans*-[Pt(py)(NH₃)(N₃)₂(OH)₂] at low dose with short irradiation times (420 nm, 100 J/cm², 2 × 30 min) survived at 35 days, while none of the control mice without drug or irradiation survived, and the complex was well tolerated.²³ A series of diazido Pt(IV) complexes could be screened *in vitro* against several types of bladder cancer cells, and the best candidate can be tested in the mouse model. Drugs can be given by injection, followed by irradiation.

7.3. References

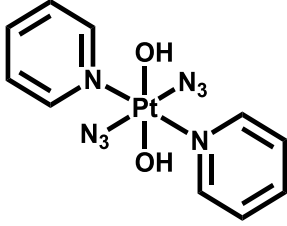
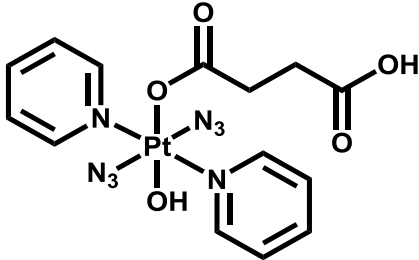
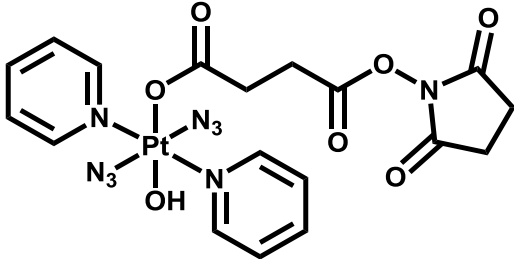
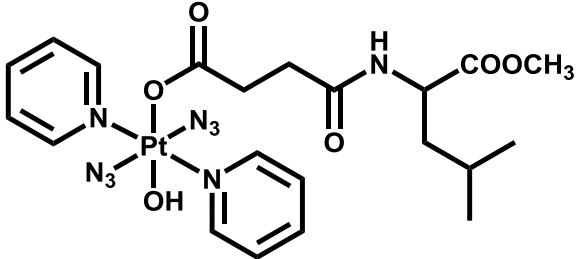
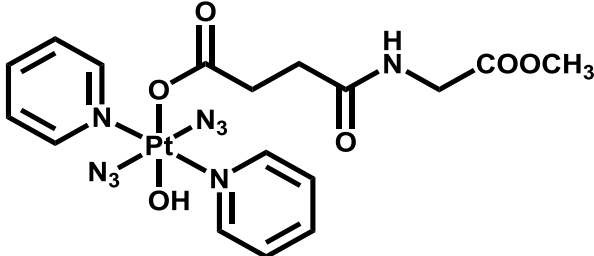
1. N. J. Farrer, J. A. Woods, L. Salassa, Y. Zhao, K. S. Robinson, G. Clarkson, F. S. Mackay, P. J. Sadler, *Angew. Chem. Int. Ed.*, 2010, **49**, 8905–8908.
2. J. S. Butler, J. A. Woods, N. J. Farrer, M. E. Newton, P. J. Sadler, *J. Am. Chem. Soc.*, 2012, **134**, 16508–16511.
3. K. Mitra, *Dalton Trans.*, 2016, **45**, 19157–19171.
4. Y. Nakabayashi, A. Erxleben, U. Létinois, G. Pratviel, B. Meunier, L. Holland, B. Lippert, *Chem. Eur. J.*, 2007, **13**, 3980–3988.
5. C. Loup, A. T. Vallina, Y. Coppel, U. Létinois, Y. Nakabayashi, B. Meunier, B. Lippert, G. Pratviel, *Chem. Eur. J.*, 2010, **16**, 11420–11431.
6. L. Cubo, A. M. Pizarro, A. Gómez Quiroga, L. Salassa, C. Navarro-Ranninger, P. J. Sadler, *J. Inorg. Biochem.*, 2010, **104**, 909–918.

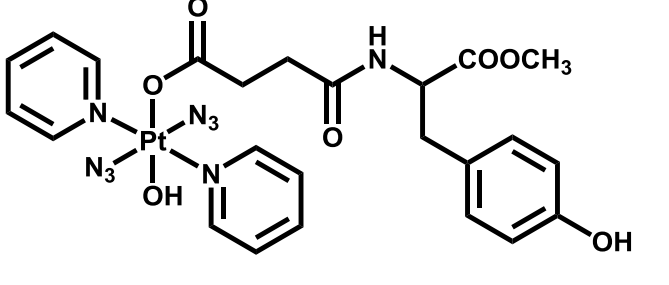
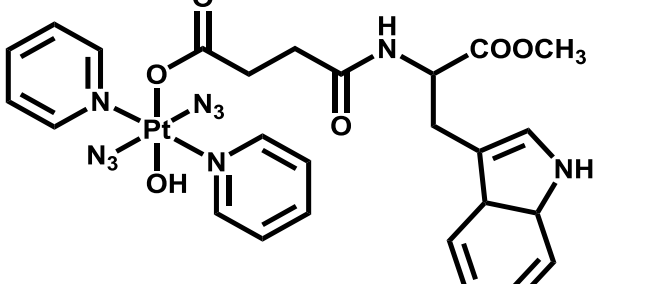
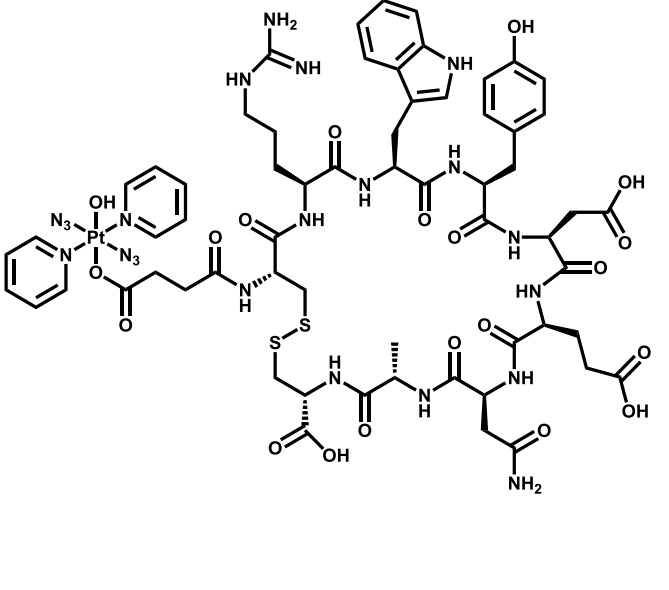
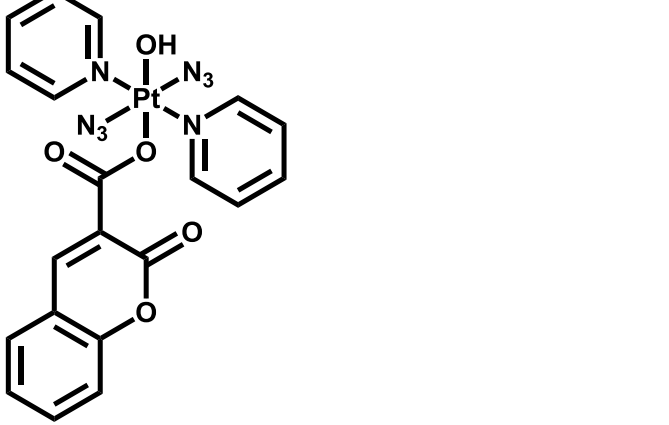
7. K. Mitra, S. Gautam, P. Kondaiah, A. R. Chakravarty, *Angew. Chem., Int. Ed.*, 2015, **54**, 13989–13993.
8. K. L. Ciesienski, L. M. Hyman, D. T. Yang, K. L. Haas, M. G. Dickens, R. J. Holbrook, K. J. Franz, *Eur. J. Inorg. Chem.*, 2010, **15**, 2224–2228.
9. Y. Zhao, G. M. Roberts, S. E. Greenough, N. J. Farrer, M. J. Paterson, W. H. Powell, V. G. Stavros, P. J. Sadler, *Angew. Chem., Int. Ed.*, 2012, **51**, 11263–11266.
10. F. S. Mackay, J. A. Woods, H. Moseley, J. Ferguson, A. Dawson, S. Parsons, P. J. Sadler, *Chem. Eur. J.*, 2006, **12**, 3155–3161.
11. F. S. Mackay, S. A. Moggach, A. Collins, S. Parsons, P. J. Sadler, *Inorg. Chim. Acta*, 2009, **362**, 811–819.
12. Y. Zhao, J. A. Woods, N. J. Farrer, K. S. Robinson, J. Pracharova, J. Kasparikova, O. Novakova, Huilin Li, Luca Salassa, Ana M. Pizarro, Guy J. Clarkson, Lijiang Song, Viktor Brabec, P. J. Sadler, *Chem. Eur. J.*, 2013, **19**, 9578–9591.
13. M. Pawlicki, H. A. Collins, R. G. Denning, H. L. Anderson, *Angew. Chem. Int. Ed.*, 2009, **48**, 3244–3266.
14. M. Albota, D. Beljonne, J. L. Bredas, J. E. Ehrlich, J. Y. Fu, A. A. Heikal, S. E. Hess, T. Kogej, M. D. Levin, S. R. Marder, D. McCord-Maughon, J. W. Perry, H. Rockel, M. Rumi, C. Subramaniam, W. W. Webb, X. L. Wu and C. Xu, *Science*, 1998, **281**, 1653–1656.
15. H. Xiao, L. Yan, E. M. Dempsey, W. Song, R. Qi, W. Li, Y. Huang, X. Jing, D. Zhou, J. Ding, X. Chen, *Prog. Polym. Sci.*, 2018, **87**, 70–106.
16. M. Imran, W. Ayub, I. S. Butler, Z. Rehman, *Coord. Chem. Rev.*, 2018, **376**, 405–429.

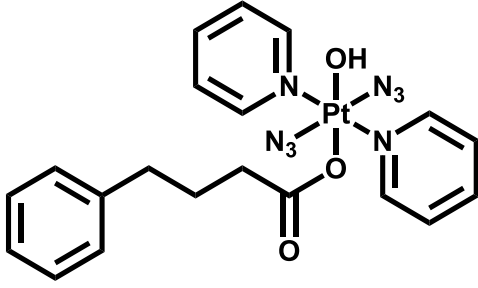
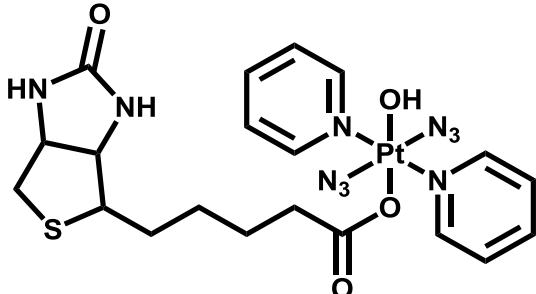
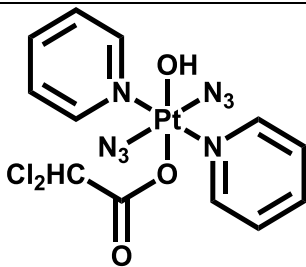
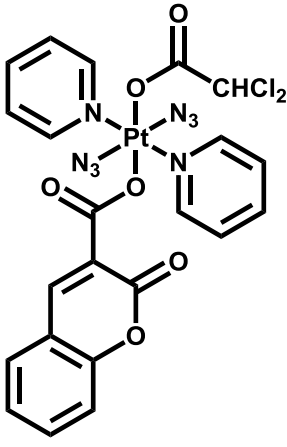
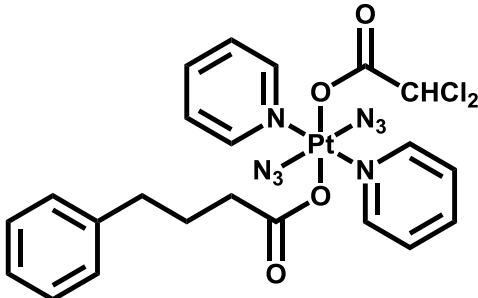
17. V. Venkatesh, N. K. Mishra, I. Romero-Canelón, R. R. Vernooij, H. Shi, J. P. C. Coverdale, A. Habtemariam, S. Verma, P. J. Sadler, *J. Am. Chem. Soc.*, 2017, **139**, 5656–5659.
18. J. Mayr, P. Heffeter, D. Groza, L. Galvez, G. Koellensperger, A. Roller, B. Alte, M. Haider, W. Berger, C. R. Kowol, B. K. Keppler, *Chem. Sci.*, 2017, **8**, 2241–2250.
19. Y. R. Zheng, K. Suntharalingam, T. C. Johnstone, H. Yoo, W. Lin, J. G. Brooks, S. J. Lippard, *J. Am. Chem. Soc.*, 2014, **136**, 8790–8798.
20. K. Singh, A. M. Rotaru, A. A. Beharry, *ACS Chem. Biol.*, 2018, **13**, 1785–1798.
21. M. Berndt-Paetz, P. Schulze, P. C. Stenglein, A. Weimann, Q. Wang, L. Horn, Y. M. Riyad, J. Griebel, R. Hermann, A. Glasow, J. Stolzenburg, J. Neuhaus, *Mol. Cancer Ther.*, 2019, 10.1158/1535-7163.MCT-18-1194.
22. P. Kaspler, S. Lazic, S. Forward, Y. Arenas, A. Mandela, L. Lilge, *Photochem. Photobiol. Sci.*, 2016, **15**, 481–495.
23. A. F. Westendorf, J. A. Woods, K. Korpis, N. J. Farrer, L. Salassa, K. Robinson, V. Appleyard, K. Murray, R. Grünert, A. M. Thompson, P. J. Sadler, P. J. Bednarski, *Mol. Cancer Ther.*, 2012, **11**, 1894–1904.

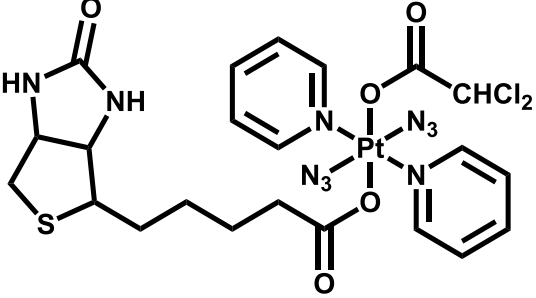
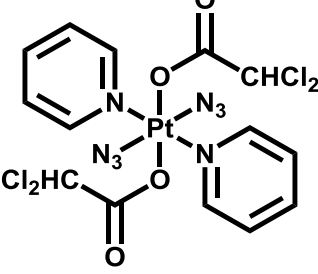
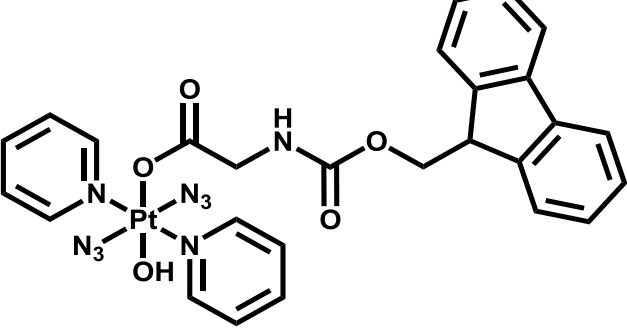
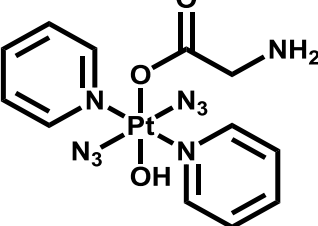
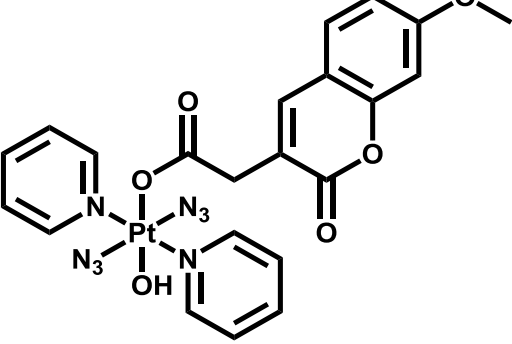
Appendix

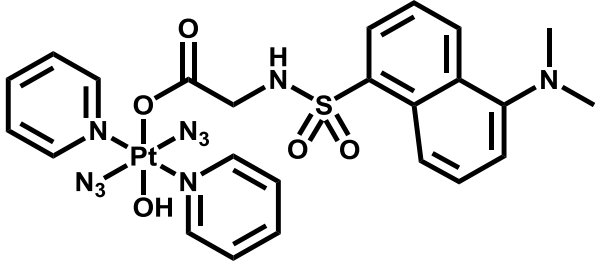
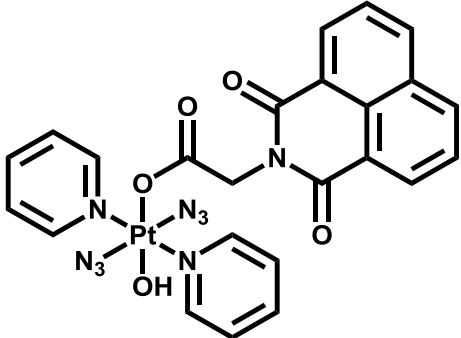
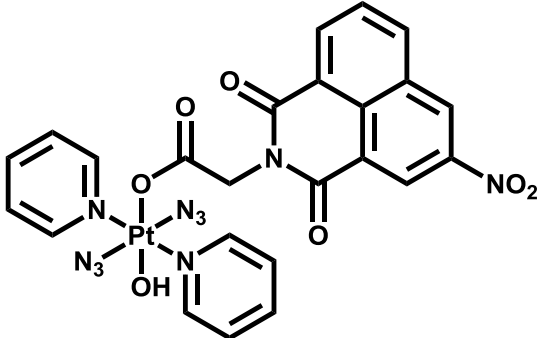
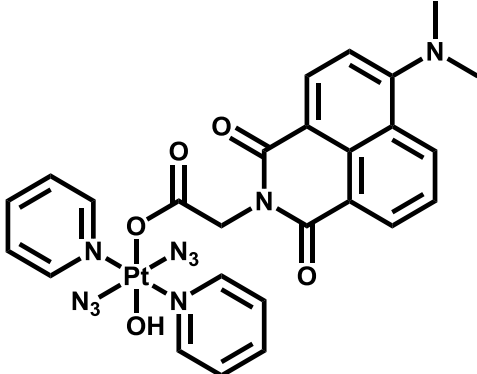
Table A1. Complexes investigated in this Thesis.

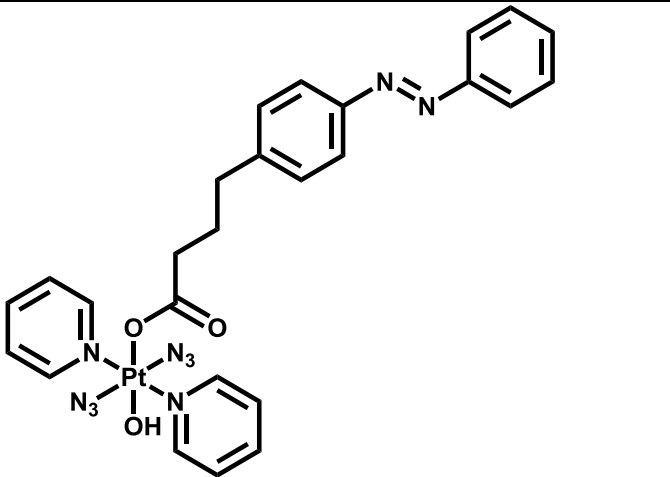
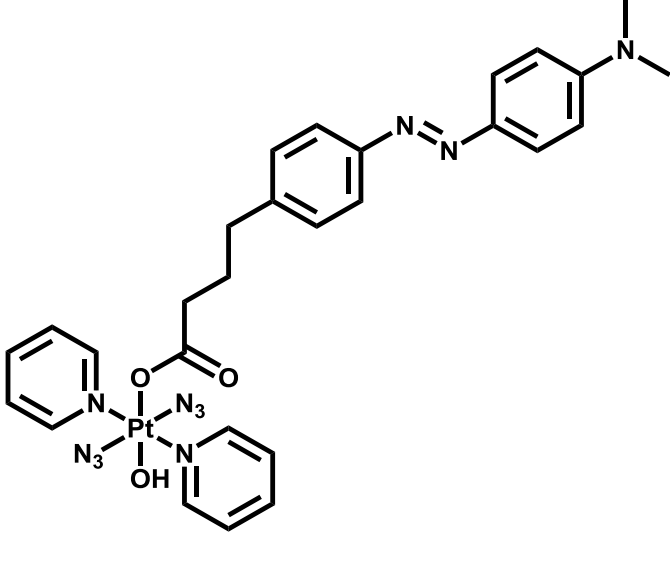
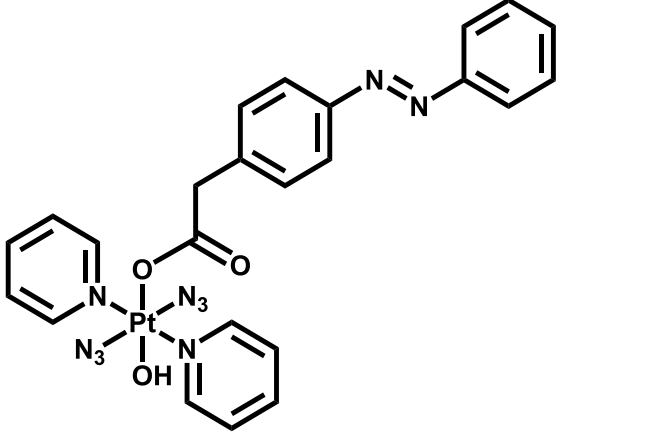
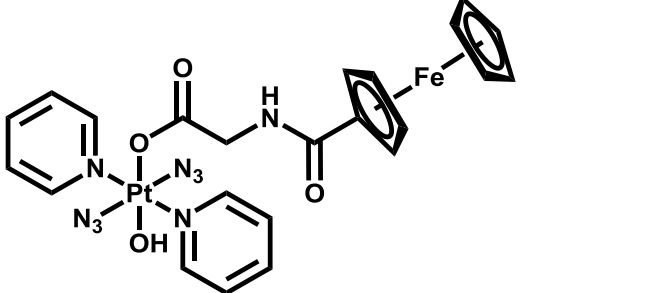
N ^o	Name	Structure
1	<i>Trans,trans,trans</i> - [Pt(py) ₂ (N ₃) ₂ (OH) ₂]	
2	<i>Trans,trans,trans</i> - [Pt(py) ₂ (N ₃) ₂ (OH)(succ)]	
3	<i>Trans,trans,trans</i> - [Pt(py) ₂ (N ₃) ₂ (OH)(succ-NHS)]	
4	<i>Trans,trans,trans</i> - [Pt(py) ₂ (N ₃) ₂ (OH)(succ-leu-OMe)]	
5	<i>Trans,trans,trans</i> - [Pt(py) ₂ (N ₃) ₂ (OH)(succ-gly-OMe)]	

6	<p><i>Trans,trans,trans-</i> [Pt(py)₂(N₃)₂(OH)(succ-tyr-OMe)]</p>	 <p>The structure shows a platinum (Pt) center in a square planar geometry. It is coordinated to two pyridine (py) rings, two azido (N₃) groups, and a hydroxyl (OH) group. The fourth coordination site is occupied by the oxygen atom of a succinyl-tyrosine methyl ester (succ-tyr-OMe) ligand. The succinyl chain is linked to the tyrosine side chain, which features a para-hydroxyphenyl group.</p>
7	<p><i>Trans,trans,trans-</i> [Pt(py)₂(N₃)₂(OH)(succ-trp-OMe)]</p>	 <p>The structure shows a platinum (Pt) center in a square planar geometry, coordinated to two pyridine (py) rings, two azido (N₃) groups, and a hydroxyl (OH) group. The fourth coordination site is occupied by the oxygen atom of a succinyl-tryptophan methyl ester (succ-trp-OMe) ligand. The succinyl chain is linked to the tryptophan side chain, which features an indol-3-ylmethyl group.</p>
8	<p><i>Trans,trans,trans-</i> [Pt(py)₂(N₃)₂(OH)(succ-cp)]</p>	 <p>The structure shows a platinum (Pt) center in a square planar geometry, coordinated to two pyridine (py) rings, two azido (N₃) groups, and a hydroxyl (OH) group. The fourth coordination site is occupied by the oxygen atom of a succinyl-cysteine peptide (succ-cp) ligand. The succinyl chain is linked to a cysteine residue, which is further connected to a complex peptide chain containing various amino acid side chains, including an indol-3-ylmethyl group, a para-hydroxyphenyl group, and a primary amine group.</p>
9	<p><i>Trans,trans,trans-</i> [Pt(py)₂(N₃)₂(cou)(OH)]</p>	 <p>The structure shows a platinum (Pt) center in a square planar geometry, coordinated to two pyridine (py) rings, two azido (N₃) groups, and a hydroxyl (OH) group. The fourth coordination site is occupied by the oxygen atom of a coumarin (cou) ligand. The coumarin moiety is shown as a fused bicyclic system consisting of a benzene ring fused to a pyrone ring.</p>

10	<i>Trans,trans,trans-</i> [Pt(py) ₂ (N ₃) ₂ (PhB)(OH)]	 <p>The structure shows a platinum (Pt) center in a square planar geometry. It is coordinated to two pyridine (py) rings, two azido (N₃) groups, a hydroxyl (OH) group, and a phenylbutyrate (PhB) ligand. The PhB ligand consists of a phenyl ring attached to a butyrate chain, which is esterified to the platinum center.</p>
11	<i>Trans,trans,trans-</i> [Pt(py) ₂ (N ₃) ₂ (biotin)(OH)]	 <p>The structure shows a platinum (Pt) center in a square planar geometry. It is coordinated to two pyridine (py) rings, two azido (N₃) groups, a hydroxyl (OH) group, and a biotin ligand. The biotin ligand is a bicyclic molecule consisting of a five-membered imidazole ring fused to a six-membered thiophene ring, with a butyrate chain attached to the thiophene ring, which is esterified to the platinum center.</p>
12	<i>Trans,trans,trans-</i> [Pt(py) ₂ (N ₃) ₂ (DCA)(OH)]	 <p>The structure shows a platinum (Pt) center in a square planar geometry. It is coordinated to two pyridine (py) rings, two azido (N₃) groups, a hydroxyl (OH) group, and a dichloroacetate (DCA) ligand. The DCA ligand consists of a dichloromethyl group (Cl₂HC) attached to a carboxylate group, which is coordinated to the platinum center.</p>
13	<i>Trans,trans,trans-</i> [Pt(py) ₂ (N ₃) ₂ (cou)(DCA)]	 <p>The structure shows a platinum (Pt) center in a square planar geometry. It is coordinated to two pyridine (py) rings, two azido (N₃) groups, a coumarin (cou) ligand, and a dichloroacetate (DCA) ligand. The coumarin ligand is a benzopyrone derivative, and the DCA ligand is a dichloromethyl group attached to a carboxylate group, both coordinated to the platinum center.</p>
14	<i>Trans,trans,trans-</i> [Pt(py) ₂ (N ₃) ₂ (PhB)(DCA)]	 <p>The structure shows a platinum (Pt) center in a square planar geometry. It is coordinated to two pyridine (py) rings, two azido (N₃) groups, a phenylbutyrate (PhB) ligand, and a dichloroacetate (DCA) ligand. The PhB ligand is a phenyl ring attached to a butyrate chain, which is esterified to the platinum center. The DCA ligand is a dichloromethyl group attached to a carboxylate group, also coordinated to the platinum center.</p>

15	<i>Trans,trans,trans</i> - [Pt(py) ₂ (N ₃) ₂ (biotin)(DCA)]	 <p>The structure shows a platinum center coordinated to two pyridine rings, two azido groups, and two bidentate ligands: biotin and dichloroacetate (DCA). The biotin ligand consists of a five-membered imidazole ring fused to a five-membered thiophene ring, with a long aliphatic chain ending in a carboxylate group. The DCA ligand is a two-carbon chain with a carboxylate group at one end and two chlorine atoms at the other.</p>
16	<i>Trans,trans,trans</i> - [Pt(py) ₂ (N ₃) ₂ (DCA) ₂]	 <p>The structure shows a platinum center coordinated to two pyridine rings, two azido groups, and two dichloroacetate (DCA) ligands. The DCA ligand is a two-carbon chain with a carboxylate group at one end and two chlorine atoms at the other.</p>
17	<i>Trans,trans,trans</i> - [Pt(py) ₂ (N ₃) ₂ (OH)(gly-Fmoc)]	 <p>The structure shows a platinum center coordinated to two pyridine rings, two azido groups, a hydroxyl group, and a glycyl-Fmoc ligand. The glycyl-Fmoc ligand consists of a glycine residue (two-carbon chain with an amino group) linked via its carboxylate group to the Fmoc (fluorenylmethyl) protecting group, which is a tricyclic system.</p>
18	<i>Trans,trans,trans</i> - [Pt(py) ₂ (N ₃) ₂ (OH)(gly)]	 <p>The structure shows a platinum center coordinated to two pyridine rings, two azido groups, a hydroxyl group, and a glycyl ligand. The glycyl ligand is a two-carbon chain with an amino group at one end and a carboxylate group at the other.</p>
19	<i>Trans,trans,trans</i> - [Pt(py) ₂ (N ₃) ₂ (cou-OMe)(OH)]	 <p>The structure shows a platinum center coordinated to two pyridine rings, two azido groups, a hydroxyl group, and a coumarin-3-carboxylate ligand with a methoxy group at the 7-position. The coumarin ligand consists of a benzene ring fused to a pyrone ring, with a carboxylate group at the 3-position and a methoxy group at the 7-position.</p>

20	<i>Trans,trans,trans-</i> [Pt(py) ₂ (N ₃) ₂ (OH)(gly-Dan)]	 <p>The structure shows a platinum (Pt) center in a square planar geometry. It is coordinated to two pyridine (py) rings, two azido (N₃) groups, and a hydroxyl (OH) group. The fourth coordination site is occupied by a gly-Dan ligand, which consists of a glycyl group (-CH₂-C(=O)-NH-) attached to a dansyl group (a benzene ring fused to an indole ring, with a dimethylamino group -N(CH₃)₂ at the 3-position).</p>
21	<i>Trans,trans,trans-</i> [Pt(py) ₂ (N ₃) ₂ (OH)(gly-NA)]	 <p>The structure shows a platinum (Pt) center in a square planar geometry. It is coordinated to two pyridine (py) rings, two azido (N₃) groups, and a hydroxyl (OH) group. The fourth coordination site is occupied by a gly-NA ligand, which consists of a glycyl group (-CH₂-C(=O)-NH-) attached to a naphthalene-1-carboxamide group.</p>
22	<i>Trans,trans,trans-</i> [Pt(py) ₂ (N ₃) ₂ (OH)(gly-NANO ₂)]	 <p>The structure shows a platinum (Pt) center in a square planar geometry. It is coordinated to two pyridine (py) rings, two azido (N₃) groups, and a hydroxyl (OH) group. The fourth coordination site is occupied by a gly-NANO₂ ligand, which consists of a glycyl group (-CH₂-C(=O)-NH-) attached to a 5-nitro-1-naphthylcarboxamide group.</p>
23	<i>Trans,trans,trans-</i> [Pt(py) ₂ (N ₃) ₂ (OH)(gly-NADM)]	 <p>The structure shows a platinum (Pt) center in a square planar geometry. It is coordinated to two pyridine (py) rings, two azido (N₃) groups, and a hydroxyl (OH) group. The fourth coordination site is occupied by a gly-NADM ligand, which consists of a glycyl group (-CH₂-C(=O)-NH-) attached to a 1-(dimethylamino)naphthalene-2-carboxamide group.</p>

24	<i>Trans,trans,trans-</i> [Pt(py) ₂ (N ₃) ₂ (OH)(b-azo)]	 <p>The structure shows a platinum (Pt) center in a square planar geometry. It is coordinated to two pyridine (py) rings, two azido (N₃) groups, and a hydroxide (OH) group. The fourth coordination site is occupied by a b-azo ligand, which consists of a propyl chain attached to a benzene ring, which is further substituted with an azo group (-N=N-) linked to another benzene ring.</p>
25	<i>Trans,trans,trans-</i> [Pt(py) ₂ (N ₃) ₂ (OH)(b-azo-NMe ₂)]	 <p>The structure is similar to entry 24, but the terminal benzene ring of the b-azo ligand is substituted with a dimethylamino group (-NMe₂).</p>
26	<i>Trans,trans,trans-</i> [Pt(py) ₂ (N ₃) ₂ (OH)(a-azo)]	 <p>The structure is similar to entry 24, but the propyl chain of the b-azo ligand is replaced by a single methylene group (-CH₂-), making it an a-azo ligand.</p>
27	<i>Trans,trans,trans-</i> [Pt(py) ₂ (N ₃) ₂ (OH)(gly-Fe)]	 <p>The structure shows a platinum (Pt) center in a square planar geometry, coordinated to two pyridine (py) rings, two azido (N₃) groups, and a hydroxide (OH) group. The fourth coordination site is occupied by a gly-Fe ligand, which consists of a propyl chain attached to a benzene ring, which is further substituted with a ferrocene group (-Fe-ferrocene).</p>

